

**EXPERIMENTAL INVESTIGATIONS OF THE STRUCTURE-PROPERTY
RELATIONS OF CO₂-SELECTIVE ZEOLITE ADSORBENTS**

by

Trong D. Pham

A dissertation submitted to the Faculty of the University of Delaware in partial fulfillment of the requirements for the degree of Doctor of Philosophy in Chemical Engineering

Spring 2015

© 2015 Trong D. Pham
All Rights Reserved

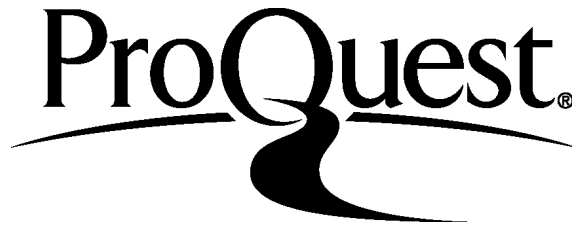
ProQuest Number: 3718370

All rights reserved

INFORMATION TO ALL USERS

The quality of this reproduction is dependent upon the quality of the copy submitted.

In the unlikely event that the author did not send a complete manuscript and there are missing pages, these will be noted. Also, if material had to be removed, a note will indicate the deletion.



ProQuest 3718370

Published by ProQuest LLC (2015). Copyright of the Dissertation is held by the Author.

All rights reserved.

This work is protected against unauthorized copying under Title 17, United States Code
Microform Edition © ProQuest LLC.

ProQuest LLC.
789 East Eisenhower Parkway
P.O. Box 1346
Ann Arbor, MI 48106 - 1346

**EXPERIMENTAL INVESTIGATIONS OF THE STRUCTURE-PROPERTY
RELATIONS OF CO₂-SELECTIVE ZEOLITE ADSORBENTS**

by

Trong D. Pham

Approved: _____
Abraham M. Lenhoff, Ph.D.
Chair of the Department of Chemical and Biomolecular Engineering

Approved: _____
Babatunde A. Ogunnaike, Ph.D.
Dean of the College of Engineering

Approved: _____
James G. Richards, Ph.D.
Vice Provost for Graduate and Professional Education

I certify that I have read this dissertation and that in my opinion it meets the academic and professional standard required by the University as a dissertation for the degree of Doctor of Philosophy.

Signed:

Raul F. Lobo, Ph.D.
Professor in charge of dissertation

I certify that I have read this dissertation and that in my opinion it meets the academic and professional standard required by the University as a dissertation for the degree of Doctor of Philosophy.

Signed:

Craig M. Brown, Ph.D.
Member of dissertation committee

I certify that I have read this dissertation and that in my opinion it meets the academic and professional standard required by the University as a dissertation for the degree of Doctor of Philosophy.

Signed:

Antony N. Beris, Ph.D.
Member of dissertation committee

I certify that I have read this dissertation and that in my opinion it meets the academic and professional standard required by the University as a dissertation for the degree of Doctor of Philosophy.

Signed:

Feng Jiao, Ph.D.
Member of dissertation committee

ACKNOWLEDGMENTS

I would like to thank you my advisor, Prof. Raul F. Lobo for all his support, thoughtfulness, and great guidance. I am very thankful to him for helping me through the difficult times during my PhD and for keeping me a part of his research group. He has also provided me with the opportunity to pursue various research topics as well as present my work at many conferences. I extremely appreciate and really grateful for all the support he has given me during my PhD. I am blessed and lucky to be his student.

I am honored to work with Prof. Craig M. Brown and Dr. Matthew Hudson at NIST Center for Neutron Research. They have helped me tremendously with the characterization techniques and with the amount of work that I presented here. I would like to also thank my thesis committee Prof. Antony N. Beris and Prof. Feng Jiao for their contributions to editing my thesis. I would also like to express my gratefulness to my great research partner, Dr. Qingling Liu.

I am thankful to have the opportunity to study at the Department of Chemical & Biomolecular Engineering at the University of Delaware. Many thanks to Mary Walsh, Kathleen Young, Rechilda Alba, George Whitmyre, and Neil Garrett for helping me with all the paperwork and lab set up. I would also like to thank all my friends and colleges at the University of Delaware, particularly, Dr. Ruichang Xiong, Dr. Nageswara Peela, Dr. Nathan D. Hould, Dr. Andrew J. Foster, and our group members Dr. Phuong Do, Dr. Matthew Wulfers, Dr. Takahiko Moteki, Dr. Shewangizaw Forsido, Jacob Weiner, Jang Ho Jun, Jason Loiland, Bahar Ipek, Molly

Koehle, Eyas Mahmoud, Edward Schreiner, and Huibo Sheng. I am especially thankful to all of my lab mates for all their support, compassion, and motivation, and for our lively discussions of science and of life in general to overcome the most stressful time in graduate school. I would also like to thank Jiao's group members, particularly Bryan Yonemoto, Greg Hutchings, and Jonathan Rosen. It is great to have close companions to relax and hangout with to get my mind off research.

Finally, I would like to thank my parents Dat Q. Pham and Thuoc T. Pham, my brother Giap Q. Pham, and my fiancée Hieu T. Nguyen for supporting me at every steps of my life. You truly have molded me into the man I am today.

Thank you again to all of you!

Trong

TABLE OF CONTENTS

LIST OF TABLES	x
LIST OF FIGURES	xiv
ABSTRACT	xxii

Chapter

1	INTRODUCTION	1
1.1	CO ₂ Emissions and the Greenhouse Effect	1
1.2	Pre-combustion and Post-combustion Capture	5
1.3	Proposed Techniques for Carbon Capture.....	6
1.3.1	Chemical absorption using aqueous amines	6
1.3.2	Cryogenic distillation	8
1.3.3	Membrane-based separation	9
1.3.4	Adsorption	10
1.4	Separation Processes	12
1.4.1	Temperature Swing Adsorption	13
1.4.2	Pressure/Vacuum Swing Adsorption.....	13
1.5	Zeolite Materials and Their Applications in CO ₂ Separation.....	14
	REFERENCES	20
2	EXPERIMENTAL PROCEDURES	23
2.1	Zeolite Synthesis	23
2.1.1	Hydrothermal method.....	23
2.1.2	Synthesis of siliceous zeolites in fluoride media.....	27
2.1.3	Ion-exchange	29
2.2	Analytical Methods	29
2.2.1	X-Ray and Neutron Powder Diffraction.....	29
2.2.2	Gas adsorption	32

2.2.3	Scanning Electron Microscopy (SEM) & Energy Dispersive X-Ray Spectroscopy (EDX) [22]	36
2.2.4	Nuclear Magnetic Resonance (NMR)	39
2.2.5	Fourier Transform Infrared Spectroscopy (FTIR) [28]	42
	REFERENCES	44
3	CARBON DIOXIDE AND NITROGEN ADSORPTION ON CATION-EXCHANGED CHABAZITE ZEOLITES	46
3.1	Introduction	46
3.2	Experimental Methods	49
3.2.1	Zeolite synthesis	49
3.2.2	Ion exchange	50
3.2.3	Characterization	50
3.3	Results and Discussion	51
3.3.1	Characterization of CHA	51
3.3.2	Fourier Transform Infrared Spectra of Adsorbed CO ₂	54
3.3.3	Adsorption isotherms of N ₂ and CO ₂ on CHA zeolites	56
3.3.4	Heats of adsorption of CO ₂ on CHA zeolites	60
3.3.5	Henry's law region	63
3.3.6	Separation ability of CO ₂ from N ₂ in a flue gas mixture for PSA and VSA processes	65
3.4	Conclusions	67
	REFERENCES	68
4	MOLECULAR BASIS FOR THE HIGH CO ₂ ADSORPTION CAPACITY OF CHABAZITE ZEOLITES	72
4.1	Introduction	72
4.2	Experimental	75
4.2.1	Zeolite Materials	75
4.2.2	Ion Exchange	76
4.2.3	Powder Diffraction	77
4.3	Results and Discussion	79
4.3.1	Cation locations in chabazite zeolites	79

4.3.2	CO ₂ adsorption sites in chabazite zeolites	88
4.3.3	Adsorption properties of sodium-exchanged zeolites	95
4.3.4	Structure-property relationship: CO ₂ adsorbed on chabazite zeolites	97
4.4	Conclusions	101
	REFERENCES	103
5	STRUCTURE-PROPERTY RELATIONSHIPS OF CATION- EXCHANGED ZK-5 ZEOLITES FOR CARBON DIOXIDE ADSORPTION.....	107
5.1	Introduction	107
5.2	Experimental.....	111
5.2.1	Preparation and characterization of zeolites.....	111
5.2.2	Volumetric adsorption of CO ₂ and N ₂ on ZK-5 zeolites	112
5.2.3	Diffraction data collection and structure determinations	113
5.3	Results and Discussion	113
5.3.1	Characterization SEM, EDX, isotherms.....	113
5.3.2	Structure of cation-exchanged ZK-5 zeolites	123
5.3.3	CO ₂ adsorption sites in Mg-ZK-5.....	131
5.3.4	CO ₂ adsorption sites in Li-ZK-5.....	138
5.3.5	N ₂ and CO ₂ co-adsorbed on Li-ZK-5	142
5.3.6	CO ₂ adsorption sites in Na-ZK-5	145
5.3.7	CO ₂ adsorption sites in K-ZK-5	147
5.3.8	Discussions on the adsorption heats and adsorption capacities.	150
5.4	Conclusions	152
	REFERENCES	153
6	EXPERIMENTAL AND COMPUTATIONAL STUDIES ON THE ADSORPTION OF CO ₂ AND N ₂ ON PURE SILICA ZEOLITES	161
6.1	Introduction	161
6.2	Methods	163
6.2.1	Experimental Section.....	163
6.2.2	Simulations	166

6.3	Results and Discussion	171
6.3.1	Materials characterization	171
6.3.2	Adsorption of CO ₂ and N ₂ on siliceous zeolites.....	176
6.4	Conclusions	187
	REFERENCES	189
7	ADSORPTION EQUILIBRIA OF CO ₂ AND SMALL HYDROCARBONS IN AEI-, CHA-, STT-, AND RRO-TYPE SILICEOUS ZEOLITES	194
7.1	Introduction	194
7.2	Experimental Section.....	196
7.2.1	Materials	196
7.2.2	Analytical Methods	198
7.2.3	Adsorption Isotherm Measurements.....	199
7.3	Results and Discussion	200
7.3.1	Materials characterization	200
7.3.2	Adsorption isotherms.....	207
7.3.3	Enthalpy and entropy of adsorption of CO ₂ and hydrocarbons in siliceous zeolites.....	222
7.4	Conclusions	227
	REFERENCES	229
8	CONCLUSIONS AND RECOMMENDATIONS.....	233
8.1	Thesis Summary	234
8.2	Recommendations for Future Studies	238
8.2.1	The adsorption of CO ₂ on various zeolite frameworks	238
8.2.2	Effect of water on the adsorption of CO ₂ in zeolites.....	240
8.2.3	Other factors on the adsorption of CO ₂	243
8.2.4	Other methods to study CO ₂ adsorption.....	244
8.3	Thesis Accomplishments.....	245
	REFERENCES	247

Appendix

LIST OF TABLES

Table 1.1.	The most important greenhouse gases and their contributions to the greenhouse effect [3].	1
Table 1.2.	Typical compositions of gases (by weight) in post-combustion and pre-combustion processes [9].	6
Table 2.1.	Synthesis cation-building unit relationship [4]	25
Table 3.1.	Compositions of metals in cation-exchanged CHA confirmed by ICP and EDX methods	53
Table 3.2.	Surface area and pore volume of cation-exchanged CHA zeolites	54
Table 3.3.	The CO ₂ adsorption heat and the Henry's law constants determined by virial plot for N ₂ and CO ₂ adsorption on CHA	66
Table 3.4.	Adsorbents evaluation parameters for flue gas separation using PSA and VSA at 303K	67
Table 4.1.	Atomic parameters from Rietveld refinement of pure silica Chabazite (Si-CHA) data at 10 K [NCNR, BT1] (Trigonal, R-3m, $a = 13.5844(3)$ Å, $c = 14.7628(5)$ Å, $V = 2359.3(1)$ Å ³). Values in parentheses indicate one standard deviation in the refined value. Goodness-of-fit parameters: $\chi^2 = 1.057$, wRp = 6.63 %, Rp = 5.27 %. Composition: Si ₃₆ O ₇₂ .	80
Table 4.2.	Cation and CO ₂ occupancies for the Chabazite zeolites in this study. The value in parentheses represents one standard deviation (in refined value).	83
Table 4.3.	Select CO ₂ bond distances (in Angstroms) for Site A (8MR) for the Chabazite zeolites in this study. The value in parentheses represents one standard deviation (in refined value).	84
Table 4.4.	Select CO ₂ bond distances (in Angstroms) for Site B (large pore) for the all-silica Chabazite zeolites in this study. The value in parentheses represents one standard deviation (in refined value).	85

Table 4.5.	Select CO ₂ bond distances (in Angstroms) and CO ₂ angles (in degrees) for Site B' (M+···CO ₂) for the Li ⁺ /Na ⁺ -exchanged Chabazite zeolites in this study. The value in parentheses represents one standard deviation (in refined value).	86
Table 4.6.	Select CO ₂ bond distances (in Angstroms) and CO ₂ angles (in degrees) for Site C (M+···CO ₂ ···M+) for the K ⁺ -exchanged Chabazite zeolites in this study. The value in parentheses represents one standard deviation (in refined value).	87
Table 4.7.	Unit cell parameters for the Chabazite zeolites in this study. The value in parentheses represents one standard deviation (in refined value).	88
Table 4.8.	Adsorption parameters of select chabazite zeolites compared to select commercial zeolites at 1 bar and 303 K.	98
Table 5.1.	Compositions of metals in cation-exchanged ZK-5 determined by inductively coupled plasma mass spectrometry (ICP) and energy-dispersive X-ray spectroscopy (EDX) methods.	114
Table 5.2.	Microporous surface area (m ² /g), external surface area (m ² /g) and micropore volume (cm ³ /g) of ZK-5 zeolites determined by liquid N ₂ adsorption measurements at 77 K.	114
Table 5.3.	Dual-site Langmuir-Freundlich parameters for CO ₂ adsorption in cation-exchanged ZK-5	120
Table 5.4.	Dual-site Langmuir parameters for CO ₂ adsorption in cation-exchanged ZK-5	121
Table 5.5.	Refined unit cell parameters, cation locations, occupancies/(atoms per unit cell), and cation-framework oxygen distances in cation-exchanged ZK-5. Values in parentheses indicate one standard deviation in the final digit.	127
Table 5.6a.	Tetrahedral bond lengths and angles for the refinement of Li-ZK-5 XRD patterns taken at 298K	129
Table 5.6b.	Tetrahedral bond lengths and angles for the refinement of Na-ZK-5 XRD patterns taken at 110K	129
Table 5.6c.	Tetrahedral bond lengths and angles for the refinement of K-ZK-5 XRD patterns taken at 110K	130

Table 5.6d.	Tetrahedral bond lengths and angles for the refinement of Mg-ZK-5 XRD patterns taken at 298K	130
Table 5.7.	T-T distances in cation-exchanged ZK-5	130
Table 5.8.	Atomic parameters from Rietveld refinement of CO ₂ /Li-ZK-5 data at 298 K [APS, 1-BM] (cubic, <i>Im3m</i> , $a = 18.6249(3) \text{ \AA}$, $V = 6460.8(2) \text{ \AA}^3$). Values in parentheses indicate one standard deviation in the refined value. Goodness-of-fit parameters: $wRp = 3.33 \%$, $Rp = 2.5 \%$. The refined composition is: [Li ₁₆ Al _{20.64} Si _{75.36} O ₁₉₂][CO ₂] _{24.9}	140
Table 5.9.	Atomic parameters from Rietveld refinement of N ₂ , CO ₂ /Li-ZK-5 data at 110 K [APS, 1-BM] (cubic, <i>Im3m</i> , $a = 18.6820(3) \text{ \AA}$, $V = 6520.3(2) \text{ \AA}^3$). Values in parentheses indicate one standard deviation in the refined value. Goodness-of-fit parameters: $wRp = 1.72 \%$, $Rp = 1.3 \%$. The refined composition is: [Li ₁₆ Al _{20.64} Si _{75.36} O ₁₉₂][CO ₂] _{24.8} [N ₂] ₁₆	144
Table 6.1.	LJ and Coulombic Potential Parameters. LJ parameters for the unlike-pair interactions are calculated with Lorentz-Berthelot combining rules.	169
Table 6.2.	Optimized unit cell dimensions and space group assigned to each of the pure silica zeolites	172
Table 6.3.	Surface area and micropore volume of pure silica zeolites.....	175
Table 6.4.	Heats of adsorption at zero coverage and Henry's constants (303K) of CO ₂ and N ₂ adsorbed on PSZ.....	184
Table 7.1.	Pore shape, dimension, and surface area (m ² /g), micropore volume (cm ³ /g) of pure silica zeolites.....	204
Table 7.2.	Properties of adsorbate gases: Kinetic diameters (K.D, \AA), liquid volume (L.V, cm ³ /mol), Polarizability (P, $\times 10^{25} \text{ cm}^3$), Dipole moment (D, $\times 10^{18} \text{ esu.cm}$), Quadrupole (Q, $\times 10^{26} \text{ esu.cm}^2$) [38].....	207
Table 7.3.	Adsorption heats at zero coverage limit (Q_o^{st}) of gases and selectivity (Sel) of CO ₂ /CH ₄ over studied zeolites	223
Table 7.4.	Experimental adsorption entropies of adsorbates in siliceous zeolites. The standard state for the gas phase hydrocarbons is taken as $P_o = 10^5 \text{ Pa}$	225

Table 8.1.	Properties of several adsorbates in flue gas mixture [13]	244
------------	---	-----

LIST OF FIGURES

Figure 1.1.	World primary energy consumption until 2013 and the predicted global energy demand until 2035. Figure based on data from BP statistical review of world energy 2013 [4]	3
Figure 1.2.	Schematic drawing of the concept of carbon capture and storage process	4
Figure 1.3.	Phase diagram of CO ₂	4
Figure 1.4.	General reaction schemes for the chemical absorption of CO ₂ by primary (or secondary) and tertiary amine-containing solvents [9]	8
Figure 1.5.	Principle of gas separation membrane [2]	10
Figure 1.6.	Schematic diagrams of idealized TSA, PSA, and VSA processes for regenerating solid adsorbent in a fixed-bed column [27]	13
Figure 1.7.	Illustration of zeolite structure	15
Figure 1.8.	Structure of FAU (left) and LTA (right) zeolites	16
Figure 1.9.	Structure of BEA (left) and MFI (right) zeolites	17
Figure 1.10.	Structure of chabazites (CHA-type) zeolite	17
Figure 1.11.	Composite building units of ZK-5 (KFI-type) zeolite	17
Figure 2.1.	Schematic of a general hydrothermal zeolite synthesis. The starting reactants (solids containing Si-O and Al-O bonds) are converted in a mineralizing medium into the crystalline zeolite product (Si-O-Al bonds) [1]	24
Figure 2.2.	Structure of commercial and synthesized organic templates for zeolite synthesis	26
Figure 2.3.	The IUPAC classification for adsorption isotherms [15]	32
Figure 2.4.	Schematic for the SEM operation	37

Figure 3.1.	Schematic view of the known cation positions in chabazite framework	47
Figure 3.2.	XRD patterns of calcined Na-CHA (Si/Al=6 and 12).....	52
Figure 3.3.	SEM images of calcined CHA (Si/Al=6 (a) and Si/Al=12 (b))	53
Figure 3.4.	FTIR spectra of adsorbed CO ₂ on Li-CHA/6 at 298K	55
Figure 3.5.	Adsorption isotherms of N ₂ on cation-exchanged CHA at 303 K	57
Figure 3.6.	Adsorption isotherms of CO ₂ on cation-exchanged CHA at 303 K.....	58
Figure 3.7.	Heat of adsorption of CO ₂ on cation-exchanged CHA zeolites (Si/Al=6 and 12).....	64
Figure 3.8.	Virial plot of N ₂ and CO ₂ on Na-CHA/6.....	64
Figure 3.9.	Isotherms of CO ₂ adsorbed on CHA at 303K and VSA, PSA separation regions on a semi-log plot.....	65
Figure 4.1.	Illustration of the chabazite structure and typical cation locations (Li ⁺ : blue, Na ⁺ : orange, and K ⁺ : purple) in the zeolite pores (right). 8MR and double 6MR (D6R) are indicated (left, Si/Al: dark blue) with oxygen atoms (red) omitted for clarity.....	82
Figure 4.2a.	Rietveld refinement of neutron powder diffraction data for 1.0 CO ₂ per 8MR dosed in Si-CHA at 10 K. <i>Note</i> : Green line, black circles, and red line represent the background, experimental, and calculated diffraction patterns, respectively. The blue line represents the difference between experimental and calculated patterns.....	89
Figure 4.2b.	Rietveld refinement of X-ray powder diffraction data for 0.5 CO ₂ per 8MR dosed in Si-CHA at 100 K. <i>Note</i> : Green line, black circles, and red line represent the background, experimental, and calculated diffraction patterns, respectively. The blue line represents the difference between experimental and calculated patterns.....	90
Figure 4.3.	(Left) CO ₂ adsorption sites in pure silica chabazite with framework oxygen atoms omitted for clarity (site A: 8MR, yellow oxygen atoms; site B: cage, green oxygen atoms). (Right) Detailed view of site A CO ₂ in the center of the 8MR (bottom) and site B with short interaction distances to the red framework oxygens given by dashed lines (top).....	93

Figure 4.4.	Partial pore views of CO ₂ adsorption sites in Li-CHA-6 (left), Na-CHA-6 (center), and K-CHA-6 (right) zeolites. Site A is similar to that previously determined for Cu ²⁺ -exchanged chabazite ^[7] (indicated by yellow oxygens) and the displacement of the cation (blue Li ⁺ ; orange Na ⁺) strongly influences the coordination of the second CO ₂ adsorption site to a site B' with the CO ₂ moving closer to the D6R with Li ⁺ . Note that site A, while present in K-CHA-6, has been omitted for clarity in depicting the dual-cation bridged via cation sites SII/SIII' or SII/SII.	94
Figure 4.5.	Total CO ₂ adsorption isotherms at 303 K for chabazite zeolites (Si-CHA: open square/dashed-line, Na-CHA-12: open square/solid line, Na-CHA-6: closed square/solid line), Linde type A zeolites: close star/solid line, and faujasite zeolites (HY40: open circle/dashed-line, NaY: open circle/solid line, Na13X: closed circle/solid line). Note: Data is in agreement with our previous publication on this ^[8]	96
Figure 4.6.	Isosteric heats of CO ₂ adsorption ($-Q_{st}$) on chabazite zeolites and faujasite zeolites as a function of amount adsorbed. * 36T atoms are equal to 1 unit cell (uc) of chabazite and 3/16 uc of faujasite zeolites....	99
Figure 5.1.	Illustration of the KFI structure and the cation locations in the zeolite pores observed in this study.	110
Figure 5.2.	SEM images of cation-exchanged ZK-5	115
Figure 5.3.	Volumetric CO ₂ adsorption isotherms (closed symbols) at 283 K (squares), 303 K (circles), 323 K (stars), and 343 K (triangles) in Li-ZK-5 (a), Na-ZK-5 (b), K-ZK-5 (c), and Mg-ZK-5 (d). The solid lines are fits to the dual-site Langmuir-Freundlich (DSLFF) model.	117
Figure 5.4a.	Pure component, volumetric CO ₂ adsorption isotherms in Li-ZK-5 at 283 K (squares), 303 K (circles), 323 K (stars), and 343 K (triangles). Dual-site Langmuir-Freundlich fit (solid line), and Dual-site Langmuir fit (dash line).....	118
Figure 5.4b.	Pure component, volumetric CO ₂ adsorption isotherms in Na-ZK-5 at 283 K (squares), 303 K (circles), 323 K (stars), and 343 K (triangles). Dual-site Langmuir-Freundlich fit (solid line), and Dual-site Langmuir fit (dash line).....	118

Figure 5.4c. Pure component, volumetric CO ₂ adsorption isotherms in K-ZK-5 at 283 K (squares), 303 K (circles), 323 K (stars), and 343 K (triangles). Dual-site Langmuir-Freundlich fit (solid line), and Dual-site Langmuir fit (dash line).....	119
Figure 5.4d. Pure component, volumetric CO ₂ adsorption isotherms in Mg-ZK-5 at 283 K (squares), 303 K (circles), 323 K (stars), and 343 K (triangles). Dual-site Langmuir-Freundlich fit (solid line), and Dual-site Langmuir fit (dash line).....	119
Figure 5.5. Isostatic heats of adsorption, Q_{st} , of CO ₂ on cation exchanged ZK-5 zeolites as a function of loading.	122
Figure 5.6. Cation sites in the hexagonal prism: Li ⁺ (a), Na ⁺ (b), K ⁺ (c); and Na ⁺ in the puckered (d, e) and K ⁺ in the flat (f) 8-membered rings	125
Figure 5.7. Mg cation site and the shrinkage of KFI unit cell	126
Figure 5.8. CO ₂ adsorption site (site A) in the flat 8-membered ring of ZK-5 zeolite and detail illustrating interactions between CO ₂ and framework oxygens (dash line).....	132
Figure 5.9. Adsorption site B (left), Fourier map (middle), and site B* (right) of CO ₂ in γ -cage of Mg-ZK-5.....	132
Figure 5.10. Close contacts (dash-line, green) of Oc-Oz ($3 \text{ \AA} < d_{Oc-Oz} < 4 \text{ \AA}$) and long-range interactions (dash-line, grey) of Oc-Oz ($4 \text{ \AA} < d_{Oc-Oz} < 5 \text{ \AA}$) of CO ₂ site B (left), B' (right) in ρ -cage of Mg-ZK-5	133
Figure 5.11. CO ₂ adsorption site in the α -cage of Mg-ZK-5 (site C) and dual-cation site between 2 Mg ²⁺ /Li ⁺ and CO ₂ (site C) in Mg-ZK-5	135
Figure 5.12. Fourier maps (yellow, left) indicated 2 adsorption sites inside α -cage of Mg-ZK-5 (right) at high loading of CO ₂	136
Figure 5.13. Visualization of adsorption sites C, D and their maximum number of CO ₂ molecules in one α -cage in Mg-ZK-5.....	137
Figure 5.14. Adsorption site D in Mg-ZK-5 and the interaction of Oc with framework oxygens	137
Figure 5.15. Adsorption site of CO ₂ at the center of the puckered 8MR in Li- ZK-5 and its interaction with framework oxygens in puckered 8MR	138
Figure 5.16. Illustration for the movement of Li ⁺ out of 6MRs upon adsorption.....	139

Figure 5.17. Illustration of CO ₂ -CO ₂ interactions of various CO ₂ adsorption sites ..	141
Figure 5.18. Positions of extraframework cations positions in faujasite zeolite	141
Figure 5.19. Fourier difference scattering length density (yellow regions) clearly indicates the adsorbed N ₂ is primarily located on top of the open Li ⁺ ions (left) and the configuration of N ₂ on Li ⁺ in 6MR of ZK-5 zeolite (right).....	143
Figure 5.20. Fourier map to assign for the adsorption site B of CO ₂ in Na-ZK-5 (left) and dual-cation adsorption site between two cation Na ⁺ (SII) and CO ₂ in <i>pau</i> -cage (right).	146
Figure 5.21. Adsorption site C of CO ₂ in Na-ZK-5. The site could be single-cation or dual-cation adsorption site due to the uncompleted occupancy of Na ⁺ (SI')	147
Figure 5.22. Dual-cation sites of CO ₂ on K-ZK-5 in α -cage (site E)	148
Figure 5.23. Adsorption site B of CO ₂ in <i>pau</i> -cage of K-ZK-5 and the close contacts between O of CO ₂ and framework oxygens (dash line, grey). 149	
Figure 5.24. Fourier maps to assign the adsorption site F in K-ZK-5	149
Figure 6.1. X-Ray diffraction patterns of calcined pure silica zeolites	173
Figure 6.2. SEM images of calcined pure silica zeolites BEA (a), CHA (b), FER (c), MFI-OH (d), MFI (e), STT (f)	174
Figure 6.3. ²⁹ Si MAS NMR spectra of BEA*, CHA, FER, MFI, MFI-OH, and STT samples	175
Figure 6.4. Computed and measured adsorption isotherms of CO ₂ (273, 303, and 343 K) and N ₂ (303 K) on BEA, CHA, FER, MFI, and STT-type zeolites.....	178
Figure 6.5. Computed adsorption isotherms of CO ₂ (303 K) on BEA*, polymorphs A, B and C.....	179
Figure 6.6. CO ₂ and N ₂ adsorbed on pure silica zeolites at 303K. Note the difference in the scale of the ordinate axis	179

Figure 6.7.	Interaction energies of CO ₂ and N ₂ adsorbed on siliceous chabazite CHA zeolite, U _{AA_LJ} : Lennard-Jones adsorbate-adsorbate interaction, U _{AA_ES} : electrostatic adsorbate-adsorbate interaction, U _{AF_LJ} : Lennard- Jones adsorbate-zeolite interaction, U _{AF_ES} : electrostatic adsorbate- zeolite interaction, Q _{st} : adsorption heat.	181
Figure 6.8.	Adsorption isotherms of CO ₂ on pure silica zeolites at 273 K	182
Figure 6.9.	Heats of adsorption of CO ₂ on PSZ at a function of amount adsorbed.	184
Figure 6.10.	Density distribution shown for CO ₂ adsorption in (a) BEA, (b) CHA, (c) FER, (d) MFI and (e) STT at low pressure. The white-color clouds show the lowest-energy adsorption sites. The number of unit cells in x, y, z dimensions used for visualization is (a) 2×2×1, (b) 2×2×2, (c) 2×1×1, (d) 1×1×1, and (e) 2×1×2. All zeolites are in show in [0,1,0] direction. Legend: orange color for silicon atoms and red color for oxygen atoms on zeolites.	187
Figure 7.1.	Structure of AEI, CHA, STT, and RRO framework-type zeolites. <i>Note:</i> Oxygen atoms were omitted for clarity. The distances reported in the pictures are Si-Si distances in each zeolite framework. The unrestrained distances for gas molecules to pass through are roughly obtained by subtracting O atoms diameters (~2.5 Å).	196
Figure 7.2a.	X-ray diffraction patterns of CHA and STT zeolites	202
Figure 7.2b.	X-ray diffraction patterns of AEI- and RRO-type materials. The second set of patterns displays the superposition of the as-made RUB- 39 and the calcined RUB-41 zeolites.	203
Figure 7.3a.	SEM images and XRD patterns of AEI (left) and RRO (right) siliceous zeolites.	204
Figure 7.3b.	SEM images of CHA (left) and STT (right) zeolites	204
Figure 7.4a.	²⁹ Si MAS NMR spectra of AEI (left) and RRO (right) siliceous zeolites	206
Figure 7.4b.	²⁹ Si MAS NMR spectra of CHA (left) and STT (right) siliceous zeolites	206
Figure 7.5a.	Adsorption isotherms of CO ₂ and CH ₄ on AEI zeolite at various temperatures up to pressure 101.325 kPa	209

Figure 7.5b. Adsorption isotherms of CO ₂ and CH ₄ on CHA zeolite at various temperatures up to pressure 101.325 kPa.....	210
Figure 7.5c. Adsorption isotherms of CO ₂ and CH ₄ on RRO zeolite at various temperatures up to pressure 101.325 kPa.....	211
Figure 7.5d. Adsorption isotherms of CO ₂ and CH ₄ on STT zeolite at various temperatures up to pressure 101.325 kPa.....	212
Figure 7.5e. Adsorption isotherms of C ₂ H ₄ and C ₂ H ₆ on AEI zeolite at various temperatures up to pressure 101.325 kPa.....	213
Figure 7.5f. Adsorption isotherms of C ₂ H ₄ and C ₂ H ₆ on CHA zeolite at various temperatures up to pressure 101.325 kPa.....	214
Figure 7.5g. Adsorption isotherms of C ₂ H ₄ and C ₂ H ₆ on RRO zeolite at various temperatures up to pressure 101.325 kPa.....	215
Figure 7.5h. Adsorption isotherms of C ₂ H ₄ and C ₂ H ₆ on STT zeolite at various temperatures up to pressure 101.325 kPa.....	216
Figure 7.5i. Adsorption isotherms of C ₃ H ₆ on CHA and RRO zeolites at various temperatures up to pressure 101.325 kPa.....	217
Figure 7.5j. Adsorption isotherms of C ₃ H ₆ and C ₃ H ₈ on STT zeolite at various temperatures up to pressure 101.325 kPa.....	218
Figure 7.6. Adsorption isotherms of CO ₂ , N ₂ , CH ₄ , C ₂ H ₄ , C ₂ H ₆ , C ₃ H ₆ and C ₃ H ₈ on STT siliceous zeolite at ambient temperature (303K) up to pressure 101.325 kPa.....	221
Figure 7.7. Adsorption isotherms of CO ₂ , CH ₄ , C ₂ H ₄ , and C ₂ H ₆ on AEI, CHA, STT, and RRO siliceous zeolites at ambient temperature (303 K) up to pressure 101.325 kPa.....	222
Figure 7.8. Interdependency between adsorption enthalpies and adsorbate polarizabilities, adsorption entropies, and the number of C atoms of alkanes in STT zeolite	225
Figure 7.9. Adsorption heats of CO ₂ and small hydrocarbons adsorbed on AEI, CHA, STT, and RRO siliceous zeolites	227
Figure 8.1. Adsorption isotherms of CO ₂ on Na-CHA and Na-AFX at 273 K and 303 K.....	238

Figure 8.2.	The composite building units (<i>gme</i> -left, <i>aft</i> -right) of AFX zeolite	239
Figure 8.3.	A schematic of the chemical modification of the zeolite surface.....	239
Figure 8.4.	Adsorption isotherms of H ₂ O on NaY, Si-CHA and cation-exchanged CHA at 303 K.....	242
Figure 8.5.	Adsorption sites of CO ₂ and H ₂ O co-adsorbed on Cu-CHA-6	243

ABSTRACT

Due to the increase in the anthropogenic CO₂ emissions, the development of carbon capture and storage technology is of profound importance to minimizing global climate change and preserving our environment. In this thesis, I have investigated the adsorption properties of cation-exchanged high silica zeolites chabazite (CHA, Si/Al=6 and 12) and ZK-5 (KFI, Si/Al=3.7) due to their high surface area, large pore volume, and moderate hydrophilic properties compared to commercial faujasite and Linde type A zeolites. Li- and Na- cation-exchanged zeolites displayed high adsorption capacity (~ 5 mmol/g at 303 K and 1 bar pressure), comparable to the commercial zeolites, and high selectivity of CO₂ over N₂. In general, Li-cation zeolites show the highest capacity for N₂ and CO₂, but lower selectivity of CO₂/N₂ compared to Na-cation zeolites. The acidity of both the adsorbate and adsorbents, in addition to the low electric field of proton-exchanged zeolites lead to the low adsorption affinity of these materials with CO₂. Large cations K⁺ occupy more space in the void pore of zeolites, thus leave less volume for CO₂ molecules. For zeolite materials to be practical and useful as adsorbents for CO₂ capture from flue gas, a number of aspects need to be carefully evaluated including adsorption and working capacities, selectivity, and adsorbent regeneration. We found that Li-, and Na-zeolites having high heats of adsorption (40-50 kJ/mol) performed better in the vacuum swing adsorption process and H- and K-zeolites or zeolites with higher Si/Al ratio (CHA, Si/Al=12) having lower heats of adsorption (30-40 kJ/mol) display properties more suited to pressure swing adsorption. The in situ FTIR CO₂ adsorption spectra show

that physisorption accounts for the largest fraction of the total CO₂ adsorbed. A shift to higher frequency of the asymmetric stretching vibration compared to CO₂ gas phase (2349 cm⁻¹) indicated the direct coordination of cations with oxygens of CO₂ molecules.

To improve zeolite adsorbents for CO₂ capture, we have determined the adsorption sites of CO₂ in Si-CHA, cation-exchanged CHA and ZK-5 zeolites using the Rietveld refinements of X-ray and neutron powder diffraction data. The structural refinements indicated that CO₂ at equilibrium is located close to zeolite framework oxygens due to dispersion interactions and CO₂ coordinates with alkali cations by electrostatic interactions. Two CO₂ adsorption sites were identified in both high and pure silica chabazite zeolites. The dispersion interactions between Si-CHA zeolite and CO₂ is the majority of the adsorption energy, and the strength of the adsorption depends on the effective close interaction distances between CO₂ molecules and the zeolites ($d[C(CO_2)-O(zeo)]$ and $d[O(CO_2)-O(zeo)]$ are 3-4 Å). Therefore, CO₂ site in the middle of 8MR (site A) having total of 24 close contacts with framework oxygens is more stable than CO₂ site in the cage (site B) with only 15 close contacts with framework oxygens in total. Even though site B* in cation-exchanged chabazites is strengthened by electrostatic interactions with zeolite frameworks, but higher occupancies of site A in the 8MRs were identified due to high quadrupole and dispersion interactions between CO₂ and 8MR zeolite. The decrease in the hardness of metal cations $Li^+ > Na^+ > K^+ > Cu^{2+}$ resulted in a decrease in the direct interactions of these cations with adsorbate CO₂. The structural analysis of CO₂ and H₂O co-adsorbed on Cu-CHA-6 showed that water is preferentially adsorbed at the copper sites, while CO₂ is located predominantly in the 8MRs.

Our refinement of X-ray diffraction patterns on bare adsorbent ZK-5 showed that Na^+ locates in three different sites in D6R and in 8MR, Li^+ prefers to locate at the center of the D6R, Mg^{2+} is located in the hexagonal prism, and larger cation K^+ is in the middle of 8-membered rings. The weighted average of T-O distances for the feldspar structure with $\text{Si}/\text{Al}=3.65$ is 1.64 \AA , which is similar to the values of 1.63 \AA - 1.64 \AA in these refinements. The average of O-T-O angles is 109.5° with small deviations around this value for all cation-exchanged ZK-5 samples in agreement with tetrahedral coordination. We observed 3 different CO_2 sites on Na-ZK-5, K-ZK-5 and Mg-ZK-5, and 4 CO_2 adsorption sites were found on Li-ZK-5. The studies of the interactions of CO_2 with Li, Na, K, and Mg-ZK-5 provide better understanding about the strength of the interactions of CO_2 with extra-framework cations in ZK-5. The Rietveld refinement results also suggested that 8-membered ring zeolites have high affinity with CO_2 molecules and are potential for CO_2 separation, especially in the presence of water. Due to the high water content in flue gases, hydrophobic zeolites need to be developed to have better separation performance. Various types of zeolite frameworks including BEA*, CHA, FER, MFI, and STT were investigated in the adsorption of CO_2 and N_2 by experimental volumetric adsorption and Grand Canonical Monte Carlo simulations. All siliceous zeolites showed low CO_2 adsorption heats (18-28 kJ/mol) due to the lack of the electric fields in the zeolite pores. FER siliceous zeolite with narrow pore openings displayed highest adsorption heats and highest selectivity of CO_2/N_2 and CHA zeolite has the highest adsorption capacity at ambient conditions of temperature and pressure. The study of adsorption of light hydrocarbons and CO_2 in siliceous AEI, CHA, RRO, and STT zeolites led to a conclusion that RRO has highest selectivity of CO_2 over CH_4 and AEI, CHA, RRO all showed their

potentials for the kinetic separation of propylene/propane mixture. The results from the thesis indicated our ability to design and tune the properties of zeolite materials to make these adsorbents better for CO₂ separation.

Chapter 1

INTRODUCTION

1.1 CO₂ Emissions and the Greenhouse Effect

The global warming of the Earth's atmosphere and surface, known as the greenhouse effect, due to the increase in anthropogenic CO₂ emissions is one of the most prominent environmental and energy policy issues of our age [1]. Its consequences will affect us all. The greenhouse effect is a process by which thermal radiation from the earth surface is absorbed by atmospheric greenhouse gases, and is re-radiated in all directions. Since part of this re-radiation reflects back towards the earth surface and the lower atmosphere, it results in an elevation of the average surface temperature above what it would be in the absence of the gases. The global-scale anthropogenic emissions of greenhouse gases into the atmosphere are responsible for various environmental problems such as the increase of the land and ocean temperatures, the continuous rise of sea water levels, the increasing number of extreme weather events such as ocean storms and floods [2].

Table 1.1. The most important greenhouse gases and their contributions to the greenhouse effect [3].

Gas	Contribution (%)	Volume (%)	Lifetime
Water	36-72	0.4	100 years
Carbon dioxide	9-26	0.039	100-1000 years
Methane	4-9	0.00018	10 years
Ozone	3-7	0-0.000007	hours to months

Table 1.1 shows that water, carbon dioxide, and methane are the most important greenhouse gasses. Additionally, ozone, nitrous oxide, and synthetic gasses such as chlorofluorocarbons (CFCs), hydrofluorocarbons (HFCs) and perfluorocarbons (PFCs), as well as sulfur hexafluoride (SF₆) also contribute to the greenhouse effects.

Beer's law states that there is a logarithmic dependence between the transmission T of light through a substance and the product of the density of the gas, ρ , the absorption coefficient of the substance, σ , and the distance the light travels through the material (i.e., the path length), ℓ .

$$T = \frac{I}{I_0} = e^{-\rho\sigma\ell} \quad (1.1)$$

According to Beer's law, if at a specific wavelength the atmosphere is fully or mostly absorbing radiation, then adding more of a substance with a similar absorption coefficient will have a smaller effect. Therefore, chemicals that absorb at the same wavelength as H₂O can be very strong greenhouse gases, but their effect will be insignificant because H₂O is already prevailing in the atmosphere. However, adding gases that are strongly absorbing at a wavelength where the atmosphere is transparent will have a stronger effect. This is the case with molecules CO₂ and CH₄, which makes them strong greenhouse gasses. Table 1.1 also indicates that the lifetime of CO₂ in the atmosphere is very long, which cause it to have more severe effects on the environment [3].

The world energy consumption in Figure 1.1 shows that fossil fuels, including oil, coal, and natural gas still remain the world's leading fuels, accounting for more than 80% of the global energy consumption. The burning of these fossil fuels produces

approximately 30 billion tons of CO₂ annually following the basic combustion equation:

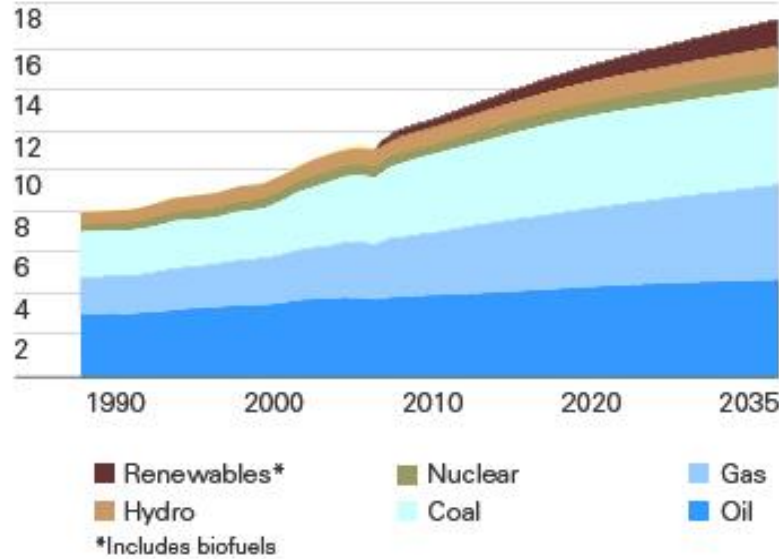
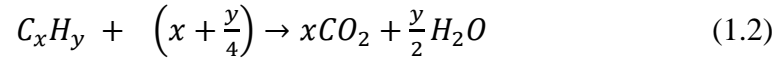


Figure 1.1. World primary energy consumption until 2013 and the predicted global energy demand until 2035. Figure based on data from BP statistical review of world energy 2013 [4]

Carbon capture and storage/sequestration (CCS) is the best solution to mitigate the effect of CO₂ on the environment. The idea of CCS is capturing CO₂ at the point of combustion, followed by compressing and transporting of the CO₂ through pipelines, and then storing it in geological formations in such a way that the CO₂ is permanently stored with minimal impact on the environment (Figure 1.2). The capture of CO₂ from power plant flue gas accounts for three quarters of the total cost of CCS and is considered to be one of the greatest challenges for the 21st century [2, 5].

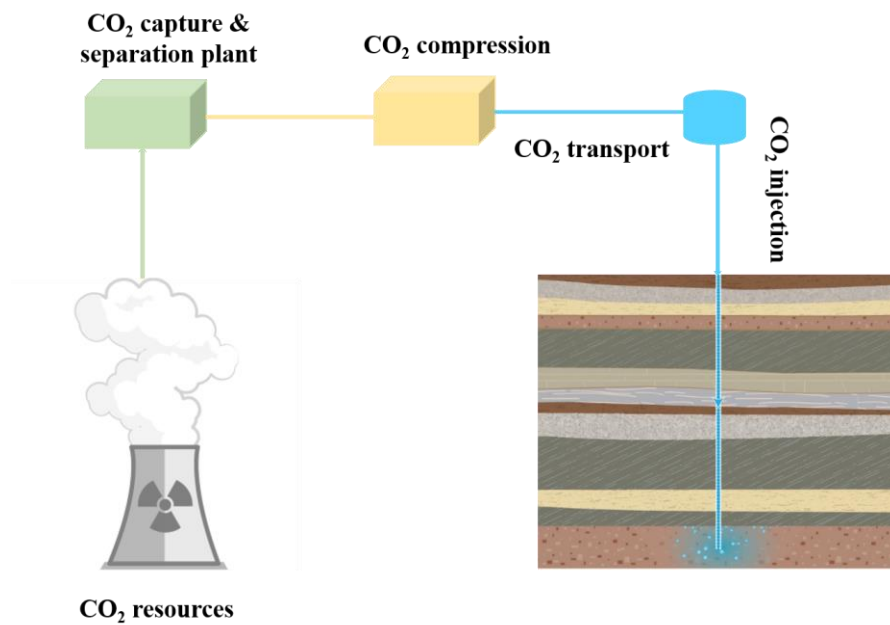


Figure 1.2. Schematic drawing of the concept of carbon capture and storage process

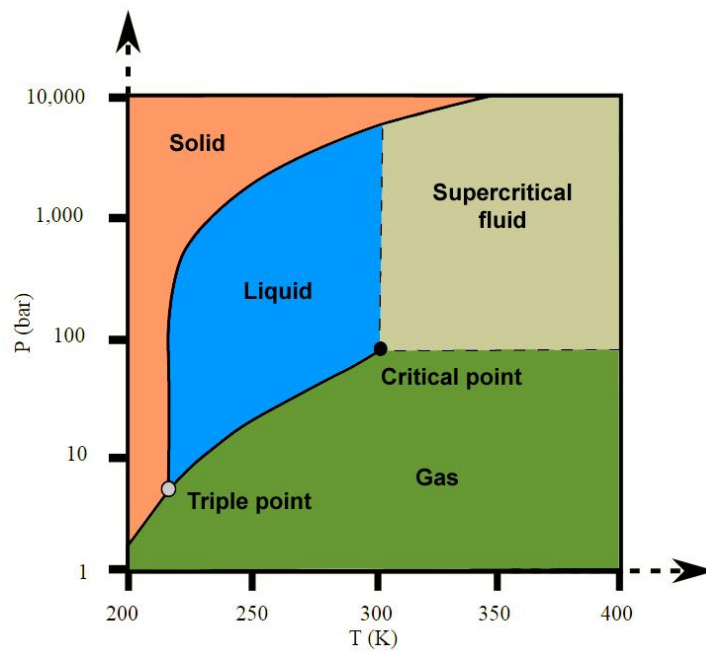


Figure 1.3. Phase diagram of CO₂

The supercritical region above the critical temperature in the CO₂ phase diagram (Figure 1.3) is of special interest for the compressing step in CCS technology [3]. In this region, where there is no liquid-vapor coexistence, CO₂ can be compressed into a dense fluid without going through a phase transition that may consume more energy, and the CO₂ can be easily pumped through pipelines. Carbon dioxide then would have to be transported through pipeline to suitable geological storage sites, such as trapping CO₂ in depleted natural gas reservoirs, where natural gas is stable in these geological formations for millions of years by some very similar mechanisms.

1.2 Pre-combustion and Post-combustion Capture

The options for CO₂ capture include pre-combustion and post-combustion capture. The post-combustion carbon capture is the simplest method because it can be added to an existing power plant without having to modify the plant itself. In addition, flue gas is a major CO₂ emission source that accounts for roughly 33-40% of global CO₂ emissions [6]. The principle of post-combustion capture is separation of CO₂ mainly from N₂ in the flue gas mixture (Table 1.2), which are the main products of the combustion of fossil fuels in air.

The pre-combustion carbon capture consists of oxy-combustion method, the integrated gasification combined cycle (IGCC) process, and chemical looping. Oxy-fuel combustion is a promising technology using pure O₂ (>95%) instead of air to combust the fuels. Thus, the flue gas contains a high concentration of CO₂ and water, which allows for easier CO₂ separation. The water is easily removed by condensation, and the remaining CO₂ can be purified at relatively low cost. However, the technique still consumes high amounts of energy due to the fact that a cryogenic air separation unit is needed to supply high purity oxygen [2]. Chemical looping uses metal to

transport oxygen (from air mixture) to the fuel reactor, and the CO₂ separation process at the end is similar to oxy-combustion method [2, 7]. IGCC is based on the syngas products (CO and H₂), which are converted to CO₂ and H₂ mixture using water gas shift reactions. The presence of CO₂ at much higher concentrations and high pressure (Table 1.2) makes IGCC less expensive for pre-combustion capture in comparison with post-combustion capture [8].

Table 1.2. Typical compositions of gases (by weight) in post-combustion and pre-combustion processes [9]

Composition	Postcombustion 323-348 K, 1 bar	Precombustion 313 K, 30 bar
CO ₂	15–16	35.50%
H ₂ O	5-7%	0.20%
H ₂	-	61.50%
O ₂	3-4%	-
CO	20 ppm	1.10%
N ₂	70–75%	-
SO _x	<800 ppm	0.25%
NO _x	500 ppm	-
H ₂ S	-	1.10%

1.3 Proposed Techniques for Carbon Capture

CO₂ separation processes include several basic methods for gas separation such as adsorption, absorption, cryogenic distillation, and membrane-based techniques.

1.3.1 Chemical absorption using aqueous amines

This technology has been employed industrially since 1930 [10] using monoethanolamine (MEA) and other amines to clean natural gas of its impurity gases. Scrubbing CO₂ from process gases with aqueous amines has been the benchmark technology for over 60 years and is still the reference to compare for other alternative

technologies [11]. Typically, the flue gas stream containing CO₂ is introduced at the bottom and an aqueous amine solution (about 30 wt.%) is passed down the top of an absorption tower. The reaction of CO₂ with the amine occurs via a mechanism that forms carbamates, as described to in Figure 1.4. The CO₂-adsorbed solvent then passes from the absorber column to a stripping tower, where the mixture is heated at 100-140°C under atmospheric pressure using steam to liberate the CO₂. The high heat of formation associated with carbamate production (40-100 kJ/mol) leads to a considerable energy penalty for regeneration of the solvent with a corresponding power plant energy penalty of 25-35% depending on the base load efficiency of the power plant in the absence of carbon capture [12]. In addition, the oxygen in the flue gas causes the amines to degenerate. At present, however, amine scrubbing is the only technology that is sufficiently advanced to be applied in CCS. Finding alternative technologies aimed at mitigating some of the disadvantages of these amine solutions is an active area of research which focuses on membrane and adsorption technologies.

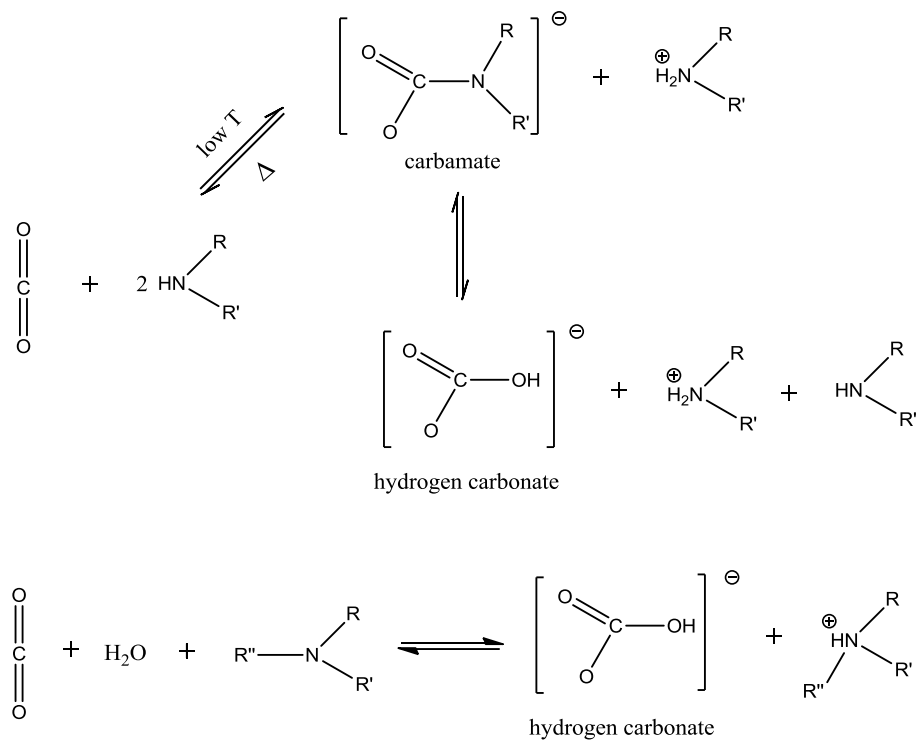


Figure 1.4. General reaction schemes for the chemical absorption of CO₂ by primary (or secondary) and tertiary amine-containing solvents [9]

1.3.2 Cryogenic distillation

Cryogenic distillation involves a process of cooling the gases to a very low temperature so that the CO₂ can be liquefied and separated. This method is considered to be efficient where there is a high concentration of CO₂ (typically more than 50%)[2] in the gas mixture. The method has the advantage of producing liquid CO₂, which is ready for transportation by pipeline, however it requires high power consumption for refrigeration and for removal of components having freezing points above normal operating temperatures (water, SO_x, NO_x); these are major disadvantages. In addition, cryogenic processes are not an attractive option for CO₂ capture since the compression of the flue gas at atmospheric pressures containing only

15 % CO₂ is not practical. These tend to make cryogenic process less economical than others in separating CO₂ from flue gas. However, this separation method might be considered for high-pressure gases such as in pre-combustion decarbonization processes.

1.3.3 Membrane-based separation

Membranes consist of thin barriers that allow selective permeation of certain gases. The driving force for membrane separation comes from the difference in the components' partial pressures on the two sides of the membrane (Figure 1.5). As such, compression is required for the feed gas in order to provide the driving force for permeation of the adsorbates. The pressure of the flue gas is too low (near ambient pressure) for a sufficient pressure gradient because the post-combustion carbon capture is an end-of- pipe technology. This pressure difference can be rectified by compressing the flue gases or by pulling vacuum that, however, requires a significant energy penalty due to the large flue gas volumes involved in the separation. These practical limitations have important consequences for the design of a membrane separation process [13]. The membrane method is more relevant for pre-combustion separation, and further study on the membrane design is needed to achieve high gas permeability (transport factor) and high selectivity (separation factor) in addition to adequate robustness and material lifetime [14].

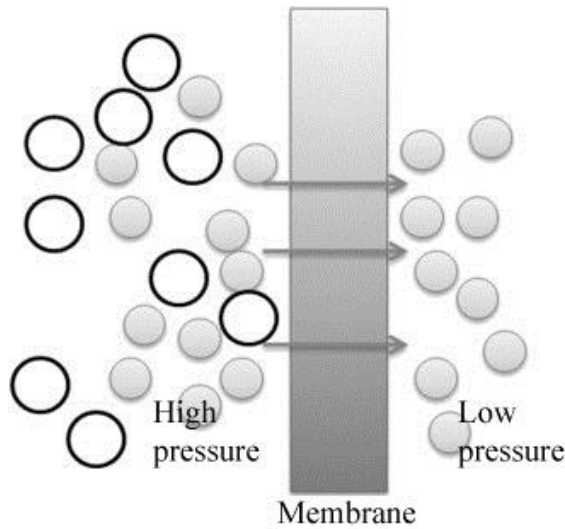


Figure 1.5. Principle of gas separation membrane [2]

1.3.4 Adsorption

Amongst several separation strategies, adsorption is regarded as a potential means to efficiently capture CO_2 from a gas stream since the method requires low energy as compared to that of cryogenic and absorption processes. This technology is based on the preferential adsorption of CO_2 in the pores of adsorbents compared to other flue gas components. In order for an adsorbent to be useful for CO_2 capture from flue gas, the following adsorbent criteria need to be considered [15-17].

The adsorbent needs to have high adsorption capacity and high working capacity for CO_2 .

- Needs to have high selectivity for CO_2 against other gases.
- Must demonstrate microstructure and morphological stability and chemical tolerance to impurities
- Should be easily synthesized in large scale with low cost.

- Should have minimal additional energy input for regeneration. A moderately high value of adsorption heats could enable high capacity and selectivity in CO₂ capture and subsequent facile desorption to regenerate adsorbents.
- It is essential to have fast adsorption/desorption kinetics for CO₂ under the operating conditions. The mass transfer and heat conductivity of the adsorbent should be good enough for the adsorbates to easily go in (adsorption) and out (desorption) under temperature or pressure swing adsorption processes.

Microporous materials such as zeolites, metal-organic frameworks (MOFs), covalent organic frameworks (COFs), zeolitic imidazolate frameworks (ZIFs), carbon molecular sieve (CMS) [18-22] have the potential to exhibit extremely favorable separation properties. This is due to the high adsorption capacity and capability of closely matching the diameter of a rate-limiting diffusion pathway in the material to that of adsorbed molecules, resulting in an effective kinetic separation. CMS materials have the advantage of being relatively inexpensive and insensitive to moisture, but the selectivity and capacity of carbonaceous adsorbents are too low for post-combustion applications [19]. MOFs currently are being studied intensively in gas storage, separation, and catalysis due to their unprecedented internal surface areas (up to 5000 m²g⁻¹), high void volumes (55–90%), and low densities (from 0.21 to 1.00 g.cm⁻³). Additionally, MOFs have the ability to modulate systematically their pore dimensions and surface chemistry within the frameworks [23, 24]. MOF materials exhibiting relatively higher CO₂ gravimetric adsorption capacity seem to be promising CO₂ adsorbents, but the materials generally have low density which would decrease the

volumetric capacity. The operations are also at high pressures and low temperatures, which are not well suited for the low pressure of flue gas and the range of temperatures available at the power plant. Many MOFs are sensitive toward atmospheric moisture and could collapse and lose their adsorption power upon extended exposure to water vapor [25].

1.4 Separation Processes

Based on the mode chosen to regenerate the adsorbent, adsorption based CO₂ capture from post combustion flue gas can be classified into temperature swing adsorption (TSA), and pressure/vacuum swing adsorption (PSA/VSA). In TSA processes (Figure 1.6), the gas components are adsorbed at room temperature and then the adsorbent is regenerated by raising the temperature. In PSA processes, the gas components are captured at elevated pressures, and the adsorbent is regenerated by lowering the pressure. Vacuum swing adsorption (VSA) is similar to PSA (Figure 1.6), in which the regeneration is conducted at reduced pressures, and the adsorption occurs at ambient or near-ambient pressures [26].

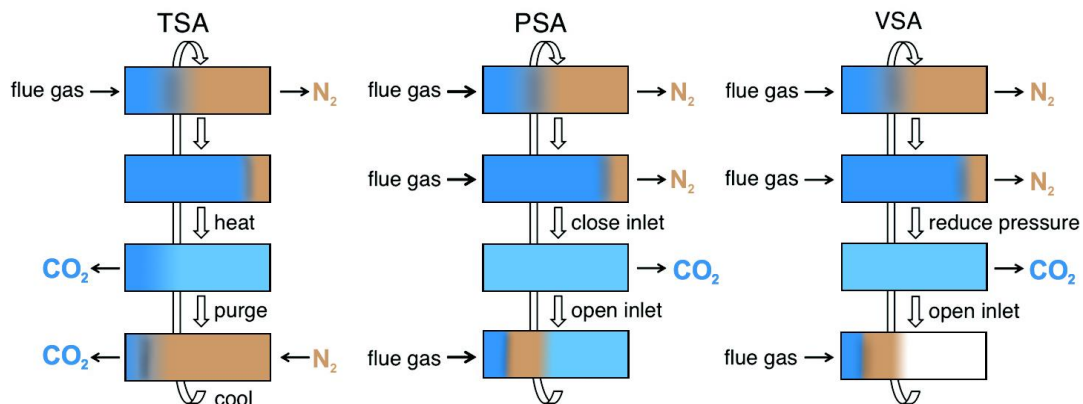


Figure 1.6. Schematic diagrams of idealized TSA, PSA, and VSA processes for regenerating solid adsorbent in a fixed-bed column [27]

1.4.1 Temperature Swing Adsorption

Adsorbents for temperature swing processes applied to post combustion flue gas must respond strongly to changes in temperature ideally in the range 300-423 K. This is the range of temperature at which heat is available at the power plant and can be used to contact directly or indirectly with the adsorbent [28]. As a result, chemisorbents with heats of adsorption in the range 40-70 kJ/mol CO_2 are suitable. The largest drawback of the thermal swing adsorption cycles are the large cycle times needed (in the order of hours) if the host-guest contacting devices are restricted to fixed beds. This effectively restricts these TSA systems to small-scale applications.

1.4.2 Pressure/Vacuum Swing Adsorption

Pressure/vacuum swing processes (Figure 1.6) have the advantage over TSA in that rapid cycling (minutes or even seconds) is possible in fixed beds leading to much

smaller bed sizes. Compression of post combustion flue gas beyond approximately 1.5 bar is not cost effective though, given the large content of nitrogen and the low flue gas pressure. For this reason, VSA (Figure 1.6) is the preferred mode of operation for post combustion flue gas.

1.5 Zeolite Materials and Their Applications in CO₂ Separation

Zeolites are crystalline microporous materials built from corner-sharing SiO_{4/2} and AlO_{4/2}¹⁻ tetrahedra. The general oxide formula of a zeolite is M_{x/n}(AlO₂)_x(SiO₂)_y.mH₂O where y ≥ x. The net negative charge of the framework is equal to the number of the aluminum atoms, which is balanced by the exchangeable cations Mⁿ⁺ (Figure 1.7).

Zeolites exchanged with metal cations can be considered as solid Lewis acid–base materials. Lewis acidity is associated with the exchangeable cations and Lewis basicity with the lattice oxygen atoms. The Lewis acidity is correlated to the charge density of cations, i.e. Li⁺ > Na⁺ > K⁺ > Cs⁺. The zeolite basicity increases with the rise in the aluminum content and with the decrease in the electronegativity of the cations [29].

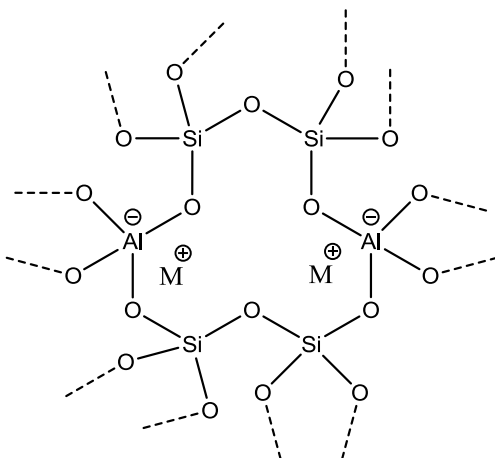


Figure 1.7. Illustration of zeolite structure

Zeolites have been widely used in the fields of petrochemical and fine chemical industries including catalysts, adsorbents, and ion-exchangers [30, 31]. Zeolites are generally characterized by a relatively high CO₂ capacity and selectivity over other gases at low pressure, which makes them promising candidates for CO₂ separation from flue gases [32, 33]. The separation of CO₂ from N₂ in the flue gas mixture is based on both size (kinetic diameters of CO₂ (3.30 Å), and N₂ (3.64 Å)) and electronic properties of the gas molecules and the zeolite framework. CO₂ has both a larger polarizability and quadrupole moment than N₂ ($1.43 \times 10^{-39} \text{ C.m}^2$, $29.11 \times 10^{25} \text{ cm}^{-3}$ for CO₂ and $4.67 \times 10^{-40} \text{ C.m}^2$, $17.403 \times 10^{25} \text{ cm}^{-3}$ for N₂, respectively[34]), which leads to stronger interactions of CO₂ with the electric field and electric field gradients within the adsorbents. CO₂ is also a Lewis acid, thus, the Lewis basicity of the zeolite framework oxygens can also play an important role in determining adsorption properties under certain pressure regime. Zeolites have shown their potential in CO₂ capture and been studied extensively using both experimental and theoretical methods [22, 35-40].

In this work, we investigated in the CO₂ adsorption properties of some of the more common and industrially important zeolites include zeolite A (LTA), zeolite Y (FAU), zeolite beta (BEA*), and ZSM-5 (MFI). Figures 1.8 and 1.9 below show the different frameworks and pore structures of these zeolites. FAU has a 3-dimensional pore structure with pores running perpendicular to each other in the x, y, and z planes similar to LTA. The pore apertures of FAU and LTA are defined by a 12- and 8-membered rings (7.4 Å and 3.8 Å, respectively) with larger cavities of diameter 12 Å and 11 Å, respectively. The cavities in the two zeolites are surrounded by small sodalite cages which are not accessible to CO₂ molecules [41, 42]. Zeolite beta is an intergrowth of two polymorphs A and polymorph B, and contains 12-membered rings pore structure with two straight channels, each with a cross-section of approximately 6.7 Å [43]. ZSM-5 (MFI) zeolite has a pore structure composed of 10-membered ring straight channels (0.56 nm x 0.53 nm) and 10-membered ring zigzag channels with windows of dimensions 0.51 x 0.55 nm [44]. The siliceous form of ZSM-5 is known as Silicalite-1 in the scientific and industrial literature.

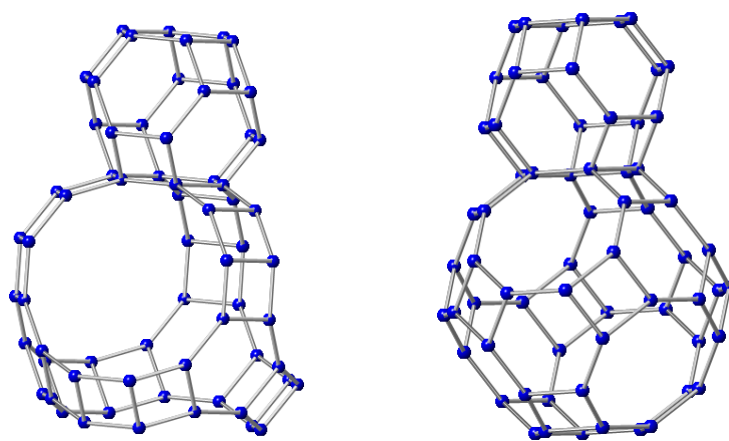


Figure 1.8. Structure of FAU (left) and LTA (right) zeolites

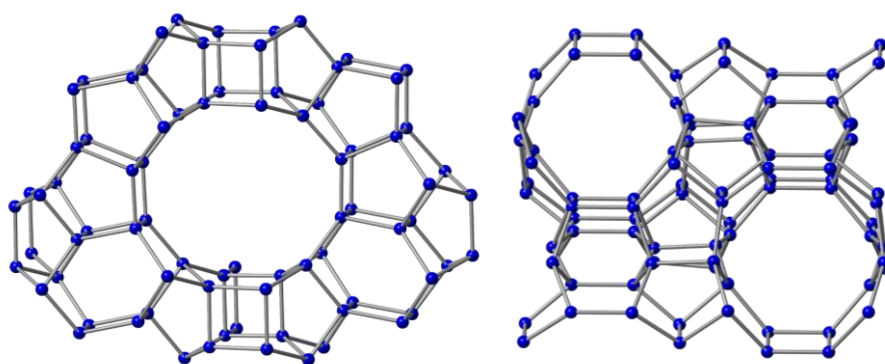


Figure 1.9. Structure of BEA (left) and MFI (right) zeolites

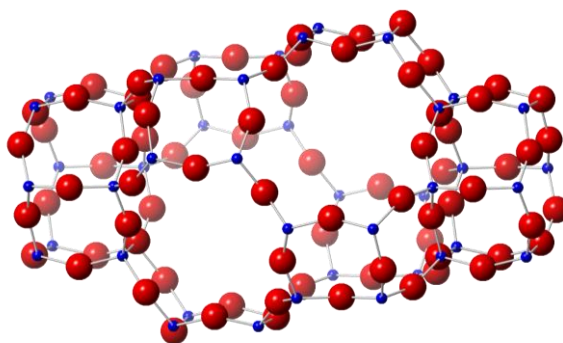


Figure 1.10. Structure of chabazites (CHA-type) zeolite

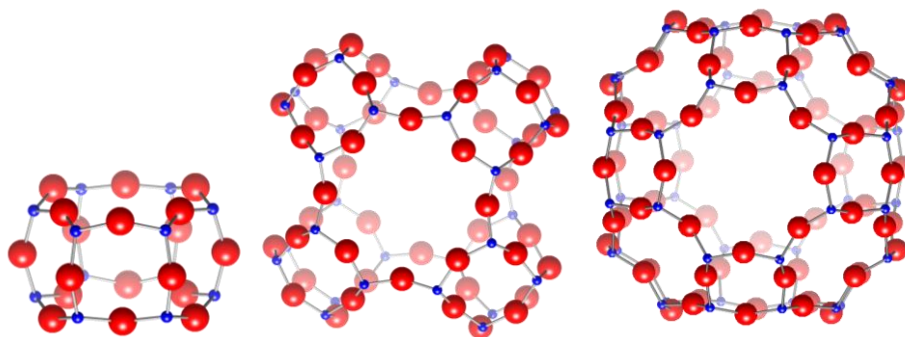


Figure 1.11. Composite building units of ZK-5 (KFI-type) zeolite

The narrow pore windows of CHA and KFI zeolites are of interest in this thesis because their overall pore dimensions fall close to the effective kinetic diameters of CO₂ and N₂. The adsorbents contain 3-dimensional networks with low framework densities (~ 15 T atoms/nm³), which show advantages of gas diffusion and high adsorption capacity. KFI (Fig 1.11) consists of double 6-rings (D6Rs), paulingite (*pau* or γ -cages) with dimensions of 5.4 Å x 9.6 Å and *lta* (α -cages) with dimensions of 11 Å x 11 Å as composite building units [45]. CHA (Figure 1.10) contains D6Rs and ellipsoidal cages with dimensions of 6.7 Å x 11 Å [46]. The adsorption performance of these zeolites can be controlled by changing internal space to host the CO₂ and modifying the electrostatic interactions between the adsorbent and CO₂ by the insertion of extra-framework cations including H⁺, Li⁺, Na⁺, K⁺, Cu²⁺, Ca²⁺, and Mg²⁺. Understanding the structure-property relations in the cation-exchanged CHA and KFI zeolites for CO₂ adsorption at molecular levels is the key factor to develop new zeolite adsorbents towards the practical separation of flue gas mixture. Other zeolite frameworks such as AEI, FER, STT, and RRO were also investigated in the CO₂, N₂, and hydrocarbons adsorption in this work.

In chapter 3, we report the synthesis and characterization of cation-exchanged chabazite zeolites (Si/Al = 6, 12), the adsorption isotherms, adsorption heats, Henry's constants, selectivity of CO₂/N₂, and the separation parameters of CO₂ in these adsorbents. Our adsorbents' performance was also compared with commercial zeolites NaY, 13X, and LTA. In chapter 4, we performed a structural analysis of CO₂ adsorption sites in pure and high silica chabazites (Si/Al= 6, 12, and infinity) by carrying out the Rietveld refinements of in situ CO₂ gas loading by X-ray and neutron diffraction. The exchanged cations (Li⁺, Na⁺, K⁺) in chabazites were identified to be

all open metal sites providing strong binding interactions with CO₂ through electrostatic and polarizability interactions with the adsorbate. Two adsorption sites of CO₂ were found in all chabazite samples, in which CO₂ site in the 8MR is dominant. Similar investigations were performed on ZK-5 materials with exchanged cations Li⁺, Na⁺, K⁺, and Mg²⁺ in chapter 5. Our findings of the adsorption sites of CO₂ in the 8-membered ring zeolites and the correlation between structure properties and the adsorption behaviors were identified and discussed in details. Chapter 4 and chapter 5 have provided a molecular understanding of interactions between CO₂ and cations, CHA and ZK-5 zeolite frameworks. Due to the presence of a quite high amount of water in the flue gas mixture, we have investigated the effect of structural properties of various hydrophobic zeolite frameworks (BEA*, CHA, FER, MFI, and STT) on the adsorption behaviors of CO₂ and N₂ by both experimental and GCMC simulation methods. The hydrophobic properties of the siliceous zeolites make them more applicable in PSA processes for CO₂ separation, especially in the presence of water. Siliceous zeolites with hydrophobic properties are not only potential for CO₂ separation from flue gas, but also potential for other gas separations. Chapter 7 studied the characterization and adsorption properties of hydrophobic siliceous zeolites of framework types AEI, CHA, RRO, and STT with CO₂ and small chain hydrocarbons. The separation ability of these zeolites for propane/propylene and for CH₄/CO₂ based on the gases kinetic diffusion properties was also discussed.

REFERENCES

1. Zhang, Z., et al., *Perspective of microporous metal-organic frameworks for CO₂ capture and separation*. Energy & Environmental Science, 2014. **7**(9): p. 2868-2899.
2. Mondal, M.K., H.K. Balsora, and P. Varshney, *Progress and trends in CO₂ capture/separation technologies: A review*. Energy, 2012. **46**(1): p. 431-441.
3. B. Smit, J.R.R., C. M. Oldenburg, and I. C. Bourg, *Introduction to carbon capture and sequestration*. Imperial College Press, 2014. **1**.
4. Report, B.A., *BP Annual Report and Form 20-F 2013*. BP Annual Report and Form 20-F 2013, 2014.
5. Jacobson, M.Z., *Review of solutions to global warming, air pollution, and energy security*. Energy & Environmental Science, 2009. **2**(2): p. 148-173.
6. Yang, H., et al., *Progress in carbon dioxide separation and capture: A review*. Journal of Environmental Sciences, 2008. **20**(1): p. 14-27.
7. Boot-Handford, M.E., et al., *Carbon capture and storage update*. Energy & Environmental Science, 2014. **7**(1): p. 130-189.
8. Gibbins, J. and H. Chalmers, *Carbon capture and storage*. Energy Policy, 2008. **36**(12): p. 4317-4322.
9. D'Alessandro, D.M., B. Smit, and J.R. Long, *Carbon Dioxide Capture: Prospects for New Materials*. Angewandte Chemie International Edition, 2010. **49**(35): p. 6058-6082.
10. Rochelle, G.T., *Amine Scrubbing for CO₂ Capture*. Science, 2009. **325**(5948): p. 1652-1654.
11. Wang, M., et al., *Post-combustion CO₂ capture with chemical absorption: A state-of-the-art review*. Chemical Engineering Research and Design, 2011. **89**(9): p. 1609-1624.
12. Bhowan, A.S. and B.C. Freeman, *Analysis and Status of Post-Combustion Carbon Dioxide Capture Technologies*. Environ. Sci. Technol., 2011. **45**(20): p. 8624-8632.
13. Brunetti, A., et al., *Membrane technologies for CO₂ separation*. Journal of Membrane Science, 2010. **359**(1-2): p. 115-125.
14. Robeson, L.M., *Correlation of separation factor versus permeability for polymeric membranes*. Journal of Membrane Science, 1991. **62**(2): p. 165-185.
15. Bae, Y.-S. and R.Q. Snurr, *Development and Evaluation of Porous Materials for Carbon Dioxide Separation and Capture*. Angewandte Chemie International Edition, 2011. **50**(49): p. 11586-11596.

16. Liu, Y., Z.U. Wang, and H.-C. Zhou, *Recent advances in carbon dioxide capture with metal-organic frameworks*. *Greenhouse Gases: Science and Technology*, 2012. **2**(4): p. 239-259.
17. Samanta, A., et al., *Post-Combustion CO₂ Capture Using Solid Sorbents: A Review*. *Industrial & Engineering Chemistry Research*, 2011. **51**(4): p. 1438-1463.
18. Huang, N., et al., *Two-Dimensional Covalent Organic Frameworks for Carbon Dioxide Capture through Channel-Wall Functionalization*. *Angewandte Chemie International Edition*, 2015: p. n/a-n/a.
19. Radosz, M., et al., *Flue-Gas Carbon Capture on Carbonaceous Sorbents: Toward a Low-Cost Multifunctional Carbon Filter for "Green" Energy Producers†*. *Industrial & Engineering Chemistry Research*, 2008. **47**(10): p. 3783-3794.
20. Banerjee, R., et al., *High-Throughput Synthesis of Zeolitic Imidazolate Frameworks and Application to CO₂ Capture*. *Science*, 2008. **319**(5865): p. 939-943.
21. Li, J.-R., et al., *Carbon dioxide capture-related gas adsorption and separation in metal-organic frameworks*. *Coordination Chemistry Reviews*, 2011. **255**(15–16): p. 1791-1823.
22. Cheung, O. and N. Hedin, *Zeolites and related sorbents with narrow pores for CO₂ separation from flue gas*. *RSC Advances*, 2014. **4**(28): p. 14480-14494.
23. Wong-Foy, A.G., A.J. Matzger, and O.M. Yaghi, *Exceptional H₂ Saturation Uptake in Microporous Metal–Organic Frameworks*. *Journal of the American Chemical Society*, 2006. **128**(11): p. 3494-3495.
24. Eddaoudi, M., et al., *Systematic Design of Pore Size and Functionality in Isoreticular MOFs and Their Application in Methane Storage*. *Science*, 2002. **295**(5554): p. 469-472.
25. Burtch, N.C., H. Jasuja, and K.S. Walton, *Water Stability and Adsorption in Metal–Organic Frameworks*. *Chemical Reviews*, 2014. **114**(20): p. 10575-10612.
26. Hedin, N., et al., *Adsorbents for the post-combustion capture of CO₂ using rapid temperature swing or vacuum swing adsorption*. *Applied Energy*, 2013. **104**(0): p. 418-433.
27. Sumida, K., et al., *Carbon Dioxide Capture in Metal–Organic Frameworks*. *Chemical Reviews*, 2011. **112**(2): p. 724-781.
28. Webley, P., *Adsorption technology for CO₂ separation and capture: a perspective*. *Adsorption*, 2014. **20**(2-3): p. 225-231.
29. Barthomeuf, D., *Conjugate acid-base pairs in zeolites*. *The Journal of Physical Chemistry*, 1984. **88**(1): p. 42-45.
30. Huddersman, K., *Zeolites and Catalysis: Synthesis, Reactions and Applications edited by Jiri Cejka, Avelino Corma and Stacey Zones*. *Appl. Organomet. Chem.*, 2012. **26**(4): p. 199.

31. Martínez, C. and A. Corma, *Inorganic molecular sieves: Preparation, modification and industrial application in catalytic processes*. Coordination Chemistry Reviews, 2011. **255**(13–14): p. 1558-1580.
32. Boot-Handford, M.E., et al., *Carbon capture and storage update*. Energy & Environmental Science, 2014. **7**(1): p. 130-189.
33. Chue, K.T., et al., *Comparison of Activated Carbon and Zeolite 13x for CO₂ Recovery from Flue-Gas by Pressure Swing Adsorption*. Industrial & Engineering Chemistry Research, 1995. **34**(2): p. 591-598.
34. Hedin, N., L.J. Chen, and A. Laaksonen, *Sorbents for CO₂ capture from flue gas-aspects from materials and theoretical chemistry*. Nanoscale, 2010. **2**(10): p. 1819-1841.
35. Kim, J., et al., *Predicting Large CO₂ Adsorption in Aluminosilicate Zeolites for Postcombustion Carbon Dioxide Capture*. Journal of the American Chemical Society, 2012. **134**(46): p. 18940-18943.
36. Lin, L.-C., et al., *In silico screening of carbon-capture materials*. Nat Mater, 2012. **11**(7): p. 633-641.
37. Shang, J., et al., *Discriminative Separation of Gases by a “Molecular Trapdoor” Mechanism in Chabazite Zeolites*. Journal of the American Chemical Society, 2012. **134**(46): p. 19246-19253.
38. Bae, T.-H., et al., *Evaluation of cation-exchanged zeolite adsorbents for post-combustion carbon dioxide capture*. Energy & Environmental Science, 2013. **6**(1): p. 128-138.
39. Fischer, M. and R.G. Bell, *Modeling CO₂ Adsorption in Zeolites Using DFT-Derived Charges: Comparing System-Specific and Generic Models*. The Journal of Physical Chemistry C, 2013. **117**(46): p. 24446-24454.
40. Liu, Q., et al., *NaKA sorbents with high CO₂-over-N₂ selectivity and high capacity to adsorb CO₂*. Chemical Communications, 2010. **46**(25): p. 4502-4504.
41. Bennett, J.M. and J.V. Smith, *Positions of cations and molecules in zeolites with the faujasite-type framework III hydrated Ca-exchanged faujasite*. Materials Research Bulletin, 1968. **3**(12): p. 933-940.
42. Reed, T.B. and D.W. Breck, *Crystalline Zeolites. II. Crystal Structure of Synthetic Zeolite, Type A*. Journal of the American Chemical Society, 1956. **78**(23): p. 5972-5977.
43. Higgins, J.B., et al., *The framework topology of zeolite beta*. Zeolites, 1988. **8**(6): p. 446-452.
44. Kokotailo, G.T., et al., *Structure of synthetic zeolite ZSM-5*. Nature, 1978. **272**(5652): p. 437-438.
45. Parise, J.B., Robert D. Shannon, Edward Prince, et al., *The crystal structures of the synthetic zeolites (Cs, K)-ZK5 and (Cs, D)-ZK5 determined from neutron powder diffraction data*, in *Zeitschrift für Kristallographie*. 1983. p. 175.
46. Dent, L.S. and J.V. Smith, *Crystal Structure of Chabazite, a Molecular Sieve*. Nature, 1958. **181**(4626): p. 1794-1796.

Chapter 2

EXPERIMENTAL PROCEDURES

This chapter provides a general overview of the hydrothermal method to synthesize zeolites in alkali and fluoride media, background and specific details on the experimental techniques used to gather and interpret the data presented in this dissertation. This includes several characterization techniques used to study the crystal structure, particle morphology, composition of the materials synthesized, and the adsorption sites of CO₂ in the zeolite adsorbents. Experimental details for the synthesis of zeolite materials and cation exchange processes studied in this thesis will not be discussed here, but can be found in the subsequent chapters.

2.1 Zeolite Synthesis

2.1.1 Hydrothermal method

A general hydrothermal zeolite synthesis can be described as depicted in figure 2.1. Inorganic reactants containing (amorphous) silica and alumina are mixed in a basic aqueous medium and then the mixture is heated (between 100-200 °C) in a sealed autoclave under autogenous conditions. After a few hours to a few weeks, a crystalline zeolite product can be usually observed at the bottom of the flasks and the solid crystals are recovered by filtration, washing with deionized water and drying.

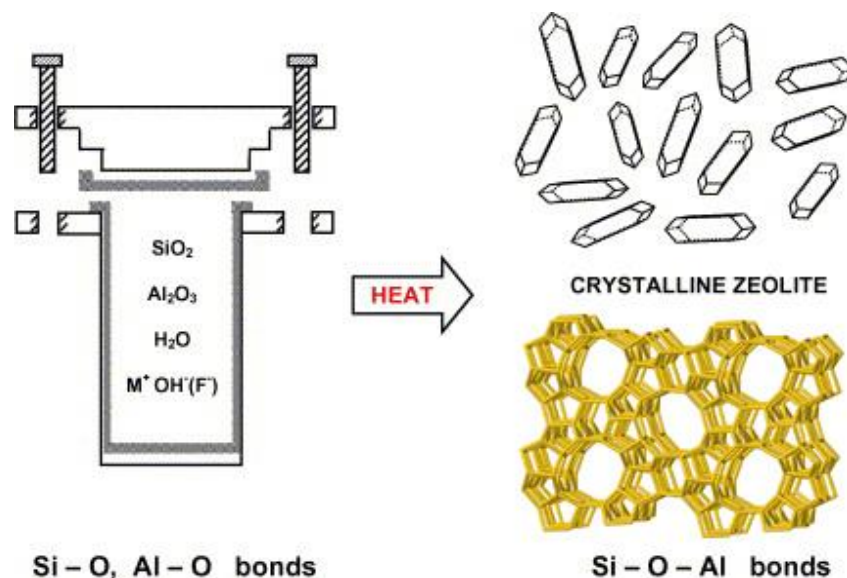


Figure 2.1. Schematic of a general hydrothermal zeolite synthesis. The starting reactants (solids containing Si-O and Al-O bonds) are converted in a mineralizing medium into the crystalline zeolite product (Si-O-Al bonds) [1]

Since the bond type of the product (Si-O-Al bond) is very similar to that presents in the precursor oxides (Si-O and Al-O bonds), the overall free energy change for a zeolite synthesis reaction is usually quite small, and the outcome is most frequently kinetically controlled [1, 2]. Crystallization from solution generally occurs via the sequential steps of nucleation of the phase in the solution, followed by growth of the nuclei to larger sizes by incorporation of material from the solution. Adding seed crystals to a crystallization system typically results in faster crystallization rates because the nucleation step is avoided [3].

Structure directors are organic or inorganic cations added to synthesis media to aid in the organization of the anionic building blocks (aluminosilicate in this case) that form the framework. The formation of a specific framework type and a polyhedral

building unit depends on the presence of one or at most two cation species are shown in table 2.1. The cation specificity is strong for the α -cage, sodalite cage, gmelinite cage and D4R unit, but weak for the D6R unit.

Table 2.1. Synthesis cation-building unit relationship [4]

Building Unit (BU)	Structure-types containing BU	Cation specificity for BU
α	LTA, KFI	Na
Sodalite	LTA, FAU	Na or TMA
Gmelinite	GME, OFF, MAZ	Na or TMA
Cancrinite	ERI, OFF, LTL	K, Ba, or Rb
D4R	LTA	Na
D6R	FAU, KFI, CHA, GME, ERI/OFF, LTL	Na, K, Sr, Ba

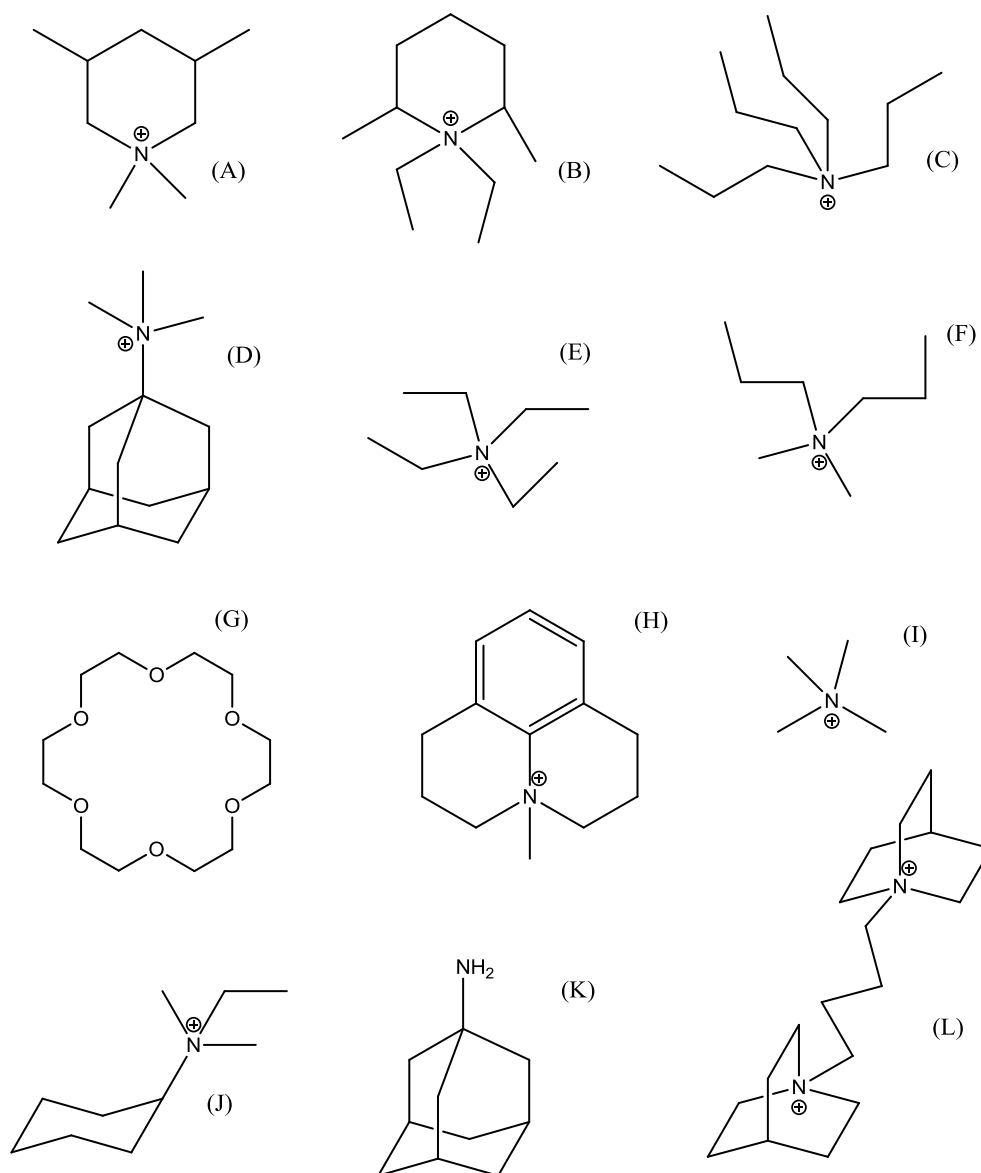


Figure 2.2. Structure of commercial and synthesized organic templates for zeolite synthesis

(A) N,N-Dimethyl-3,5-dimethylpiperidinium cation, a template for AEI zeolite synthesis

(B) N-Ethyl-N-methyl-2,6-dimethylpiperidinium cation, a template for AEI zeolite synthesis

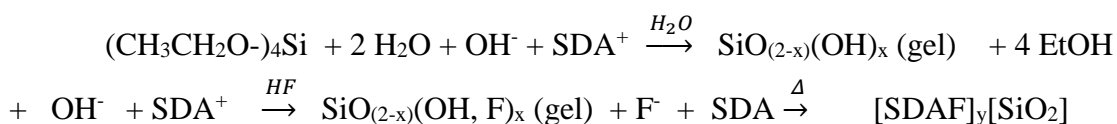
(C) Tetrapropylammonium (TPA), a template for MFI zeolite synthesis

- (D) N,N,N-trimethyl-1-adamantanammonium cation (TMAda), a template for CHA and STT zeolite synthesis
- (E) Tetraethylammonium (TEA), a template for BEA zeolite synthesis
- (F) Dimethyldipropylammonium (DMDP), a template for RRO zeolite synthesis
- (G) 18-Crown-6 ether, a template for EMT, KFI and RHO zeolite synthesis
- (H) 4-methyl-2,3,6,7-tetrahydro-1H,5H-pirido[3,2,1-ij]-quinolinium, a template for LTA zeolite synthesis
- (I) Tetramethylammonium (TMA), a template for LTA zeolite synthesis
- (J) Dimethylcyclohexylamine (DMCHA), a template for CHA zeolite synthesis
- (K) 1-Adamantylamine, a template for LEV zeolite synthesis
- (L) 1,4-di(1-azoniabicyclo[2.2.2]octane), a template for AFX zeolite synthesis

High silica zeolites are normally synthesized in lower pH medium ($10 < \text{pH} < 12$) with the presence of bulk organic compounds as structure directors. Zones[5] has observed that the organic molecules with C/N^+ ratios between 11 and 15 are good structure directing agents that can yield variety of high-silica molecular sieve. One structure director can give rise to several different structures such as (G) compound is used to prepare RHO, KFI, and EMT zeolites, (L) compound is used to prepare BEA and AFX zeolites. At the same time, many organic species can yield the same structure: for example, DMCHA, TMAda, TEPA (tetraethylenepentamine), and benzyltrimethylammonium can be used to prepare CHA-type zeolites.

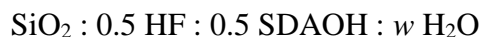
2.1.2 Synthesis of siliceous zeolites in fluoride media

In general, tetraethyl orthosilicate (TEOS) is hydrolyzed in an aqueous SDA-OH at room temperature for few hours, then the resulting mixture is heated to about 343 K under stirring to complete evaporation of the ethanol (scheme 2.1).



Scheme 2.1. Steps in the synthesis of siliceous zeolites in fluoride media [6]

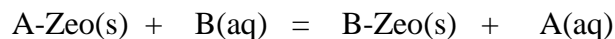
After that, HF (48 %wt) - NH₄F or NaF may be used in some cases-is added and the mixture is homogenized by hand stirring. The common final gel composition of the mixture is:



In most cases of siliceous zeolites, F⁻ is occluded in small cages such as [4⁶] in AST and [4¹5⁴6²] in NON [6]. Water content may have a strong influence on the phase selectivity of the zeolite crystallization. The higher w value (or H₂O/SiO₂ ratio) is, the higher density phase is obtained. For example, in our experiment, using the same SDA (TMAdaOH), $w = 7.5\text{-}10$ gave STT (FD=17.0), $w = 3$ gave CHA (FD=15.4). This could be due to the increased concentration of guest species inside zeolitic cavities [6]. Pure silica frameworks prepared in fluoride media have a much lower concentration of connectivity defects (Si(OSi)₃OH groups or Q₃ species) compared to the materials prepared in alkaline media. This could be due to various factors including the charge balance between F⁻ and SDA⁺, low pH medium, the absence of hydrogen bonding Si-O⁻...HO-Si, and the removal of HF after calcination as reported by Cambor *et al* [6]. The amount of Si-O⁻ and Si-OH species is roughly 4 times higher than the amount of SDA charges [7], therefore, the concentration of defects Q₃ outnumbers the SDA concentration occluded in the zeolite frameworks by a factor of about 4 in many cases. A large concentration of connectivity defects may destabilize the formation of stable nuclei under hydrothermal synthesis conditions at high pH. Thus, it is generally more restricted to synthesize pure silica phase of zeolites under alkali media. Due to the slow rate in the oligomerization process of SiO_(2-x)(OH, F)_x monomers in fluoride media, the nucleation step is slow and the final zeolite particles are normally larger than the one prepared in alkali media.

Aluminum may be incorporated into the framework of high-silica materials in fluoride media. Increasing the Al content in fluoride media causes a decrease in the fluoride content of the zeolite and sometimes leads to a less dense phase of zeolite [6].

2.1.3 Ion-exchange



The objective of zeolite cation exchange is to displace “as-synthesized” cation A of the zeolite by cation B from the aqueous phase. The solid/solution volume ratio should be at least 1/20, the temperature is increased into the range of 60-70°C, and the concentration of incoming cation B should be at least 5-fold excess of A cation. It is not necessary to wash zeolite with too excess amount of water since zeolite frameworks are well known to hydrolyze [8]. Details on the cation-exchanged experiment are described in the experimental parts of each chapter.

2.2 Analytical Methods

2.2.1 X-Ray and Neutron Powder Diffraction

X-ray diffraction (XRD) [9] is used to analyze structural properties of crystalline materials. The position of peaks in an XRD pattern is a function of the dimensions of the crystal unit cell following the Bragg’s law:

$$n\lambda = 2d \sin \theta \quad (2.1)$$

where n is an integer, λ is radiation wavelength, d is the distance between diffracting planes, and θ is diffraction angle.

Analysis of XRD patterns can also be used to approximately determine the size of crystalline domains in a material. Using the formula developed by Scherrer, the size of crystalline domains can be calculated as:

$$\tau = \frac{K\lambda}{\beta \cos \theta} \quad (2.2)$$

where τ is correlation length of sample, K is a “shape factor” (approximately 0.9 for nearly spherical or cubic crystallites) [10], β is the full width at half maximum (FWHM) peak broadening caused by the sample, λ is radiation wavelength (1.54 Å for the Cu K α radiation used in this thesis), and θ is diffraction angle. Therefore, materials containing smaller crystal domains will give rise to broader peaks in the measured diffraction patterns. The use of this equation is limited to correlation lengths below about 100 μm , and loses accuracy above this length scale [11].

XRD measurements were obtained using a Philips X’pert diffractometer with a CuK α source ($\lambda = 1.54060$ Å for $\kappa\alpha_1$) run at 45 kV and 40 mA between the angles 5.00° and 50.00° using a step size of 0.02° and between 2–6 seconds per time step. An internal standard, such as silicon, is often used to obtain accurate cell measurements and to index peaks, since the position of the silicon peaks is well known and suitable as a calibration standard.

Rietveld Refinement of Diffraction Patterns:[12]

The Rietveld method uses a least-squares refinements technique to minimize the difference between the observed and calculated intensities diffraction patterns. The neutron and X-ray diffraction of powder samples results in a pattern characterized by reflections (peaks in intensity) at certain positions. The height, width and position of these reflections can be used to determine many aspects of the zeolites’ structure.

The calculated intensities y_{ci} are determined using the following equation:

$$y_{ci} = s \sum_K L_K |F_K|^2 \phi(2\theta_i - 2\theta_K) P_K A + y_{bi} \quad (2.3)$$

where S is a scale factor, K represents the Miller indices, L_K contains Lorentz, polarization, multiplicity factors, ϕ is the reflection profile function, P_K is the preferred

orientation function, A is an adsorption factor, F_K is the structure factor, and Y_b is the background intensity.

$$R_p = \frac{\sum |y_i - y_{ci}|}{\sum y_i} \quad (2.4)$$

$$R_{wp} = \left\{ \frac{\sum w_i (y_i - y_{ci})^2}{\sum w_i (y_i)^2} \right\}^{1/2} \quad (2.5)$$

where $w_i = 1/y_i$.

In this thesis, Rietveld refinements were carried out using the EXPGUI/GSAS package for NPD and XPRD data [13, 14]. For zeolite frameworks, the difference in scattering intensity of Al and Si is too small to be accurately determined with NPD, and to reduce the variables in the Rietveld refinement, was fixed based on the average compositions measured by ICP and EDX methods. Similarly, since ICP and EDX can determine sample composition more precisely than powder diffraction, the extra-framework cations occupancies are fixed at values from the ICP and EDX since no observable impact on the quality of the refinement is noted with this as a variable. Fourier difference methods were then employed to elucidate the adsorbed molecules in the data collected from the samples subsequently loaded CO_2 . Additional refinement details include the restraining of the CO_2 angle in the secondary sites (sites B, B', C as subsequently discussed) to be 180° , and the restraint of CO_2 distance to $\text{dC-O}(\text{CO}_2) = 1.16 \text{ \AA}$ (due to the symmetric nature of the CO_2 across symmetry sites, bonds tended to an “average” longer than ideal), and atomic displacement parameters (ADPs) and fractional occupations for C and O in the same site CO_2 were constrained to be the same as well for clarity.

NPD data was collected on BT-1 instrument using a Ge(311) monochromator with a 75° take-off angle, $\lambda = 2.0785(2) \text{ \AA}$, and in-pile collimation of 15 minutes of arc. Data were collected over the 2θ range of $1.3\text{--}166.3^\circ$ with a step size of 0.05° via

32 detectors with the sample at approximately 4 K. A closed-cycle helium refrigerator (CCR) was used for temperature control. Synchrotron X-ray diffraction measurements were carried out at the Advanced Photon Source (Argonne National Laboratory) on the 17-BM materials diffractometer ($\lambda = 0.6124 \text{ \AA}$). Data were measured at both about 110 K and 298 K for each sample, with integration of the 2-dimensional powder pattern being performed with Fit-2D.

2.2.2 Gas adsorption

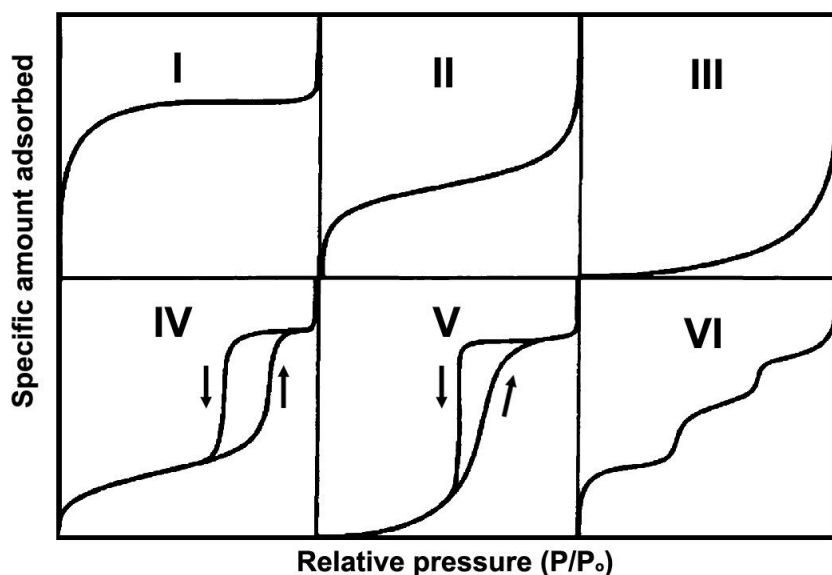


Figure 2.3. The IUPAC classification for adsorption isotherms [15]

Figure 2.3 shows 5 different classical types of adsorption isotherms plus a sixth that involved steps. Type I isotherms (the Langmuir isotherm) is typical of many microporous adsorbents (pore widths below 2 nm). Types II and III are typical of nonporous materials with strong or weak fluid-wall attractive forces, respectively.

Types IV and V exhibit hysteresis loops that occur in mesoporous materials for strong and weak fluid-wall forces, respectively. Type VI occurs for some materials with relatively strong fluid-wall forces, usually when the temperature is near the melting point for the adsorbed gas.

The Brunauer-Emmett-Teller (BET) method is a useful technique for quantifying the surface area of materials from physisorption isotherms using the following equations:

$$\frac{1}{\frac{p_0}{p}-1} \cdot \frac{1}{V} = \frac{c-1}{cV_{mono}} \left(\frac{p}{p_0} \right) + \frac{1}{cV_{mono}} \quad (2.6)$$

where V is the volume of gas adsorbed at pressure p , V_{mono} is the volume of gas that would constitute one monolayer, p/p_0 is the ratio of the pressure of the gas to the pressure at surface saturation, and c is the so-called BET constant.

A plot of $\frac{1}{V\left(\frac{p_0}{p}-1\right)}$ vs p/p_0 gives slope $\frac{c-1}{cV_{mono}}$ and intercept at $p/p_0=0$, and

the V_{mono} could be determined, thus:

$$S_{BET} = \frac{V_{mono}N_A A}{m\underline{V}} \quad (2.7)$$

where N_A is Avogadro's number, A is the cross-sectional area of the adsorbate ($16.2 \times 10^{-20} \text{ m}^2$ with N_2), m is the mass of adsorbent material, and \underline{V} is the molar volume of the adsorbate gas ($22.4 \text{ liter/mole} = 22400 \text{ cm}^3/\text{mol}$).

The BET model assumes that all adsorption sites are equivalent, and that an infinite number of layers of adsorbate may be formed under adsorption conditions. The model does a poor job characterizing microporous materials, as a limited number of layers can form within the micropores of a material, and the binding energy of adsorbates is often much higher than on external particle surfaces.

For microporous materials, the t-plot method can be used to calculate the total volume of micropores in a sample. In the low-pressure regime, the amount of adsorption within micropores increases rapidly with adsorbate pressure, and they are filled much earlier than the larger macro- and mesopores. To determine the microporosity of the material, an empirical formula developed by Harkins and Jura was used:

$$t_{HJ} = \left(\frac{13.99}{0.034 + \ln\left(\frac{p}{p_0}\right)} \right)^{0.5} \quad (2.8)$$

The Harkins-Jura formula has been shown to accurately describe the system for a reduced pressure ranging from 0.001 to 0.7. Multi-layer formation is modeled mathematically to calculate a layer “thickness, t ” as a function of increasing relative pressure (P/P_0). The resulting t -curve is compared with the experimental isotherm in the form of a t -plot. That is, experimental volume adsorbed is plotted versus statistical thickness for each experimental P/P_0 value. The linear range lies between monolayer and capillary condensation. The slope of the t -plot (V/t) is equal to the “external area”, i.e. the area of those pores that are micropores.

Textural characterization of the samples was carried out with a Micromeritics ASAP 2020 and 3Flex adsorption instruments using N_2 gas (or other gases as needed). Samples were degassed for 6 h under vacuum at 523 K prior to measurements. The weight of the dry, degassed sample was used in the data analysis. Samples were immersed in a liquid N_2 bath (77 K) during measurement of isotherms. Analysis of data was performed using Micromeritics software.

Adsorption models

Single site *Langmuir* isotherm [16] refers to homogeneous adsorption, a model where each molecule possess a constant enthalpy and sorption activation energy (eq. 2.9). The *Toth* isotherm model [17] can be applied to multilayer adsorption, with non-uniform distribution of adsorption heat and affinities over the heterogeneous surface (eq. 2.10). The *Toth* isotherms have three fitting parameters while *Langmuir's* equations has only two, and as a result fit the data on rough surfaces better than the *Langmuir's* equations. These two models are not sufficient to describe the adsorption isotherms in the whole range of temperature (283 K-343 K) and pressure (up to 1 bar).

$$q = \frac{q_m b P}{1 + b P} \quad (2.9)$$

$$q = \frac{q_m b P}{(1 + (b P)^t)^{1/t}} \quad (2.10)$$

A *dual-site Langmuir (DSL)* model [18, 19] was used to describe the CO₂ adsorption of aluminosilicate zeolites over the entire pressure range:

$$q = \frac{q_{m,1} b_1 P}{1 + b_1 P} + \frac{q_{m,2} b_2 P}{1 + b_2 P} \quad (2.11)$$

where, q is the quantity adsorbed, P is the pressure, $q_{m,1}$ and $q_{m,2}$ are the saturation loadings for sites 1 and 2, and b_1 and b_2 are the Langmuir parameters for sites 1 and 2, respectively.

Dual-site Langmuir-Freundlich (DSL_F) model [20, 21]

$$q = \frac{q_{m,1} b_1 P^{k_1}}{1 + b_1 P^{k_1}} + \frac{q_{m,2} b_2 P^{k_2}}{1 + b_2 P^{k_2}} \quad (2.12)$$

The isosteric heat of adsorption (Q_{st}) at constant adsorbate loading q , is determined using Clausius–Clapeyron equation:

$$Q_{st} = RT^2 \left(\frac{\partial \ln P}{\partial T} \right)_q = R \left(\frac{\partial \ln P}{\partial \left(\frac{1}{T} \right)} \right)_q \quad (2.13)$$

P values at a given loading of CO₂ for dual-site Langmuir isotherm were evaluated by the following equation:

$$\ln P = \ln(\sqrt{\beta + 4\alpha q} - \beta) - \ln 2\alpha \quad (2.14)$$

where

$$\alpha = (q_{m,1} + q_{m,2} - q)b_1b_2 \quad (2.15)$$

$$\beta = (q_{m,1} - q)b_1 + (q_{m,2} - q)b_2 \quad (2.16)$$

$$P = \frac{q}{K_H} \exp(A_1q + A_2q^2 + \dots) \quad (2.17)$$

$$Q_{st}^o = -R \left[\frac{\partial \ln K_H}{\partial \left(\frac{1}{T}\right)} \right] \quad (2.18)$$

where ΔH_{iso} is the isosteric heat of adsorption and q indicates constant equilibrium adsorption quantities. The isosteric heat of adsorption ΔH_{iso} can be calculated by measuring adsorption isotherms at different temperatures and employing the thermodynamic relationship of eq 2.17. A plot of $\ln P$ against $(1/T)$ at constant adsorption amount yields a straight line with a slope equal to $(-\Delta H_{iso}/R)$.

2.2.3 Scanning Electron Microscopy (SEM) & Energy Dispersive X-Ray Spectroscopy (EDX) [22]

A scanning electron microscope (SEM) is a type of electron microscope that produces morphological features of a sample by scanning it with a focused beam of electrons inside a vacuum chamber. The morphological characteristics of materials can be imaged on length scales that are normally between ~tens nanometers and hundreds of micrometers, depending on the resolution of each SEM instrument. In a SEM, a sample is bombarded with a focused beam of electrons-instead of light, to form an image (Figure 2.4) [23]. A beam of electrons is produced at the top of the microscope by heating a metallic filament. The electron beam follows a vertical path through the column of the microscope. It makes its way through electromagnetic lenses, which focus and direct the beam down towards the sample. Once the beam hits the sample, it is quickly swept across the observed area of the sample, and backscattered or

secondary electrons coming off the sample are gathered at a detector to form the image. Detectors collect the secondary or backscattered electrons, and convert them to a signal that is sent to a viewing screen similar to the one in an ordinary television, producing an image. Because secondary electrons coming off the sample are used to construct the SEM images and the electron beam is very narrow, the images give the appearance of three-dimensional depth. This makes it easy to distinguish the morphology and size of individual crystallites from an SEM image. Because this technique relies on the detection of electrons, the SEM must be operated under vacuum (10^{-6} torr), to prevent any absorption or scattering of the electron beam by gases within the microscope and to make sure the filament is well functioning.

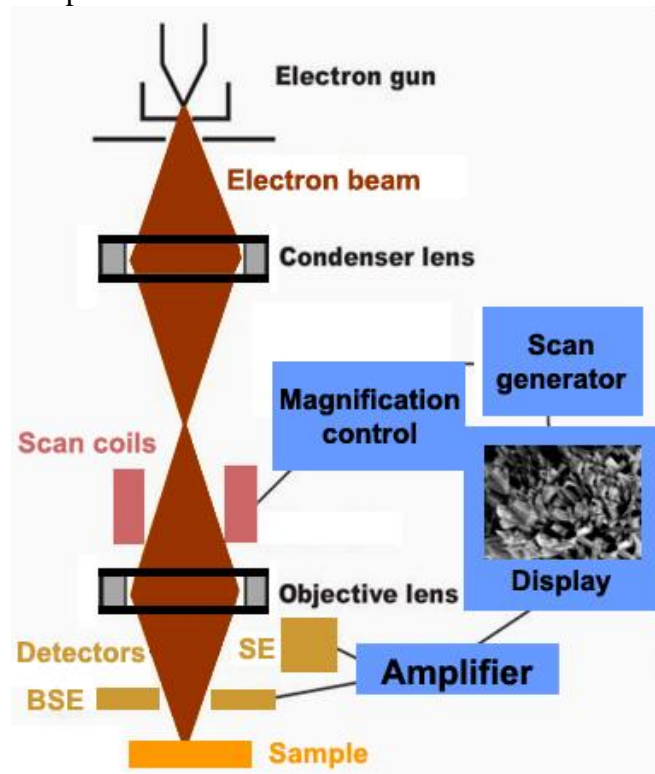


Figure 2.4. Schematic for the SEM operation

Electrons collide constantly with the surface of a sample, and non-conducting material (or insulating material) such as zeolite may accumulate charge over time. Because the charge of a material deflects the incoming electron beam, it results in a loss of resolution in the obtained images. To prevent this phenomenon, non-conducting zeolite is usually coated with a thin layer of a conductive metal such as Au or Pt to allow absorbed electrons to pass through the zeolite sample. Prior to imaging, zeolite samples were mounted on a layer of conductive carbon tape affixed to an aluminum specimen mount. The samples were subsequently sputter coated with Au metal using a Denton Vacuum Desk IV sputtering system. The scanning electron micrographs presented in this thesis were obtained on a JEOL JSM7400F microscope, operated at an acceleration voltage of 3 keV and a current of 10 μ A.

Energy dispersive X-ray spectroscopy (EDX), or energy dispersive X-ray analysis (EDXA), or energy dispersive X-ray microanalysis (EDXMA) is another technique that can be applied to a sample using a scanning electron microscope. The inner shell electrons in the specimen can be energetically excited by a high energy of the incoming electron beam. The excited electron is then ejected from the shell, and created an electron hole. An electron from outer shell then fills the hole, and the difference in energy between the higher-energy shell and the lower energy shell results in the emission of a photon in the X-ray energy range. The energy of the released X-ray is characteristic of specific atom with specific energy difference between outer and inner shells. Therefore, the elemental composition of the sample can be measured by detecting all the X-rays emitted by the sample. The high energy electrons used for these experiments can penetrate several microns into a sample, and the resulting EDX spectra is a measurement of the bulk composition of samples with micron sizes [24].

EDX experiments were also performed using a JEOL 7400 SEM operated at the same current setting of 10 mA, but at a higher voltage (8-10 kV). A more intense electron beam was necessary to generate strong EDX signal for the analysis. Because the SEM electron beam is very narrow, EDX spectra must be collected at various locations within a specimen, and the element compositions of the sample are the average of multiple EDX measurements. In this thesis, all EDX data are the average of at least 3 measurements of different spots within a sample. In the cases of light atoms such as Li, Be and B, or various atoms within a sample having similar or overlapped energy-dispersive spectra such as (Br, Al), and (Si, Sr), the element compositions need to be analyzed by the Inductively Coupled Plasma (ICP) technique through Galbraith Laboratories at Knoxville, Tennessee.

2.2.4 Nuclear Magnetic Resonance (NMR)

Nuclear magnetic resonance spectroscopy is a powerful analytical technique used to characterize organic and inorganic molecules. Only nuclei that contain odd mass numbers (such as ^1H , ^{13}C , ^{19}F and ^{31}P) or odd atomic numbers (such as ^2H and ^{14}N) give rise to NMR signals. ^1H NMR and ^{13}C NMR are by far the most common types of NMR spectroscopy are used to characterize organic structure, due to the prevalence of H and C in organic compounds [25].

In the presence of an external magnetic field, nuclei in a sample will precess at a frequency known as the Larmor frequency:

$$\omega = -\gamma B \quad (2.19)$$

where γ is the gyromagnetic ratio of the nucleus and B is the strength of the magnetic field. Chemical bonding within a compound alters the magnetic field around the nucleus, and leads to a shift in the frequency of precession which can be detected by

NMR. In a typical NMR experiment, the nuclei being probed are first aligned by exposure to a strong magnetic field. The nuclei are irradiated with a short radio-frequency magnetic pulse applied perpendicular to the external magnetic field, causing the nuclei in the sample to magnetically precess. NMR absorptions are measured relative to the position of a reference peak at 0 ppm on the δ scale due to tetramethylsilane (TMS). TMS is a volatile inert compound that gives a single peak up-field from typical NMR absorptions. ^1H nuclei are shielded by the magnetic field produced by the surrounding electrons. The higher the electron density around the nucleus, the higher the magnetic field required to cause resonance. Four different features of a ^1H NMR spectrum provide information about a compound's structure. Number of signals: how many different types of hydrogens in the molecule; position of signals (chemical shift): types of hydrogens; relative areas under signals (integration): how many hydrogens of each type; splitting pattern (^1H - ^1H coupling): how many neighboring hydrogens. Peaks in the ^1H NMR spectrum can also be integrated to quantitatively determine the relative concentration of protons at different chemical shifts in a sample, and thus is particularly valuable for calculating the purity of synthesized organic compounds.

The natural abundance of ^{13}C is only 1.1%, thus the lack of splitting in a ^{13}C spectrum is a consequence of the low natural abundance of ^{13}C . Moreover, the chance of two ^{13}C nuclei being bonded to each other is very small (0.01%), and so no carbon-carbon splitting is observed. A ^{13}C NMR signal can also be split by nearby protons. This ^1H - ^{13}C splitting is usually eliminated from the spectrum by using an instrumental technique that decouples the proton-carbon interactions, so that every peak in a ^{13}C NMR spectrum appears as a singlet. The two features of a ^{13}C NMR spectrum that

provide the most structural information are the number of signals observed and the chemical shifts of those signals.

In a typical NMR experiment, approximately 10 mg of the sample (organic structure directing agents for zeolites synthesis in this case) to be analyzed was first dissolved in roughly 1 mL of D₂O/CDCl₃ and loaded into a 5 mm diameter borosilicate NMR tube. ¹³C and ¹H spectra were recorded using a Bruker AV 400/600 NMR Spectrometer. The NMR data were analyzed using MNova software.

Solid-State NMR Spectroscopy [26, 27]. ²⁹Si magic-angle-spinning (MAS) NMR has provided new insights into the structure and chemistry of zeolites. There are five different possible environments of a Si atom in the tetrahedral coordinated zeolite frameworks (Si(nAl), n≤4). The Si/Al ratio in the aluminosilicate zeolites can be calculated from ²⁹Si MAS NMR using the following formula:

$$\frac{Si}{Al} = \frac{\sum_{n=1}^4 I_{Si(nAl)}}{\sum_{n=1}^4 0.25nI_{Si(nAl)}} \quad (2.20)$$

By combining (Si/Al ratio) using NMR with the result from chemical analysis, the amount of extra-framework Al can be calculated.

²⁹Si NMR is also used to calculate the concentration of defects (Si-OH groups) in calcined siliceous zeolites by dividing the peaks area (by integration) at chemical shifts of 100-105 ppm (belong to Si-OH or Q³ groups) and at chemical shifts of 105-120 ppm (belong to Q⁴ groups).

²⁷Al is a favorable nucleus for solid NMR because of its high natural abundance (100%). The detection and quantification of aluminum by solid NMR is often difficult due to the large quadrupolar interactions. The primary information obtained from the ²⁷Al-NMR spectra is related to its state of coordination. ²⁷Al NMR

spectra reveal the existence of extra-framework Al (at about 0 ppm) besides the lattice aluminum (tetrahedrally coordinated Al at about 40-65 ppm).

^{29}Si and ^{27}Al magic angle spinning nuclear magnetic resonance (MAS NMR) spectra were recorded on a Bruker AVIII-500 solid-state NMR spectrometer, operating at a Larmor frequency of 500.138 MHz at the department of Chemistry, University of Delaware.

2.2.5 Fourier Transform Infrared Spectroscopy (FTIR) [28]

Infrared spectroscopy is a vibrational spectroscopic technique, which takes advantage of asymmetric molecular stretching, vibration, and rotation of chemical bonds as they are exposed to designated wavelengths of light. In order for a vibration mode to absorb in the infrared, the vibrational motion must cause a change in the dipole moment of the bond. The intensity of the IR “peaks” is proportional to the change in dipole moment that a bond undergoes during a vibration, for example C=O bonds with higher dipole moment absorb much stronger than C=C bonds. The vibrational frequency is increasing with increasing force constant f or increasing bond strength, and decreasing atomic mass. Weaker transitions called “*overtones*” are sometimes observed. These correspond to $\Delta v=2$ or 3, and their frequencies are two or three times the fundamental frequency ($\Delta v=1$) because of anharmonicity. When two bond oscillators share a common atom, there is a strong mechanical coupling between them. For example, the frequency of the asymmetric stretching vibration in CO_2 is at a higher frequency (around 2300 cm^{-1}) than for a carbonyl group in aliphatic ketones (around 1700 cm^{-1}) due to coupled interaction.

Most commonly, the spectrum is obtained by measuring the absorption of IR radiation, although infrared emission and reflection are also used. Fourier transform is

a mathematical method to transform the signal from the time domain to its representation in the frequency domain. Michelson interferometer is the simplest interferometer design. In this work, FTIR spectra were recorded on a Thermo Nicolet Nexus 470 spectrometer equipped with a MCT-A (mercury cadmium telluride) detector. The samples were prepared by pressing 35 mg zeolite powders together to a partly IR transparent self-supporting pellet. Before each measurement, the samples were first heated up to 623 K for degasing, then CO₂ was introduced into the chamber at room temperature, and then the in situ measurement was conducted at different pressures.

REFERENCES

1. Cundy, C.S. and P.A. Cox, *The hydrothermal synthesis of zeolites: Precursors, intermediates and reaction mechanism*. Microporous and Mesoporous Materials, 2005. **82**(1–2): p. 1-78.
2. Cundy, C.S. and P.A. Cox, *The Hydrothermal Synthesis of Zeolites: History and Development from the Earliest Days to the Present Time*. Chemical Reviews, 2003. **103**(3): p. 663-702.
3. Thompson, R.W., *Chapter 2 - Nucleation, growth, and seeding in zeolite synthesis*, in *Verified Syntheses of Zeolitic Materials*, H. Robson and K.P. Lillerud, Editors. 2001, Elsevier Science: Amsterdam. p. 21-23.
4. Wilson, S.T., *Chapter 4 - Templating in molecular sieve synthesis*, in *Verified Syntheses of Zeolitic Materials*, H. Robson and K.P. Lillerud, Editors. 2001, Elsevier Science: Amsterdam. p. 27-31.
5. Goretsky, A.V., et al., *Influence of the hydrophobic character of structure-directing agents for the synthesis of pure-silica zeolites*. Microporous and Mesoporous Materials, 1999. **28**(3): p. 387-393.
6. Cambor, M.A., L.A. Villaescusa, and M.J. Díaz-Cabañas, *Synthesis of all-silica and high-silica molecular sieves in fluoride media*. Topics in Catalysis, 1999. **9**(1-2): p. 59-76.
7. Koller, H., et al., *SiO₂-cndot. .cndot. .cndot.HOSi Hydrogen Bonds in As-Synthesized High-Silica Zeolites*. The Journal of Physical Chemistry, 1995. **99**(33): p. 12588-12596.
8. Dyer, A., *Chapter 14 - Ion exchange capacity*, in *Verified Syntheses of Zeolitic Materials*, H. Robson and K.P. Lillerud, Editors. 2001, Elsevier Science: Amsterdam. p. 67-68.
9. McCusker, L.B., *Chapter 9 - Product characterization by x-ray powder diffraction*, in *Verified Syntheses of Zeolitic Materials*, H. Robson and K.P. Lillerud, Editors. 2001, Elsevier Science: Amsterdam. p. 47-49.
10. Langford, J.I. and A.J.C. Wilson, *Scherrer after sixty years: A survey and some new results in the determination of crystallite size*. Journal of Applied Crystallography, 1978. **11**: p. 102-113.
11. Weibel, A., et al., *The big problem of small particles: a comparison of methods for determination of particle size in nanocrystalline anatase powders*. Chemistry of Materials, 2005. **17**: p. 2378-2385.
12. Young, R.A., *The Rietveld Method*, in *The Rietveld Method* 1981, Oxford University Press p. 41-72.
13. Dreele, A.C.L.a.R.B.V., *General Structure Analysis System (GSAS)*. Los

- Alamos National Laboratory Report LAUR, 2004: p. 86-748.
14. Toby, B., *EXPGUI, a graphical user interface for GSAS*. Journal of Applied Crystallography, 2001. **34**(2): p. 210-213.
 15. Balbuena, P.B. and K.E. Gubbins, *Theoretical Interpretation of Adsorption Behavior of Simple Fluids in Slit Pores*. Langmuir, 1993. **9**(7): p. 1801-1814.
 16. Langmuir, I., *The constitution and fundamental properties of solids and liquids Part I Solids*. Journal of the American Chemical Society, 1916. **38**: p. 2221-2295.
 17. Do, D.D., *Adsorption Analysis: Equilibrium and Kinetics*. Imperical College Press, 1998: p. 64-70.
 18. Mason, J.A., et al., *Evaluating metal-organic frameworks for post-combustion carbon dioxide capture via temperature swing adsorption*. Energy & Environmental Science, 2011. **4**(8): p. 3030-3040.
 19. Nguyen, C. and D.D. Do, *Dual Langmuir kinetic model for adsorption in carbon molecular sieve materials*. Langmuir, 2000. **16**(4): p. 1868-1873.
 20. Bae, Y.-S., et al., *Separation of CO(2) from CH(4) using mixed-ligand metal-organic frameworks*. Langmuir, 2008. **24**(16): p. 8592-8598.
 21. Queen, W.L., et al., *Hydrogen adsorption in the metal-organic frameworks Fe-2(dobdc) and Fe-2(O-2)(dobdc)*. Dalton Transactions, 2012. **41**(14): p. 4180-4187.
 22. Jansen, K., *Chapter 11 - Characterization of zeolites by SEM*, in *Verified Syntheses of Zeolitic Materials*, H. Robson and K.P. Lillerud, Editors. 2001, Elsevier Science: Amsterdam. p. 55-56.
 23. Kliewer, C., *Electron Microscopy and Imaging*, in *Zeolite Characterization and Catalysis*, A. Chester and E.G. Derouane, Editors. 2009, Springer Netherlands. p. 169-196.
 24. Russ, J.C., *Fundamentals of Energy Dispersive X-Ray Analysis*. Butterworths Monographs in Materials. 1994, London, UK: Butterworths & Co.
 25. Wong, K.C., *Review of NMR Spectroscopy: Basic Principles, Concepts and Applications in Chemistry*. Journal of Chemical Education, 2014. **91**(8): p. 1103-1104.
 26. Klinowski, J., *Solid-state NMR studies of molecular sieve catalysts*. Chemical Reviews, 1991. **91**(7): p. 1459-1479.
 27. Fyfe, C.A., et al., *One- and two-dimensional high-resolution solid-state NMR studies of zeolite lattice structures*. Chemical Reviews, 1991. **91**(7): p. 1525-1543.
 28. Liu, X., *Infrared and Raman Spectroscopy*, in *Zeolite Characterization and Catalysis*, A. Chester and E.G. Derouane, Editors. 2009, Springer Netherlands. p. 197-222.

Chapter 3

CARBON DIOXIDE AND NITROGEN ADSORPTION ON CATION-EXCHANGED CHABAZITE ZEOLITES

3.1 Introduction

Due to an increasing dependence on the combustion of fossil fuels to power the global economy, the annual global emissions of anthropogenic greenhouse gases have increased drastically and are causing changes on the atmosphere and the environment [1]. The growing concerns for global climate change have motivated research towards developing improved processes for carbon dioxide capture, such as the separation of CO₂ from N₂ in the flue gas (post-combustion), the separation of CO₂ in hydrogen (pre-combustion H₂/CO₂), and the separation of CO₂ from CH₄ in natural gas reserves [2-3]. Solid adsorbents such as zeolites and metal organic frameworks (MOFs) have potential advantages over existing processes such as reduced energy use during regeneration, greater capacity, high selectivity, ease of handling, and fast adsorption kinetics [4-5]. Low silica zeolites (types A, 13X, zeolite Y) are among the most commonly used adsorbents in industrial gas separations and Li-X,Y and Na-X,Y are known to have among the highest capacities (5.0-5.6 mmol/g) at atmospheric pressure and temperature [6-7], but are generally strong adsorbents and this property makes regeneration difficult [8]. Because of lower Al content, high silica zeolites with a less hydrophilic surface is an interesting option with respect to the regeneration and the presence of polar impurities in the feed gas such as water vapor and sulfur compounds [9]; particularly, 8-membered ring window zeolites are found to have high interaction

with adsorbed molecules, CO₂ [10-11]. Here we report an investigation of CO₂ adsorption on high-silica zeolites SSZ-13 (CHA framework-type) examining the effects of framework Si/Al ratio and extra-framework cations (H⁺, Li⁺, Na⁺, K⁺) on CO₂ adsorption isotherms and heats of adsorption.

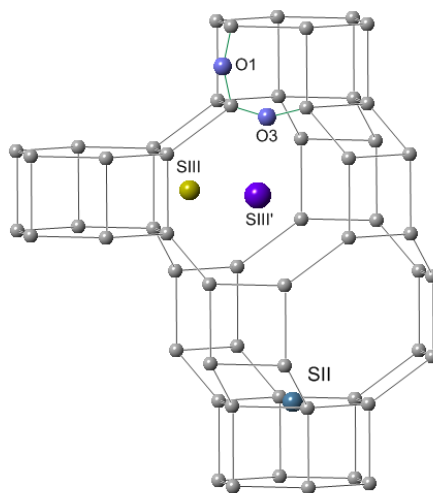


Figure 3.1. Schematic view of the known cation positions in chabazite framework

The composite building-units of zeolite chabazite are the double 6-membered ring (D6MR) and one large ellipsoidal cavity (7.3 Å x 12 Å) [12] accessed by six 8-membered ring windows (free aperture ~3.8 Å) [13]. The topological symmetry of the chabazite framework is $R\bar{3}m$ (trigonal), where $a \approx 13.2$ Å, $c \approx 15.1$ Å (pseudo-hexagonal cell) or equivalently, setting $a=b=c \approx 9.4$ Å, $\alpha=\beta=\gamma \approx 94^\circ$ in the rhombohedral setting [14]. In the rhombohedral setting the structure has 12 T-atoms per unit cell but only one T-atom in the asymmetric unit. Alkali-metal cations can be located in 3 different coordination sites (figure 3.1): On the 6-membered ring window of the D6MR (site SII, two sites per unit cell), in the 8-ring, closed to the corner of the

4- ring (site SIII, four sites per unit cell), or near the center of the 8-membered ring (site SIII', two sites per unit cell). Cheetham and co-workers studied the location of alkali cations in chabazite (Si/Al~2.5) by neutron diffraction and Magic Angle Spinning Nuclear Magnetic Resonance (MAS-NMR) and found that K^+ is preferentially located at site SIII' [15], Li^+ prefers site SII than site SIII, Na^+ is located in both site SII and SIII [16]. Using Ab initio periodic calculations, Ugliengo et al [17-18] reported that SII site is more stable than SIII site in Na-chabazite (Si/Al=11). H-CHA (Si/Al=16,[19] and Si/Al=11) [17] shows the presence of two distinct acid sites in the unit cell, one on the 6-membered ring at O1 and the other in the 8-membered ring window at O3. CHA differs from faujasite and zeolite A in one important point: in faujasite and zeolite A, a large fraction of the cations are located in the sodalite cages and are not directly accessible to adsorbed molecules: All cations in chabazite framework, on the other hand, are accessible to CO_2 molecule and are expected to interact with adsorbed molecules even with low aluminum content. Webley [20,21,22] and Zverev [23] have studied the sorption of carbon dioxide on the ion-exchanged forms of synthetic chabazite (Si/Al~2-2.5) but their work has focused on low-silica chabazite samples. Herein, we investigated the interaction of CO_2 and N_2 on CHA zeolites having higher Si/Al ratios of 6 and 12, with approximate 2 and 1 aluminum atoms per unit cell, respectively. Fourier Transform Infrared Spectroscopy (FTIR) was used to confirm the presence of chemical and physical adsorption of CO_2 on CHA and adsorption isotherms were analyzed to understand the interaction between adsorbates and chabazite zeolites. CHA zeolites are found to have high adsorption uptake and interaction energy with CO_2 at atmosphere temperature and pressure and are interesting candidates for separation processes.

3.2 Experimental Methods

3.2.1 Zeolite synthesis

CHA/6 (Si/Al=6) was synthesized using a procedure similar to that reported by Fickel and Lobo [24]. A solution of 10 g of sodium silicate (Sigma Aldrich, 26.5% SiO₂), 0.32 g of NaOH (Fisher Scientific, >98%) and 24 g of DI water was stirred at room temperature for about 15 min. Then, 1 g of Na-Y (Zeolyst CBV100, Si/Al=2.47) and 1.6 g of N,N,N-trimethyl-1-adamantanammonium iodide were added to the solution and stirred for another 30 min. The resulting solution was then transferred into 43 ml Teflon-lined autoclaves (Parr) and heated at 423K under rotation for 6 days. The solid product was separated by vacuum filtration, washed extensively with DI water, and dried at 353K overnight. The as-made product was then calcined in air at 823 K for 8 h using a ramping rate of 5K/min to prepare the starting form of Na-CHA/6.

CHA/12 (Si/Al=12) was prepared by modifying the formula described in literature [25]: A mixture of tetraethyl orthosilicate (TEOS, sigma 98%), N,N,N-trimethyl-1-adamantanamine hydroxide (TMAdaOH, 25%wt, Sachem Inc) and DI water were mixed for 2 hours, then Al(OEt)₃ (Strem Chemical, 99%) was added to the solution to obtain a final gel composition of SiO₂: H₂O: TMAdaOH: Al₂O₃ is 1: 20: 0.5: 0.035 and stirred for another 12 hours. The resulting solution was then transferred into Teflon-lined autoclaves and heated at a temperature of 423 K under static condition for 6 days. After that, the sample was washed with DI water, and dried at 353 K overnight. The as-made product was then calcined in air at 823 K for 8 h heating at a ramping rate of 5 K/min to prepare the starting form of H-CHA/12.

3.2.2 Ion exchange

Ammonium exchanged NH_4 -CHA (Si/Al=6 & 12) was prepared by mixing 1g Na-CHA/6 (or H-CHA/12) with 500ml NH_4NO_3 0.1M overnight at 353 K. The solution was then filtered and washed with deionized water, and the resulting NH_4 -CHA product was dried at 353 K overnight. The ion-exchanged Li-CHA, Na-CHA, K-CHA were prepared by mixing 0.1 g NH_4 -CHA and 50g 2 M LiCl ($\geq 99.0\%$, Sigma), NaCl ($\geq 99.0\%$, Sigma), KCl ($\geq 99.0\%$, Sigma) for 12 h at 353 K respectively, and the resulting cation-exchanged CHA products were dried at 353 K overnight. The ion exchange was repeated 2-3 times to obtain the completely exchanged form of alkali-metal CHA. H-CHA/6 was prepared by calcining NH_4 -CHA/6 at 823 K for 5 hours in air at a heating rate of 5K/minute.

3.2.3 Characterization

The Scanning Electron Microscopy (SEM) images and chemical compositions by Energy-dispersive X-ray spectroscopy (EDX) of the cation-exchanged CHA zeolites were obtained on a JEOL JSM7400F microscope, operating at an acceleration voltage of 3-10 keV, and current of 10 μ A. Li-CHA element analysis was carried out by the ICP method.

The X-Ray Powder Diffraction (XRD) patterns were collected on a Philips X'Pert powder diffractometer using a Cu $K\alpha$ source ($\lambda=1.5418 \text{ \AA}$) over the range of $2\theta=5.0\text{--}50.0$ with a step size of 0.02° and 2s per step. The CHA samples were mixed with silicon standard sample to correct the peak positions, and then celref software developed by Jean Laugier and Alain Filhol [26] was used to refine the unit cell parameters of chabazite framework structure.

The micropore volume and surface area of CHA were measured using N₂ at 77 K on a Micromeritics ASAP 2020 device. The CO₂ and N₂ adsorption isotherms of the CHA samples at different temperatures (273K, 303K and 343K) were also measured on this instrument up to ambient pressure. Before the experiments, each sample was degased at a temperature of 623 K for 6 h.

Fourier Transform Infrared (FTIR) spectra were recorded on a Thermo Nicolet Nexus 470 spectrometer equipped with a MCT-A (mercury cadmium telluride) detector. The sample is prepared by pressing 35 mg zeolite powder together to form a partly IR transparent self-supporting pellet. Before the measurement, the sample was first heated up to 623 K for degasing and then CO₂ was introduced into the chamber at room temperature and started the in-situ measurement at different pressures.

3.3 Results and Discussion

3.3.1 Characterization of CHA

The XRD patterns of the calcined Na-CHA (Si/Al=6 and 12) reveal that all samples are pure chabazite zeolite with high crystallinity (Figure 3.2). The unit cell parameters of the calcined samples were refined in the rhombohedral setting giving values of $a=9.3166 (\pm 0.0198) \text{ \AA}$, $\alpha=94.29^\circ$, $V_{u.c}=802 \text{ \AA}^3$ and $a=9.2759 (\pm 0.0036) \text{ \AA}$, $\alpha=94.30^\circ$, $V_{u.c}=791 \text{ \AA}^3$ for Na-CHA/6 and Na-CHA/12, respectively. As expected, the positions of the peaks shift to higher angles when the Si/Al ratio increases indicating that the unit cell of CHA increases as the Al content increases ($d_{Al-O}=1.78 \text{ \AA}$, $d_{Si-O}=1.62 \text{ \AA}$) [27].

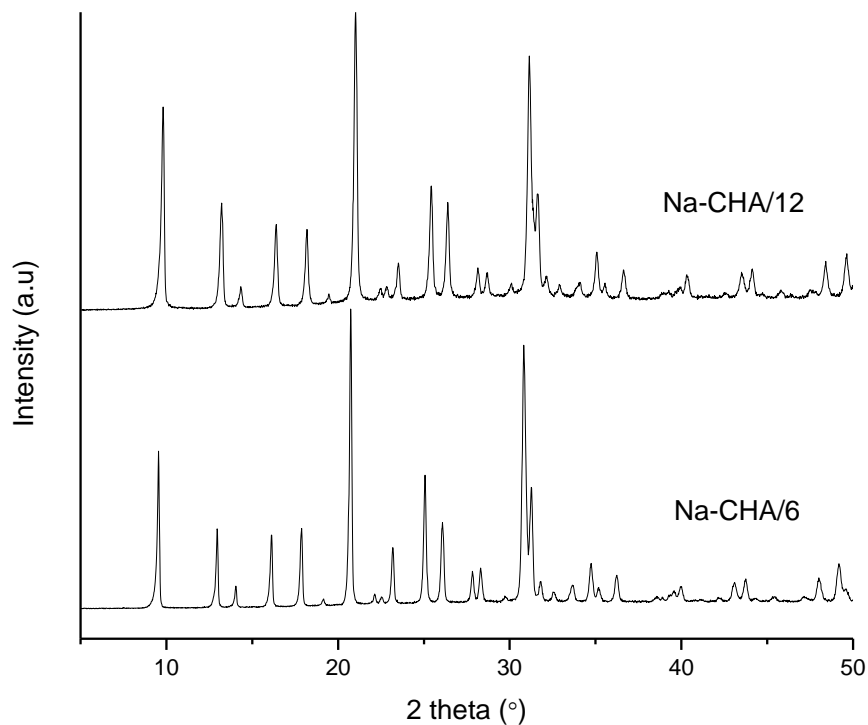


Figure 3.2. XRD patterns of calcined Na-CHA (Si/Al=6 and 12)

Chemical analysis of the as-made CHA samples confirms that they have approximate silicon-to-aluminum (Si/Al) ratios of 6 and 12 (Table 3.1). The particles of CHA (Si/Al=6) and CHA (Si/Al=12) are formed of smaller individual rhombohedral and spherical units with approximately 1 μm in size (Figure 3.3). The particles in Figure 3.3(a) appear as distorted cubes because the rhombohedral angle is 94.3° .

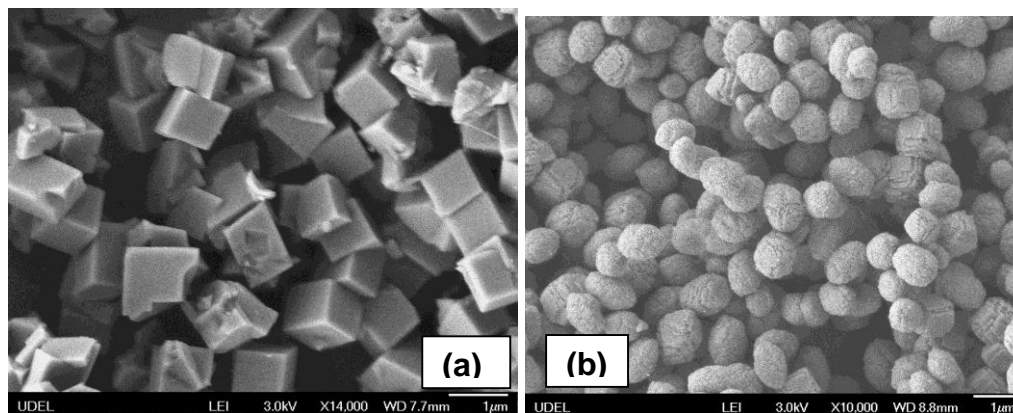


Figure 3.3. SEM images of calcined CHA (Si/Al=6 (a) and Si/Al=12 (b))

Table 3.1. Compositions of metals in cation-exchanged CHA confirmed by ICP and EDX methods

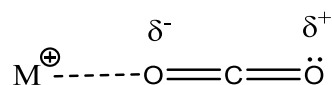
Materials	Molar ratios		Note
	Si/Al	M (cation)/Al	
H-CHA/6	6.21	-	No trace of Na ⁺
Li-CHA/6	-	1.02	ICP method
Na-CHA/6	5.95	0.95	Original form
K-CHA/6	6.6	0.96	-
H-CHA/12	12.43	-	Original form
Li-CHA/12	-	0.97	ICP method
Na-CHA/12	11.55	1.12	-
K-CHA/12	12.32	1.06	-

Most of the samples have comparable total micropore volume, except for K-CHA (Table 3.2). This difference reflects the space occupied by the larger potassium cations in the ellipsoidal cavity of chabazite framework and that perhaps K⁺ may blocks the access of gases to some cavities, while most of Li⁺ and Na⁺ are located in the 6-membered ring window of the hexagonal prism whereby they do not decrease the effective pore volume of the sample or block access to the cage.

Table 3.2. Surface area and pore volume of cation-exchanged CHA zeolites

Samples	Si/Al=6		Si/Al=12	
	External	Pore	External	Pore
	Area m ² /g	Volume cm ³ /g	Area m ² /g	Volume cm ³ /g
H-CHA	11	0.27	80	0.29
Li-CHA	27	0.27	129	0.26
Na-CHA	7	0.24	123	0.25
K-CHA	65	0.18	121	0.19

3.3.2 Fourier Transform Infrared Spectra of Adsorbed CO₂



Scheme 3.1: Ion-dipole interaction between the cation and CO₂

The FTIR spectra in the adsorbed phase (Figure 3.4) show a band near 2350 cm⁻¹ attributed to CO₂ in a linear configuration. This band shifts slightly to higher frequencies compared to the gas phase depending on the identity of the cations, a result from the ion-dipole interaction between the cation and CO₂ as suggested by Little and Amberg (Scheme 3.1) [28]. The shifts are more evident in the low pressure region since CO₂ directly interact with cations and at pressure of 6.58x10⁻⁴ atm, it is observed that this absorption peak is located at higher frequency on the sample with the lower Si/Al ratio. CO₂ adsorbed on Li-CHA/6 has a higher frequency than Li-CHA/12 sample, 2356 cm⁻¹ (Figure 3.4) and 2354 cm⁻¹ (not shown here), respectively. As the pressure of the IR cell is increased, (Figure 3.4) there is a shift in the band assigned to the asymmetric stretching vibration of linear CO₂ in the gas phase at 2349 cm⁻¹[29]. Two combination bands (ν₃+ν₁) and (ν₃+2ν₂) in Fermi resonance in the frequency range of 3598-3725 cm⁻¹ are also observed: these bands also shift to lower

frequency when the partial pressure of CO₂ increases. In addition to linear CO₂ species observed in the sample micropores, more strongly bound CO₂ was also found in CHA as revealed by the presence of absorption bands due to bent CO₂ moieties. These absorption bands 1700 and 1360 cm⁻¹ are associated with carbonate-like species [30-31] but note that the intensity of these peaks are very small compared to asymmetric stretching vibration: this indicates the dominance of physical over chemical adsorption of CO₂ on these zeolite samples. The intensity of all peaks also increases proportionally with the loading amount of CO₂, except for the carbonate species bands that do not increase at the pressure higher than 1.31x10⁻¹atm showing that chemical adsorption only appears at low loadings of CO₂.

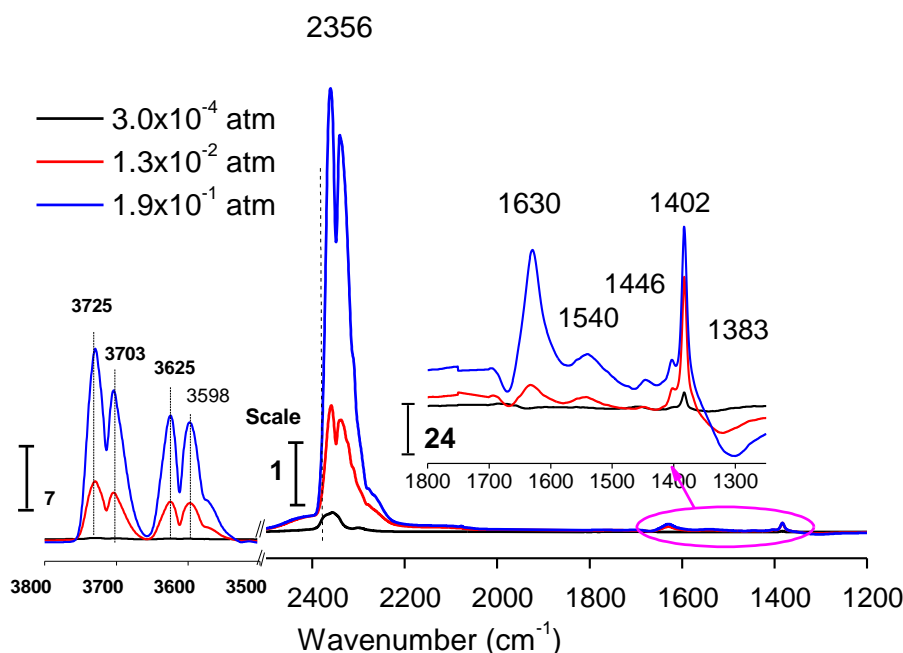


Figure 3.4. FTIR spectra of adsorbed CO₂ on Li-CHA/6 at 298K

3.3.3 Adsorption isotherms of N₂ and CO₂ on CHA zeolites

The total energy of physical adsorption can be described by the sum of multiple interaction terms:

$$\phi = \phi_D + \phi_R + \phi_P + \phi_{F\mu} + \phi_{FQ} + \phi_{sp} \quad (3.1)$$

where ϕ_D is dispersion energy, ϕ_R is close-range repulsion energy, ϕ_P is polarization energy, $\phi_{F\mu}$ is field-dipole energy, ϕ_{FQ} is field gradient-quadrupole energy, and ϕ_{sp} is adsorbate-adsorbate interaction energy [32-33].

The kinetic diameters of CO₂ (3.33 Å) and N₂ (3.64 Å) [34] are smaller than the pore aperture of CHA (3.8 Å) allows these adsorbates to diffuse freely. But there are important differences between the molecular properties of CO₂ and N₂. Besides their size and geometry, CO₂ has a much larger polarizability [21] and electric quadrupole moment (4.3×10^{-26} esu.cm² and 26.5×10^{-25} cm³ for CO₂; and 1.52×10^{-26} esu.cm² and 17.6×10^{-25} cm³ for N₂) [35]. Consequently the energy of interaction between CO₂ and the zeolite framework is much higher than with N₂, even in the presence of very low electric fields for zeolite materials like silicalite ($Q_{stCO_2}=27.2$ kJ/mol, $Q_{stN_2}=17.7$ kJ/mol) [36]. This is also confirmed by the adsorption capacities for CO₂ and N₂ as shown in Figures 3.5 and 3.6.

The adsorption isotherms of CO₂ and N₂ on CHA (Figures 3.5 and 3.6) show that the samples with Si/Al ratio of 6, that is containing higher cation content, have larger adsorption capacities than the ones with Si/Al ratio of 12 at equivalent pressures. The trend of the adsorption isotherms of nitrogen clearly depends on the strength of the electric field in the zeolites. In general, the polarizing power of the cations is inversely proportional to the charge density or ionic radius in Group 1A elements [37-38]. The electric field in the proton form is different because it is strongly shielded by the short distance between O and H ($d_{O-H} \approx 1 \text{ Å}$). The electric field

of cations in zeolites ranks in order of $H^+ < K^+ < Na^+ < Li^+$; therefore, Li-CHA/6 has the highest and H-CHA/12 has the lowest adsorption capacity. The results of nitrogen adsorption on alkali zeolites are similar to the results found on zeolite X, Y [39] and low-silica chabazite (Si/Al=2.5) [21].

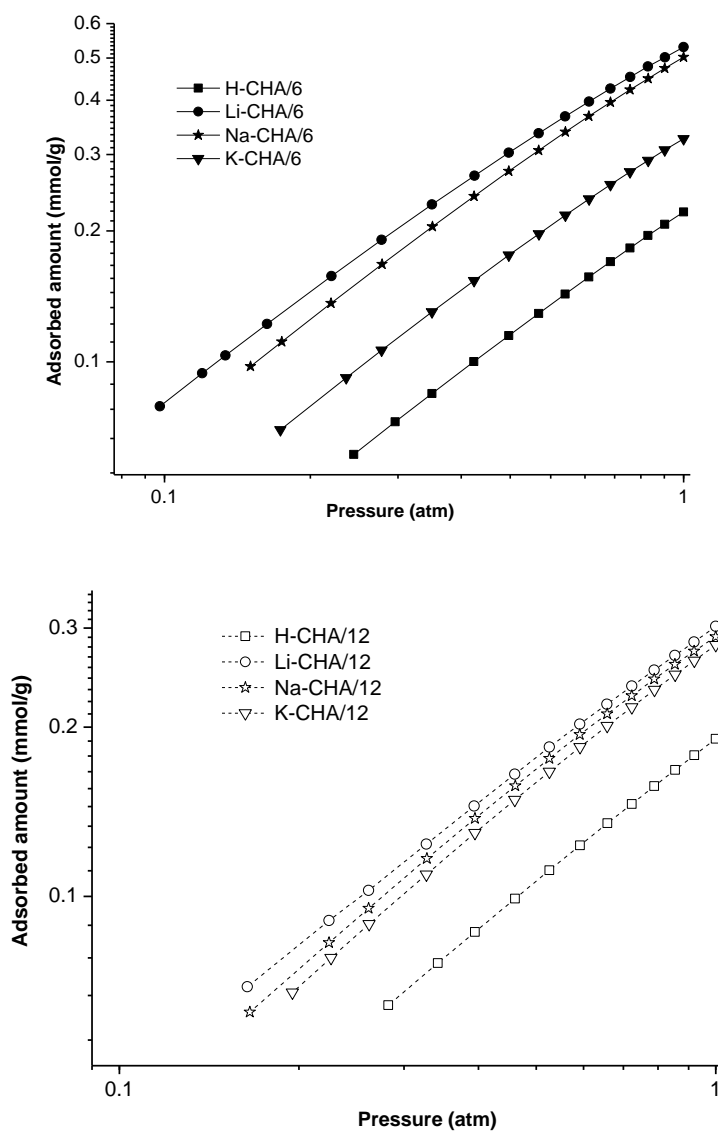


Figure 3.5. Adsorption isotherms of N₂ on cation-exchanged CHA at 303 K

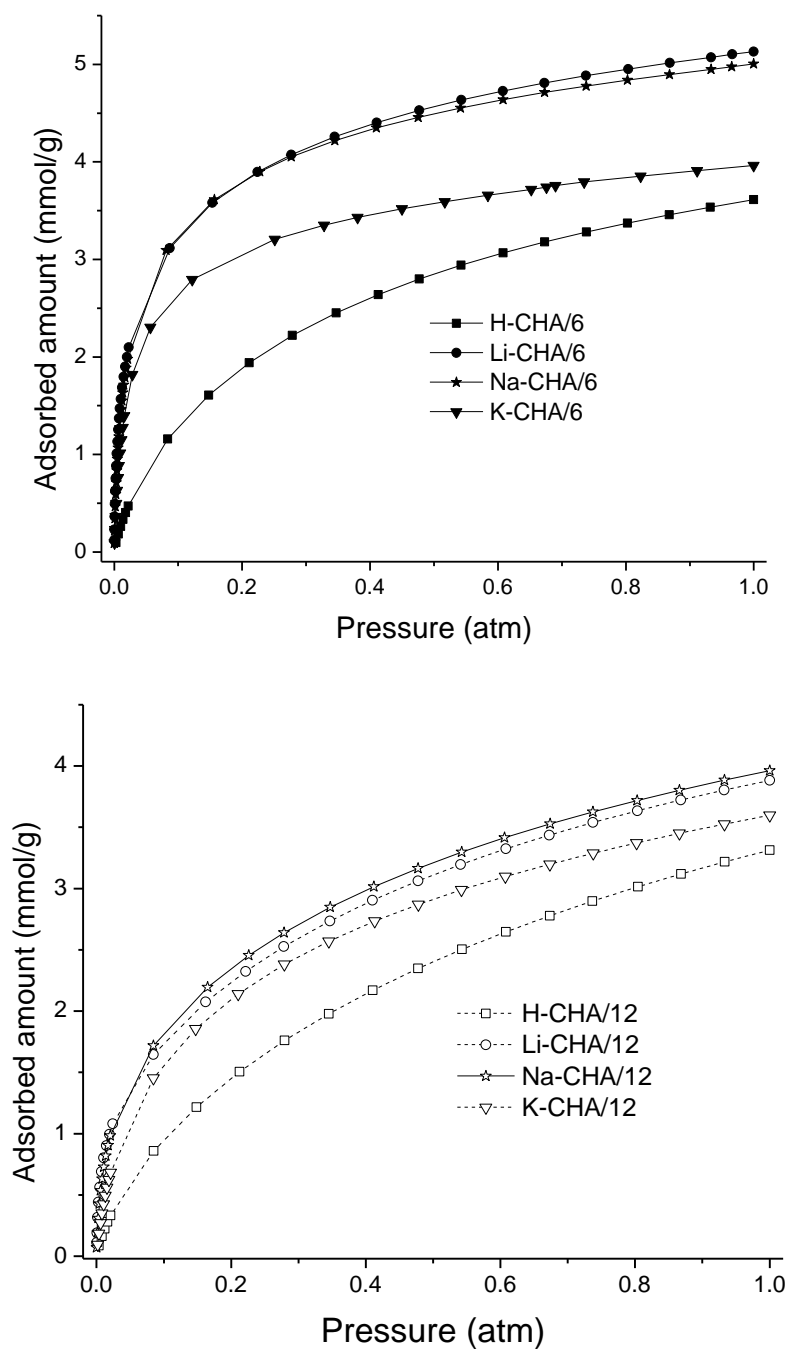


Figure 3.6. Adsorption isotherms of CO₂ on cation-exchanged CHA at 303 K

For CO₂ the adsorption trends are more complex. Since CO₂ is a Lewis acid and the oxygen atoms bonded to alkali cations can behave as Lewis bases, CO₂ adsorbed on zeolites includes contributions from physical and chemical adsorption and these contributions are governed by the alkali cation identity, location within the cavities of zeolites and Si/Al ratio [40]. For chemisorbed CO₂, oxygen basicity plays an important role and the basicity of the oxygens bonded to cations in zeolites is in the order: K⁺>Na⁺>Li⁺>>H⁺ (because neighboring lattice oxygen atoms transfer less charge to larger cations) [41], that is inversely proportional to electric field strength; therefore, the interaction between CO₂ and zeolites at low loading of CO₂ is due to the inversely contribution of physical and chemical energies and depends on the temperature. The CO₂ adsorption isotherms of Na- and Li-CHA are very similar, higher than K-CHA and much higher than H-CHA (the additional mass of large cations inside the zeolites is also detrimental to CO₂ capacity on a per mass basis) (Figure 3.6). In the very low pressure region Li-CHA has higher CO₂ capacity, but upon loading of more CO₂ on the adsorbents, there is a small increase in the equilibrium uptake of CO₂ on Na-CHA relative to Li-CHA. The reason for the crossing of isotherms could be that at higher loading of CO₂, the adsorbate-adsorbate interaction becomes important, and with higher basicity, Na-CHA forms carbonate-like species easier leading to a strong interaction with CO₂ molecules by induce-dipole interaction. The adsorbed CO₂ molecules on Na⁺ cations (which are located in both 6-membered ring window and the cavity) [16] are closer than two Li⁺ cations (which are located in only 6-membered ring) might contribute to a higher adsorption capacity of Na-CHA to Li-CHA at the higher pressure.

Owing to the higher micropore volume of CHA ($V_{\text{mic}} \sim 0.27 \text{ cm}^3/\text{g}$), at 303 K and 1 atm, the CO_2 uptakes on Na-, Li-CHA/6 materials can reach up to 5.0 and 5.1 mmol/g, respectively; higher than that on Na-, Li-ZK-5 (Si/Al \sim 5, $V_{\text{mic}} \sim 0.22 \text{ cm}^3/\text{g}$) (4.0 and 4.9 mmol/g, respectively) [42]. ZK-5 consists of 3 small *pau*-cages per unit cell and a bigger N_2 molecule (kinetic diameter = 3.64 Å) might be not accessible to these cages. This could be the reason for very low N_2 uptake of ZK-5 ($< 0.3 \text{ mmol/g}$) compared to CHA ($\sim 0.6 \text{ mmol/g}$) at 303 K and 1 atm, and explains a higher selectivity of CO_2/N_2 on ZK-5 in the PSA and VSA regions than that on CHA (see below Table 3.3 and the reference [42]). At 1 atm of CO_2 , Li,Na-CHA show higher adsorption capacity than Cu-CHA of similar Si/Al ratios as reported by Hudson et al [10]. This is probably because there are twice as many cations per unit of volume in Na-CHA than in Cu(II)-CHA.

3.3.4 Heats of adsorption of CO_2 on CHA zeolites

Toth and Langmuir adsorption isotherm models for CO_2 adsorption on cation-exchanged CHA at 273 K, 303 K and 343 K (not shown here) showed that the Toth model fits better the experimental data. Therefore, Toth model was used to fit the experimental data and combined with the Clausius–Clapeyron equation was used to estimate the heat of adsorption for cation-exchanged zeolites (Figure 3.7).

For the same cation, the sample with the lower Si/Al ratio showed higher CO_2 heats of adsorption. The low basicity of H-CHA and the small ionic radius of H^+ lead to the lowest heats of adsorption of all materials considered. When increasing the pressure, because more cations are already occupied by carbon dioxide, the chemical energy and physical interaction energy between adsorbate-adsorbent decreases. More adsorbed CO_2 leads to a higher contribution due to adsorbate-adsorbate interactions,

but this increase is not enough to offset the decrease of total energy caused by the drop of adsorbent-adsorbate interaction energy resulting in a drop in the heat of adsorption in all cases (Figure 3.7). The trend is consistent with the results reported by the Paul group on alkali chabazite (Si/Al=2.5) [32]. Li-CHA showed a steeper decrease in the heat of adsorption compared to Na-CHA with increasing CO₂ adsorption (that is, CO₂-CO₂ interaction becomes important), which could be explained by the difference in the induce-dipole interaction between CO₂ molecules as mentioned before. A large ionic radius and higher basicity of oxygen bound to K⁺ would increase the van der Waals force and chemical energy of K-CHA with CO₂. Brown *et al*[10] have used Rietveld refinement of neutron diffraction data, and the Scholl group[11] have used PBE-D₂ calculations to show that the CO₂ configuration is perpendicular to the plane of the 8-membered ring (8MR) and located at the middle of the ring. K⁺ is also located near the middle of 8MR, therefore the direct interaction between K⁺ and CO₂ increases the heat of adsorption of adsorbed CO₂ on K-CHA. Because of the low micropore volume, CO₂ adsorbed on K-CHA/6 will reach saturation faster than in the other zeolites; therefore, after a loading 2.5 mmol/g, the adsorption heat drops faster in K-CHA/6 zeolite. With high heat of adsorption and high adsorption capacity, Na- and Li-CHA/6 are potentially good candidates for CO₂ separation by temperature swing adsorption (TSA) processes.

The results from Čejka *et al.* [43] on the adsorption of CO₂ over alkali metal exchanged ferrierites with Si/Al = 8.7 and 26.6 also showed a significant dependence of adsorption heats on cation size, cation concentration, and the amount of adsorbed CO₂. The trend of adsorption heats on FER is similar to CHA with a steeper decrease of adsorption heat on Li-exchanged zeolite. The dispersion and quadrupole-electric

field gradient energies between zeolite and CO₂ are inversely proportional to the window and pore sizes of zeolite [10]. Therefore, adsorbed CO₂ would interact more strongly with FER containing 8-ring and 10-ring window/pore [44] size than CHA containing ellipsoidal cage that is bounded by 12-rings and has 8-ring windows that allow motion of molecules between the cages [14]. Besides, FER with Si/Al ratio of 8.7 has the additional energy contribution of dual cation site (one CO₂ molecule interacts with two cation site in zeolite) [43] that explain a higher heat of adsorption of FER/8.7 (51-55 kJ/mol) compared to CHA/6 (41-46 kJ/mol) at low loading of CO₂ even though the cation concentration in FER is a little less than in CHA. At higher loadings of CO₂, the adsorbate-adsorbate interaction becomes more important leading to equivalent adsorption heats of these two zeolite adsorbents. With lower energy requirement for desorption and higher loading amount of CO₂ at high pressure (micropore volume CHA: 0.27cm³/g and FER 0.12cm³/g), CHA zeolites seem to be more favorable to practical adsorption processes.

At similar conditions of ambient temperature and pressure, Na-STI (Si/Al=15) [45] possessing 2-D pore channels with 10-ring and 8-ring pore windows has lower adsorption capacity compared to Na-CHA (Si/Al=12) possessing 3-D pore channels and higher micropore volume (Na-CHA: 0.27cm³/g and Na-STI 0.15 cm³/g). Neither Na-CHA and Na-STI have no dual cation site, the higher dispersion and quadrupole-electric field gradient energies in smaller pore would increase the heat of adsorption in Na-STI, but a little higher ratio of Si/Al in Na-STI would cause the inverse effect to the interaction energy, leading to an equivalent heat of adsorption (≈37 kJ/mol) at a loading of one CO₂ molecule per one Na⁺ cation in these two zeolites.

3.3.5 Henry's law region

The Henry's constant is directly related to the interaction of adsorbate with the adsorbent since at low pressure, adsorbate-adsorbent forces predominate. In order to evaluate adsorption affinity between adsorbate and adsorbent, the Henry's constant was investigated using virial plots (Eq. 3.2).

$$P = \frac{q}{K_H} \exp(A_1 q + A_2 q^2 + \dots) \quad (3.2)$$

$$Q_{st}^o = -R \left[\frac{\partial \ln K_H}{\partial \left(\frac{1}{T} \right)} \right] \quad (3.3)$$

where A_1 , A_2 are the virial coefficients, q is the loading amount (mmol/g). A plot of $\ln(P/q)$ vs the adsorbed amount, q , should approach the axis linearly as $q \rightarrow 0$ with the intercept $-\ln(K_H)$ [46].

The heat of adsorption at zero coverage can be determined from the Henry's law constants according to the van't Hoff equation (Eq. 3.3) [20].

The smaller the intercept is, the higher Henry's constant is, and the virial plot (Figure 3.8) shows weak interaction of N_2 with the adsorbents compared to CO_2 . Since adsorption is an exothermic process, increments in temperature will decrease the adsorbate-adsorbent interaction and results in the decrease of Henry's constants (Figure 3.8 and Table 3.3). Adsorption isotherms on Li-CHA have the steepest slope in the low pressure region at all temperatures, consequently the Henry's constants values are highest for N_2 and CO_2 adsorbed on Li-CHA and this sample also shows the highest selectivity of CO_2 over N_2 in the low pressure region (Table 3.3). Compared to ZK-5 (Si/Al~5), the selectivity of CO_2/N_2 in the Henry's region shows similar trends: Li, Na>K>H. The higher selectivity on Na-ZK-5 than Li-ZK-5 is also explained by dual cation site existing in Na-ZK-5 adsorbent [42]. The heats of adsorption of CO_2 at near zero coverage were calculated based on equation (3.3) and the results are consistent with the results reported in Table 3.3.

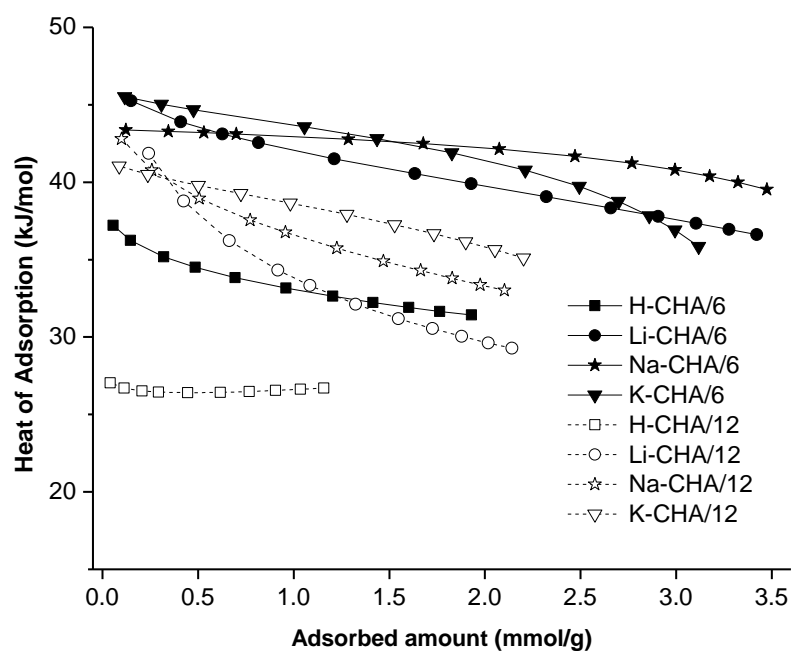


Figure 3.7. Heat of adsorption of CO₂ on cation-exchanged CHA zeolites (Si/Al=6 and 12)

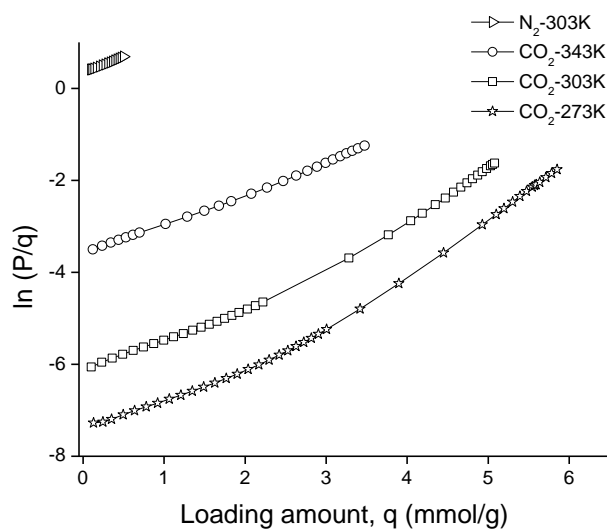


Figure 3.8. Virial plot of N₂ and CO₂ on Na-CHA/6

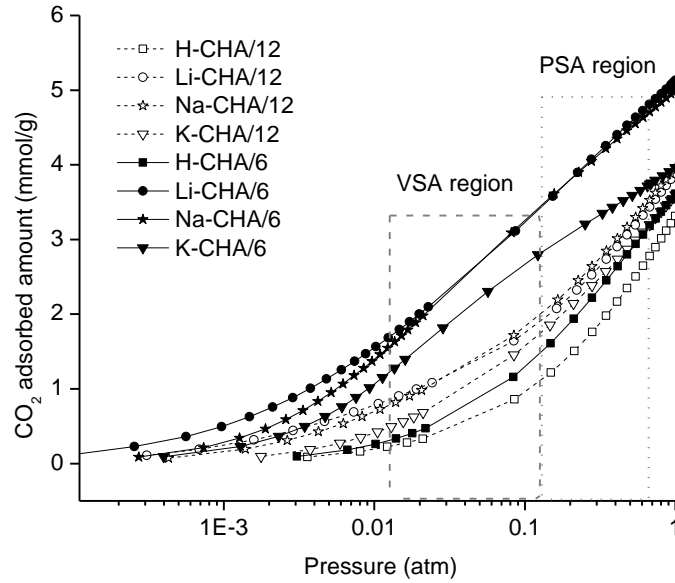


Figure 3.9. Isotherms of CO₂ adsorbed on CHA at 303K and VSA, PSA separation regions on a semi-log plot.

3.3.6 Separation ability of CO₂ from N₂ in a flue gas mixture for PSA and VSA processes

Because of low energy requirements and fast generation times, Pressure Swing Adsorption (PSA) and Vacuum Swing Adsorption (VSA) are used for a number of gas separation applications [47-48]. Carbon dioxide capture and sequestration were evaluated by the criteria reported in reference[49] assuming a flue gas composition is 13% CO₂ and 75% N₂ [50] at total pressures of 1-5 atm for Pressure Swing Adsorption (PSA), and 0.1-1 atm for Vacuum Pressure Adsorption (VSA) region:

1. CO₂ uptake under adsorption conditions (mol.kg⁻¹), N_1^{ads}
2. Working CO₂ capacity (mol.kg⁻¹), $\Delta N_1 = N_1^{ads} - N_1^{des}$
3. Regenerability (%), $R = (\Delta N_1 / N_1^{ads}) \times 100$

4. Selectivity under adsorption conditions, $\alpha_{12}^{ads}=(N_1^{ads}/N_2^{ads})(y_2/y_1)$

As we can see from Table 3.4, the selectivity of CO₂ over N₂ in PSA and VSA regions are all lower than in Henry region (Table 3.3). In the VSA region, both Na- and Li-CHA are excellent adsorbent candidates because of high working capacity. Since alkali cation-exchanged zeolites CHA have high capacity in the low pressure region and get saturated at high pressure, the working capacity of these samples in the PSA region are lower than H-CHA. Hence, H-CHA is in principle a better adsorbent in terms of working capacity, regenerability and also selectivity in PSA processes.

Table 3.3. The CO₂ adsorption heat and the Henry's law constants determined by virial plot for N₂ and CO₂ adsorption on CHA

Samples	Henry's constant (K _H -mmol.g ⁻¹ .atm ⁻¹)				Selectivity K _{HCO2} /K _{HN2}	Q _{st} (kJ/mol)
	CO ₂			N ₂		
	273K	303K	343K	303K	303K	
H-CHA/6	115	21	5	0.28	76	35.2
Li-CHA/6	3860	810	73	0.95	853	44.2
Na-CHA/6	1755	447	37	0.73	617	43.0
K-CHA/6	1561	211	26	0.81	260	45.5
H-CHA/12	22	13	2	0.25	54	26.8
Li-CHA/12	2106	411	41	0.45	906	44.0
Na-CHA/12	671	137	16	0.41	336	41.3
K-CHA/12	353	58	9	0.37	156	35.3

Table 3.4. Adsorbents evaluation parameters for flue gas separation using PSA and VSA at 303K

Adsorbent	Vacuum Swing Adsorption				Pressure Swing Adsorption			
	$N_{CO_2}^{ads}$	ΔN_{CO_2}	R	α_{CO_2/N_2}	$N_{CO_2}^{ads}$	ΔN_{CO_2}	R	α_{CO_2/N_2}
	mmol/g	mmol/g	%		mmol/g	mmol/g	%	
H-CHA/6	1.50	1.20	80	49	3.14	1.63	52	34
Li-CHA/6	3.45	1.75	51	46	4.78	1.33	28	26
Na-CHA/6	3.49	1.92	55	49	4.69	1.21	26	26
K-CHA/6	2.84	1.63	57	62	3.73	0.88	24	32
H-CHA/12	1.13	0.90	80	43	2.73	1.59	58	32
Li-CHA/12	2.03	1.23	60	48	3.38	1.35	40	27
Na-CHA/12	2.04	1.27	62	50	3.48	1.45	41	34
K-CHA/12	1.75	1.26	72	45	3.17	1.42	45	30

*: Adsorbed amount of N_2 at total pressure 5 atm (partial pressure of N_2 3.5 atm) were calculated by extrapolation method based on Toth model, so the selectivity in the PSA region is only for reference

3.4 Conclusions

CHA has a high thermal stability compared to low silica zeolites, and has a high potential for CO_2 capture, reaching an adsorption capacity at ambient temperature and pressure of 5.1 mmol CO_2 per gram of zeolite, a value comparable with the best known zeolite adsorbents (X, Y). The adsorption characteristics of CHA are strongly dependent upon the cation concentration, cation-type exchanged into the zeolite, and the CO_2 loading amount. The adsorption isotherms show that all zeolite adsorbents have much higher affinity with CO_2 than N_2 , and Li-CHA gives the highest total capacity and selectivity in Henry's law region because of the higher electric field of Li^+ than that of other cations. In industrial applications, Li-, Na- with high capacity and heats of adsorption are potential in TSA processes, and depending on the chosen PSA, VSA pressure regions, Li-, Na-CHA or H-CHA are found to be promising adsorbents for this application.

REFERENCES

1. D'Alessandro, D.M., B. Smit, and J.R. Long, *Carbon Dioxide Capture: Prospects for New Materials*. Angewandte Chemie-International Edition, 2010. **49**(35): p. 6058-6082.
2. Herzog, H., *What future for carbon capture and sequestration?* Environmental Science & Technology, 2001. **35**(7): p. 148A-153A.
3. Yang, H., et al., *Progress in carbon dioxide separation and capture: A review*. Journal of Environmental Sciences-China, 2008. **20**(1): p. 14-27.
4. Choi, S., J.H. Drese, and C.W. Jones, *Adsorbent Materials for Carbon Dioxide Capture from Large Anthropogenic Point Sources*. Chemsuschem, 2009. **2**(9): p. 796-854.
5. Hedin, N., L. Chen, and A. Laaksonen, *Sorbents for CO₂ capture from flue gas-aspects from materials and theoretical chemistry*. Nanoscale, 2010. **2**(10): p. 1819-1841.
6. Walton, K.S., M.B. Abney, and M.D. LeVan, *CO₂ adsorption in Y and X zeolites modified by alkali metal cation exchange*. Microporous and Mesoporous Materials, 2006. **91**(1-3): p. 78-84.
7. Beutkamp, S. and P. Harting, *Experimental determination and analysis of high pressure adsorption data of pure gases and gas mixtures*. Adsorption-Journal of the International Adsorption Society, 2002. **8**(4): p. 255-269.
8. Harlick, P.J.E. and F.H. Tezel, *An experimental adsorbent screening study for CO₂ removal from N₂*. Microporous and Mesoporous Materials, 2004. **76**(1-3): p. 71-79.
9. Bao, Z., et al., *Adsorption Equilibria of CO₂, CH₄, N₂, O₂, and Ar on High Silica Zeolites*. Journal of Chemical and Engineering Data, 2011. **56**(11): p. 4017-4023.
10. Hudson, M.R., et al., *Unconventional, Highly Selective CO₂ Adsorption in Zeolite SSZ-13*. Journal of the American Chemical Society, 2012. **134**(4): p. 1970-1973.
11. Fang, H., et al., *Prediction of CO₂ Adsorption Properties in Zeolites Using Force Fields Derived from Periodic Dispersion-Corrected DFT Calculations*. Journal of Physical Chemistry C, 2012. **116**(19): p. 10692-10701.
12. Hereijgers, B.P.C., et al., *Product shape selectivity dominates the Methanol-to-Olefins (MTO) reaction over H-SAPO-34 catalysts*. Journal of Catalysis, 2009. **264**(1): p. 77-87.

13. Smith, J.V., *CRYSTAL STRUCTURES WITH A CHABAZITE FRAMEWORK .1. DEHYDRATED CA-CHABAZITE*. Acta Crystallographica, 1962. **15**(SEP): p. 835-&.
14. Smith, J.V., L.S.D. Glasser, and F. Rinaldi, *CRYSTAL STRUCTURES WITH A CHABAZITE FRAMEWORK .2. HYDRATED CA-CHABAZITE AT ROOM TEMPERATURE*. Acta Crystallographica, 1963. **16**(1): p. 45-&.
15. Smith, L.J., H. Eckert, and A.K. Cheetham, *Potassium cation effects on site preferences in the mixed cation zeolite Li,Na-chabazite*. Chemistry of Materials, 2001. **13**(2): p. 385-391.
16. Smith, L.J., H. Eckert, and A.K. Cheetham, *Site preferences in the mixed cation zeolite, Li,Na-chabazite: A combined solid-state NMR and neutron diffraction study*. Journal of the American Chemical Society, 2000. **122**(8): p. 1700-1708.
17. Civalieri, B., et al., *Cation selectivity in alkali-exchanged chabazite: An ab initio periodic study*. Chemistry of Materials, 2003. **15**(21): p. 3996-4004.
18. Ugliengo, P., et al., *Carbon monoxide adsorption on alkali and proton-exchanged chabazite: an ab-initio periodic study using the CRYSTAL code*. Molecular Physics, 2005. **103**(18): p. 2559-2571.
19. Smith, L.J., A. Davidson, and A.K. Cheetham, *A neutron diffraction and infrared spectroscopy study of the acid form of the aluminosilicate zeolite, chabazite (H-SSZ-13)*. Catalysis Letters, 1997. **49**(3-4): p. 143-146.
20. Ridha, F.N. and P.A. Webley, *Anomalous Henry's law behavior of nitrogen and carbon dioxide adsorption on alkali-exchanged chabazite zeolites*. Separation and Purification Technology, 2009. **67**(3): p. 336-343.
21. Ridha, F.N., Y. Yang, and P.A. Webley, *Adsorption characteristics of a fully exchanged potassium chabazite zeolite prepared from decomposition of zeolite Y*. Microporous and Mesoporous Materials, 2009. **117**(1-2): p. 497-507.
22. Ridha, F.N. and P.A. Webley, *Entropic effects and isosteric heats of nitrogen and carbon dioxide adsorption on chabazite zeolites*. Microporous and Mesoporous Materials, 2010. **132**(1-2): p. 22-30.
23. Khvoshchev, S.S. and A.V. Zverev, *HEATS OF SORPTION OF CARBON-DIOXIDE AND AMMONIA ON ION-EXCHANGE FORMS OF SYNTHETIC CHABAZITE*. Zeolites, 1991. **11**(7): p. 742-744.
24. Fickel, D.W., J.M. Fedeyko, and R.F. Lobo, *Copper Coordination in Cu-SSZ-13 and Cu-SSZ-16 Investigated by Variable-Temperature XRD*. Journal of Physical Chemistry C, 2010. **114**(3): p. 1633-1640.
25. Eilertsen, E.A., et al., *NMR and SAXS Analysis of Connectivity of Aluminum and Silicon Atoms in the Clear Sol Precursor of SSZ-13 Zeolite*. Chemistry of Materials, 2012. **24**(3): p. 571-578.
26. *Chapter 35 - CHA SSZ-13 Si(93), Al(7)*, in *Verified Syntheses of Zeolitic Materials*, H. Robson and K.P. Lillerud, Editors. 2001, Elsevier Science: Amsterdam. p. 126-128.

27. Smith, J.V. and S.W. Bailey, *SECOND REVIEW OF Al-O AND Si-O TETRAHEDRAL DISTANCES*. Acta Crystallographica, 1963. **16**(8): p. 801-&.
28. Little, L.H. and C.H. Amberg, *INFRARED SPECTRA OF CARBON MONOXIDE AND CARBON DIOXIDE ADSORBED ON CHROMIA-ALUMINA AND ON ALUMINA*. Canadian Journal of Chemistry-Revue Canadienne De Chimie, 1962. **40**(10): p. 1997-&.
29. Delaval, Y. and E.C. Delara, *STUDY OF PHYSISORPTION OF CARBON-DIOXIDE ON NAA ZEOLITE .1. EXPERIMENTAL RESULTS OBTAINED BY INFRARED-SPECTROSCOPY*. Journal of the Chemical Society-Faraday Transactions I, 1981. **77**: p. 869-877.
30. Montanari, T. and G. Busca, *On the mechanism of adsorption and separation of CO₂ on LTA zeolites: An IR investigation*. Vibrational Spectroscopy, 2008. **46**(1): p. 45-51.
31. Ramis, G., G. Busca, and V. Lorenzelli, *LOW-TEMPERATURE CO-2 ADSORPTION ON METAL-OXIDES - SPECTROSCOPIC CHARACTERIZATION OF SOME WEAKLY ADSORBED SPECIES*. Materials Chemistry and Physics, 1991. **29**(1-4): p. 425-435.
32. Zhang, J., R. Singh, and P.A. Webley, *Alkali and alkaline-earth cation exchanged chabazite zeolites for adsorption based CO₂ capture*. Microporous and Mesoporous Materials, 2008. **111**(1-3): p. 478-487.
33. Barrer, R.M., *SPECIFICITY IN PHYSICAL SORPTION*. Journal of Colloid and Interface Science, 1966. **21**(4): p. 415-&.
34. Aguilar-Armenta, G., et al., *Adsorption kinetics of CO₂, O-2, N-2, and CH₄ in cation-exchanged clinoptilolite*. Journal of Physical Chemistry B, 2001. **105**(7): p. 1313-1319.
35. Golden, T.C. and S. Sircar, *GAS-ADSORPTION ON SILICALITE*. Journal of Colloid and Interface Science, 1994. **162**(1): p. 182-188.
36. Dunne, J.A., et al., *Calorimetric heats of adsorption and adsorption isotherms .1. O-2, N-2, Ar, CO₂, CH₄, C₂H₆ and SF₆ on silicalite*. Langmuir, 1996. **12**(24): p. 5888-5895.
37. Xu, B. and L. Kevan, *FORMATION OF ALKALI-METAL PARTICLES IN ALKALI-METAL CATION EXCHANGED X-ZEOLITE EXPOSED TO ALKALI-METAL VAPOR - CONTROL OF METAL-PARTICLE IDENTITY*. Journal of Physical Chemistry, 1992. **96**(6): p. 2642-2645.
38. Lavalley, J.C., *Infrared spectrometric studies of the surface basicity of metal oxides and zeolites using adsorbed probe molecules*. Catalysis Today, 1996. **27**(3-4): p. 377-401.
39. Papai, I., et al., *MODELING OF N-2 AND O-2 ADSORPTION IN ZEOLITES*. Journal of Physical Chemistry, 1995. **99**(34): p. 12925-12932.
40. Bonenfant, D., et al., *Advances in principal factors influencing carbon dioxide adsorption on zeolites*. Science and Technology of Advanced Materials, 2008. **9**(1).

41. Huang, M.M. and S. Kaliaguine, *ZEOLITE BASICITY CHARACTERIZED BY PYRROLE CHEMISORPTION - AN INFRARED STUDY*. Journal of the Chemical Society-Faraday Transactions, 1992. **88**(5): p. 751-758.
42. Qingling Liu, T.P., Marc D. Porosoff, and Raul F. Lobo, *ZK-5: A CO₂-Selective Zeolite with High Working Capacity at Ambient Temperature and Pressure*. ChemSusChem, 2012.
43. Zukal, A., et al., *Experimental and theoretical determination of adsorption heats of CO₂ over alkali metal exchanged ferrierites with different Si/Al ratio*. Physical Chemistry Chemical Physics, 2010. **12**(24): p. 6413-6422.
44. VAUGHAN, P.A., *The Crystal Structure of the Zeolite Ferrierite*. Acta Cryst., 1966(21): p. 983-990.
45. Zukal, A., et al., *Adsorption of Carbon Dioxide on Sodium and Potassium Forms of STI Zeolite*. Chempluschem, 2012. **77**(8): p. 675-681.
46. Pawar, R.R., et al., *Selective adsorption of carbon dioxide over nitrogen on calcined synthetic hectorites with tailor-made porosity*. Applied Clay Science, 2009. **46**(1): p. 109-113.
47. Chaffee, A.L., et al., *CO₂ capture by adsorption: Materials and process development*. International Journal of Greenhouse Gas Control, 2007. **1**(1): p. 11-18.
48. Aaron, D. and C. Tsouris, *Separation of CO₂ from flue gas: A review*. Separation Science and Technology, 2005. **40**(1-3): p. 321-348.
49. Bae, Y.-S. and R.Q. Snurr, *Development and Evaluation of Porous Materials for Carbon Dioxide Separation and Capture*. Angewandte Chemie-International Edition, 2011. **50**(49): p. 11586-11596.
50. Ho, M.T., G.W. Allinson, and D.E. Wiley, *Reducing the cost of CO₂ capture from flue gases using membrane technology*. Industrial & Engineering Chemistry Research, 2008. **47**(5): p. 1562-1568.

Chapter 4

MOLECULAR BASIS FOR THE HIGH CO₂ ADSORPTION CAPACITY OF CHABAZITE ZEOLITES

4.1 Introduction

The large-scale capture and sequestration of CO₂ from pre-combustion (CO₂/H₂), post-combustion (CO₂/N₂), and natural gas mixtures (CO₂/CH₄) have become important technological and environmental targets to mitigate the effect of greenhouse gases on global climate change [1, 2]. Conventional CO₂ capture using primary alkanolamine scrubbers consumes large amounts of energy for regeneration due to the high heat of formation of carbamates and the large heat capacity of the aqueous solution [3]. In addition, this technology uses inhibitors to improve corrosion resistance and prevent oxidative degradation caused by residual oxygen in the flue stream [4, 5]. Nanoporous materials such as carbon molecular sieves [2, 6], zeolites [7-10], and metal organic frameworks (MOFs) [11-14] have been studied for CO₂ separations and capture because of their high internal surface area, high micropore volume, chemical tunability, fast adsorption/desorption kinetics, and low heats of adsorption. For zeolitic adsorbents, isosteric heats of adsorption, $-Q_{st}$, on the order of 20 kJ/mol to 60 kJ/mol have been measured by techniques such as microcalorimetry [15, 16] and volumetric adsorption measurements [8, 17-22]. Spectroscopic techniques have identified a range of adsorbed CO₂ surface species in zeolite materials including primarily physisorbed CO₂, bidentate carbonates, monodentate carbonates, and carboxylates [23-25]. By combining variable temperature infrared spectroscopy with

periodic DFT calculations, Nachtigall *et al* reported that the CO₂ adsorption sites could be classified as single- or dual-cation sites in a number of various zeolite types [26-29]. Molecular simulation methods, such as Grand Canonical Monte Carlo (GCMC) and molecular dynamics (MD) [30-38], have been used to study the adsorption of CO₂ in porous materials to compute the thermodynamics and transport properties, and identify optimal capture materials. More recently, X-ray and neutron diffraction have been applied to investigate the CO₂ adsorption sites in highly crystalline porous materials at the molecular level [7, 39-42].

Chabazite (CHA) is a small pore zeolite consisting of a double 6-membered ring (D6R) as the basic building unit with one large ellipsoidal cavity accessed by six 8-membered ring windows (8MR) (free aperture ≈ 3.8 Å) [43, 44]. It is also a model material because it contains only one T-atom in its asymmetric unit. Chabazite-type zeolites provide improved hydrothermal stability over other zeolites, an important property for example, in the selective catalytic reduction of NO_x [45, 46] and moist flue-gas applications. Chabazite has also been shown to have high selectivity for light olefins (ethylene/propylene) in the conversion of methanol to olefins process and demonstrated potential in gas separations, such as the separation of propane/propene mixtures [47], and CO₂ from N₂ in flue gas mixtures [8, 48-50] due to its large cavities and small window sizes.

Extra-framework cations present in aluminum-exchanged zeolite frameworks play important roles in determining the adsorption properties of zeolites [8, 18]. Cheetham *et al.* [51, 52] used neutron diffraction and nuclear magnetic resonance while Ugliengo *et al.* [53] used *ab initio* periodic calculations to study the location of alkali cations in chabazite zeolites with Si/Al ≈ 2.5 and ≈ 11 , respectively. It was

found that K^+ is preferentially located at the 8-membered ring (site SIII'), Li^+ prefers to sit at the 6-membered ring window (6MR, site SII) rather than site SIII (close to the corner of the 4-membered ring, 4MR), and Na^+ prefers locating at site SII. Additionally, Webley *et al.* [16b] identified a “trapdoor” filtering mechanism in chabazite zeolites in which CO_2 has sufficient strong interaction to induce large 8MR blocking cations (K^+ and Cs^+) to temporarily deviate from the center of pore apertures for the admission of CO_2 molecules, thus providing a temperature dependent and high selectivity for separation of important industrial gas mixtures such as CO_2/CH_4 and CO_2/N_2 .

The impact of zeolite composition on adsorption properties can be observed in comparing the adsorption isotherms of Si-CHA [22], Na-CHA-12 and Na-CHA-6 [8] to zeolites NaY (Si/Al = 2.5) and HY40 (Si/Al = 40) which shows that siliceous chabazite is in fact a better adsorbent than HY40 at room temperature (Figure 4.5). Further, adsorption measurements reveal that the chabazite samples with higher aluminum content have higher adsorption capacity. At 1 atm pressure, the adsorption capacity of Na-CHA-6 is very similar to the adsorption capacity of NaY, and at low pressure, Na-CHA-6 has much higher adsorption capacity.

This report investigates the adsorption properties and site-specific adsorption properties of carbon dioxide in pure, high and medium silica chabazites (Si-CHA, CHA-12, CHA-6 with Si/Al = ∞ , = 12, = 6, respectively). The information is obtained by combining *in-situ* X-ray and neutron powder diffraction methods using Fourier difference mapping to locate the adsorbed CO_2 and correlating this with available volumetric adsorption measurements. The results help elucidate the atomic origin of

the adsorption properties across a series of cation-exchanged zeolites which can be the bases for the engineering of improved CO₂ adsorbents.

4.2 Experimental

4.2.1 Zeolite Materials

Zeolite NaA (Si/Al = 1) was purchased from Sigma Aldrich,* Na13X (Si/Al = 1.25) and NaY (CBV100, Si/Al = 2.47), HY (CBV780, Si/Al = 40) were purchased from Zeolyst.

Pure silica chabazite Si-CHA [22, 71]: 11.8 g of TEOS was hydrolyzed in 23.9 g of TMAOH and heated to remove the ethanol and water (23.8 g in total). Then 1.2 g of HF was added to the mixture to produce the final composition of 3 H₂O : 1 SiO₂ : 0.5 TMAOH : 0.5 HF. This thick paste was homogenized by hand in a Teflon container, and transferred to a 23 mL Teflon-lined stainless steel autoclave (Parr). The autoclave was kept at 423 K with rotation (~ 40 rpm) for 48 h in a convection oven. The as-made product was then calcined in air at 873 K for 16 h heating at a ramping rate of 5 K/min to prepare Si-CHA.

CHA-6 (Si/Al = 6) [8, 46]: A solution of 10 g of sodium silicate (Sigma Aldrich, 26.5 % SiO₂), 0.32 g of NaOH (Fisher Scientific, > 98 %) and 24 g of DI water was stirred at room temperature for about 15 min. Then, 1 g of Na-Y (Zeolyst CBV100, Si/Al = 2.47) and 1.6 g of N,N,N-trimethyl-1-adamantanammonium iodide were added to the solution and stirred for another 30 min. The resulting solution was then transferred into 43 ml Teflon-lined autoclaves (Parr) and heated at 423 K under

* Any mention of commercial products is for information only; it does not imply recommendation or endorsement by NIST.

rotation for 6 d. The solid product was separated by vacuum filtration, washed extensively with DI water, and dried at 353 K overnight. The as-made product was then calcined in air at 823 K for 8 h using a ramping rate of 5 K/min to prepare the starting form of Na-CHA-6.

CHA-12 (Si/Al = 12) [8]: A mixture of tetraethyl orthosilicate (TEOS, sigma 98 %), N,N,N-trimethyl-1-adamantanamine hydroxide (TMAdaOH, 25 % wt., Sachem Inc.) and DI water were mixed for 2 h, then Al(OEt)₃ (Strem Chemical, 99 %) was added to the solution to obtain a final gel composition of SiO₂ : H₂O : TMAdaOH : Al₂O₃ is 1 : 20 : 0.5 : 0.035 and stirred for another 12 h. The resulting solution was then transferred into Teflon-lined autoclaves and heated at a temperature of 423 K under static condition for 6 d. After that, the sample was washed with DI water, and dried at 353 K overnight. The as-made product was then calcined in air at 823 K for 8 h heating at a ramping rate of 5 K/min to prepare the starting form of H-CHA-12.

4.2.2 Ion Exchange

Ammonium exchanged NH₄-CHA (Si/Al = 6, = 12) was prepared by mixing 1g Na-CHA-6 (or H-CHA-12) with 500 ml NH₄NO₃ 0.1 M overnight at 353 K. The solution was then filtered and washed with deionized water, and the resulting NH₄-CHA product was dried at 353 K overnight. The ion-exchanged Li-CHA, Na-CHA, K-CHA were prepared by mixing 0.1 g NH₄-CHA and 50 g 2 M LiCl (≥ 99.0 %, Sigma), NaCl (≥ 99.0 %, Sigma), KCl (≥ 99.0 %, Sigma) for 12 h at 353 K respectively, and the resulting cation-exchanged CHA products were dried at 353 K overnight. The ion exchange was repeated several times to obtain the completely exchanged form of alkali-metal chabazites. Compositions of metals in cation-exchanged chabazites were determined by inductively coupled plasma mass spectrometry (ICP) and energy-

dispersive X-ray spectroscopy (EDX) methods (Table 3.1). Porosity and surface areas of all zeolite materials were characterized by 77 K N₂ adsorption (Table 3.2).

4.2.3 Powder Diffraction

Neutron powder diffraction (NPD) experiments were carried out on activated chabazite zeolites using the high-resolution neutron powder diffractometer, BT1, at the National Institute of Standards and Technology Center for Neutron Research (NCNR). All samples (neutron and X-ray) were activated (dehydrated) by turbomolecular pump while heating at a temperature of ca. 250 °C for 18 – 24 hrs. The evacuated samples were placed in a He purged glove box, each loaded into a vanadium can equipped with a gas loading valve, and sealed using an indium O-ring. NPD data were collected using a Ge(311) monochromator with an in-pile 60' collimator corresponding to a wavelength of 2.0782 Å. The samples were loaded onto a bottom-loading closed cycle refrigerator, glove box He evacuated by turbomolecular pump (RT) and data were collected on the bare frameworks at 10 K. For the *in-situ* NPD runs, the samples were warmed to 300 K and then exposed to a predetermined amount of CO₂ gas from a volumetric gas manifold. Upon reaching an equilibrium pressure at the loading temperature, the sample was then slowly cooled to ensure equilibrium and complete adsorption of the CO₂ (<1 K/min). Data were again collected at 10 K reducing the thermal motions for the framework and adsorbate.

Similarly, synchrotron X-ray powder diffraction (XRPD) data for pure silica chabazite and K-CHA-6 were measured at the Advanced Photon Source (APS) at Argonne National Laboratory on the 1-BM materials diffractometer ($\lambda = 0.6124$ Å). For XRPD measurement, adsorbents were activated, as described previously, loaded into glass capillaries, and attached to a valve assembly via ultra-Torr fitting all while

inside a N₂ glove box. N₂ was evacuated from the samples in-line via turbomolecular pump and then samples were dosed with known quantities of CO₂ using a custom built gas dosing manifold of known volume. Data were collected at 100 K to again reduce thermal parameters in the materials. Reasons for collecting synchrotron XRPD data on the two selected samples (Si-CHA and K-CHA-6) are as follows: In the case of Si-CHA, the very low affinity for CO₂ adsorption led to questions about the positional accuracy of the refinements from initial NPD and so higher resolution XRPD was considered to remove questions of ambiguity. For K-CHA-6, based on the fact that large cation mobility has been observed in other CHA samples when CO₂ adsorption is considered [49, 50, 72]. XRPD measurements were warranted due the relatively low coherent neutron scattering cross section for potassium (around half that of Si, C, O) vs. higher X-ray scattering cross section (relative to C, O) for K. Accurately determining the positions of the K⁺ cations compared with that of CO₂ are critical.

Rietveld refinements were carried out using the EXPGUI package/GSAS for NPD and XRPD data [73][†]. For the zeolite frameworks, the occupancy of aluminum (vs. Si) is too small to be accurately determined with NPD and to reduce the variables in the Rietveld refinement was fixed based on the average compositions measured by ICP and EDX methods (Table 3.1). Similarly, since ICP and EDX can better determine sample composition than powder diffraction, the extra-framework cations

[†]Further details of the crystal structure investigations may be obtained from the Fachinformationszentrum Karlsruhe, 76344 Eggenstein-Leopoldshafen, Germany (fax: (+49) 7247-808-666; e-mail: crysdata@fiz-karlsruhe.de) on quoting the deposition numbers CSD (-427822, -427823, -427824, -427825, -427826, -427827, -427828, -427829, -427830, -427831, -427832, -427833, -427834, -427835, -427836, -427837, -427838, -427839, -427840, -427841, and -427842).

occupancies are fixed at values from the ICP and EDX since no observable impact on the quality of the refinement is noted.

Fourier difference methods were then employed to elucidate the adsorbed molecules in the data collected from the samples subsequently loaded CO₂. This has been described previously [7] CO₂ doses that range from 0.33 to 0.66 CO₂ molecules per 8-membered ring (8MR) window in the CHA-12 samples and 0.5 to 1.0 CO₂ molecules per 8MR window in CHA-6 were chosen based on simplifying the discussion (and refinements) in these materials. Keeping the occupancy of CO₂ lower in the low-cation exchanged materials is key to determining the primary adsorption site. Similarly, not exceeding 1.0 CO₂ per 8MR in the CHA-6 samples allows for either full adsorption at the window site or occupation of a secondary site while reducing the likelihood of potential bulk like disorder. Additional refinement details include the restraining of the CO₂ angle in the secondary sites (sites B, B', C as subsequently discussed) to be 180°, and the restraint of CO₂ distance to $d_{C-O}(CO_2) = 1.16 \text{ \AA}$ (due to the symmetric nature of the CO₂ across symmetry sites, bonds tended to an “average” longer than ideal), and atomic displacement parameters (ADPs) and fractional occupations for C and O in the same site CO₂ were constrained to be the same as well for clarity.

4.3 Results and Discussion

4.3.1 Cation locations in chabazite zeolites

To obtain molecular insights into the dominant factors affecting isosteric heat of adsorption and total CO₂ uptake capacity, *in-situ* neutron and X-ray powder diffraction experiments were performed. Rietveld refinements were carried out in the

$R\text{-}3m$ space group using a hexagonal unit cell containing 36 symmetry-equivalent tetrahedral Si or Al atoms and 72 oxygen atoms for the activated zeolite materials (Table 4.1 showing here is one example).

Table 4.1. Atomic parameters from Rietveld refinement of pure silica Chabazite (Si-CHA) data at 10 K [NCNR, BT1] (Trigonal, $R\text{-}3m$, $a = 13.5844(3) \text{ \AA}$, $c = 14.7628(5) \text{ \AA}$, $V = 2359.3(1) \text{ \AA}^3$). Values in parentheses indicate one standard deviation in the refined value. Goodness-of-fit parameters: $\chi^2 = 1.057$, $wRp = 6.63 \%$, $Rp = 5.27 \%$. Composition: $\text{Si}_{36}\text{O}_{72}$.

Si-CHA	X	Y	Z	Multipl.	Occup.	Uiso (\AA^2)
O1	0.9006(1)	0.0994(1)	0.1225(2)	18	1	0.005(1)
O2	0.9802(2)	0.3136(2)	0.1667	18	1	0.006(1)
O3	0.1201(1)	0.2400(3)	0.1317(2)	18	1	0.009(1)
O4	0	0.2616(2)	0	18	1	0.011(1)
Si	0.0001(3)	0.2288(2)	0.1046(2)	36	1	0.004(1)

Figure 4.1 depicts the locations of alkali metal cations typically observed in high silica chabazites [53]. Lithium and sodium are located at the 6MR window of the hexagonal prism (SII). Fourier difference maps of the activated, dehydrated zeolites indicate that there are no measurable amounts of Li^+ cations in the elliptical cage, at the four-ring (4MR) window of the hexagonal prism, and that no Na^+ cations were found in the 8MR window of the channel (close to site SIII'). The lithium and sodium cations are observed at position SII, as expected, because this coordination environment is the most favorable in chabazite for a small cation and is in agreement with the lower alkali-cation concentrations in high silica chabazites ($\text{Si}/\text{Al} = 6$ and $= 12$).

This is contrast to the low silica chabazites ($\text{Si}/\text{Al} = 2.5$) where cations are additionally located at SIII and close to SIII' as reported by Smith *et al.* [51, 52]. The

lithium and sodium locations in the chabazite are very similar to the sites observed in a number of synthetic faujasites, LSX, X, and Y [54-56]. Each Li^+ or Na^+ is effectively coordinated with 3 oxygen atoms of the chabazite framework. Due to ionic radii difference ($r_{\text{Na}^+} = 1.16 \text{ \AA}$ and $r_{\text{Li}^+} = 0.73 \text{ \AA}$), Na^+ lies higher above the plane of the 6MR, by an angle of approximately 22° measured from the Si in the ring (Na-CHA-6) compared to Li-CHA-6 with an angle of approximately 9.6° . These angles are slightly larger in the case of Li- and Na-CHA-12, and higher than the values observed for the low silica zeolites faujasites 13X and Y where cations are located almost at the center of the ring. In 6MRs with two or three aluminum atoms, cations bind strongly with the basic oxygen (O-Al) atoms. In contrast, in the case of a ring with only one aluminum atom, the cations are situated near the oxygen (O-Al) atoms and further from oxygen (O-Si) atoms giving the longer average distance of oxygen-cation in the 6MR. The out-of-plane location of Li^+ and Na^+ in high-silica chabazites is also due to the contraction of the 6MR due to the smaller average bond lengths of T-O ($d_{\text{Al-O}} = 1.76 \text{ \AA}$ and $d_{\text{Si-O}} = 1.59 \text{ \AA}$).

With respect to Li^+ and Na^+ , the bigger K^+ cation sits preferentially in the middle of the 8MR where it is coordinated with 4 oxygen atoms of the zeolite framework. In addition K^+ is observed on a position above the 6MR (site SII) where it is only coordinated with 3 oxygen atoms of the zeolite framework. However, this difference is minor since K-O distances in 8MR ($d_{\text{K-O3}} = 3.117(4) \text{ \AA}$, $d_{\text{K-O4}} = 3.270(3) \text{ \AA}$) are longer than K-O distance in 6MR ($d_{\text{K-O3}} = 2.86(6) \text{ \AA}$).

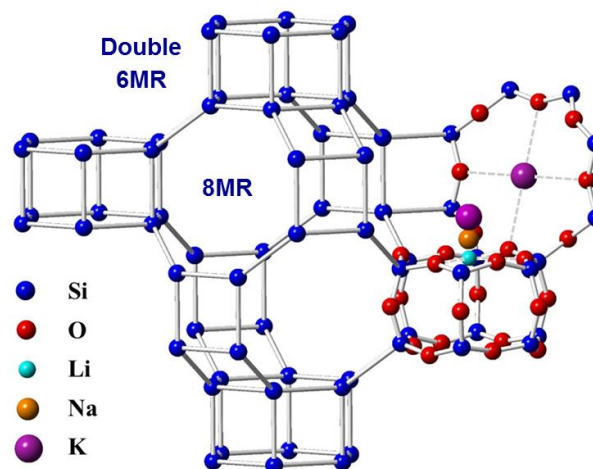


Figure 4.1. Illustration of the chabazite structure and typical cation locations (Li^+ : blue, Na^+ : orange, and K^+ : purple) in the zeolite pores (right). 8MR and double 6MR (D6R) are indicated (left, Si/Al: dark blue) with oxygen atoms (red) omitted for clarity.

Table 4.2. Cation and CO₂ occupancies for the Chabazite zeolites in this study. The value in parentheses represents one standard deviation (in refined value).

Sample	Occupancy		
	Cation*	CO ₂ Site I (8MR)	CO ₂ Site II (M+)
Si-CHA	--	--	--
0.5 CO ₂ /Si-CHA (ND)	--	0.117(7)	0.033(2)
1.0 CO ₂ /Si-CHA (ND)	--	0.237(7)	0.094(2)
0.5 CO ₂ /Si-CHA (XRD)	--	0.163(9)	0.068(2)
1.0 CO ₂ /Si-CHA (XRD)	--	0.405(8)	0.154(3)
Li-CHA-12	0.462	--	--
0.33 CO ₂ /Li-CHA-12	0.462	0.082(5)	0.094(4)
0.66 CO ₂ /Li-CHA-12	0.462	0.303(8)	0.153(7)
Li-CHA-6	0.876	--	--
0.5 CO ₂ /Li-CHA-6	0.876	0.169(8)	0.141(6)
1.0 CO ₂ /Li-CHA-6	0.876	0.490(8)	0.211(4)
Na-CHA-12	0.462	--	--
0.66 CO ₂ /Na-CHA-12	0.462	0.372(8)	0.096(4)
Na-CHA-6	0.876	--	--
0.5 CO ₂ /Na-CHA-6	0.876	0.251(6)	0.064(3)
1.0 CO ₂ /Na-CHA-6	0.876	0.576(8)	0.166(4)
K-CHA-12	0.149(2)/0.21(1)(8MR)	--	--
0.33 CO ₂ /K-CHA-12	0.149/0.209(8MR)	0.199(6)	0.023(3)
0.66 CO ₂ /K-CHA-12	0.149/0.209(8MR)	0.246(7)	0.037(3)
K-CHA-6	0.21(3)/0.44(2)(8MR)	--	--
0.5 CO ₂ /K-CHA-6	0.209/0.444(8MR)	0.27(2)	0.121(4)
1.5 CO ₂ /K-CHA-6	0.209/0.444(8MR)	0.335(9)	0.190(5)

*fixed at the value determined from ICP/EDX

Table 4.3. Select CO₂ bond distances (in Angstroms) for Site A (8MR) for the Chabazite zeolites in this study. The value in parentheses represents one standard deviation (in refined value).

Sample	CO ₂ Site A (8MR) Bond distances								M+...- O1a
	C1-O2	C1-O3	C1-O4	O1a- O2(s)	O1a- O2(l)	O1a- O3(s)	O1a- O3(l)	O1a-O4	
Si-CHA	--	--	--	--	--	--	--	--	--
0.5 CO ₂ /Si-CHA (ND)	3.441(2)	3.180(4)	3.230(2)	3.60(3)	3.66(3)	3.13(4)	3.62(4)	3.432(5)	--
1.0 CO ₂ /Si-CHA (ND)	3.433(2)	3.193(4)	3.230(3)	3.53(3)	3.72(1)	3.23(2)	3.56(2)	3.432(7)	--
0.5 CO ₂ /Si-CHA	3.410(4)	3.129(6)	3.196(5)	3.18(4)	3.98(5)	3.04(5)	3.61(6)	3.40(3)	--
1.0 CO ₂ /Si-CHA	3.411(6)	3.130(6)	3.220(5)	3.35(2)	3.84(2)	3.29(2)	3.38(2)	3.422(7)	--
Li-CHA12	--	--	--	--	--	--	--	--	--
0.33 CO ₂ /Li-CHA12	3.483(3)	3.182(4)	3.219(4)	3.54(3)	3.79(4)	3.31(5)	3.46(4)	3.42(1)	4.27(6)
0.66 CO ₂ /Li-CHA12	3.473(6)	3.175(6)	3.212(4)	3.56(2)	3.76(2)	3.26(2)	3.50(2)	3.415(5)	4.15(8)
Li-CHA-6	--	--	--	--	--	--	--	--	--
0.5 CO ₂ /Li-CHA6	3.585(3)	3.169(5)	3.204(3)	3.73(3)	3.80(4)	3.27(5)	3.48(4)	3.41(1)	4.30(6)
1.0 CO ₂ /Li-CHA6	3.566(3)	3.178(5)	3.204(3)	3.680(9)	3.82(1)	3.30(1)	3.46(1)	3.408(5)	4.32(3)
Na-CHA-12	--	--	--	--	--	--	--	--	--
0.66 CO ₂ /Na-CHA12	3.465(3)	3.207(5)	3.220(4)	3.63(2)	3.68(2)	3.10(2)	3.70(2)	3.423(4)	3.57(3)
Na-CHA-6	--	--	--	--	--	--	--	--	--
0.5 CO ₂ /Na-CHA6	3.489(4)	3.226(4)	3.231(3)	3.62(2)	3.73(2)	3.08(2)	3.75(2)	3.433(3)	3.60(2)
1.0 CO ₂ /Na-CHA6	3.489(3)	3.255(4)	3.238(3)	3.601(9)	3.750(8)	3.08(1)	3.79(1)	3.439(4)	3.57(1)
K-CHA-12	--	--	--	--	--	--	--	--	--
0.33 CO ₂ /K-CHA12	3.440(4)	3.172(4)	3.249(3)	3.60(2)	3.66(2)	3.13(3)	3.61(2)	3.450(8)	3.19(2)
0.66 CO ₂ /K-CHA12	3.443(3)	3.161(4)	3.242(4)	3.61(2)	3.65(2)	3.09(2)	3.62(2)	3.443(6)	3.19(2)
K-CHA-6	--	--	--	--	--	--	--	--	--
0.5 CO ₂ /K-CHA6	3.442(5)	3.089(7)	3.232(7)	3.31(4)	3.93(5)	3.18(5)	3.42(6)	3.44(5)	3.51(4)
1.5 CO ₂ /K-CHA6	3.473(5)	3.141(7)	3.204(5)	3.49(2)	3.83(2)	3.141(7)	3.42(2)	3.41(2)	3.37(2)

Table 4.4. Select CO₂ bond distances (in Angstroms) for Site B (large pore) for the all-silica Chabazite zeolites in this study. The value in parentheses represents one standard deviation (in refined value).

Sample	CO ₂ Sites B (pore) Bond Distances (Å)									
	Site C-Framework				Sites A-B		Sites B-B (in <i>ab</i> -plane)		Sites B-B (along <i>c</i> -axis)	
	O2a-O4	O2b-O4	O2a-O2	O2b-O2	O1a-O2a	O1a-O2b	O2a-O2a	O2a-O2b	O2b-O2b	O2b-O2b
Si-CHA	--	--	--	--	--	--	--	--	--	--
0.5 CO ₂ /Si-CHA (ND)	3.30(3)	3.48(4)	3.44(5)	3.23(3)	1.50(5)	1.76(5)	1.78(5)	2.22(7)	2.64(8)	3.22(7)
1.0 CO ₂ /Si-CHA (ND)	3.29(2)	3.48(2)	3.44(2)	3.21(2)	1.53(1)	1.73(2)	1.78(2)	2.22(3)	2.62(4)	3.20(4)
0.5 CO ₂ /Si-CHA (XRD)	3.44(5)	3.74(5)	3.57(4)	3.25(4)	1.90(5)	1.93(5)	1.62(5)	2.31(6)	1.94(8)	2.54(7)
1.0 CO ₂ /Si-CHA (XRD)	3.35(1)	3.58(1)	3.41(2)	3.21(2)	1.74(2)	1.79(2)	1.76(2)	2.35(3)	2.30(3)	2.89(3)

Table 4.5. Select CO₂ bond distances (in Angstroms) and CO₂ angles (in degrees) for Site B' (M+...CO₂) for the Li⁺/Na⁺-exchanged Chabazite zeolites in this study. The value in parentheses represents one standard deviation (in refined value).

Sample	Bond Angle (°)		CO ₂ Site B' (M+) Bond Distances (Å)			
	M+...O2a=C=O2b	Site B-M+ M+...O2a	Site B-Framework			Sites A-B O1a-O2b
			O2b-O2	O2b-O3	O2b-O4	
Li-CHA12	--	--	--	--	--	--
0.33 CO ₂ /Li-CHA-12	146.(6)	2.45(8)	3.56(5)	3.15(5)	3.56(5)	2.66(5)
0.66 CO ₂ /Li-CHA-12		2.302(5)	3.63(7)	3.26(6)	3.63(7)	2.63(7)
Li-CHA-6	--	--	--	--	--	--
0.5 CO ₂ /Li-CHA-6	143.(10)	2.3(2)	3.95(9)	3.33(9)	3.60(8)	2.54(7)
1.0 CO ₂ /Li-CHA-6	151.(4)	2.26(6)	4.17(3)	3.76(3)	4.11(3)	2.62(3)
Na-CHA12	--	--	--	--	--	--
0.66 CO ₂ /Na-CHA-12	166.1(9)	2.59(8)	3.30(2)	3.11(3)	4.06(4)	2.71(6)
Na-CHA-6	--	--	--	--	--	--
0.5 CO ₂ /Na-CHA-6	163.0(9)	2.68(7)	3.30(2)	3.07(3)	4.03(4)	2.78(6)
1.0 CO ₂ /Na-CHA-6	162.9(4)	2.686(8)	3.30(1)	3.08(1)	4.04(1)	2.79(2)

Table 4.6. Select CO₂ bond distances (in Angstroms) and CO₂ angles (in degrees) for Site C (M+...CO₂...M+) for the K⁺-exchanged Chabazite zeolites in this study. The value in parentheses represents one standard deviation (in refined value).

Sample	Bond Angle	CO ₂ Site C (M+/M+) Bond Distances (Å)							
	(°)	Sites A/B-M+			Site B-Framework			Site A-B'	
	M+...O2a= C=O2b	K1...O 2a	K1...O 2b	K2...O 2a	O2b-O2	O2b- O3	O2b- O4	O1a- O2a	O1a- O2b
K-CHA-12	--	--	--	--	--	--	--	--	--
0.33 CO ₂ /K- CHA-12	154.(5)	3.02(5)	2.99(5)	2.92(6)	3.89(4)	3.77(7)	4.10(8)	1.87(6)	2.66(7)
0.66 CO ₂ /K- CHA-12	155.(2)	3.00(3)	3.04(3)	2.95(4)	3.91(4)	3.82(4)	4.14(3)	1.89(4)	2.69(4)
K-CHA-6	--	--	--	--	--	--	--	--	--
0.5 CO ₂ /K- CHA-6	156(2)	3.04(2)	2.87(2)	3.05(2)	3.99(3)	3.94(3)	4.15(2)	1.89(4)	2.63(4)
1.5 CO ₂ /K- CHA-6	155(1)	3.08(1)	3.00(1)	2.96(1)	3.97(2)	3.88(2)	4.09(2)	1.82(2)	2.63(2)

Table 4.7. Unit cell parameters for the Chabazite zeolites in this study. The value in parentheses represents one standard deviation (in refined value).

Sample	Cell Parameters		
	a (Å)	c (Å)	V (Å ³)
Si-CHA	13.5844(3)	14.7628(5)	2359.3(1)
0.5 CO ₂ /Si-CHA (ND)	13.5913(4)	14.7636(6)	2361.8(1)
1.0 CO ₂ /Si-CHA (ND)	13.5833(3)	14.7526(5)	2357.3(1)
0.5 CO ₂ /Si-CHA (XRD)	13.4748(2)	14.6568(3)	2304.7(1)
1.0 CO ₂ /Si-CHA (XRD)	13.4715(2)	14.6471(3)	2302.0(1)
Li-CHA-12	13.5774(4)	14.8816(7)	2375.8(2)
0.33 CO ₂ /Li-CHA-12	13.5971(4)	14.8395(6)	2376.0(1)
0.66 CO ₂ /Li-CHA-12	13.5992(5)	14.8348(8)	2376.0(2)
Li-CHA-6	13.5798(4)	15.0034(6)	2396.1(1)
0.5 CO ₂ /Li-CHA-6	13.5830(4)	14.9919(7)	2395.4(1)
1.0 CO ₂ /Li-CHA-6	13.5973(5)	14.9674(7)	2396.5(2)
Na-CHA-12	13.6417(4)	14.8121(7)	2387.2(1)
0.66 CO ₂ /Na-CHA-12	13.6092(4)	14.8567(7)	2383.0(1)
Na-CHA-6	13.6852(3)	14.9436(6)	2423.8(1)
0.5 CO ₂ /Na-CHA-6	13.6689(4)	14.9473(6)	2418.6(1)
1.0 CO ₂ /Na-CHA-6	13.6418(4)	14.9670(6)	2412.2(1)
K-CHA-12	13.6423(4)	14.6843(7)	2366.8(2)
0.33 CO ₂ /K-CHA-12	13.6205(4)	14.7667(7)	2372.5(2)
0.66 CO ₂ /K-CHA-12	13.5992(5)	14.8348(8)	2376.0(2)
K-CHA-6	13.7536(6)	14.4752(9)	2371.3(2)
0.5 CO ₂ /K-CHA-6	13.7138(3)	14.7280(4)	2398.8(1)
1.5 CO ₂ /K-CHA-6	13.7001(3)	14.8091(4)	2407.2(1)

4.3.2 CO₂ adsorption sites in chabazite zeolites

Using GCMC simulation, Bell *et al.* [36, 37] estimated that dispersive interactions are the primary contributors to the adsorption energy in this sample and are determined by the distances between the carbon atoms (C_{CO2}) and oxygen atoms (O_{CO2}) of CO₂ molecule to the surrounding oxygen atoms of the zeolite framework

(O_{CHA}). Their calculations suggest equilibrium distances for strong dispersive interaction are $d(\text{O}_{\text{CO}_2}\text{-O}_{\text{CHA}}) = 3.44 \text{ \AA}$ and $d(\text{C}_{\text{CO}_2}\text{-O}_{\text{CHA}}) = 3.30 \text{ \AA}$, and those contact distances at below 4 \AA are considered to have attractive effective *van der Waals* interactions. The refinement of XRPD and NPD patterns of CO₂ on pure silica chabazite (Figures 4.2a, 4.2b) resulted in the identification of two adsorption sites for CO₂: (1) locating in the 8MR and (2) in the ellipsoid cages of chabazite framework. In the chabazite 8MR, the preferred adsorption site (site A) is the center of the chabazite window in which each carbon atom in CO₂ molecule has maximal close contacts with the 8 oxygen atoms of the 8MR (O_{8MR}) such that two O_{8MR} across the ring from each other give an angle O_{8MR}-C_{CO2}-O_{8MR} = 180°.

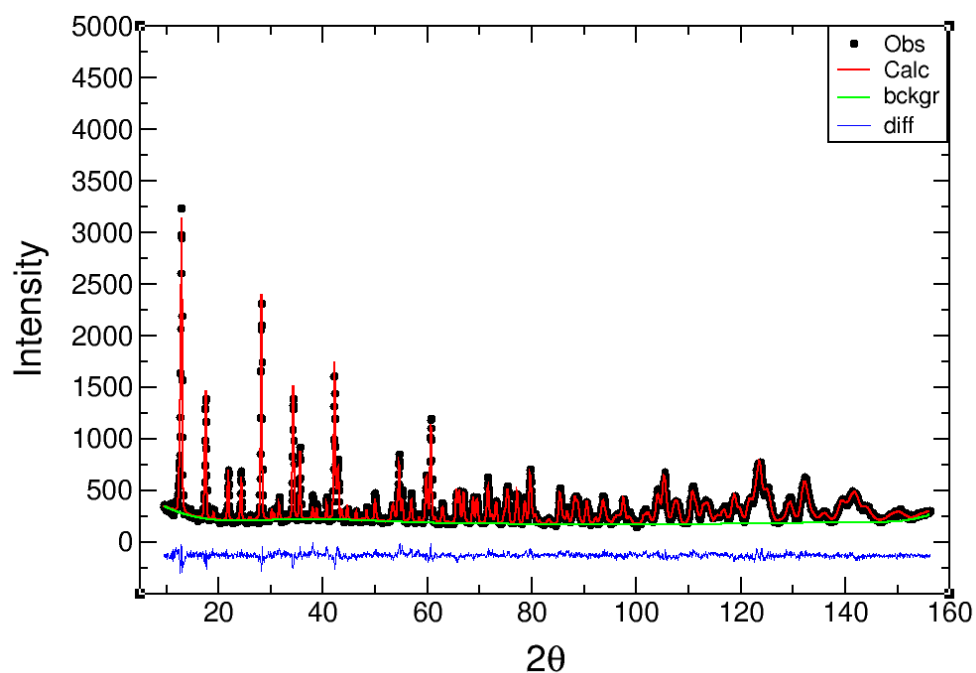


Figure 4.2a. Rietveld refinement of neutron powder diffraction data for 1.0 CO₂ per 8MR dosed in Si-CHA at 10 K. *Note:* Green line, black circles, and red line represent the background, experimental, and calculated diffraction patterns, respectively. The blue line represents the difference between experimental and calculated patterns.

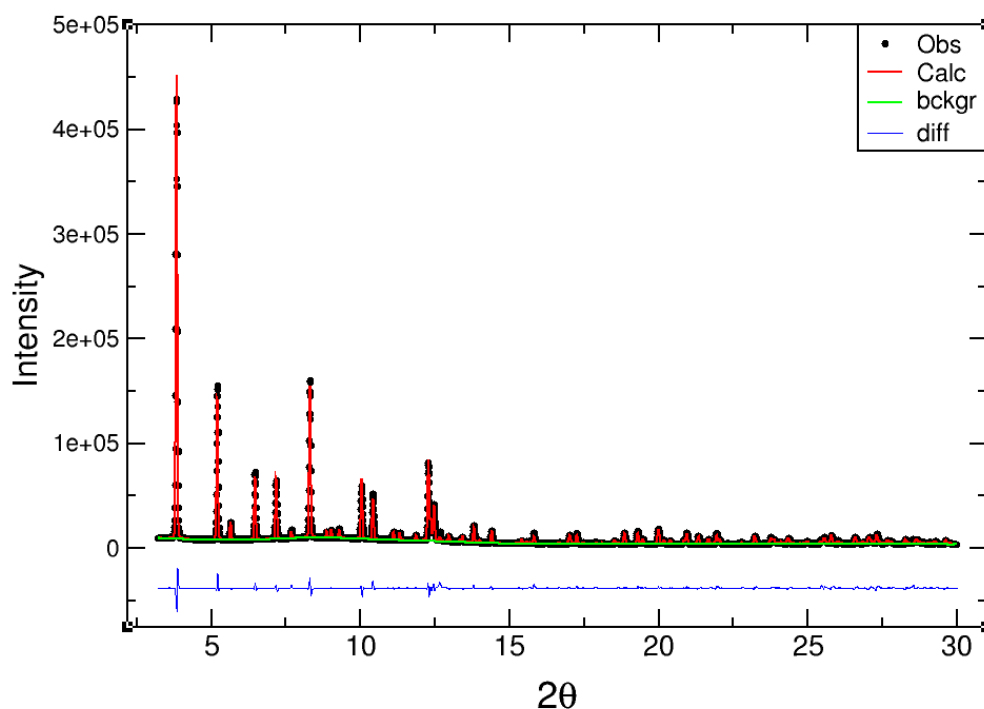


Figure 4.2b. Rietveld refinement of X-ray powder diffraction data for 0.5 CO₂ per 8MR dosed in Si-CHA at 100 K. *Note:* Green line, black circles, and red line represent the background, experimental, and calculated diffraction patterns, respectively. The blue line represents the difference between experimental and calculated patterns.

From X-ray diffraction refinement of 0.5 CO₂/8MR in Si-CHA, the CO₂-8MR oxygen atom distances were determined to be $d(\text{C}_{\text{CO}_2}\text{-O}_3) = 3.129(6) \text{ \AA}$, $d(\text{C}_{\text{CO}_2}\text{-O}_4) = 3.196(5) \text{ \AA}$, $d(\text{C}_{\text{CO}_2}\text{-O}_2) = 3.410(4) \text{ \AA}$, and with $d(\text{O}_{\text{CO}_2}\text{-O}_{\text{CHA}})$ between ca. 3.18 – 3.98 \AA (Tables 4.2 and 4.3). Another CO₂ adsorption site in pure silica chabazite is inside the ellipsoidal cage where the carbon atom has the most effective contact distances with 4 framework oxygen atoms and the CO₂ oxygen atoms also have effective contact distances with 4 to 5 framework oxygen atoms each (Figure 4.3). The isotropic atomic displacement parameters (ADPs) for CO₂ in the cage site are higher than those

in the window site, indicating the increase in static disorder of the weaker adsorption sites and possibly a more concave potential energy minimum. Overall, these considerations explain the high occupancy of CO₂ at site A in chabazite zeolites, or indeed in 8MR zeolites in general [36, 37].

A physical effect of the adsorption of CO₂ in all-silica chabazite is a slight change the unit cell parameters, with an initial expansion and evidence of a small contraction with increased loadings from 0.5 to 1.0 CO₂ on the order of a few thousandths of an Ångstrom (Table 4.7). There is also a small contraction of the unit cell with increasing measurement temperature between 10 K neutron and 100 K X-ray diffraction experiments. The negative thermal expansion due to the changes in Si-O-Si interpolyhedral bond angles is also observed in chabazite and typical other siliceous zeolites [57-59] and typically assigned to the larger amplitude of rigid-unit type modes [60, 61].

Two CO₂ adsorption sites were determined in Li-CHA and Na-CHA zeolites by Fourier difference map analysis (Figure 4.4). The distance between Na⁺ cation and O_{CO2} in site A is much shorter than that for the Li⁺ cation (3.605(0) Å and 4.307(0) Å in 0.5CO₂/Li-, Na-CHA-6, respectively) leading to a more effective electrostatic interaction. Further structural details and occupancies of site A in Na-CHA compared to Li-CHA are reported in Table 4.5. The CO₂ second site in these zeolites is end-on CO₂ coordination with the cation (M⁺...O=C=O) where M⁺...O=C=O bond distances are longer than the distances of the CO₂ oxygen to the D6R oxygen atoms, d(Na⁺-O_{CO2}) = 2.68 (7) Å, d(Li⁺-O_{CO2}) = 2.3 (2) Å and d(Na⁺-O_{CHA}) = 2.447 (7) Å, d(Li⁺-O_{CHA}) = 2.033 (5) Å (Table 4.5). In this configuration, the linear CO₂ molecule is tilted toward the 4MR window to achieve closer contact with other oxygen atoms of

the zeolite framework, which is similar to the CO₂ configuration in NaY as reported by Nachtigall *et al* [29]. This adsorption site is labeled as site B' since it can be viewed as a rotation and translation of the all-silica site while remaining in the cage.

Since the Li⁺...O=C=O distance is shorter than that in Na⁺-CHA, the contact angle of the CO₂ is more acute with $\angle \text{Li}^+ \cdots \text{O}=\text{C}=\text{O} \approx 144^\circ$, compared to the equivalent $\angle \text{Na}^+ \cdots \text{O}=\text{C}=\text{O} \approx 163^\circ$, having more effective dispersive interaction with the zeolite framework and additionally exhibiting close ($\approx 3 \text{ \AA}$) interactions with the 6MR oxygen atoms. The resulting high ADPs and coordinate standard deviations for site B' could be the result of slight rotation of the CO₂ around the cation and 4MRs. There is likely a slight position difference across the bulk powder and the model is fitting the average position. Because the energy contribution of the dispersion interaction, and the large quadrupole moment of CO₂ ($14.3 \times 10^{-40} \text{ C m}^2$) [62] with an inhomogeneous electric field of zeolite is highest in 8MR zeolites [7], site A (at the 8MR) is still a major adsorption site in alkali-exchanged chabazites (Table 4.3) even though open metal cations provide an additional strong binding site in the cage (site B') through enhanced electrostatic interaction of the adsorbate-adsorbent. The result is also observed in NaA and FER zeolites as reported in references [29, 41].

The structure of solid carbon dioxide refined by Peters *et al.* [63] in space group Pa3, shows that an O atom of the CO₂ molecule is in close contact with more than 10 oxygen atoms of other CO₂ molecules (contact distances of approximately 3.45 Å and 3.18 Å). In Li-CHA, it may be possible to have two molecules in neighbor sites A and B' in the same cage with O-O distances comparable to the ones observed in solid CO₂. Due to the symmetry, however, there could be 3 possible positions of CO₂-site B' around Li⁺ cation, and the stable configuration of CO₂ sites A and B'

coexist in the same cage is where site B in close contact with the 4MR opposite to site A ($d_{O-O} = 3.105 \text{ \AA}$). Moreover, in solid CO_2 , the C atom has close contact with 6 oxygen atoms of other CO_2 molecules ($d_{C-O} \approx 3.11 \text{ \AA}$), which is the distance we found in the 8MR due to the interaction between the partially positive charge of C_{CO_2} and the negative charge of O in the zeolite framework. This is also observed in Na-CHA. In the cases of low CO_2 doses in Li- and Na-CHA-12, there is an overall similarity of the positions and occupancies of the two CO_2 sites with $\angle \text{Li}^+ \cdots \text{O}=\text{C}=\text{O} \approx 142^\circ$, $\angle \text{Na}^+ \cdots \text{O}=\text{C}=\text{O} \approx 166^\circ$, and the distance between $\text{Li}^+-\text{O}_{\text{CO}_2}$ and $\text{Na}^+-\text{O}_{\text{CO}_2}$ (site B') are identical to Li-/Na-CHA-6 at $2.302(5) \text{ \AA}$ and $2.59(8) \text{ \AA}$, respectively, (Tables 4.3, 4.5).

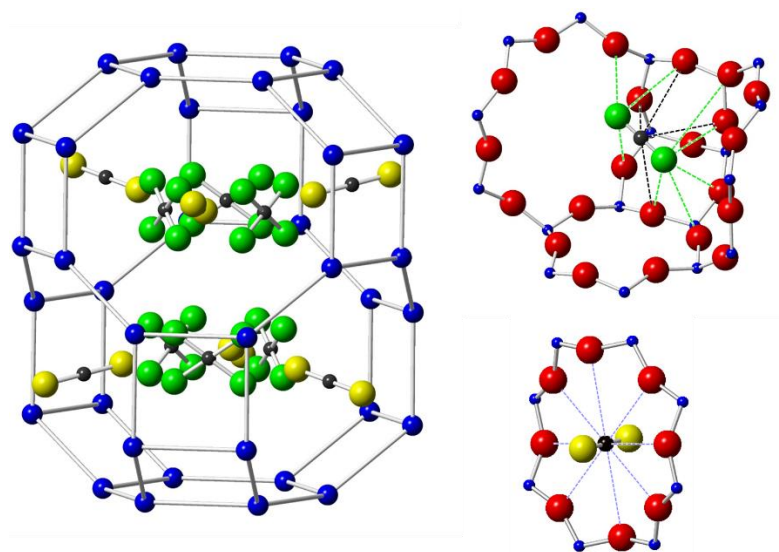


Figure 4.3. (Left) CO_2 adsorption sites in pure silica chabazite with framework oxygen atoms omitted for clarity (site A: 8MR, yellow oxygen atoms; site B: cage, green oxygen atoms). (Right) Detailed view of site A CO_2 in the center of the 8MR (bottom) and site B with short interaction distances to the red framework oxygens given by dashed lines (top).

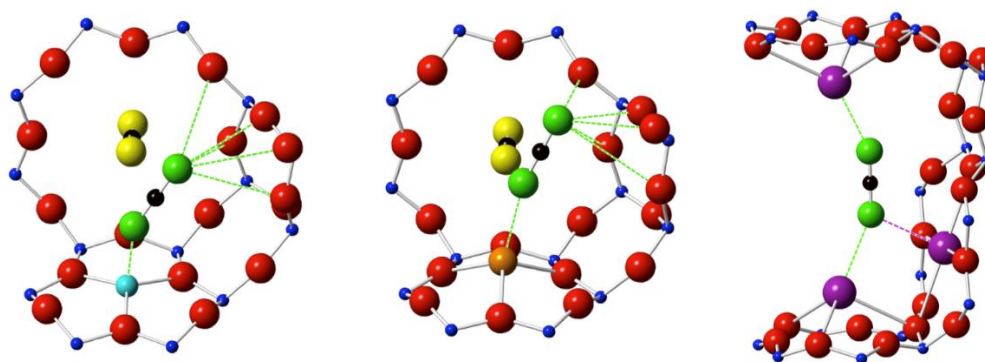


Figure 4.4. Partial pore views of CO₂ adsorption sites in Li-CHA-6 (left), Na-CHA-6 (center), and K-CHA-6 (right) zeolites. Site A is similar to that previously determined for Cu²⁺-exchanged chabazite^[7] (indicated by yellow oxygens) and the displacement of the cation (blue Li⁺; orange Na⁺) strongly influences the coordination of the second CO₂ adsorption site to a site B' with the CO₂ moving closer to the D6R with Li⁺. Note that site A, while present in K-CHA-6, has been omitted for clarity in depicting the dual-cation bridged via cation sites SII/SIII' or SII/SII.

Refinement of the K-CHA-12 data show that K⁺ behaves quite similarly to Cu²⁺ in which the majority of the CO₂ is found in the 8MR and only a small fraction of the adsorbate is found with an end-on CO₂ coordination with the cations (Tables 4.3, 4.6). Interestingly, in K-CHA-6 with the higher concentration of K⁺ in both SII and SIII' (partially blocking more of the 8MR window), the occupancy of the second CO₂ site (site C) in the cage is significantly increased. The increase in interaction energy is due to the CO₂ coordination to two K⁺ cations (either cations in sites SII/SIII' or SII/SII) being more efficient in lower silica K-CHA-6 with a distance from O_{CO2} to K⁺ of approximately 3 Å. Nachtigall *et al.* report this as the dual-cation site

[26-29]. In this configuration, the oxygen and carbon atoms also have a number of attractive interactions with framework oxygen atoms. From Fourier analysis, there is some disorder indicated from adsorption at site C in K-CHA since this site can be coordinated with potassium either by single- or dual-cation sites resulting in an average CO₂ position with high ADPs. Various models for the configuration of site C were considered and this location (with high ADPs), shown in Figure 4.4, resulted in the best refinement.

4.3.3 Adsorption properties of sodium-exchanged zeolites

Chemical analysis of the samples by ICP and EDX (see Table 3.1) show that Si/Al ratios for the chabazite samples are near the expected Si/Al = 12 for CHA-12, and Si/Al = 5.95 - 6.6 for CHA-6 samples. The ratio of cation (Li, Na and K) to Al is close to one in all cases. Si-CHA, Li-CHA and Na-CHA have a microporous volume determined by the t-plot method of approximately 0.27 cc g⁻¹, while for both potassium samples the microporous volume is much lower (0.18 - 0.20 cc g⁻¹). This is in part due to the larger size of potassium cations, but may reflect the presence of some inaccessible cages.

CO₂ adsorption isotherms, isosteric heats of adsorption, and the adsorption capacity of Na-chabazite zeolites are compared to selected commercial zeolites samples at 1 bar and 303 K in Table 4.8 (and Figure 4.5). At low loadings, NaA and Na13X have higher adsorption capacity than Na-CHA-6, as expected due to the high cation density of low silica zeolites. On the other hand, Si-CHA has a higher adsorption capacity than HY40 up to 1 bar. GCMC simulations [32, 36, 37] and DFT calculations [26-29] have shown the importance of dispersive interaction between CO₂ and the walls of microporous materials. This explains why the isosteric heats of CO₂

adsorption on chabazite zeolites are higher than those in faujasite zeolites; specifically Na-CHA-6 > NaY, and Si-CHA > HY40 even though faujasites have higher charge density than the chabazite samples. At high loading, the adsorption capacity depends on both the relative strength of adsorbate-adsorbent interactions and the micropore volume of the adsorbents [8, 64, 65].

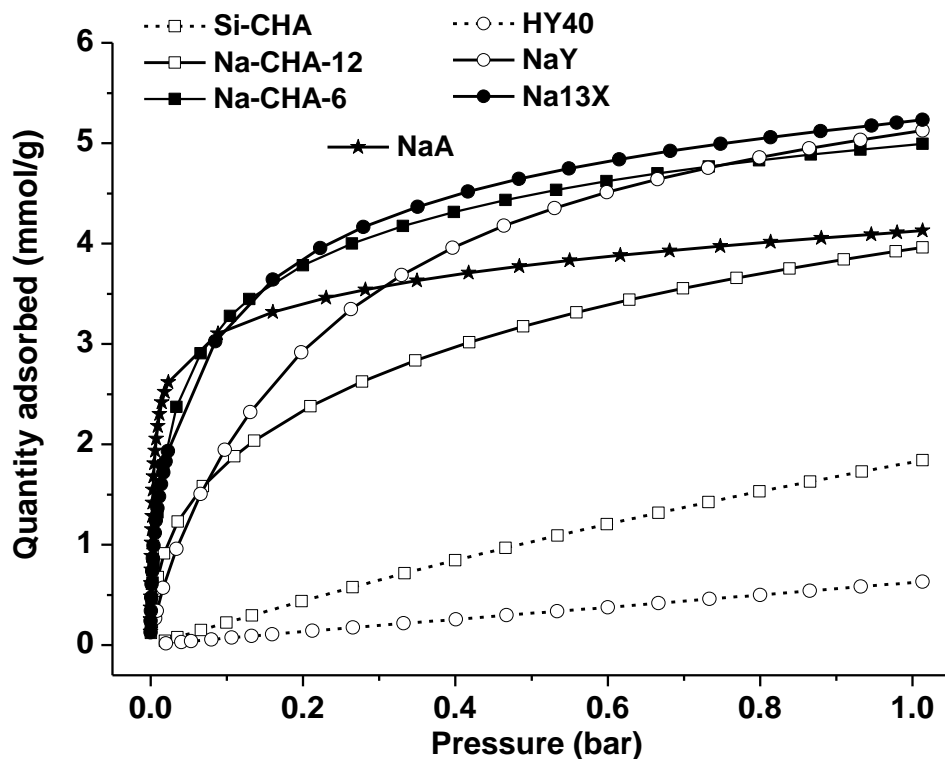


Figure 4.5. Total CO₂ adsorption isotherms at 303 K for chabazite zeolites (Si-CHA: open square/dashed-line, Na-CHA-12: open square/solid line, Na-CHA-6: closed square/solid line), Linde type A zeolites: close star/solid line, and faujasite zeolites (HY40: open circle/dashed-line, NaY: open circle/solid line, Na13X: closed circle/solid line). Note: Data is in agreement with our previous publication on this^[8].

The equilibrium CO₂ capacity of Na-CHA-6 is 5.0 mmol CO₂ per gram of zeolite at 303 K and 1 bar, which is comparable to the value of zeolites Na13X and NaY, but appreciably higher than that of NaA, even though the cation density in Na-CHA-6 is significantly lower. Note that the amount adsorbed and the isosteric heat of adsorption of Na-CHA-6 is higher than those of Na-CHA-12 and Si-CHA as expected for increasing concentration of Al³⁺ in the zeolite framework. Ferrierite containing 8- and 10-ring straight channels showed slightly higher heats of adsorption at zero coverage, but significantly lower adsorption capacity (Table 4.8) as compared to Na-CHA-12 with similar Si/Al ratio due to its smaller pore size and much smaller micropore volume.

4.3.4 Structure-property relationship: CO₂ adsorbed on chabazite zeolites

In cation-exchanged zeolites, the cations act as Lewis acid sites and the framework oxygen atoms, bearing partial negative charges, behave as basic sites. The basicity of framework oxygen atoms of alkali-exchanged zeolites is in the order of Li⁺ < Na⁺ < K⁺ < Cu²⁺ based on local Hard-Soft Acid-Base (HSAB) descriptors [68, 69]. Based on this principle, the interaction between the Lewis acid site (the carbon in CO₂) and basic zeolite oxygen atoms is the highest in Cu²⁺ and is the lowest in Li⁺. This observation accounts for the very high occupancy of CO₂ in the middle of 8MR in Cu-CHA-6 and the lowest occupancy in Li-CHA [7]. Extra-framework cations are hard Lewis acid sites following the order of Li⁺ > Na⁺ > K⁺ > Cu²⁺ while O atoms in CO₂ act as hard base sites. Given that hard-hard and soft-soft interactions dominate the hard-soft interactions as demonstrated in HSAB theory, the end-on CO₂ coordination with these cations (Mⁿ⁺...O=C=O) is more stable in Li⁺ than in other cation sites. This was also observed in the adsorption of the O-atom (in CH₃OH molecule) on alkali-

exchanged faujasite ($\text{Li}^+ > \text{Na}^+ > \text{K}^+ > \text{Rb}^+ > \text{Cs}^+$) [28]. This explains the highest CO_2 occupancy in the second site for Li^+ and the lowest occupancy in Cu-CHA-6 (Table 4.3, Ref.[7]).

Table 4.8. Adsorption parameters of select chabazite zeolites compared to select commercial zeolites at 1 bar and 303 K.								
Adsorbent	Na13 X	Na Y	NaA	Na- CHA-6	Na- CHA-12	[66] Na- FER	Si- CHA	HY40
Si/Al ratio	1.25	2.47	1	6	12	8.7	∞	40
M.V	0.29	0.31	0.21 *	0.25	0.27	0.12	0.27	0.3
Capacity	5.2	5.1	4.1	5.0	4.0	2.6	1.9	0.6
$-Q_{\text{st}}$	51.5	35	53.4	43.0	41.3	45.2	24	17.4
M.V: Micropore volume (cm^3/g), Cap: capacity (mmol/g), Q_{st} : adsorption heats (kJ/mol)								
* N_2 is not able to access the pores of NaA; micropore volume at a relative pressure of 0.029 P/P_0 calculating from CO_2 adsorption at 0 °C was taken from ref [67].								

Figure 4.6 shows the isosteric heats of adsorption as a function of CO_2 loading for all CHA samples. There is a noticeable decrease in $-Q_{\text{st}}$ with increased CO_2 quantity due to a decrease in the electric field. Based on very similar location of cations Li^+ and Na^+ in the chabazite framework, Li-CHA and Na-CHA have quite similar CO_2 adsorption capacities and heats of adsorption (Figure 4.6 and Ref.[8]). As per above, Li^+ is located closer to the 6MRs than Na^+ and leaves more empty space for the adsorbate. Therefore, at 1 atm, the adsorption capacity of CO_2 in Li-CHA-6 is slightly higher than in Na-CHA-6 (5.1 mmol/g and 5.0 mmol/g , respectively [8]). The adsorption site B' in Li-CHA has higher energy than in Na-CHA, but this site only adsorbs a maximum of 5.2 CO_2/uc , while site A allows for a maximum of 9 CO_2/uc .

This higher dependence of interaction energy on Li^+ , or the higher consumption of Li^+ cation by coordinating with adsorbates at high CO_2 coverage, could be the reason for a faster drop of the heats of adsorption on Li-CHA over CO_2 loading amounts as compared to Na-CHA adsorbents. This result is consistent with the study on Li-, Na-, K-ZSM-5 by Nachtigal *et al.* [29].

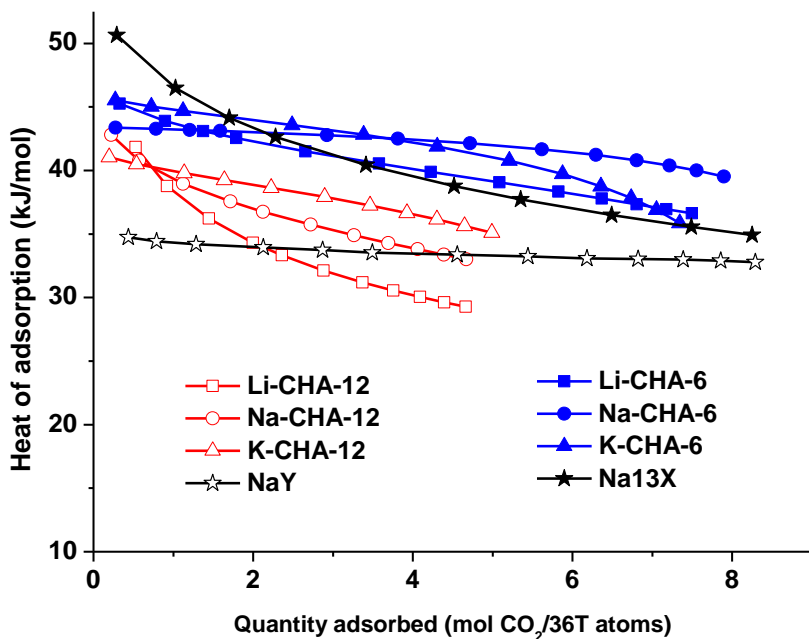


Figure 4.6. Isosteric heats of CO_2 adsorption ($-Q_{\text{st}}$) on chabazite zeolites and faujasite zeolites as a function of amount adsorbed. * 36T atoms are equal to 1 unit cell (uc) of chabazite and 3/16 uc of faujasite zeolites.

The electric field in K-CHA-12 is lower than that in Li-, Na-CHA-12 due to its larger cationic size. Thus, a lower adsorption heat at zero coverage was observed for K-CHA-12. As discussed earlier, most of CO_2 in K-CHA-12 is located in the 8MR (accommodating a maximum of 9 CO_2 /uc on this site) is less susceptible to the electric

field generated by potassium cations. This explains a slight drop in heat of adsorption on this sample. A dual-site cation is more effective in K-CHA-6 due to higher possibility of two K^+ ions in one cage or one in 6MR with a distance of approximately 7.5 Å to the other K^+ in 8MR. The formation of dual-site cation leads to comparable adsorption heat for this sample at zero coverage as compared to zeolites Li-, and Na-CHA-6. At higher loading of CO_2 ($> 6 CO_2/uc$) when the dual-cation and 8MR adsorption sites are mostly occupied, the heats of adsorption drops faster than in Li- and Na-CHA-6. The lower adsorption heat in Cu-CHA-6 (33.1 kJ/mol)[7] associating with the depopulation Cu^{2+} cation content (compared to alkali-cations) leads to a decrease of electric field in the zeolite. In addition, the lower electrostatic energy between CO_2 and Cu^{2+} is due to the fact that the major adsorption site of CO_2 /Cu-CHA-6 is in the 8MR, whereas the largest electric field is located around Cu^{2+} in the D6R.

Low dispersion interaction energy is observed in large cages, and according to Bell [34] and Nachtigall [29], the adsorption sites of CO_2 in low silica faujasites reflect a high level of interaction with Na^+ cations instead of interacting with the framework, as observed here for small pore chabazites. In NaY, most Na^+ cations coordinate to 6MRs inside the sodalite cages, where they are inaccessible to the adsorbate, thus the adsorption energy in NaY is lower than that in high silica chabazite zeolites. The presence of Na^+ site SIII in low silica faujasite Na13X has led to the formation of dual-cation adsorption sites [29]. Thus, Na13X has the highest adsorption heat at low CO_2 coverage among the studied zeolites and a steep drop in the heats of adsorption due to the high consumption of cation sites over CO_2 loading amount. Because of the high dependence of the CO_2 adsorption on the cations in faujasite zeolites, the

presence of water and other polar molecules in flue gas streams will dramatically decrease their CO₂ adsorption capacity, making this class of zeolites less efficient and impractical compared to high silica chabazites

4.4 Conclusions

Structural analysis of cation-exchanged high and pure silica chabazites was completed with *in-situ* CO₂ gas loading by X-ray and neutron diffraction and the relationship of zeolite structures to their adsorption energy interactions discussed. Site A (8MR) was identified as the major CO₂ adsorption site in pure silica chabazites due to the high number of close contacts to the framework oxygen atoms to the CO₂. Li⁺ and Na⁺ cations were only observed at site SII of the D6R, where larger K⁺ cation can occupy D6R and 8MR. These exchanged cations in chabazites are all open metal ions providing strong binding sites through induced polarizability of the adsorbate, whereas a majority of these cations residing in sodalite cages of zeolites A and faujasites are not accessible to adsorbates. Carbon dioxide is coordinated end-on to alkali-metal cations (M⁺...O=C=O) with the molecular axis tilted to the 4MR to maximize its dispersion interaction with the framework oxygens. High disorder of the second adsorption site in K-CHA, particularly K-CHA-6, is due to a mix population of single- and dual-cation adsorption sites in the chabazite cage. The population of the direct coordinated adsorption sites of CO₂ with these metal cations decreases with the hardness of cation Li⁺>Na⁺>K⁺>Cu²⁺, except for the case of K-CHA-6, where the bridged complexes of CO₂ and two K⁺ cation sites were formed with higher interaction energy than a single cation adsorption site. Additionally, a major CO₂ adsorption site in the 8MR (site A) was still observed in these cation-exchanged chabazites due to high *van der Waals* and quadrupole interactions. At low CO₂

coverage, the heats of adsorption in Li-, Na-, and K-CHA are quite similar due to the inverse effect of electric fields caused by cations and basicity caused by framework oxygens. A faster drop of heat of adsorption over the CO₂ loading amount in Li-CHA compared to Na-CHA is due to a higher dependence of the interaction energy on Li-exchanged adsorbents.

REFERENCES

1. Y. S. Bae, R. Q. Snurr, *Angew Chem Int Edit* 2011, *50*, 11586-11596.
2. N. Hedin, L. J. Chen, A. Laaksonen, *Nanoscale* 2010, *2*, 1819-1841.
3. A. B. Rao, E. S. Rubin, *Environmental Science & Technology* 2002, *36*, 4467-4475.
4. D. M. D'Alessandro, B. Smit, J. R. Long, *Angew Chem Int Edit* 2010, *49*, 6058-6082.
5. G. T. Rochelle, *Science* 2009, *325*, 1652-1654.
6. S. Choi, J. H. Drese, C. W. Jones, *Chemsuschem* 2009, *2*, 796-854.
7. M. R. Hudson, W. L. Queen, J. A. Mason, D. W. Fickel, R. F. Lobo, C. M. Brown, *J Am Chem Soc* 2012, *134*, 1970-1973.
8. T. D. Pham, Q. L. Liu, R. F. Lobo, *Langmuir* 2013, *29*, 832-839.
9. J. Kim, L. C. Lin, J. A. Swisher, M. Haranczyk, B. Smit, *J Am Chem Soc* 2012, *134*, 18940-18943.
10. O. Cheung, N. Hedin, *Rsc Advances* 2014, *4*, 14480-14494.
11. Z. R. Herm, K. Sumida, Z. R. Herm, T. McDonald, H. J. Choi, L. J. Murray, D. M. D'Alessandro, A. Demessence, M. L. Foo, J. R. Long, *Abstr Pap Am Chem S* 2011, *241*.
12. L. C. Lin, J. Kim, X. Q. Kong, E. Scott, T. M. McDonald, J. R. Long, J. A. Reimer, B. Smit, *Angew Chem Int Edit* 2013, *52*, 4410-4413.
13. Y. Y. Liu, Z. Y. U. Wang, H. C. Zhou, *Greenh Gases* 2012, *2*, 239-259.
14. P. Nugent, Y. Belmabkhout, S. D. Burd, A. J. Cairns, R. Luebke, K. Forrest, T. Pham, S. Q. Ma, B. Space, L. Wojtas, M. Eddaoudi, M. J. Zaworotko, *Nature* 2013, *495*, 80-84.
15. J. A. Dunne, R. Mariwals, M. Rao, S. Sircar, R. J. Gorte, A. L. Myers, *Langmuir* 1996, *12*, 5888-5895.
16. J. A. Dunne, M. Rao, S. Sircar, R. J. Gorte, A. L. Myers, *Langmuir* 1996, *12*, 5896-5904.
17. Q. L. Liu, T. Pham, M. D. Porosoff, R. F. Lobo, *Chemsuschem* 2012, *5*, 2237-2242;
18. G. D. Pirngruber, P. Raybaud, Y. Belmabkhout, J. Cejka, A. Zukal, *Phys Chem Chem Phys* 2010, *12*, 13534-13546.
19. R. Bulanek, K. Frolich, E. Frydova, P. Cicmanec, *Top Catal* 2010, *53*, 1349-1360.
20. J. Zhang, R. Singh, P. A. Webley, *Micropor Mesopor Mat* 2008, *111*, 478-487.
21. P. J. E. Harlick, F. H. Tezel, *Micropor Mesopor Mat* 2004, *76*, 71-79.

22. T. D. Pham, R. Xiong, S. I. Sandler, R. F. Lobo, *Microporous Mesoporous Mater.* 2014, *185*, 157-166.
23. R. W. Stevens, R. V. Siriwardane, J. Logan, *Energ Fuel* 2008, *22*, 3070-3079.
24. P. A. Jacobs, Vancauwe.Fh, E. F. Vansatn, *Journal of the Chemical Society-Faraday Transactions I* 1973, *69*, 2130-2139.
25. T. Montanari, G. Busca, *Vibrational Spectroscopy* 2008, *46*, 45-51.
26. C. O. Arean, M. R. Delgado, G. F. Bibiloni, O. Bludsky, P. Nachtigall, *Chemphyschem* 2011, *12*, 1435-1443.
27. P. Nachtigall, M. R. Delgado, D. Nachtigallova, C. O. Arean, *Phys Chem Chem Phys* 2012, *14*, 1552-1569.
28. A. Pulido, P. Nachtigall, A. Zukal, I. Dominguez, J. Cejka, *J Phys Chem C* 2009, *113*, 2928-2935.
29. L. Grajciar, J. Cejka, A. Zukal, C. O. Arean, G. T. Palomino, P. Nachtigall, *Chemsuschem* 2012, *5*, 2011-2022
30. L. C. Lin, A. H. Berger, R. L. Martin, J. Kim, J. A. Swisher, K. Jariwala, C. H. Rycroft, A. S. Bhowan, M. Deem, M. Haranczyk, B. Smit, *Nat Mater* 2012, *11*, 633-641.
31. A. Garcia-Sanchez, C. O. Ania, J. B. Parra, D. Dubbeldam, T. J. H. Vlught, R. Krishna, S. Calero, *J Phys Chem C* 2009, *113*, 8814-8820.
32. R. Krishna, J. M. van Baten, *Sep Purif Technol* 2008, *61*, 414-423.
33. R. Krishna, J. M. van Baten, *Micropor Mesopor Mat* 2011, *137*, 83-91.
34. G. Maurin, P. L. Llewellyn, R. G. Bell, *J Phys Chem B* 2005, *109*, 16084-16091.
35. M. Fischer, R. G. Bell, *J Phys Chem C* 2013, *117*, 24446-24454.
36. M. Fischer, R. G. Bell, *J Phys Chem C* 2013, *117*, 17099-17110.
37. M. Fischer, R. G. Bell, *J Phys Chem C* 2012, *116*, 26449-26463.
38. H. J. Fang, P. Kamakoti, J. Zang, S. Cundy, C. Paur, P. I. Ravikovitch, D. S. Sholl, *J Phys Chem C* 2012, *116*, 10692-10701.
39. M. M. Lozinska, E. Mangano, J. P. S. Mowat, A. M. Shepherd, R. F. Howe, S. P. Thompson, J. E. Parker, S. Brandani, P. A. Wright, *J Am Chem Soc* 2012, *134*, 17628-17642.
40. W. L. Queen, C. M. Brown, D. K. Britt, P. Zajdel, M. R. Hudson, O. M. Yaghi, *J Phys Chem C* 2011, *115*, 24915-24919.
41. T. H. Bae, M. R. Hudson, J. A. Mason, W. L. Queen, J. J. Dutton, K. Sumida, K. J. Micklash, S. S. Kaye, C. M. Brown, J. R. Long, *Energ Environ Sci* 2013, *6*, 128-138.
42. H. Wu, J. M. Simmons, G. Srinivas, W. Zhou, T. Yildirim, *J Phys Chem Lett* 2010, *1*, 1946-1951.
43. J. V. Smith, L. S. D. Glasser, F. Rinaldi, *Acta Crystallogr* 1963, *16*, 45-48.
44. J. V. Smith, *Acta Crystallogr* 1962, *15*, 835-840.
45. F. Gao, J. H. Kwak, J. Szanyi, C. H. F. Peden, *Top Catal* 2013, *56*, 1441-1459.
46. D. W. Fickel, J. M. Fedeyko, R. F. Lobo, *J Phys Chem C* 2010, *114*, 1633-1640.

47. D. H. Olson, M. A. Camblor, L. A. Villaescusa, G. H. Kuehl, *Micropor Mesopor Mat* 2004, *67*, 27-33.
48. M. Miyamoto, Y. Fujiokax, K. Yogo, *J Mater Chem* 2012, *22*, 20186-20189.
49. J. Shang, G. Li, R. Singh, Q. F. Gu, K. M. Nairn, T. J. Bastow, N. Medhekar, C. M. Doherty, A. J. Hill, J. Z. Liu, P. A. Webley, *J Am Chem Soc* 2012, *134*, 19246-19253.
50. J. Shang, G. Li, R. Singh, P. Xiao, J. Z. Liu, P. A. Webley, *J Phys Chem C* 2010, *114*, 22025-22031.
51. L. J. Smith, H. Eckert, A. K. Cheetham, *Chem Mater* 2001, *13*, 385-391.
52. L. J. Smith, H. Eckert, A. K. Cheetham, *J Am Chem Soc* 2000, *122*, 1700-1708.
53. B. Civalieri, A. M. Ferrari, M. Llunell, R. Orlando, M. Merawa, P. Ugliengo, *Chem Mater* 2003, *15*, 3996-4004.
54. T. Frising, P. Leflaive, *Micropor Mesopor Mat* 2008, *114*, 27-63.
55. G. Vitale, C. F. Mellot, L. M. Bull, A. K. Cheetham, *J Phys Chem B* 1997, *101*, 4559-4564.
55. M. Feuerstein, R. F. Lobo, *Chem Mater* 1998, *10*, 2197-2204.
56. M. P. Attfield, A. W. Sleight, *Chem Commun* 1998, 601-602.
57. D. A. Woodcock, P. Lightfoot, P. A. Wright, L. A. Villaescusa, M. J. Diaz-Cabanas, M. A. Camblor, *J Mater Chem* 1999, *9*, 349-351.
58. D. A. Woodcock, P. Lightfoot, L. A. Villaescusa, M. J. Diaz-Cabanas, M. A. Camblor, D. Engberg, *Chem Mater* 1999, *11*, 2508-2514.
59. A. K. A. Pryde, K. D. Hammonds, M. T. Dove, V. Heine, J. D. Gale, M. C. Warren, *J Phys-Condens Mat* 1996, *8*, 10973-10982.
60. K. D. Hammonds, V. Heine, M. T. Dove, *J Phys Chem B* 1998, *102*, 1759-1767.
61. C. Graham, D. A. Imrie, R. E. Raab, *Mol Phys* 1998, *93*, 49-56.
62. A. Simon, K. Peters, *Acta Crystallogr B* 1980, *36*, 2750-2751.
63. D. Bonenfant, M. Kharoune, P. Niquette, M. Mimeault, R. Hausler, *Sci Technol Adv Mat* 2008, *9*.
64. M. Palomino, A. Corma, F. Rey, S. Valencia, *Langmuir* 2010, *26*, 1910-1917.
65. A. Zukal, A. Pulido, B. Gil, P. Nachtigall, O. Bludsky, M. Rubes, J. Cejka, *Phys Chem Chem Phys* 2010, *12*, 6413-6422.
66. F. Akhtar, Q. L. Liu, N. Hedin, L. Bergstrom, *Energ Environ Sci* 2012, *5*, 9947-9947.
67. R. C. Deka, R. K. Roy, K. Hirao, *Chem Phys Lett* 2000, *332*, 576-582.
68. T. L. Ho, *Chem Rev* 1975, *75*, 1-20.
69. P. Mignon, P. Geerlings, R. Schoonheydt, *J Phys Chem B* 2006, *110*, 24947-24954.
70. M. J. Diaz-Cabanas, P. A. Barrett, M. A. Camblor, *Chem Commun* 1998, 1881-1882.
71. J. Shang, G. Li, Q. Gu, R. Singh, P. Xiao, J. Z. Liu, P. A. Webley, *Chem Commun* 2014, *50*, 4544-4546.

- 72. B. H. Toby, *J Appl Crystallogr* 2001, 34, 210-213.
- 73. A. C. L. a. R. B. V. Dreele, *Los Alamos National Laboratory Report, LAUR* 1994, 86.

Chapter 5

STRUCTURE-PROPERTY RELATIONSHIPS OF CATION-EXCHANGED ZK-5 ZEOLITES FOR CARBON DIOXIDE ADSORPTION

5.1 Introduction

Carbon dioxide capture and storage (CCS) technology to reduce anthropogenic CO₂ emission has become one of the most urgent environmental issues in the 21st century [1-4]. Adsorption is one of the most promising techniques for commercial and industrial CCS applications among other techniques such as cryogenic distillation [5], membrane-based separation [6, 7], electrochemical sequestration in ionic liquid [8], chemical absorption with amine and ionic liquid solvents[9, 10]. This is due, in part, to its lower energy requirements, easy processing of materials, and broad applicability over a relatively wide range of temperatures and pressures [11, 12]. Porous adsorbents such as metal organic framework (MOFs), activated carbon, and zeolites have been studied extensively for CCS because of their versatile structures, high porosity, and promising, tunable adsorptive properties [13-22]. Recent efforts have focused on correlating sample structural characteristics and CO₂ adsorption properties to improve the performance of existent adsorbents and potentially design new adsorbent materials [17, 23, 24]. The separation of CO₂ from other gases can be based on both size and electronic properties of the gas molecules and the framework. Although the relatively small difference in kinetic diameters between CO₂ (3.30 Å), N₂ (3.64 Å), and CH₄ (3.80 Å) makes kinetic separation very challenging, microporous adsorbents with tailored narrow pore openings have high selectivity for CO₂ over of the larger kinetic

diameter molecules. For example, Liu *et al.* reported high selectivity of CO₂ over N₂ on NaKA with $K^+/(K^++Na^+) = 17\%$ due to the exclusion of N₂ which appears to be related to its slightly larger kinetic diameter [25]. Palomino *et al.* proposed that the extremely high selectivity of CO₂/CH₄ on zeolite RHO is mainly due to the pore aperture, which strongly blocks the adsorption of CH₄ [26]. Lozinska *et al.* [27] studied the structure of Na-, K-, and Cs-forms of zeolite RHO and suggest that the cations in the intercage window sites effectively block CH₄ adsorption but relocate during the adsorption of CO₂ in a ‘trapdoor’ mechanism originally proposed by Webley *et al.* [28].

Beyond size selectivity, CO₂ has a larger polarizability and quadrupole moment than N₂ ($1.43 \times 10^{-39} \text{ C.m}^2$, $29.11 \times 10^{-25} \text{ cm}^{-3}$ for CO₂ and $4.67 \times 10^{-40} \text{ C.m}^2$, $17.403 \times 10^{-25} \text{ cm}^{-3}$ for N₂, respectively [4]), which leads to stronger interactions of CO₂ with the electric field and electric field gradients within the adsorbents. The lack of electric quadrupole moment for CH₄ is a key factor in designing adsorbents. CO₂ is also a Lewis acid and has been used as a probe for elucidating the basic character of zeolites by infrared spectroscopy (IR) and temperature programmed desorption (TPD) [29-32]. Hence, the Lewis basicity of the adsorbents can also play an important role in determining adsorption properties under certain pressure regimes. Walton *et al.* [33] and Pirngruber *et al.* [34] have reported that the adsorption capacity at low pressure in faujasite zeolites are in the order $Cs^+ > K^+ > Na^+ > Li^+$ due to the high basicity of the framework oxygens, which is dominant relative to the strength of the quadrupole interaction. MOFs functionalized with basic nitrogen-containing organic groups have been studied to improve the selectivity of CO₂ over N₂/CH₄ due to the strong acid-base interaction between the lone-pair of nitrogen and CO₂ [35-38].

The presence of open metal sites in microporous materials is very important for high selectivity of CO₂ over other gases [15, 39, 40], but these materials are usually moisture-sensitive and chemically unstable [41]. MOFs without open metal sites that could be suitable in the humid environment of a flue gas, generally show higher CO₂ capacity at high pressures compared to zeolites due to their high surface areas and porosities, but also relatively low capacity at low partial pressures that make them very promising materials for pressure-swing processes [1]. However, the materials are not well suited to current post-combustion capture technologies due to either the low partial pressure of CO₂ in a low pressure flue gas mixture or lower CO₂ selectivity at high pressure [41]. On the other hand, while chemically robust and inexpensive, activated carbon has a lower uptake and selectivity at low pressures relative to zeolites [42, 43]. The complex factors of cation type, acidity/basicity, and electrostatic interactions within zeolites distinguish them from other types of adsorbates. Zeolites are generally characterized by a relatively high CO₂ capacity and selectivity over other gases at low pressure, which makes them promising candidates for CO₂ separation from flue gases [1, 43]. The high affinity for CO₂ in low silica zeolites hinders desorption and hence regeneration. The optimum Si/Al ratio for CO₂ adsorption/desorption cycles in LTA has been found to be higher than 5 [44], and there have been some reports showing the potential of small pore, high silica zeolites for CO₂ separations [45-47]. ZK-5 has been shown to be a good candidate for CO₂ separation [48-50] and has also been studied for adsorption and catalytic applications such as the selective synthesis of dimethylamine [51], selective catalytic reduction [52], and adsorption of hydrocarbons [53], water, methanol, and acetonitrile [54].

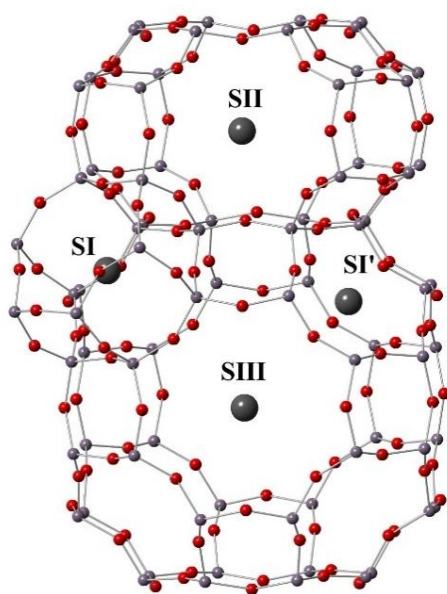


Figure 5.1. Illustration of the KFI structure and the cation locations in the zeolite pores observed in this study.

Zeolite ZK-5 (KFI framework type, *Zeolite Kerr* with sequence number *five*) was first synthesized by Kerr in 1966 [55]. The framework structure (Figure 5.1) can be built from an alternating sequence of *grc* and *pau* units (so-called α - and γ -cages, respectively). Each α -cage is connected through flat 8-membered ring faces to six γ -cages and each γ -cage is connected to two α -cages and four other γ -cages. While the flat eight-membered rings have a diameter of 3.9 Å, there is a puckered eight-membered ring of ~3.0 Å connecting the γ -cages with each other. The largest α -cage in KFI has a maximum potential diameter of an included sphere of 10.6 Å [56], and a free volume of approximately 707 Å³, smaller than the α -cage of LTA and RHO which also contain α -cage (811 Å³ and 722 Å³, respectively) [57]. The γ -cage has dimensions of 5.4 Å by 9.6 Å with a free volume of 264 Å³ [57]. The nature and the

distribution of the extra-framework cations play a crucial role in the adsorption properties of CO₂ in zeolite adsorbents [33, 34]. Their presence not only induces modifications of the basicity and electrical field inside the pores, but it can also change the available pore volume and morphological structure of the zeolites, influencing the adsorption kinetics. In this study, we investigated the CO₂ adsorption sites in Li-, Na-, K-, and Mg-ZK-5 zeolites by Synchrotron X-ray powder diffraction (SXRD) and correlate the results with volumetric adsorption measurements. The excellent correlation between the structure-property relationships of ZK-5 zeolite materials for CO₂ adsorption can be the basis in designing and optimizing novel adsorbents for CO₂ capture.

5.2 Experimental

5.2.1 Preparation and characterization of zeolites

ZK-5 was prepared as described in a previous study[48] and a method reported by Schulz *et al.*[58] with all starting chemicals obtained from Sigma-Aldrich and used without further purification.[†] Solution A was obtained by dissolving 1.64 g of KOH (85%) in 10 g deionized (DI) water, to which 0.29 g Al powder (99.9%) was slowly added with mild stirring until a clear solution was obtained. Solution B was prepared by dissolving 1.43 g 18-crown-6 (99.0%) and 0.114 g Sr(NO₃)₂ (99.0 %) into 6.3 g DI water, and then 8.1 g of Ludox AS40 was slowly added. Solution B was poured into solution A to give a final gel with molar compositions of:



[†] Any mention of commercial products is for information only; it does not imply recommendation or endorsement by NIST.

The gel was sealed in an autoclave and placed in convection oven at 423 K for 7 days under static conditions. The solid ZK-5 obtained after filtration was dried overnight at 373 K and then calcined at 833 K for 8 hours at a heating rate of 2 K/min. The calcined sample ZK-5 (primarily K-ZK-5, but with a small amount of Strontium) was first exchanged to the ammonium form by mixing 2 g ZK-5 with 1 liter of 1M NH_4NO_3 overnight at 353 K. The ion-exchange was repeated twice. Li-ZK-5, Na-ZK-5, and Mg-ZK-5 were obtained by exchanging $\text{NH}_4\text{-ZK-5}$ (0.5 g) and 500 ml of 2M solutions of LiCl, NaCl, MgCl_2 , respectively overnight at 353 K. The exchange was repeated 2-3 times. Pure K-ZK-5 was obtained by directly exchanging 0.5 g of the original ZK-5 with 500 ml 2M KCl, twice.

The morphological features and chemical compositions of the cation-exchanged ZK-5 zeolites were investigated by scanning electron microscopy and Energy-dispersive X-ray spectroscopy (EDX) using a JEOL JSM7400F scanning electron microscope, operating at an acceleration voltage of 3 keV and a current of 10 μA . EDX measurements were taken over at least 3 spots and the results averaged. Inductively coupled plasma mass spectrometry (ICP) measurements were also performed on the Li- and Mg-exchanged ZK-5's to obtain Si/Al and metal/Al ratios. The micropore surface area and the pore volume of ZK-5 were measured using N_2 at 77 K using a Micromeritics 3Flex device.

5.2.2 Volumetric adsorption of CO_2 and N_2 on ZK-5 zeolites

The CO_2 and N_2 adsorption isotherms on the ZK-5 samples at different temperatures (273 K, 303 K and 343 K) up to the ambient pressure were measured on a Micromeritics 3Flex instrument. Before the adsorption measurements each sample was degased at a temperature of 623 K for 6 h. Data were analysed according to both a

dual-site Langmuir (DSL) and a Dual-site Langmuir-Freundlich (DSL_F) models with isosteric heats of adsorption (Q_{st}) determined using the Clausius–Clapeyron equation.

5.2.3 Diffraction data collection and structure determinations

Capillaries of each de-gassed ZK-5 were individually mounted on a homemade gas delivery system attached to the goniometer of the 17-BM powder diffraction hutch at the Advanced Photon Source (Argonne National Laboratory). Care was taken to load only enough sample to fit under the cryo-stream and so estimated dosing amounts could be made with the 10 mbar gauge on the gas manifold. Data were measured at both 110 K and 295 K for each sample, with integration of the 2-dimensional powder pattern being performed with Fit-2D. Rietveld analysis of the 1-dimensional powder patterns was performed using GSAS/EXPGUI packages [59, 60] and visualization of electron Fourier difference densities through VESTA [61]. *Note: The X-ray diffraction data presented in this chapter does not have very high quality due to the effects of the instrument and small impurities within the samples.*

5.3 Results and Discussion

5.3.1 Characterization SEM, EDX, isotherms

ZK-5 (Figure 5.2) consists of cubic crystals with a uniform particle size of 3-5 μm . The results from chemical analysis by ICP and EDX (Table 5.1) showed that all samples have consistent Si/Al values in a range of 3.5-3.8, and are fully cation exchanged for Na-ZK-5 and K-ZK-5, and over 75% exchanged in the case of Mg^{2+} and 87% for Li^+ . Protons are most likely the remaining cations in Mg-ZK-5 and Li-ZK-5 since no K^+ was found. Protons could form during the ion exchange or after heating samples containing residual NH_4^+ . Surface areas calculated by the Brunauer–

Emmett–Teller (BET) method and micropore volumes extracted using the t-plot method are shown in Table 5.2. The highest micropore volume was found for Li⁺ and is probably due to the smaller volume occupied by Li⁺, but it could be also influenced by the stronger interaction between Li⁺ and N₂. The low surface area and pore volume of Na-, K-ZK-5 is due to the larger volume occupied by Na⁺, K⁺, the increase in the mass of the unit cell of heavy atoms, in the case of K⁺ maybe due to potassium blocking the adsorption of N₂ in some cages.

Table 5.1. Compositions of metals in cation-exchanged ZK-5 determined by inductively coupled plasma mass spectrometry (ICP) and energy-dispersive X-ray spectroscopy (EDX) methods.

Materials	Molar ratios		Method
	Si/Al	M(cation)/Al	
NH ₄ -ZK-5	3.6	-	EDX, no detection of K ⁺
Li-ZK-5	3.8	0.86	ICP
Na-ZK-5	3.7	0.95	EDX
K-ZK-5	3.5	1.0	EDX
Mg-ZK-5	3.65	0.38	ICP

Table 5.2. Microporous surface area (m²/g), external surface area (m²/g) and micropore volume (cm³/g) of ZK-5 zeolites determined by liquid N₂ adsorption measurements at 77 K.

Samples	Li-ZK-5	Na- ZK-5	K-ZK-5	Mg-ZK-5
Mic. Surf. Area	498	320	309	447
Ext. Surf. Area	10	50	18	45
Pore Vol.	0.23	0.17	0.14	0.21

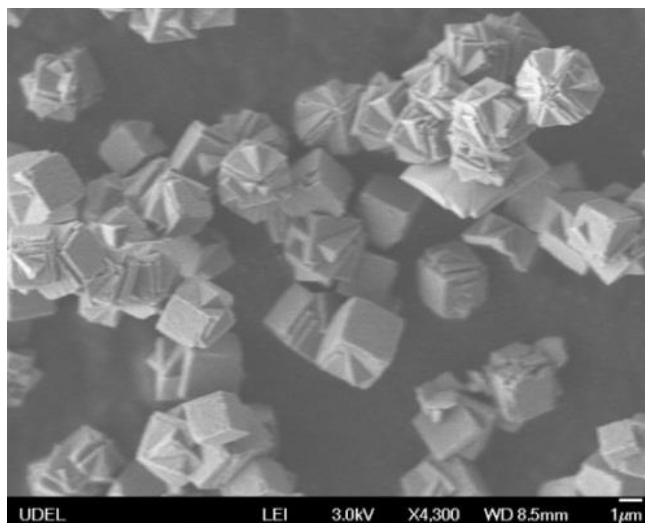
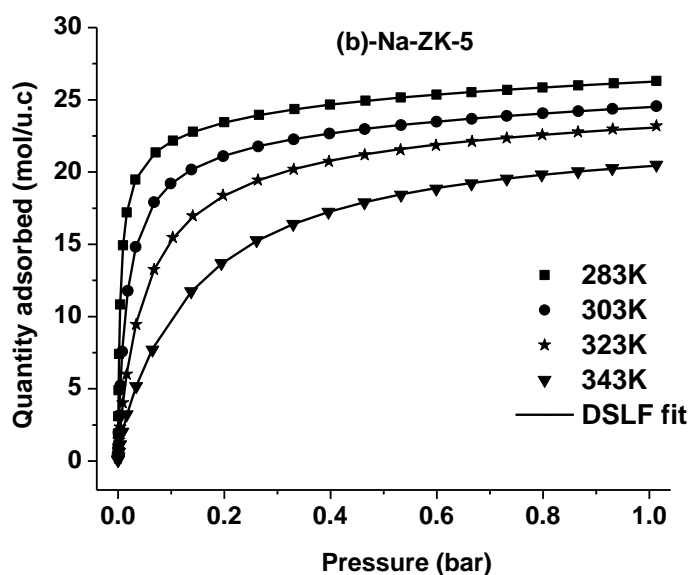
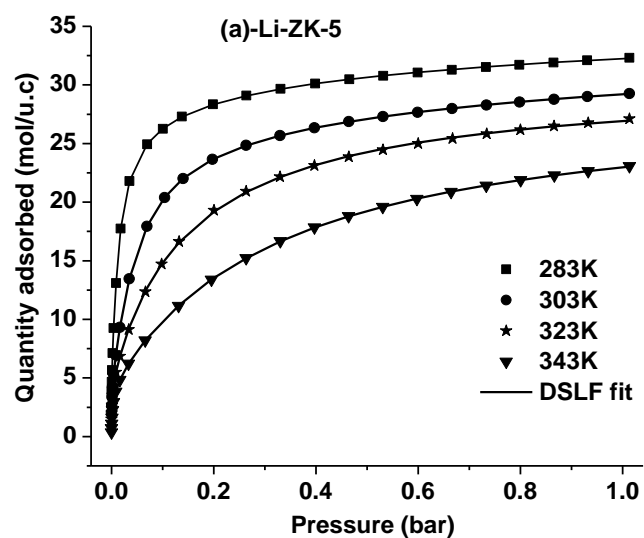


Figure 5.2. SEM images of cation-exchanged ZK-5

The adsorption isotherms up to 1.01 bar at various temperatures (283 K, 303 K, 323 K, and 343 K) on cation-exchanged ZK-5 with DSLF fits are expressed in terms of molecules per unit cell (u.c) to allow comparison between the samples (Figure 5.3). The adsorption capacities of cation-exchanged ZK-5 at a given pressure all decreases with temperature as expected from physical adsorption. The adsorption isotherms, in the conventional mol kg^{-1} units are plotted in Figures 5.4a-d, with the DSL and DSLF fits and fitting parameters included in Tables 5.3-5.4. Comparison of DSL and DSLF fits on a mass basis unit shows that both models give good fits to the experimental isotherms, except in the case of Li-ZK-5 where only the DSLF model fits the isotherm well. On an equal footing, the trend of adsorption capacity per u.c at a particular temperature is $\text{Li} \sim \text{Na-ZK-5} > \text{K-ZK-5} > \text{Mg-ZK-5}$ at low pressure (the reasons behind this trend will become evident as we determine the adsorbed structures). The adsorption capacity trend towards higher pressures for Li-, Na- and K-

ZK-5 is explained by increasing volume occupied by the cations, which reduces the volume available for adsorption of CO₂ when close to saturation. In the case of Mg²⁺ there is evidently a weaker interaction with CO₂, and this shifts the saturation pressure to higher values.



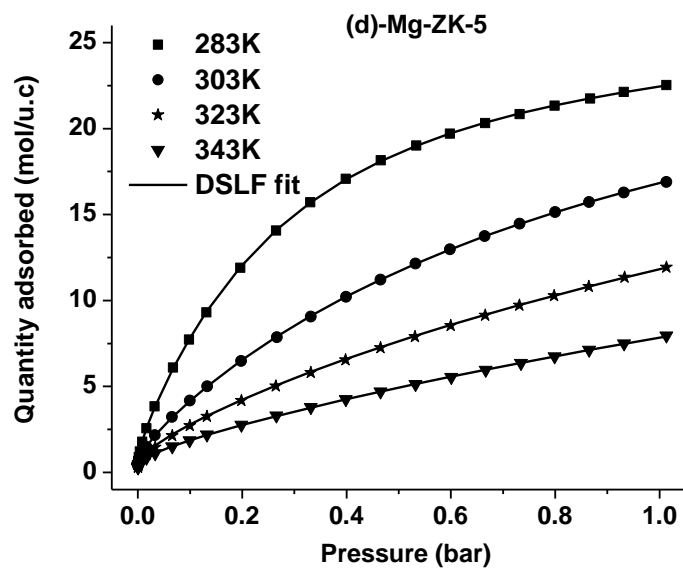
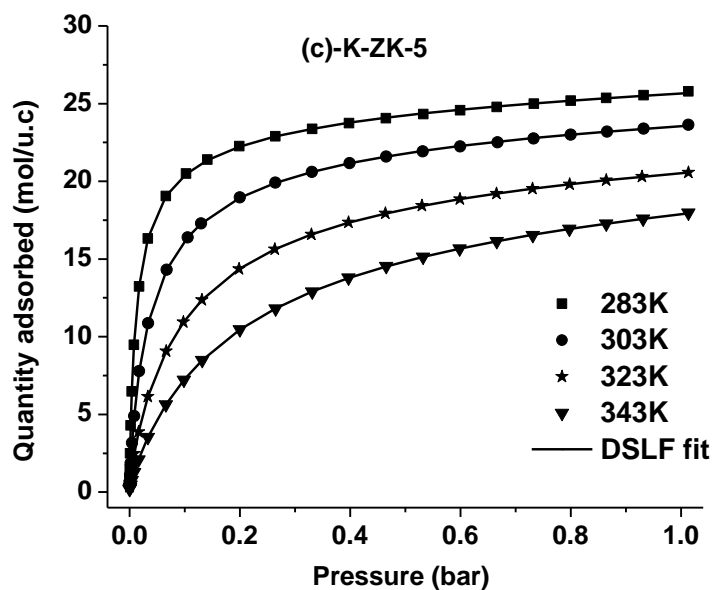


Figure 5.3. Volumetric CO₂ adsorption isotherms (closed symbols) at 283 K (squares), 303 K (circles), 323 K (stars), and 343 K (triangles) in Li-ZK-5 (a), Na-ZK-5 (b), K-ZK-5 (c), and Mg-ZK-5 (d). The solid lines are fits to the dual-site Langmuir-Freundlich (DSLFF) model.

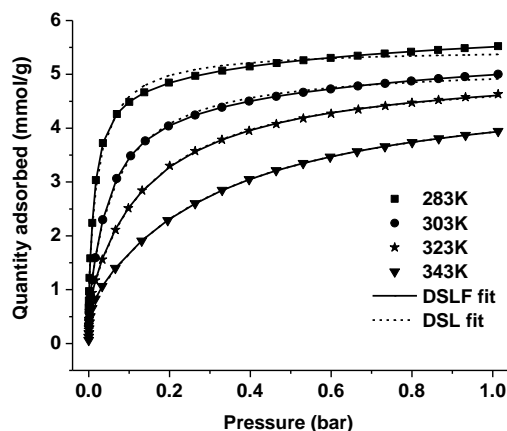


Figure 5.4a. Pure component, volumetric CO₂ adsorption isotherms in Li-ZK-5 at 283 K (squares), 303 K (circles), 323 K (stars), and 343 K (triangles). Dual-site Langmuir-Freundlich fit (solid line), and Dual-site Langmuir fit (dash line).

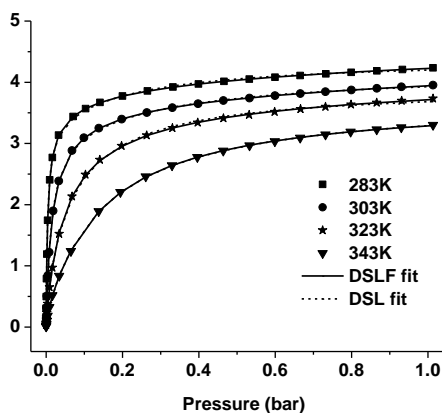


Figure 5.4b. Pure component, volumetric CO₂ adsorption isotherms in Na-ZK-5 at 283 K (squares), 303 K (circles), 323 K (stars), and 343 K (triangles). Dual-site Langmuir-Freundlich fit (solid line), and Dual-site Langmuir fit (dash line).

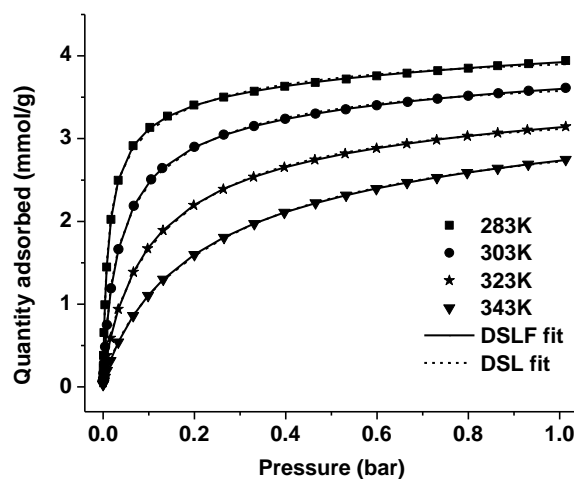


Figure 5.4c. Pure component, volumetric CO₂ adsorption isotherms in K-ZK-5 at 283 K (squares), 303 K (circles), 323 K (stars), and 343 K (triangles). Dual-site Langmuir-Freundlich fit (solid line), and Dual-site Langmuir fit (dash line).

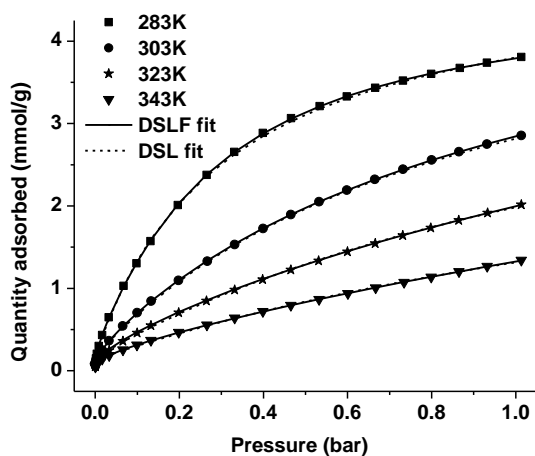


Figure 5.4d. Pure component, volumetric CO₂ adsorption isotherms in Mg-ZK-5 at 283 K (squares), 303 K (circles), 323 K (stars), and 343 K (triangles). Dual-site Langmuir-Freundlich fit (solid line), and Dual-site Langmuir fit (dash line).

Table 5.3. Dual-site Langmuir-Freundlich parameters for CO₂ adsorption in cation-exchanged ZK-5

Li-ZK-5	283K	303K	323K	343K
b ₁ (bar ⁻¹)	297.6	1.263	196.5	41.73
b ₂ (bar ⁻¹)	1.264	83.01	6.092	3.203
k ₁	1.35	0.3454	0.7353	0.6818
k ₂	0.2717	1.458	0.9618	1.072
q _{m,1} (mol/kg)	2.413	5.347	0.7736	0.9424
q _{m,2} (mol/kg)	5.563	2.031	4.461	3.944

Na-ZK-5	283K	303K	323K	343K
b ₁ (bar ⁻¹)	263.5	57.5	22.23	6.948
b ₂ (bar ⁻¹)	0.9148	0.2355	1.312	514.4
k ₁	1.024	0.9829	1.018	1.029
k ₂	0.3334	0.3426	0.4893	1.194
q _{m,1} (mol/kg)	2.719	3.047	2.835	3.487
q _{m,2} (mol/kg)	3.174	4.972	1.763	0.2392

K-ZK-5	283K	303K	323K	343K
b ₁ (bar ⁻¹)	0.3058	20.35	9.982	6.138
b ₂ (bar ⁻¹)	53.42	0.2753	0.4102	0.566
k ₁	0.4012	0.9102	0.9692	1.017
k ₂	0.8992	0.406	0.4259	0.5648
q _{m,1} (mol/kg)	3.62	2.971	2.485	1.898
q _{m,2} (mol/kg)	3.132	3.56	3.022	3.05

Mg-ZK-5	283K	303K	323K	343K
b ₁ (bar ⁻¹)	1.782	0.2557	0.32	0.1871
b ₂ (bar ⁻¹)	4.886	1.025	0.2011	0.2646
k ₁	0.4768	0.3028	0.9185	0.9528
k ₂	1.267	1.037	0.2498	0.2545
q _{m,1} (mol/kg)	1.737	2.79	6.745	6.521
q _{m,2} (mol/kg)	3.228	4.497	2.158	1.421

Table 5.4. Dual-site Langmuir parameters for CO₂ adsorption in cation-exchanged ZK-5

Li-ZK-5	283K	303K	323K	343K
b ₁ (bar ⁻¹)	4384	3099	1547	589.5
b ₂ (bar ⁻¹)	39.78	15.44	6.888	3.127
q _{m,1} (mol/kg)	1.052	0.6948	0.7313	0.6686
q _{m,2} (mol/kg)	4.425	4.493	4.418	4.3

Na-ZK-5	283K	303K	323K	343K
b ₁ (bar ⁻¹)	4.996	3.096	99.94	168.2
b ₂ (bar ⁻¹)	282.4	78.02	12.28	6.572
q _{m,1} (mol/kg)	1.129	1.026	0.7514	0.2184
q _{m,2} (mol/kg)	3.27	3.192	3.177	3.541

K-ZK-5	283K	303K	323K	343K
b ₁ (bar ⁻¹)	4.601	5.737	61.2	30.77
b ₂ (bar ⁻¹)	118.1	56.51	5.826	3.079
q _{m,1} (mol/kg)	1.188	1.736	0.7463	0.5729
q _{m,2} (mol/kg)	2.946	2.135	2.791	2.872

Mg-ZK-5	283K	303K	323K	343K
b ₁ (bar ⁻¹)	1519	1.11	399.7	700.4
b ₂ (bar ⁻¹)	3.271	724.9	0.6184	0.4733
q _{m,1} (mol/kg)	0.175	5.035	0.1722	0.1387
q _{m,2} (mol/kg)	4.748	0.1862	4.745	3.663

For low amounts of adsorbed CO₂ (less than 12 CO₂ molecules/ u.c), the heats of adsorption are in the order of Na-> Li-> K->> Mg-ZK-5 as reflected by the steepness of the low-pressure portion of the isotherms. The Q_{st} drops off quickly for Na-ZK-5 and less for Li-ZK-5 at higher loadings, yet the heat of adsorption for K-ZK-5 increases slightly with more adsorbed CO₂. Interestingly, Mg²⁺, with less than half the cation density, has much lower heat of adsorption compared to other cations (see below).

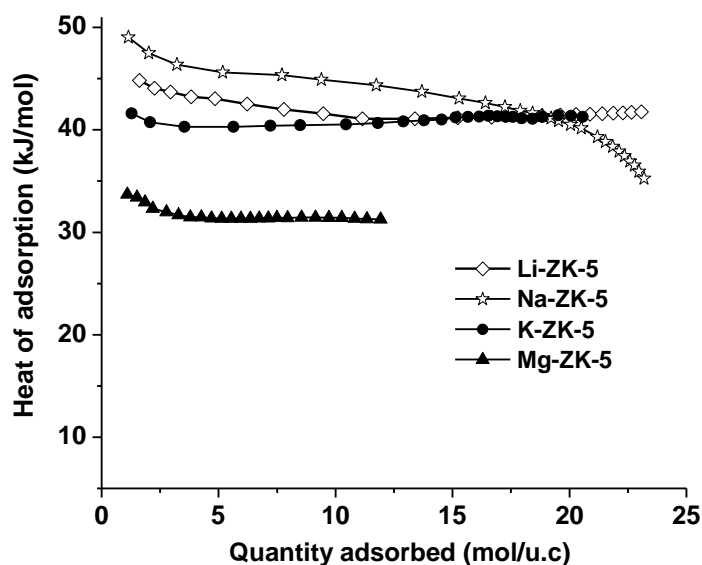


Figure 5.5. Isosteric heats of adsorption, Q_{st}, of CO₂ on cation exchanged ZK-5 zeolites as a function of loading.

The adsorption capacity and heat of adsorption in this study (Figure 5.5) are similar to the trend observed in higher silica (Si/Al=4.75) ZK-5 in our previous report [48]. At ambient temperature and pressure (~303 K and 1 bar), Li-ZK-5 showed

similar adsorption capacity to Li-, Na-CHA (Si/Al=6) [47], NaY, NaX (~5 mmol/g) [62] [60] [59] and much higher than that of other zeolites with higher framework density such as FER, STI, MFI, MEL, TUN (< 3 mmol/g) [63]. Due to the higher micropore volume of CHA ($V_{mic} \sim 0.27 \text{ cm}^3/\text{g}$) and faujasites Na13X, NaY ($V_{mic} \sim 0.3 \text{ cm}^3/\text{g}$), above atmosphere pressure, the slopes of CO₂ adsorption isotherms on Na-, Li-CHA/6, NaY, Na13X materials are higher than those of ZK-5, indicating that their saturation capacity is higher than cation-exchanged ZK-5 adsorbents. The heats of adsorption of Na-ZK-5 near zero coverage are close to the values observed for Na13X, higher than Li-, Na-CHA/6, and much higher than NaY.

5.3.2 Structure of cation-exchanged ZK-5 zeolites

Rietveld refinements of model ZK-5 frameworks to the X-ray data indicate Si-O connectivity is as expected for the evacuated zeolite [64] [62] [61]. Elucidation of extra-framework cation locations is necessary to understand the structure-property relationships of CO₂ adsorption on cation-exchanged ZK-5. The KFI structure was initially refined in the body-centered cubic space group $Im\bar{3}m$, with a unit cell containing 96 symmetry-equivalent tetrahedral Si or Al atoms and 192 oxygen atoms. One unit cell (u.c) consists of two α -cages and six γ -cages. Four cation sites were located using Fourier difference maps of the de-gassed cation-exchanged zeolites. Site I is in the center of the hexagonal prism where cations have an octahedral coordination with the neighboring framework oxygen atoms. Site I' is in the alpha cage, close to the hexagonal window of the hexagonal prism. Here each cation is coordinated to three oxygen atoms. Site II is placed in the center of the puckered eight-ring and site III is in the flat eight-ring window, where each cation is coordinated to 4 framework oxygens. The refined unit cell parameters, cation locations, occupancies, number of atoms per

unit cell, and cation-framework oxygen distances in cation-exchanged ZK-5 are reported in Table 5.5.

Lithium is only observed at position SI' (Figure 5.6a) because this coordination environment is the most favorable for a small cation, as has been found for faujasite and chabazites [62, 65]. Li⁺ is displaced out of the plane of the 3 framework oxygens in the 6-ring by an axial distance of 0.433 Å. Sodium cations are observed in 3 sites (SI, SI', and SII), a result consistent with a previous study by Mortier *et al.* [66]. The data in Table 5.5 show that site II, in the puckered 8-rings (Figure 5.6d, 5.6e), is preferred than over the 6-rings since it has full occupancy. The Na-Oz distances in sites I and II are higher than that in site I' due to their higher coordination with the framework oxygens (6, 4, and 3, respectively). The distances between Na(I)-Na(I') in the same 6MR are too short (1.948(0) Å) for these sites to occupied at the same time. With larger ionic radius ($r_{\text{Na}^+}=1.16$ Å, $r_{\text{Li}^+}=0.72$ Å), the relative small distance between Na(I)-Na(I) (3.897(0) Å) might also lead to repulsive interactions. The total occupancy of Na⁺ in the 6MR (occupancy of site I + (¹/₂) occupancy of site I') is 0.505 (4), indicating that Na⁺ cations fully occupied with one cation in the D6R. The shorter Li-Oz distances compared to Na-Oz (Table 5.5) explain why both have a similar displacement away from the 3 oxygen plane in the 6-ring (0.455 Å), even though Na⁺ radius is larger than Li⁺. Potassium cations in K-ZK-5 were found in site I', II, III, which as was reported by Mortier *et al.* [66], except for the fact K⁺ was not observed at site I in our model. The preferred site of K⁺ is the puckered eight-ring (II), which has optimal distance to 4 framework oxygens; a similar site has been found in merlinoite [67, 68] and agreed with a report by Cox *et al.* [69]. The biggest cation K⁺ at site SI', is displaced 1.359 Å out of the 6MR plane (Figure

5.6c). Contrary to Li^+ , Mg^{2+} prefers site I despite its small ionic radius (0.72 \AA) as has been observed before in Mg-faujasite zeolites [70, 71]. The short Mg-O distance ($2.281(5) \text{ \AA}$) compared to $d(\text{Na}(\text{SI})-\text{O}) = 2.704(6) \text{ \AA}$ leads to a strong distortion of the D6R (Figure 5.7).

The refined cation compositions (Table 5.5) agreed well with the results measured by ICP and EDX (Table 5.1). The model has slightly lower Li^+ content than the values found from ICP, perhaps the remaining Li^+ is on sites of low occupancy due to the weak scattering from Li^+ (only 2 electrons) with the X-ray sources. The distances K-O, Na-O, Li-O (Table 5.5) are close to the crystal radii values predicted by Shannon [72]. The distances are higher in site II, III and I compared to site I' due to a cation higher coordination number in these sites.

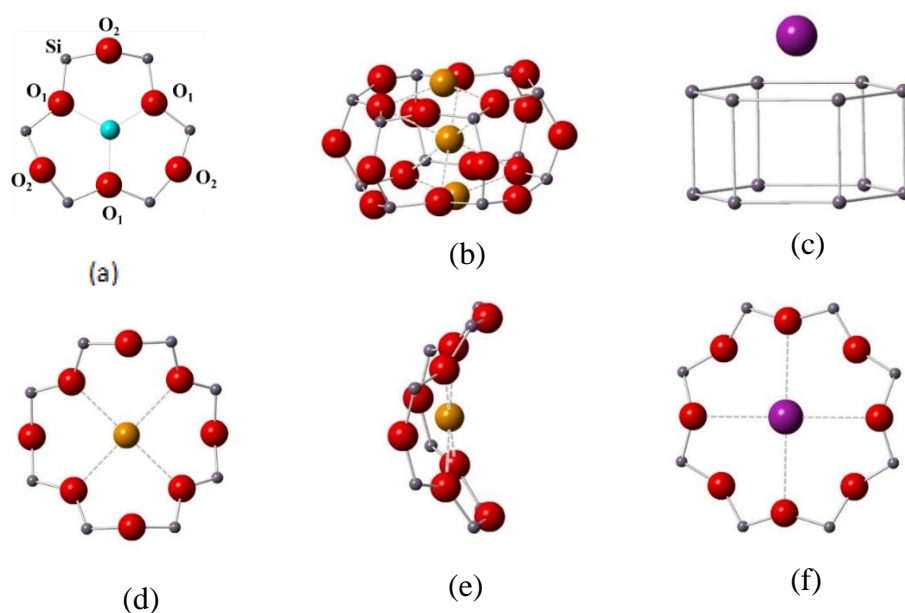


Figure 5.6. Cation sites in the hexagonal prism: Li^+ (a), Na^+ (b), K^+ (c); and Na^+ in the puckerd (d, e) and K^+ in the flat (f) 8-membered rings

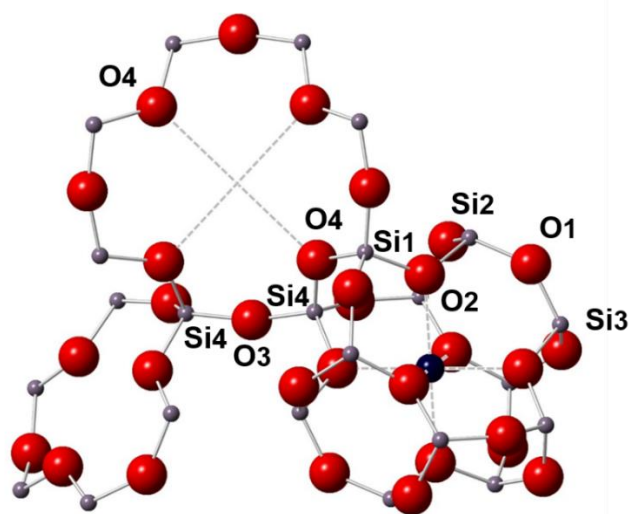


Figure 5.7. Mg cation site and the shrinkage of KFI unit cell

Table 5.5. Refined unit cell parameters, cation locations, occupancies/(atoms per unit cell), and cation-framework oxygen distances in cation-exchanged ZK-5. Values in parentheses indicate one standard deviation in the final digit.

Sample	U.C (Å)	site I		site I'		site II		site III	
		Occ./ atoms	d _{M-O} (Å)	Occ./ atoms	d _{M-O} (Å)	Occ./ atoms	d _{M-O} (Å)	Occ./ atoms	d _{M-O} (Å)
Li-ZK-5	18.6414(4)	0/0	-	1/16	2.062(6)	0/0	-	0/0	-
Na-ZK-5	18.5929(4)	0.2/1.6	2.704(6)	0.41/6.6	2.299(7)	1/12	2.703(6)	0/0	-
K-ZK-5	18.6854(3)	0/0	-	0.21/3.4	2.76(1)	0.94/11	2.827(7)	0.5/6.3	3.331(6)
Mg-ZK-5	18.2498(3)	0.9/7.4	2.281(5)	0/0	-	0/0	-	0/0	-

Compositions: Li-ZK-5 = Li₁₆Al_{20.64}Si_{75.36}O₁₉₂; Na-ZK-5 = Na_{20.16} Al_{20.64}Si_{75.36}O₁₉₂; K-ZK-5 = K_{20.88} Al_{20.64}Si_{75.36}O₁₉₂; Mg-ZK-5 = Mg_{7.36} Al_{20.64}Si_{75.36}O₁₉₂. Average Si/Al = 3.65.

Tables 5.6a-d report the tetrahedral bond lengths and angles for the refinement of cation-exchanged ZK-5 SXRD patterns. The distribution of the tetrahedrally coordinated Si/Al to oxygen (T-O) distances for ZK-5 (Si/Al=3.65) are reasonable compared to the Si-O and Al-O distances of 1.61 Å and 1.75 Å, respectively, reported by Smith and Bailey [73] for structures with the feldspar framework. The weighted average of T-O distances for the feldspar structure with Si/Al=3.65 is 1.64 Å, which is similar to the values of 1.63 Å -1.64 Å in our refinements. The average O-T-O angles are 109.5° with small deviations around this value for all samples in agreement with tetrahedral coordination. In silicates, the Si-O-Si bond angles are more flexible and lie between 120° and 180° with a mean value near 140°[74]. In fact, the Si-O-Si angle is the parameter showing the greatest variability. There is a clear contraction in the Si-O1-Si, Si-O2-Si, and Si-O4-Si angles of Mg-ZK-5 compared to the other samples. Although occupying site I as observed for Na⁺, Mg²⁺ has higher charge density and a stronger interaction with the framework oxygen leading to the contraction of Si-O1-Si and Si-O2-Si angles, thus Si atoms move closer together suggesting a narrowing of the single six-membered ring (Table 5.7). There is an expansion of the distance between T4 and T4 atoms that bridging two D6R together, but the high contraction of the D6R is dominant and clearly responsible for the contraction of the unit cell parameter in Mg-ZK-5. This phenomena was also observed in MgX with smaller unit cell (24.671(5) Å)[71] compared to NaX (25.099(5) Å)[75] and KX (25.076 (3) Å)[76] and the mechanism for this contraction is similar to the negative thermal expansion in siliceous zeolites reported by Cambor *et al.* [77].

Table 5.6a. Tetrahedral bond lengths and angles for the refinement of Li-ZK-5 XRD patterns taken at 298K

T-O distance	Length (Å)	O-T-O angle	Degree (°)	T-O-T angle	Degree (°)
T-O1	1.611(2)	O1-T-O2	107.0(3)	T-O1-T	143.9(4)
T-O2	1.664(2)	O1-T-O3	111.2(2)	T-O2-T	134.8(3)
T-O3	1.617(1)	O1-T-O4	111.4(2)	T-O3-T	168.1(3)
T-O4	1.667(3)	O2-T-O3	111.8(2)	T-O4-T	133.8(3)
T-O (avg)	1.640(4)	T-O-T			
		(avg)		(avg)	145.2(7)
		O2-T-O4	109.1(2)		
		O3-T-O4	106.5(2)		
		O-T-O			
		(avg)	109.5(5)		

Table 5.6b. Tetrahedral bond lengths and angles for the refinement of Na-ZK-5 XRD patterns taken at 110K

T-O distance	Length (Å)	O-T-O angle	Degree (°)	T-O-T angle	Degree (°)
T-O1	1.613(2)	O1-T-O2	105.3(3)	T-O1-T	159.9(5)
T-O2	1.659(2)	O1-T-O3	111.5(3)	T-O2-T	145.3(5)
T-O3	1.597(2)	O1-T-O4	109.9(3)	T-O3-T	151.9(4)
T-O4	1.638(3)	O2-T-O3	112.6(3)	T-O4-T	129.5(5)
T-O (avg)	1.627(5)	T-O-T			
		O2-T-O4	108.8(3)	(avg)	146.7(9)
		O3-T-O4	108.6(3)		
		O-T-O (avg)	109.5(7)		

Table 5.6c. Tetrahedral bond lengths and angles for the refinement of K-ZK-5 XRD patterns taken at 110K

T-O distance	Length (Å)	O-T-O angle	Degree (°)	T-O-T angle	Degree (°)
T-O1	1.641(3)	O1-T-O2	108.6(4)	T-O1-T	150.5(5)
T-O2	1.635(3)	O1-T-O3	105.0(3)	T-O2-T	150.3(6)
T-O3	1.652(3)	O1-T-O4	112.7(4)	T-O3-T	140.4(5)
T-O4	1.641(3)	O2-T-O3	112.5(4)	T-O4-T	135.9(5)
T-O (avg)	1.642(6)	O2-T-O4	113.0(3)	T-O-T (avg)	144(1)
		O3-T-O4	104.9(4)		
		O-T-O			
		(avg)	109.5 (9)		

Table 5.6d. Tetrahedral bond lengths and angles for the refinement of Mg-ZK-5 XRD patterns taken at 298K

T-O distance	Length (Å)	O-T-O angle	Degree (°)	T-O-T angle	Degree (°)
T-O1	1.619(2)	O1-T-O2	108.4(3)	T-O1-T	138.5(4)
T-O2	1.671(2)	O1-T-O3	108.8(3)	T-O2-T	127.2(3)
T-O3	1.612(2)	O1-T-O4	111.8(3)	T-O3-T	161.6(4)
T-O4	1.641(3)	O2-T-O3	111.1(3)	T-O4-T	124.5(3)
T-O (avg)	1.636(5)	O2-T-O4	107.0(2)	T-O-T (avg)	138.0(5)
		O3-T-O4	109.7(2)		
		O-T-O			
		(avg)	109.5(7)		

Table 5.7. T-T distances in cation-exchanged ZK-5

T-T distance (Å)	Li-ZK-5	Na-ZK-5	K-ZK-5	Mg-ZK-5
T1-T2	3.072(3)	3.167(3)	3.160(4)	2.994(3)
T2-T3	3.062(3)	3.176(3)	3.175(4)	3.028(3)
T1-T4	3.067(4)	2.962(4)	3.043(4)	2.904(4)
T4-T4	3.215(1)	3.099(3)	3.108(4)	3.183(3)

5.3.3 CO₂ adsorption sites in Mg-ZK-5

The structure of solid carbon dioxide reported by Peters *et al*[78] shows that the O of one CO₂ molecule closely interacting with 12 oxygen atoms of other CO₂ molecules (contact distances of 3.446 Å and 3.177 Å). Each C atom has close contact with 6 oxygen atoms of other CO₂ molecules ($d_{C-O}=3.107$ Å). This minimum energy configuration reveals the importance of van der Waals interactions, particularly between O-O of CO₂-CO₂ and CO₂-adsorbents in adsorption. By using GCMC simulation, Bell *et al.*[23] concluded that the contacts close to the equilibrium distances for Cc-Oz and Oc-Oz interactions of 3.3 Å and 3.44 Å, respectively lead to a strong attractive dispersive interaction. Some of the contacts are shorter or longer than the equilibrium distance, thus the optimal energy interactions of CO₂ with zeolite frameworks are determined by the sum of all neighboring framework atoms. To be consistent throughout this report, we will highlight guest–framework close contacts that are between 3-4 Å.

Mg²⁺ cations are located in the center of the hexagonal prism and are not accessible to most adsorbates. This fact is responsible for the very low heats of adsorption of CO₂ on Mg-ZK-5 and suggesting that dispersive interactions are the dominant contribution to the total energy of adsorption. The structural arrangement of CO₂ within the ZK-5 pores then should be such that it allows as many close contacts as possible. Adsorption of CO₂ at the center of the flat 8MR window of ZK-5 (site A, Figure 5.8) has a total of 24 guest-framework contacts (8 contacts of Cc-Oz and 16 close contacts of Oc-Oz). The CO₂ occupancy is the maximum possible for site A (~1), or a total of 12 CO₂ site A in one unit cell or, equivalently 6 CO₂ of site A in one α -cage. As we showed earlier, the distortion of the puckered 8MR window by Mg²⁺ cations leads to a decrease in this window size. The distance of the carbon atom of

CO₂ to the nearest framework oxygens (~ 2.76 Å) is now significantly less than the sum of the van der Waals radius of C atom and crystal radius of O_z (~ 2.94 Å). The interaction is repulsive, thus no CO₂ electron density is observed in the puckered 8MR center by Fourier maps.

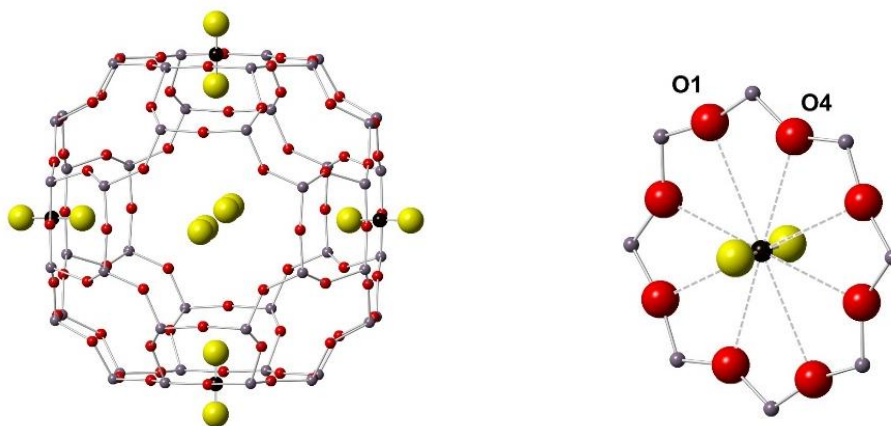


Figure 5.8. CO₂ adsorption site (site A) in the flat 8-membered ring of ZK-5 zeolite and detail illustrating interactions between CO₂ and framework oxygens (dash line)

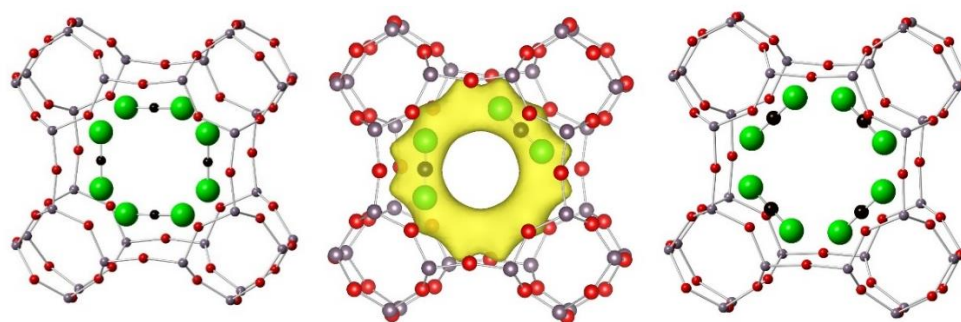


Figure 5.9. Adsorption site B (left), Fourier map (middle), and site B* (right) of CO₂ in γ -cage of Mg-ZK-5

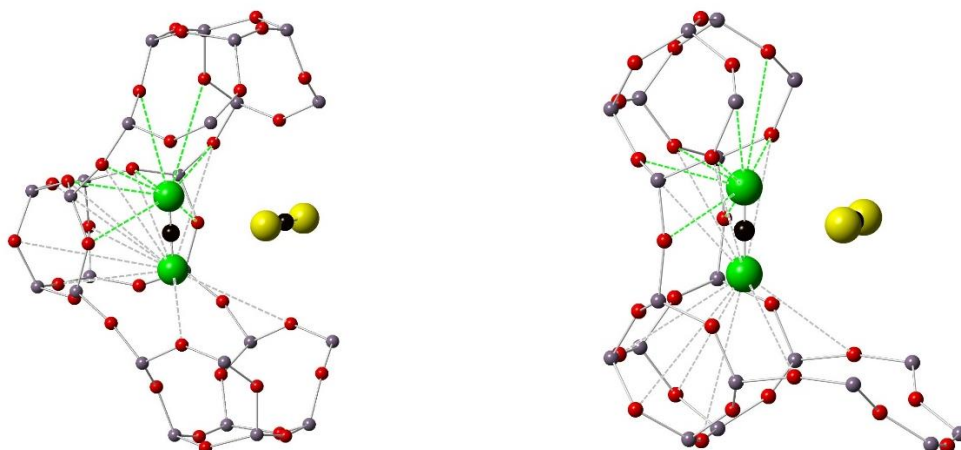


Figure 5.10. Close contacts (dash-line, green) of Oc-Oz ($3 \text{ \AA} < d_{\text{Oc-Oz}} < 4 \text{ \AA}$) and long-range interactions (dash-line, grey) of Oc-Oz ($4 \text{ \AA} < d_{\text{Oc-Oz}} < 5 \text{ \AA}$) of CO₂ site B (left), B' (right) in *pau*-cage of Mg-ZK-5

Secondary adsorption site was found in the *paulingite* cage with a total of 16 Oc-Oz and 6 Cc-Oz close contacts. The distance between two oxygens of two closest CO₂ molecules is about 1.45 Å, which is too close to be sit in the same cage. Therefore, the maximum occupancy of this site is 0.5, or 2 CO₂ molecules per one γ -cage, or 12 CO₂ molecules per one unit cell of ZK-5. Based on the Fourier maps (Figure 5.9, middle), this adsorption site can be modeled as site B (Figure 5.9 and Figure 5.10, left), where two O atoms of CO₂ oriented toward the pucker of 8MR of the γ -cage, or modeled as site B* (Figure 5.9 and Figure 5.10, right) where two O atoms of CO₂ oriented toward the 4MR of the γ -cage. Site B* has observed by Bell *et al.* [23] (Figure 1, ref 23) where the CO₂ molecule fits nicely into the space surrounded by a crankshaft-like arrangement of three 4MR of the γ -cage in Merlinoite zeolite. Our refinements of X-ray diffraction data showed no preference for these two difference configuration in Mg-ZK-5. Both sites have the same number of close contacts with the

framework oxygens (Figure 5.10) and similar occupancy, good of fit parameters obtained for the models with each distinct adsorption site or mix of these two adsorption sites. For the third adsorption site of CO₂ in Mg-ZK-5 was found in the large α -cage of the KFI framework (site C, Figure 5.11), there is a total of 14 such close guest–framework contacts (Figure 5.11, middle). Each O of CO₂ oriented toward the 6MR, where Mg²⁺ cations situated (Figure 5.11), and each C of CO₂ has 4 close contacts with O of the 4MR (Figure 5.11, middle). Due to the close distances between two neighbor CO₂ molecules, only a maximum occupancy of 0.34 (8 mol/u.c) can be obtained by this site. Our Fourier maps indicated that upon the adsorption, a portion of Mg²⁺ cations moved from its preferable site I of the hexagonal prism to the 6MR window (Figure 5.11, right). Mg-MOF-74 (or Mg-CPO-27) has been shown to exhibit exceptionally high CO₂ adsorption capacity under atmospheric conditions and the heat of adsorption (47 kJ/mol) is generally higher than other members of the M₂(dhtp)(H₂O)₂·8H₂O family (M=Mg, Mn, Fe, Co, Ni, or Zn) [1]. X-Ray diffraction study [79] showed “end on” coordination of CO₂ molecule to the unsaturated site Mg²⁺ with a short distance of 2.39(6) Å (Figure 5.11, right). Mg²⁺ has also been found in the 6-ring window of faujasite zeolites (site I' and site II) with fairly high occupancy compared to site I [71]. The high affinity of Mg²⁺ with O of CO₂ site C would overcome the penalty energy for the movement of Mg²⁺ site I to less preferable site I'.

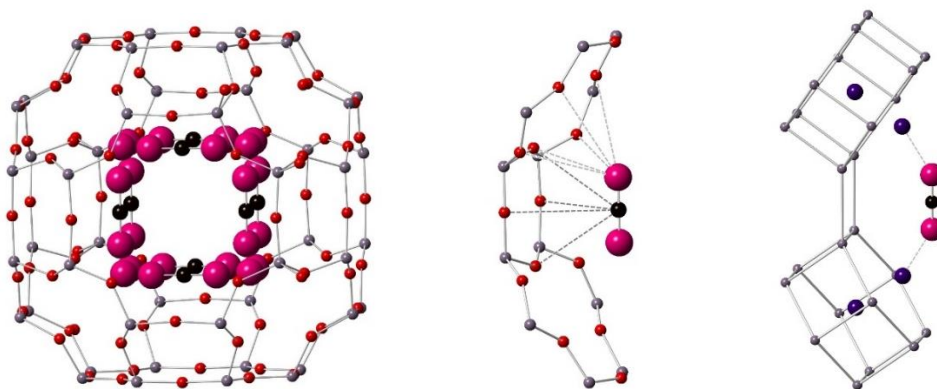


Figure 5.11. CO₂ adsorption site in the α -cage of Mg-ZK-5 (site C) and dual-cation site between 2 Mg²⁺/Li⁺ and CO₂ (site C) in Mg-ZK-5

The increase of unit cell upon adsorption of CO₂ on Mg-ZK-5 (from 18.2498(3) Å to 18.3663(4) Å) is also an indication of a decrease in the population of cations Mg²⁺ in site I, a cause for the shrinkage of KFI unit cell. Our result is also in agreement with an increase in unit cell volume of CO₂ adsorbed on Mg-MOF-74 compared to the bare sample as reported by Bordiga *et al.*[80] using the *ab initio* periodic DFT-D calculations. The migration of extra-framework cations during adsorption and desorption process of zeolites has also been observed with various adsorbate molecules [81-86]. The motion of cations in faujasite Y upon adsorption of CO₂ has been reported by Plant *et al.* using quasi-elastic neutron scattering experiments and molecular dynamics modeling methods [87, 88].

At room temperature, CO₂ was determined with small occupancies of all sites (5.9 mol CO₂/u.c) with highest occupancy of site B (not shown here). It is generally observed that energetically favorable adsorption sites were found at the center of 8MR windows.[46, 62, 89] To compare, both sites have the same number of short-range van

der Waals interactions (total of 16 close contacts between Oc and Oz, green dash line, Figure 5.10), but the long-range van der Waals (vdW) interactions ($4\text{\AA} < d_{\text{Oc-Oz}} < 5\text{\AA}$, grey dash line) contributing slightly to the adsorption energies are only observed at site B. This is the reason for the higher dispersion interactions of CO₂ site B with the framework oxygens as compared to CO₂ site A. This finding is also consistent with the preferred adsorption sites for small alkanes such as propane and n-butane in smaller γ -cages observed by Van Santen *et al.*[53] in ZK-5 zeolite. The lowest occupancy of site C is due to the lowest number of close contacts of the adsorbate with framework oxygens. The phenomenon is observed to a similar extent in Li-ZK-5, and Na-ZK-5.

There are only a maximum of 4 molecules of CO₂ site C in one α -cage, thus higher loading amount of CO₂ on Mg-ZK-5 (higher than 32 CO₂/u.c) leads to the rearrangement of CO₂ in the large α -cage (Figure 5.12-5.14), in which a maximum of 6 molecules of CO₂ in one α -cage can be reached (site D, Figure 5.14). In this configuration, each Oc has close contacts with 5 framework oxygens in the 4- and 6-rings. This D adsorption site is not responsible for the movement of cation Mg²⁺ from SI to SI' due to the short distance between Cc and Mg²⁺ ($d_{\text{Cc-Mg}} = 2.73\text{\AA}$, Figure 5.14).

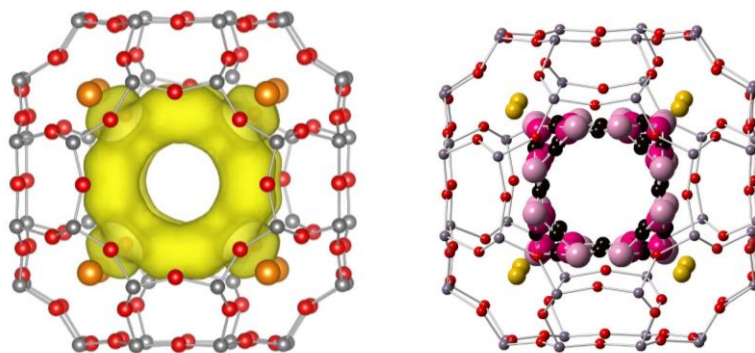


Figure 5.12. Fourier maps (yellow, left) indicated 2 adsorption sites inside α -cage of Mg-ZK-5 (right) at high loading of CO₂

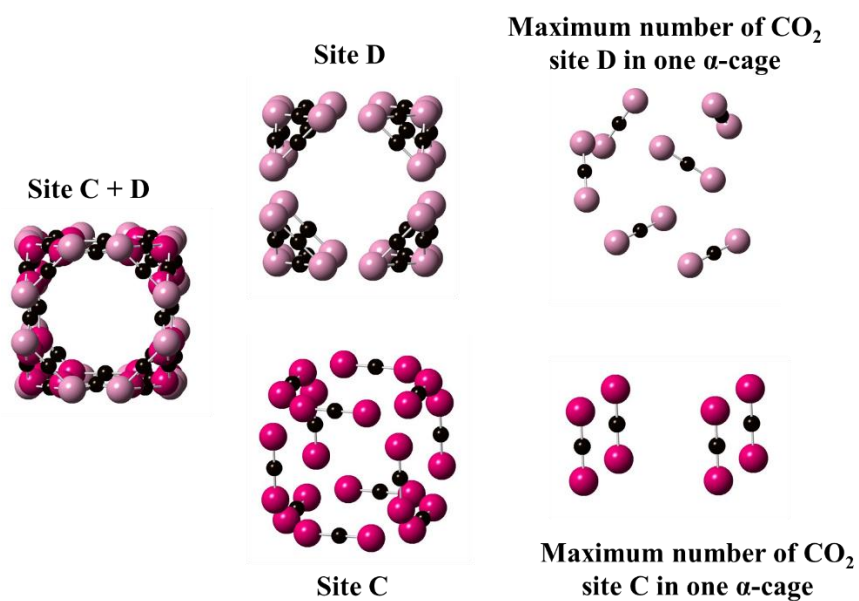


Figure 5.13. Visualization of adsorption sites C, D and their maximum number of CO₂ molecules in one α -cage in Mg-ZK-5

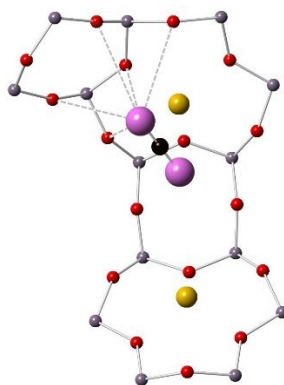


Figure 5.14. Adsorption site D in Mg-ZK-5 and the interaction of Oc with framework oxygens

5.3.4 CO₂ adsorption sites in Li-ZK-5

Besides three similar adsorption sites A, B (B*), C were found in Mg-ZK-5, another adsorption site where C atom of CO₂ situates at the center of the puckered 8MR (site E, figure 5.15) was located by Fourier maps in Li-ZK-5 sample. Similar to site A with total of 24 close contacts between the guess molecule and the oxygens of zeolite framework, but the occupancy of site E is still the lowest compared to the other adsorption sites because of the repulsion interaction between Cc and Oz ($d_{Cc-O4} = 2.89 \text{ \AA}$). The total occupancy of site B and E ($2 \times \text{occupancy of site B} + 1 \times \text{occupancy of site E}$) should not be over 1 due to the short distance between two O of site B and site E ($d = 1.35 \text{ \AA}$).

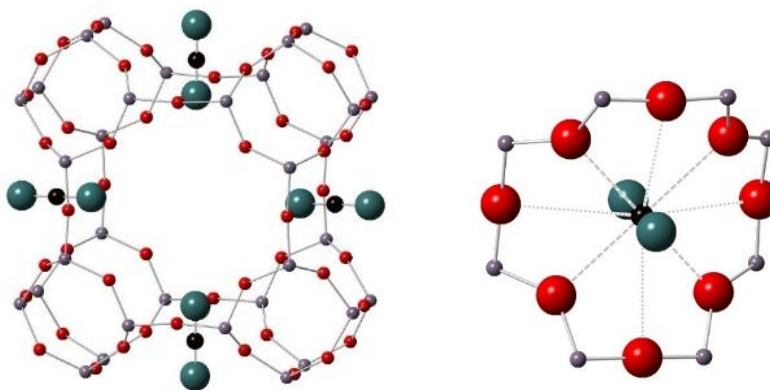


Figure 5.15. Adsorption site of CO₂ at the center of the puckered 8MR in Li- ZK-5 and its interaction with framework oxygens in puckered 8MR

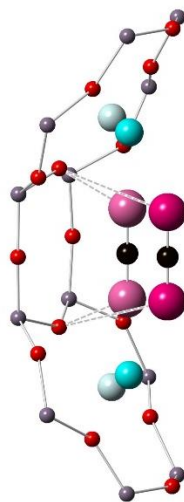


Figure 5.16. Illustration for the movement of Li^+ out of 6MRs upon adsorption

Due to the short distance between O of CO_2 molecule and Li^+ in the ‘end-on’ coordination ($\sim 2.3 \text{ \AA}$), and the fact that CO_2 cannot get too close to the zeolites wall due to high repulsive interactions between CO_2 molecule and framework oxygens, Li^+ cations have to shift slightly toward to the α -cages ($d_{\text{Li-Oz}} = 2.29 \text{ \AA}$ as compared to 2.09 \AA in the undosed Li-ZK-5) to form the bridged CO_2 complexes between a pair of Li^+ cations and one CO_2 molecule (Illustration in Figure 5.16). Therefore, the energy loss of Li^+ site SI’ orienting further from the 6MR is compensated by the strong interaction between one molecule CO_2 and two cation Li^+ in this site. There is an evident that the unit cell parameter of Li-ZK-5 decreases slightly with the small movement of Li^+ toward the α -cages.

Table 5.8. Atomic parameters from Rietveld refinement of CO₂/Li-ZK-5 data at 298 K [APS, 1-BM] (cubic, $Im\bar{3}m$, $a = 18.6249(3)$ Å, $V = 6460.8(2)$ Å³). Values in parentheses indicate one standard deviation in the refined value. Goodness-of-fit parameters: wRp = 3.33 %, Rp = 2.5 %. The refined composition is: [Li₁₆Al_{20.64}Si_{75.36}O₁₉₂][CO₂]_{24.9}.

LIZK51P5RT	X	Y	Z	Uiso (Å ²)	Mul.	Occup.
O1	0.1238(2)	0.1238(2)	0.3170(3)	0.038(2)	48	1
O2	0.2557(2)	0.2557(2)	0.3889(2)	0.012(2)	48	1
O3	0	0.1940(3)	0.3210(3)	0.015(2)	48	1
O4	0.25	0.1097(2)	0.3903(2)	0.018(2)	48	1
Si	0.0861(1)	0.2023(1)	0.3198(1)	0.016(1)	96	0.785
Al	0.0861(1)	0.2023(1)	0.3198(1)	0.016(1)	96	0.215
Li	0.1740(8)	0.1740(8)	0.1740(8)	0.1(1)	16	1
C1	0	0	0.3195(1)	0.1(1)	12	0.652(7)
O1a	0	0	0.2572(1)	0.1(1)	12	0.652(7)
O1b	0	0	0.6182(1)	0.1(1)	12	0.652(7)
C2	0.0868(4)	0.0868(4)	0.5	0.19(2)	24	0.431(5)
O2a	0.1308(4)	0.0427(4)	0.5	0.19(2)	48	0.431(5)
O3a	0.1217(6)	0.1217(6)	0.0623(0)	0.14(2)	48	0.217(3)
C3	0.1217(6)	0.1217(6)	0	0.14(2)	24	0.217(3)
C4	0	0.5	0.25	0.014(3)	12	0.126(6)
O4a	0	0.5	0.1877(1)	0.014(3)	24	0.126(6)

At low loading amount of CO₂, site A and B in Li-ZK-5 are the majority adsorption sites, in which the occupancy of site B is higher than that of site A as also observed in Mg-ZK-5. The occupancy of adsorption sites in Table 5.8 revealed that site A population is gradually increased at a higher dosing of gas molecules and become the dominant adsorption site. This can be explained by favorable guess-guess interactions. Figure 5.17 represents the distance of CO₂ molecules between each adsorption site. We can see that each CO₂ site B or C interacts only with one molecule of CO₂ site A, whereas each CO₂ site A interacts effectively with 4 molecules of CO₂

site B and site C, which leads to higher adsorbate-adsorbate interactions of site A with the increase of CO₂ loading amount.

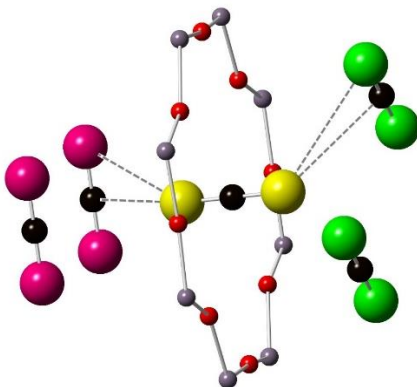


Figure 5.17. Illustration of CO₂-CO₂ interactions of various CO₂ adsorption sites

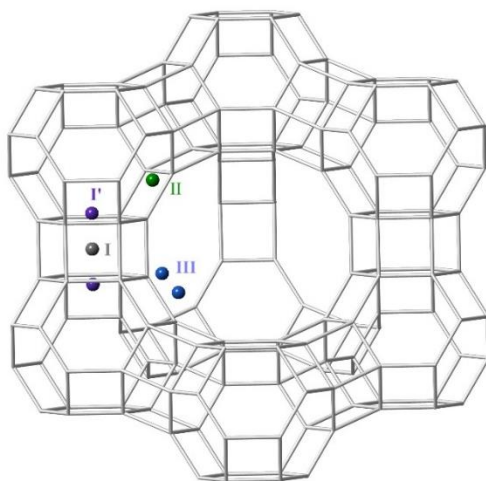


Figure 5.18. Positions of extraframework cations positions in faujasite zeolite

5.3.5 N₂ and CO₂ co-adsorbed on Li-ZK-5

Li-containing zeolites have been shown to be among the most effective adsorbents for N₂ and Li-LSX has been used to produce O₂ from air based on high selective adsorption between N₂ molecules and extra-framework Li⁺ cations [90, 91]. Two sites of Li⁺ in front of six-ring windows (SI'x inside the β -cages, SIIx inside the supercages), and a third position near the four-ring windows (inside the supercages at SIIIx) were found in Li-LSX (Figure 5.18) [92, 93]. Due to the van der Waals radius of N₂ is too large to enter the β -cages, nitrogen molecules can interact only with cations located in the supercages. Site SIIIx protrudes from the 4-ring into the supercage, which is more accessible and only shielded by 2 closet negative framework oxygen atoms, thus exhibits higher interactions with the sorbate molecules. Specific adsorption sites for nitrogen in Li-LSX studying by Monte Carlo simulation [94], DRIFT [95], NMR [96] indicated that Li⁺ site Ix in Li-LSX is not involved in the sorption process. Our X-ray diffraction results showed that Li⁺ in 6MR directly interact with nitrogen molecules, which is consistent with the highest N₂ adsorption capacity of Li-ZK-5 among other studied cation-exchanged ZK-5 [48, 49], and contradict with the study in Li-LSX. Figure 5.19 showed that N₂ molecules adsorbed on Li⁺ site I' of ZK-5 zeolite with Li-Na distance of 2.21(2) Å, Li-Na-Nb angle of 180°, and the adsorbates situate along (111) direction of the KFI framework, which is consistent with the nitrogen coordinates end on with an Fe-N-N angle of 179(1)° and an Fe-N distance of 2.30(1) Å reported by Long *et al.*[97] The Li⁺...N₂ linear coordination is to maximize the monopole-dipole interaction or an indication of the high symmetry obtained by powder diffraction method. Each Na, Nb atoms of N₂ molecule have effective Van der Waals distances with 6 and 3 framework oxygens of 6MR, respectively (dNa-O2=3.110(0) Å, dNa-O1=3.599(0) Å, and dNb-O1=4.000(0)

Å), and the N₂ molecules adsorbed on Li⁺ bearing a small positive charge would have higher interaction with the negative framework oxygens. The distance between Nb-O(CO₂-site A, 3.906(0) Å) is shorter than Na-O(CO₂-site A, 4.128(0) Å).

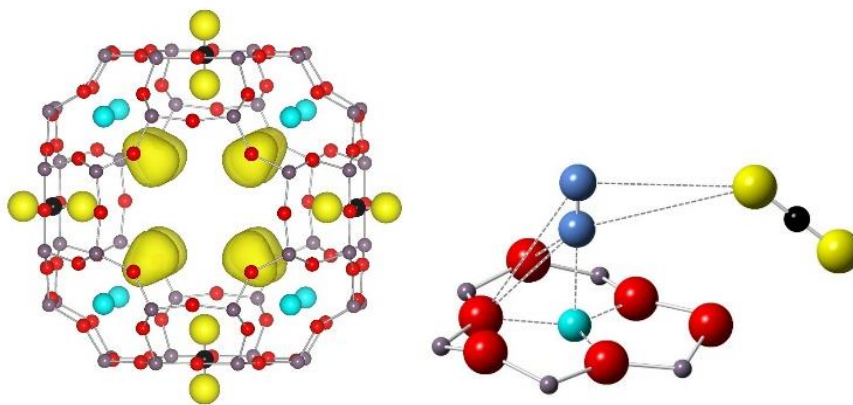


Figure 5.19. Fourier difference scattering length density (yellow regions) clearly indicates the adsorbed N₂ is primarily located on top of the open Li⁺ ions (left) and the configuration of N₂ on Li⁺ in 6MR of ZK-5 zeolite (right).

The configuration of Li⁺ 6MR in Li-LSX is similar to Li-ZK-5, but the distance to the closet framework oxygens is shorter ($d_{\text{Li-O}}=1.969$ Å in Li-LSX). This is due to the fact that in Li-LSX (Si/Al=1), 6MR contains three aluminum atoms, thus cations bind strongly with the basic oxygen (O-Al) atoms. In higher silica zeolite Li-ZK-5 (Si/Al=3.65), the ring contains an average of 1.25 aluminum atoms, thus Li⁺ situates near the oxygen (O-Al) atom and further from two other oxygens (O-Si) giving the longer average distance of oxygen-Li⁺ in the 6MR. Thus, the charge density of Li⁺ cations at 6MR in Li-LSX are highly shielded by negative framework oxygen atoms [98, 99], but less screened in the case of Li-ZK-5. A higher distortion of D6R in LiX compared to Li-ZK-5 also explains for the shrinkage of unit cell in LiX (24.6657

Å) [93], but not in Li-ZK-5. Li⁺ in ZK-5 is more accessible to the adsorbates due to its higher displacement out of the 6MR compared to Li-LSX (0.212 Å). Nachtigall *et al.* [100] demonstrated that the weaker the cation is coordinated, the stronger its polarizing interaction with adsorbates is, and this explains a higher contribution of electrostatic interaction between Li⁺ and N₂ in 6MR of ZK-5 zeolite. Due to both contribution of Van der Waals and electrostatic interaction, N₂ has optimized energy interactions with Li-ZK-5 in end-on configuration. The three other adsorption sites of CO₂ were found in the γ -cages, flat and puckered 8MRs (Table 5.9).

Table 5.9. Atomic parameters from Rietveld refinement of N₂, CO₂/Li-ZK-5 data at 110 K [APS, 1-BM] (cubic, $Im\bar{3}m$, $a = 18.6820(3)$ Å, $V = 6520.3(2)$ Å³). Values in parentheses indicate one standard deviation in the refined value. Goodness-of-fit parameters: wRp = 1.72 %, Rp = 1.3 %. The refined composition is: [Li₁₆Al_{20.64}Si_{75.36}O₁₉₂][CO₂]_{24.8}[N₂]₁₆.

LIZK5N24X	X	Y	Z	Uiso (Å ²)	Mult.	Occup.
O1	0	0.1913(3)	0.3192(2)	0.017(2)	48	1
O2	0.1088(2)	0.2448(2)	0.2448(2)	0.016(2)	48	1
O3	0.1087(2)	0.25	0.3913(2)	0.040(2)	48	1
O4	0.1236(2)	0.1236(2)	0.3209(3)	0.023(2)	48	1
Si	0.0858(1)	0.2024(1)	0.3194(1)	0.019(1)	96	0.785
Al	0.0858(1)	0.2024(1)	0.3194(1)	0.019(1)	96	0.215
Li	0.1988(6)	0.1988(6)	0.1988(6)	0.04(1)	16	1
Na	0.3717(3)	0.3717(3)	0.3717(3)	0.160(6)	16	1.036(6)
Nb	0.4057(3)	0.4057(3)	0.4057(3)	0.160(6)	16	1.036(6)
C1	0	0	0.3183(5)	0.087(5)	12	0.964(8)
O1a	0	0	0.2563(5)	0.087(5)	12	0.964(8)
O1b	0	0	0.6196(5)	0.087(5)	12	0.964(8)
C2	0	0.5	0.25	0.13(2)	12	0.306(8)
O2a	0	0.5	0.1879(0)	0.13(2)	24	0.306(8)
C3	0.0811(2)	0.0811(2)	0.5	0.14(1)	24	0.388(5)
O3a	0.1250(3)	0.0372(3)	0.5	0.14(1)	48	0.388(5)

5.3.6 CO₂ adsorption sites in Na-ZK-5

Below a loading of 32 CO₂/u.c, Na-ZK-5 also has 3 adsorption sites A, B, C as found in Mg-ZK-5 and no observation of CO₂ site E because of the full occupancy of Na⁺ in the puckered 8MR. Although having similar adsorption sites, but due to the differences in the local cation environment, there is a large difference in the electrostatic contributions of these two cations to their adsorption energies. The addition of weak long-range electrostatic interaction between Na⁺ (site I', II) and CO₂ site A (dOc-NaI'=4.934 Å, and dOc-NaII=5.136 Å) and an increase in the dispersive part of higher partial negative framework oxygens with electropositive C atoms of CO₂ account for higher adsorption energy of this site on Na-ZK-5. The electrostatic adsorption energy of site B in Na-ZK-5 is highly increased by the bridging of one CO₂ with 2 Na⁺ cations in the puckered 8MR (dNa⁺-O_c=2.490 Å, Figure 5.20). Moreover, CO₂ molecules in this site bear small partial positive charges would increase their interactions with the negative framework oxygens. CO₂ molecules at site B are also oriented further from the zeolite walls compared to Mg-, and Li-ZK-5, which leads to the reduction of the van der Waals interaction energy. The Fourier map (Figure 5.20) indicated a small bending mode of CO₂ configuration at site B. The high interaction of dual-cation Na⁺ (SII) with CO₂ (about 10 kJ/mol higher than single-cation adsorption site)[101] can facilitate a slight bending motion for CO₂ (8.3° bond angle distortion), which has been reported to have a minimal energy penalty [102]. The large rotational disorder on metal sites could also result in the observed bending angle of CO₂ site B [79, 102]. The refinements of our X-ray diffraction patterns resulted in excellent goodness-of-fit parameters with both unrestrained and restrained models of CO₂ at site B on Na-ZK-5. To be consistent over various loading of CO₂ on Na-ZK-5, we restrained the bond angle of CO₂ site B to be 180° during the refinements. Since CO₂

site B oriented toward the center of *pau*-cage makes its distance to CO₂ site A shorter compared to Li-, Mg-ZK-5, and the interaction of these two CO₂ sites at high adsorbate loading tends to be repulsive.

Only 40 % of Na⁺ occupied in the 6-ring window, hence CO₂ in adsorption site C in Na-ZK-5 is coordinated with one or two Na⁺ (single or dual cation sites, Figure 5.21). Unlike Li⁺, the Na-Oc distance is long enough, thus the coordination of Na⁺ ion (site I') with framework oxygens remains the same upon interaction with the CO₂ molecule. At higher loading of CO₂ (>32 molecules/u.c), when all three adsorption sites A, B, C in Na-ZK-5 get saturated, we also observed the rearrangement of CO₂ within α -cages as in the case of Mg-ZK-5 (site C').

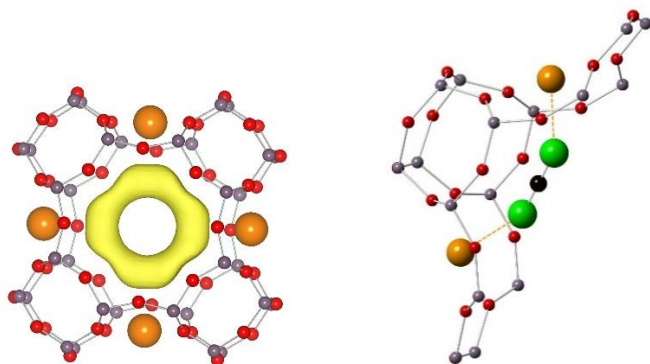


Figure 5.20. Fourier map to assign for the adsorption site B of CO₂ in Na-ZK-5 (left) and dual-cation adsorption site between two cation Na⁺ (SII) and CO₂ in *pau*-cage (right).

Polarization of CO₂ by the cations Li⁺, Na⁺ was indeed evidenced by a blue shift of CO₂ stretch vibrations in adsorbed-phase compared to the gas phase of IR spectra in our previous studied [48].

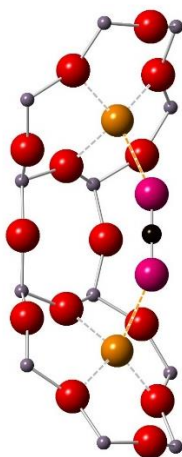


Figure 5.21. Adsorption site C of CO₂ in Na-ZK-5. The site could be single-cation or dual-cation adsorption site due to the uncompleted occupancy of Na⁺ (SI')

5.3.7 CO₂ adsorption sites in K-ZK-5

K⁺ cation is fairly soft Lewis acid compared to smaller cations Li⁺ and Na⁺, thus its end-on coordination with hard base oxygens of CO₂ is weaker and is often seen in dual-cation adsorption sites [34, 62, 103], in which the electrostatic interaction is strengthened by 2 cations. Three adsorption sites of CO₂ on K-ZK-5 were elucidated by our Rietveld refinements of the X-ray diffraction patterns, one of which is located in the middle of the flat 8MR (site A), and the other two sites in the α - and γ -cages where each CO₂ molecule coordinates with two K⁺ cations. Site A of CO₂ and site III of K⁺ are in the same location of the flat 8MR, thus their summation of occupancy would be smaller or equal to 1, or the maximum occupancy of CO₂ on this site is 0.48. Site B of CO₂ in the γ -cage of K-ZK-5 has similar configuration as site B in Na-ZK-5 (Figure 5.23), but the cation-Oc distance is much longer (~ 3 Å), the CO₂ molecule toward to the center of the pau cage and further from the framework oxygens (only 4

close contacts of Oc-Oz). There is only a maximum of 1 CO₂ molecule per γ -cage or 6 molecules per one unit cell due to highly repulsive interaction between CO₂ molecules in the same γ -cage.

Another dual-cation site (site F, Figure 5.24) was found in the α -cage where one molecule CO₂ is bridged to one K⁺ cation in the 6MR and another K⁺ cation in the flat 8MR. At first, this adsorption site could be misinterpreted to be between CO₂ and two K⁺ cation in the diagonal position of alpha cage due to the distance between two K⁺ (site I') in this diagonal position ($d_{K-K}=8 \text{ \AA}$) is close to the optimum distance values for effective dual-cation adsorption site in K-FER ($d_{K-K}=7.8 \text{ \AA}$) reported by Nachtigall [104]. In theory, each α -cage can accommodate 6 CO₂ molecules site F (12 CO₂ molecules per unit cell), but due to the low occupancy of K⁺ in site I' (only 3.4 K⁺ per u.c), site F in K-ZK-5 might not be saturated. The distance between O (CO₂-site A) and O (CO₂-site B) ($d_{OA-OB}\sim 3 \text{ \AA}$) is too close to be populated at the same time, and the distances from C of CO₂ (site B and F) to K⁺ SIII (d_{K-CB} , d_{K-CF} , Figure 5.23) might lead to repulsive interaction of these CO₂ with K⁺ SIII. Hence, there might not have CO₂ at site B or F if K⁺ already occupied SIII.

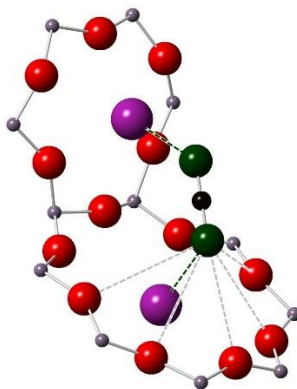


Figure 5.22. Dual-cation sites of CO₂ on K-ZK-5 in α -cage (site E)

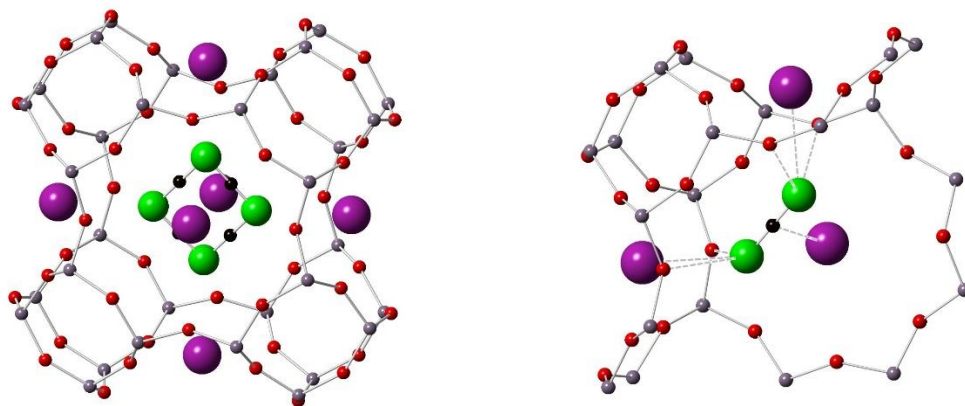


Figure 5.23. Adsorption site B of CO₂ in *pau*-cage of K-ZK-5 and the close contacts between O of CO₂ and framework oxygens (dash line, grey)

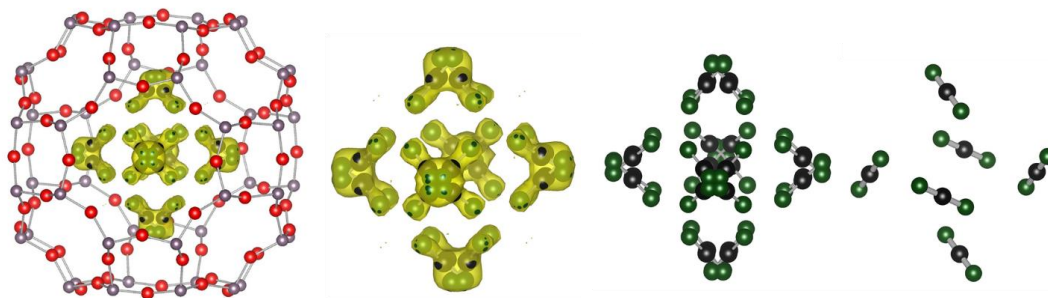


Figure 5.24. Fourier maps to assign the adsorption site F in K-ZK-5

At the loading amounts of CO₂ in our diffraction experiments, the total numbers of CO₂ molecules site B in γ -cages is less than or roughly equal to the number of opened flat and puckered 8MRs. Therefore, we have not yet observed the temporary deviation of K⁺ from the center of 8MR to allow CO₂ molecules as described as ‘trap-door’ mechanism [28]. Higher loading of CO₂ on K-ZK-5 leads to

highly disordered arrangement of CO₂ in the zeolite cages and we would not be able to locate the adsorption sites by X-ray diffraction.

5.3.8 Discussions on the adsorption heats and adsorption capacities

Mg²⁺ cations situate at the center of the hexagonal prism, which is not accessible to the adsorbate molecules. Moreover, Mg²⁺ was not fully exchanged and the electric field created by the cation is highly shielded by 6 framework oxygens. Therefore, dispersion interaction is the major contribution to the total adsorption energy in Mg-ZK-5 and this explains for the very low adsorption heats of CO₂ on Mg-ZK-5 compared to other adsorbents. Upon the adsorption, Mg²⁺ partially moved out of the center of D6R to increase the electrostatic interaction by forming a complex with CO₂ molecules. The increase in the electrostatic interaction is compensated by the loss of energy by migrating Mg²⁺ out of its stable position. Therefore, the adsorption heats are almost constant over CO₂ coverage and close to the values of adsorption heats reported for siliceous zeolites [23]. The interaction of CO₂-cation and the electric field created by cations are in the same order as the hardness of monovalent cations (Li⁺>Na⁺>K⁺). Experimental and DFT calculation studied by Cejka *et al.* in Na-, K-FER also indicated the higher adsorption heat of Na-FER in the case of dual-cation sites [101]. Besides, there are much less close contacts of oxygen atoms of CO₂ sites with framework oxygens in the case of K⁺, indicating lower dispersion energy in K-ZK-5 compared to Li-, Na-ZK-5. This explained for the highest adsorption energy in Na-ZK-5, and lowest in K-ZK-5 at low CO₂ coverage. The number of CO₂ molecules at different adsorption sites in K-ZK-5 are similar with various loading amounts of CO₂ indicated a similar adsorption energy of these three adsorption sites. Therefore, the adsorption energy only changed slightly over loading amount of CO₂ and increase

slightly at high loading due to the contribution of CO₂-CO₂ interaction. On the other hand, neighboring molecules occupying site B and site A in Na-ZK-5 would point toward each other with the carbon, oxygen atoms at a very close distance (below 3 Å), indicating that adsorbate-adsorbate interactions between adjacent molecules will tend to be repulsive. Therefore, we observed a steep drop of the adsorption heats at high CO₂ loading amount in Na-ZK-5.

The motion of CO₂ molecules at room temperature (298 K) is higher than at low temperature (110 K), thus these two adsorption sites cannot be postulated within one *paulingite* cavity. It is therefore easy to understand why the adsorption capacity of CO₂ in Na-ZK-5 is much lower than Li-ZK-5 at high pressure. Cations Li⁺ and Mg²⁺ are located at the 6MR plane and center of the hexagonal prism, respectively, which do not occupy much pore volume of the ZK-5 framework, thus leave higher void pore volume to accommodate the adsorbate molecules. Up to 1 bar pressure we studied, the CO₂ capacity in Mg-ZK-5 is lowest due to its low adsorption heat, but the steepness of the isotherms (Figure 5.3) combining with the population of adsorption sites A, B, C in Mg-ZK-5 indicated that the saturation capacity in Mg-ZK-5 at very low temperature of high pressure is as high as Li-ZK-5. Saturation capacity of adsorption site B in K-ZK-5 is half of that of other adsorbents, and K⁺ site SIII also competes with adsorption site A, thus K-ZK-5 would display lowest saturation capacity among the ZK-5 adsorbents investigating. Overall, KFI-type zeolite containing 2 different cages has shown multiple adsorption sites in high structure order compared to one cage CHA-, RHO-, LTA-type zeolites[27, 46, 89, 105] with only 2 adsorption sites.

5.4 Conclusions

In conclusion, we have performed a detailed structural analysis of cation sites Li^+ , Na^+ , K^+ , Mg^{2+} and the major CO_2 adsorption sites in ZK-5 zeolite framework. Strong interaction of high density charge cation Mg^{2+} with negative framework oxygens leads to a shrinkage of the D6R, thus decrease the unit cell of Mg-ZK-5. Li-ZK-5 displayed the highest adsorption capacity at 1 bar pressure and highest theoretical saturation capacity according to the adsorption site distribution obtained from Rietveld refinements. At least 3 different adsorption sites of CO_2 at the flat 8MR, α -cage, γ -cage were elucidated in all different adsorbents. The X-ray diffraction data provides direct evidence for a slight migration of the extra-framework Li^+ and Mg^{2+} cations away from the D6R toward the α -cages upon the adsorption to form the complex with CO_2 molecules. The dual-cation site between two Na^+ cation SII and CO_2 in γ -cage leads to high adsorption heat at low coverage. The heats decrease more sharply compared to other zeolites when this site was close to saturated and slightly repulsively interact with CO_2 site A. The analysis of Fourier maps and high adsorption energy obtained from volumetric measurements of CO_2 on Na-ZK-5 indicated a slight bent configuration of CO_2 at this site. Similar adsorption energy of three adsorption sites in K-ZK-5 and an increase in adsorbate-adsorbate interactions leads to a slight increase in the adsorption heats with the increase of CO_2 coverage. Nitrogen showed high interaction with Li^+ at 6MR and replaced the weak CO_2 adsorption site C in the co-adsorption experiment of N_2 , CO_2 on Li-ZK-5. Our findings provided a molecule understanding of interactions between CO_2 and cations, ZK-5 zeolite frameworks, and useful information for further development of new zeolite adsorbents toward CO_2 adsorption-related applications.

REFERENCES

1. Boot-Handford, M.E., et al., *Carbon capture and storage update*. Energy & Environmental Science, 2014. **7**(1): p. 130-189.
2. Choi, S., J.H. Drese, and C.W. Jones, *Adsorbent Materials for Carbon Dioxide Capture from Large Anthropogenic Point Sources*. Chemsuschem, 2009. **2**(9): p. 796-854.
3. D'Alessandro, D.M., B. Smit, and J.R. Long, *Carbon Dioxide Capture: Prospects for New Materials*. Angewandte Chemie-International Edition, 2010. **49**(35): p. 6058-6082.
4. Hedin, N., L.J. Chen, and A. Laaksonen, *Sorbents for CO₂ capture from flue gas-aspects from materials and theoretical chemistry*. Nanoscale, 2010. **2**(10): p. 1819-1841.
5. Chiesa, P., S. Campanari, and G. Manzolini, *CO₂ cryogenic separation from combined cycles integrated with molten carbonate fuel cells*. International Journal of Hydrogen Energy, 2011. **36**(16): p. 10355-10365.
6. Bernardo, P., E. Drioli, and G. Golemme, *Membrane Gas Separation: A Review/State of the Art*. Industrial & Engineering Chemistry Research, 2009. **48**(10): p. 4638-4663.
7. Brunetti, A., et al., *Membrane technologies for CO₂ separation*. Journal of Membrane Science, 2010. **359**(1-2): p. 115-125.
8. Rees, N.V. and R.G. Compton, *Electrochemical CO₂ sequestration in ionic liquids; a perspective*. Energy & Environmental Science, 2011. **4**(2): p. 403-408.
9. Karadas, F., M. Atilhan, and S. Aparicio, *Review on the Use of Ionic Liquids (ILs) as Alternative Fluids for CO₂ Capture and Natural Gas Sweetening*. Energy & Fuels, 2010. **24**: p. 5817-5828.
10. Zhao, B.T., et al., *Post-combustion CO₂ capture by aqueous ammonia: A state-of-the-art review*. International Journal of Greenhouse Gas Control, 2012. **9**: p. 355-371.
11. Zhang, Z.J., et al., *MOFs for CO₂ capture and separation from flue gas mixtures: the effect of multifunctional sites on their adsorption capacity and selectivity*. Chemical Communications, 2013. **49**(7): p. 653-661.
12. Samanta, A., et al., *Post-Combustion CO₂ Capture Using Solid Sorbents: A Review*. Industrial & Engineering Chemistry Research, 2012. **51**(4): p. 1438-1463.
13. Guo, B., L. Chang, and K. Xie, *Adsorption of carbon dioxide on activated carbon*. J. Nat. Gas Chem., 2006. **15**(3): p. 223-229.

14. Huang, Y.-f., Z.-f. Ma, and H.-q. Yao, *Relation between adsorption of CO₂ on activated carbon and micropore volume*. *Ranliao Huaxue Xuebao*, 2008. **36**(3): p. 343-348.
15. Dzubak, A.L., et al., *Ab initio carbon capture in open-site metal-organic frameworks*. *Nature Chemistry*, 2012. **4**(10): p. 810-816.
16. Hasan, M.M.F., E.L. First, and C.A. Floudas, *Cost-effective CO₂ capture based on in silico screening of zeolites and process optimization*. *Physical Chemistry Chemical Physics*, 2013. **15**(40): p. 17601-17618.
17. Wilmer, C.E., et al., *Structure-property relationships of porous materials for carbon dioxide separation and capture*. *Energy & Environmental Science*, 2012. **5**(12): p. 9849-9856.
18. Kim, J., et al., *Predicting Large CO₂ Adsorption in Aluminosilicate Zeolites for Postcombustion Carbon Dioxide Capture*. *Journal of the American Chemical Society*, 2012. **134**(46): p. 18940-18943.
19. Lin, L.C., et al., *In silico screening of carbon-capture materials*. *Nature Materials*, 2012. **11**(7): p. 633-641.
20. Banerjee, R., et al., *High-throughput synthesis of zeolitic imidazolate frameworks and application to CO₂ capture*. *Science*, 2008. **319**(5865): p. 939-943.
21. Wang, B., et al., *Colossal cages in zeolitic imidazolate frameworks as selective carbon dioxide reservoirs*. *Nature*, 2008. **453**(7192): p. 207-U6.
22. Radosz, M., et al., *Flue-gas carbon capture on carbonaceous sorbents: Toward a low-cost multifunctional Carbon Filter for "Green" energy producers*. *Industrial & Engineering Chemistry Research*, 2008. **47**(10): p. 3783-3794.
23. Fischer, M. and R.G. Bell, *Identifying Promising Zeolite Frameworks for Separation Applications: A Building-Block-Based Approach*. *Journal of Physical Chemistry C*, 2013. **117**(33): p. 17099-17110.
24. Wu, D., et al., *Revealing the Structure-Property Relationships of Metal-Organic Frameworks for CO₂ Capture from Flue Gas*. *Langmuir*, 2012. **28**(33): p. 12094-12099.
25. Liu, Q.L., et al., *NaKA sorbents with high CO₂-over-N₂ selectivity and high capacity to adsorb CO₂*. *Chemical Communications*, 2010. **46**(25): p. 4502-4504.
26. Palomino, M., et al., *Zeolite Rho: a highly selective adsorbent for CO₂/CH₄ separation induced by a structural phase modification*. *Chemical Communications*, 2012. **48**(2): p. 215-217.
27. Lozinska, M.M., et al., *Cation Gating and Relocation during the Highly Selective "Trapdoor" Adsorption of CO₂ on Univalent Cation Forms of Zeolite Rho*. *Chem. Mater.*, 2014. **26**(6): p. 2052-2061.
28. Shang, J., et al., *Discriminative Separation of Gases by a "Molecular Trapdoor" Mechanism in Chabazite Zeolites*. *Journal of the American Chemical Society*, 2012. **134**(46): p. 19246-19253.

29. Davis, R.J., E.J. Dосkocil, and S. Bordawekar, *Structure/function relationships for basic zeolite catalysts containing occluded alkali species*. Catalysis Today, 2000. **62**(2-3): p. 241-247.
30. Martra, G., et al., *Alkali and alkaline-earth exchanged faujasites: strength of Lewis base and acid centres and cation site occupancy in Na- and BaY and Na- and BaX zeolites*. Catalysis Today, 2002. **73**(1-2): p. 83-93.
31. Waghmode, S.B., et al., *Physicochemical investigations of the basicity of the cation exchanged ETS-10 molecular sieves*. Journal of Physical Chemistry B, 2003. **107**(33): p. 8517-8523.
32. Knozinger, H. and S. Huber, *IR spectroscopy of small and weakly interacting molecular probes for acidic and basic zeolites*. Journal of the Chemical Society-Faraday Transactions, 1998. **94**(15): p. 2047-2059.
33. Walton, K.S., M.B. Abney, and M.D. LeVan, *CO₂ adsorption in Y and X zeolites modified by alkali metal cation exchange*. Microporous and Mesoporous Materials, 2006. **91**(1-3): p. 78-84.
34. Pirngruber, G.D., et al., *The role of the extra-framework cations in the adsorption of CO₂ on faujasite Y*. Physical Chemistry Chemical Physics, 2010. **12**(41): p. 13534-13546.
35. Park, H.J., Y.E. Cheon, and M.P. Suh, *Post-Synthetic Reversible Incorporation of Organic Linkers into Porous Metal-Organic Frameworks through Single-Crystal-to-Single-Crystal Transformations and Modification of Gas-Sorption Properties*. Chemistry-a European Journal, 2010. **16**(38): p. 11662-11669.
36. Garcia-Ricard, O.J. and A.J. Hernandez-Maldonado, *Cu-2(pyrazine-2,3-dicarboxylate)(2)(4,4'-bipyridine) Porous Coordination Sorbents: Activation Temperature, Textural Properties, and CO₂ Adsorption at Low Pressure Range*. Journal of Physical Chemistry C, 2010. **114**(4): p. 1827-1834.
37. Prasad, T.K., D.H. Hong, and M.P. Suh, *High Gas Sorption and Metal-Ion Exchange of Microporous Metal-Organic Frameworks with Incorporated Imide Groups*. Chemistry-a European Journal, 2010. **16**(47): p. 14043-14050.
38. Demessence, A., et al., *Strong CO₂ Binding in a Water-Stable, Triazolate-Bridged Metal-Organic Framework Functionalized with Ethylenediamine*. Journal of the American Chemical Society, 2009. **131**(25): p. 8784-+.
39. Britt, D., et al., *Highly efficient separation of carbon dioxide by a metal-organic framework replete with open metal sites*. Proceedings of the National Academy of Sciences of the United States of America, 2009. **106**(49): p. 20637-20640.
40. Liu, Y.Y., Z.Y.U. Wang, and H.C. Zhou, *Recent advances in carbon dioxide capture with metal-organic frameworks*. Greenhouse Gases-Science and Technology, 2012. **2**(4): p. 239-259.
41. Sumida, K., et al., *Carbon Dioxide Capture in Metal-Organic Frameworks*. Chemical Reviews, 2012. **112**(2): p. 724-781.
42. Siriwardane, R.V., et al., *Adsorption of CO₂ on molecular sieves and activated carbon*. Energy & Fuels, 2001. **15**(2): p. 279-284.

43. Chue, K.T., et al., *Comparison of Activated Carbon and Zeolite 13x for CO₂ Recovery from Flue-Gas by Pressure Swing Adsorption*. Industrial & Engineering Chemistry Research, 1995. **34**(2): p. 591-598.
44. Palomino, M., et al., *New Insights on CO₂-Methane Separation Using LTA Zeolites with Different Si/Al Ratios and a First Comparison with MOFs*. Langmuir, 2010. **26**(3): p. 1910-1917.
45. Miyamoto, M., Y. Fujioka, and K. Yogo, *Pure silica CHA type zeolite for CO₂ separation using pressure swing adsorption at high pressure*. Journal of Materials Chemistry, 2012. **22**(38): p. 20186-20189.
46. Hudson, M.R., et al., *Unconventional, Highly Selective CO₂ Adsorption in Zeolite SSZ-13*. Journal of the American Chemical Society, 2012. **134**(4): p. 1970-1973.
47. Pham, T.D., Q.L. Liu, and R.F. Lobo, *Carbon Dioxide and Nitrogen Adsorption on Cation-Exchanged SSZ-13 Zeolites*. Langmuir, 2013. **29**(2): p. 832-839.
48. Liu, Q.L., et al., *ZK-5: A CO₂-Selective Zeolite with High Working Capacity at Ambient Temperature and Pressure*. Chemsuschem, 2012. **5**(11): p. 2237-2242.
49. Remy, T., et al., *Adsorption and Separation of CO₂ on KFI Zeolites: Effect of Cation Type and Si/Al Ratio on Equilibrium and Kinetic Properties*. Langmuir, 2013. **29**(16): p. 4998-5012.
50. Yang, J., et al., *Experiments and simulations on separating a CO₂/CH₄ mixture using K-KFI at low and high pressures*. Microporous Mesoporous Mater., 2014. **184**: p. 21-27.
51. Shannon, R.D., et al., *Selective Synthesis of Dimethylamine over Small-Pore Zeolites .3. H-Zk-5*. Journal of Catalysis, 1989. **115**(1): p. 79-85.
52. Reichinger, M., G. Maletz, and K. Eisert, *Copper-containing zeolite of KFI-type and its use in SCR catalysis*. 2011, Sued-Chemie AG, Germany . p. 43pp.; Chemical Indexing Equivalent to 155:250091 (DE).
53. van Well, W.J.M., et al., *Adsorption of linear alkanes in the alpha-cages and gamma-cages of H-ZK-5 and K-ZK-5*. Journal of Physical Chemistry B, 1999. **103**(11): p. 1841-1853.
54. Janchen, J., et al., *Adsorption of water, methanol and acetonitrile in ZK-5 investigated by temperature programmed desorption, microcalorimetry and FTIR*. Thermochimica Acta, 2001. **379**(1-2): p. 213-225.
55. Kerr, G.T., *Zeolite Zk-5 - a New Molecular Sieve*. Science, 1963. **140**(357): p. 1412-&.
56. Foster, M.D., et al., *A geometric solution to the largest-free-sphere problem in zeolite frameworks*. Microporous and Mesoporous Materials, 2006. **90**(1-3): p. 32-38.
57. Abrams, L. and D.R. Corbin, *PROBING INTRAZEOLITE SPACE*. Journal of Inclusion Phenomena and Molecular Recognition in Chemistry, 1995. **21**(1-4): p. 1-46.

58. Chatelain, T., et al., *Synthesis and characterization of 18-crown-6 ether-containing KFI-type zeolite*. Zeolites, 1996. **17**(4): p. 328-333.
59. Dreele, A.C.L.a.R.B.V., *General Structure Analysis System (GSAS)*. Los Alamos National Laboratory Report LAUR 1994: p. 86-748.
60. Toby, B., *EXPGUI, a graphical user interface for GSAS*. Journal of Applied Crystallography, 2001. **34**(2): p. 210-213.
61. Momma, K. and F. Izumi, *VESTA 3 for three-dimensional visualization of crystal, volumetric and morphology data*. Journal of Applied Crystallography, 2011. **44**(6): p. 1272-1276.
62. Trong D. Pham, M.R.H., Craig M. Brown, and Raul F. Lobo, *The Molecular Basis for the High CO₂ Adsorption Capacity of Chabazite Zeolites*. Chemsuschem, submitted, 2014.
63. Zukal, A., et al., *Adsorption of Carbon Dioxide on Sodium and Potassium Forms of STI Zeolite*. Chempluschem, 2012. **77**(8): p. 675-681.
64. McCusker, C.B.a.L.B., *Database of Zeolite Structures*. <http://www.iza-structure.org/databases/>.
65. Frising, T. and P. Leflaive, *Extraframework cation distributions in X and Y faujasite zeolites: A review*. Microporous and Mesoporous Materials, 2008. **114**(1-3): p. 27-63.
66. Lievens, J.L., J.P. Verduijn, and W.J. Mortier, *Cation Site Energies in Dehydrated Kfl-Type Zeolites - D-Nakfl, D-Nahkfl, and D-Kkfl*. Zeolites, 1992. **12**(6): p. 690-697.
67. Barrett, P.A., S. Valencia, and M.A. Cambor, *Synthesis of a merlinoite-type zeolite with an enhanced Si/Al ratio via pore filling with tetraethylammonium cations*. Journal of Materials Chemistry, 1998. **8**(10): p. 2263-2268.
68. Skofteland, B.M., O.H. Ellestad, and K.P. Lillerud, *Potassium merlinoite: crystallization, structural and thermal properties*. Microporous and Mesoporous Materials, 2001. **43**(1): p. 61-71.
69. Parise, J.B., et al., *The Crystal-Structures of the Synthetic Zeolites (Cs,K)-Zk5 and (Cs,D)-Zk5 Determined from Neutron Powder Diffraction Data*. Zeitschrift Fur Kristallographie, 1983. **165**(1-4): p. 175-190.
70. Nenoff, T.M., et al., *Structural Characterization of a Dehydrated Magnesium Sodium Beryllophosphate Faujasite Phase*. Zeolites, 1992. **12**(7): p. 770-775.
71. Yeom, Y.H., et al., *Three crystal structures of vacuum-dehydrated zeolite X, M₄₆Si₁₀₀Al₉₂O₃₈₄, M=Mg²⁺, Ca²⁺, and Ba²⁺*. Journal of Physical Chemistry B, 1997. **101**(35): p. 6914-6920.
72. Shannon, R.D., *Revised Effective Ionic-Radii and Systematic Studies of Interatomic Distances in Halides and Chalcogenides*. Acta Crystallographica Section A, 1976. **32**(Sep1): p. 751-767.
73. Smith, J.V. and S.W. Bailey, *Second Review of Al-O and Si-O Tetrahedral Distances*. Acta Crystallographica, 1963. **16**(8): p. 801-&.

74. Liebau, F., *Untersuchungen an Schichtsilikaten Des Formeltyps $Am(Si_2O_5)_N$. I. Die Kristallstruktur Der Zimmertemperatuuform Des $Li_2Si_2O_5$* . Acta Crystallographica, 1961. **14**(4): p. 389-395.
75. Olson, D.H., *The Crystal-Structure of Dehydrated Nax. Zeolites*, 1995. **15**(5): p. 439-443.
76. Mortier, W.J., H.J. Bosmans, and J.B. Uytterhoeven, *Location of univalent cations in synthetic zeolites of the Y and X type with varying silicon to aluminum ratio. II. Dehydrated potassium exchanged forms*. The Journal of Physical Chemistry, 1972. **76**(5): p. 650-656.
77. Woodcock, D.A., et al., *Negative thermal expansion in the siliceous zeolites chabazite and ITQ-4: A neutron powder diffraction study*. Chemistry of Materials, 1999. **11**(9): p. 2508-2514.
78. Simon, A. and K. Peters, *Single-Crystal Refinement of the Structure of Carbon-Dioxide*. Acta Crystallographica Section B-Structural Science, 1980. **36**(Nov): p. 2750-2751.
79. Queen, W.L., et al., *Site-Specific CO₂ Adsorption and Zero Thermal Expansion in an An isotropic Pore Network*. Journal of Physical Chemistry C, 2011. **115**(50): p. 24915-24919.
80. Valenzano, L., et al., *Computational and Experimental Studies on the Adsorption of CO, N₂, and CO₂ on Mg-MOF-74*. Journal of Physical Chemistry C, 2010. **114**(25): p. 11185-11191.
81. Ramsahye, N.A. and R.G. Bell, *Cation mobility and the sorption of chloroform in zeolite NaY: Molecular dynamics study*. Journal of Physical Chemistry B, 2005. **109**(10): p. 4738-4747.
82. Naccache, C. and Y.B. Taarit, *ESR STUDY OF COPPER(II) IONS IN Y ZEOLITE - EFFECT OF WATER, AMMONIA AND PYRIDINE ADSORPTION*. Chemistry and Physics of Lipids, 1971. **11**(1): p. 11-&.
83. Gallezot, P., Y.B. Taarit, and B. Imelik, *X-RAY-DIFFRACTION STUDY OF CUPRIC ION MIGRATIONS IN 2 Y-TYPE ZEOLITES CONTAINING ADSORBED REAGENTS*. Journal of Catalysis, 1972. **26**(3): p. 295-&.
84. Yu, J.S. and L. Kevan, *TEMPERATURE-DEPENDENCE OF COPPER(II) MIGRATION AND FORMATION OF NEW COPPER(II) SPECIES DURING CATALYTIC PROPYLENE OXIDATION ON COPPER(II)-EXCHANGED Y-ZEOLITE AND COMPARISON WITH X-ZEOLITE*. Journal of Physical Chemistry, 1990. **94**(19): p. 7612-7620.
85. Palomino, G.T., et al., *XRD, XAS, and IR characterization of copper-exchanged Y zeolite*. Journal of Physical Chemistry B, 2000. **104**(36): p. 8641-8651.
86. Zema, M., S.C. Tarantino, and G. Montagna, *Hydration/dehydration and cation migration processes at high temperature in zeolite chabazite*. Chemistry of Materials, 2008. **20**(18): p. 5876-5887.

87. Plant, D.F., et al., *Molecular dynamics simulation of the cation motion upon adsorption of CO₂ in faujasite zeolite systems*. Journal of Physical Chemistry B, 2006. **110**(29): p. 14372-14378.
88. Plant, D., et al., *CO₂ diffusivity in LiY and NaY faujasite systems: A combination of molecular dynamics simulations and quasi-elastic neutron scattering experiments*. Adsorption-Journal of the International Adsorption Society, 2007. **13**(3-4): p. 209-214.
89. Bae, T.-H., et al., *Evaluation of cation-exchanged zeolite adsorbents for post-combustion carbon dioxide capture*. Energy & Environmental Science, 2013. **6**(1): p. 128-138.
90. Gaffney, T.R., *Porous solids for air separation*. Current Opinion in Solid State & Materials Science, 1996. **1**(1): p. 69-75.
91. Charles G. Coe, J.F.K., Ronald Pierantozzi, Thomas R. White, *Divalent cation exchanged lithium X-zeolite for nitrogen adsorption*, in US Patents. 1995, Air Products And Chemicals, Inc.: US.
92. Plevart, J., et al., *Structure of dehydrated zeolite Li-LSX by neutron diffraction: Evidence for a low-temperature orthorhombic faujasite*. Journal of Physical Chemistry B, 1997. **101**(49): p. 10340-10346.
93. Feuerstein, M. and R.F. Lobo, *Characterization of Li cations in zeolite LiX by solid-state NMR spectroscopy and neutron diffraction*. Chemistry of Materials, 1998. **10**(8): p. 2197-2204.
94. Jale, S.R., et al., *Monte Carlo simulation of sorption equilibria for nitrogen and oxygen on LiLSX zeolite*. Journal of Physical Chemistry B, 2000. **104**(22): p. 5272-5280.
95. Kazansky, V.B., M. Bulow, and E. Tichomirova, *Specific sorption sites for nitrogen in zeolites NaLSX and LiLSX*. Adsorption-Journal of the International Adsorption Society, 2001. **7**(4): p. 291-299.
96. Feuerstein, M., R.J. Accardi, and R.J. Lobo, *Adsorption of nitrogen and oxygen in the zeolites LiA and LiX investigated by Li-6 and Li-7 MAS NMR spectroscopy*. Journal of Physical Chemistry B, 2000. **104**(44): p. 10282-10287.
97. Bloch, E.D., et al., *Selective Binding of O₂ over N₂ in a Redox-Active Metal-Organic Framework with Open Iron(II) Coordination Sites*. Journal of the American Chemical Society, 2011. **133**(37): p. 14814-14822.
98. Jasra, R.V., N.V. Choudary, and S.G.T. Bhat, *Correlation of sorption behavior of nitrogen, oxygen, and argon with cation locations in zeolite X*. Industrial & Engineering Chemistry Research, 1996. **35**(11): p. 4221-4229.
99. Pillai, R.S., S.A. Peter, and R.V. Jasra, *Correlation of sorption behavior of nitrogen, oxygen, and argon with Ca²⁺ locations in zeolite a: a grand canonical Monte Carlo simulation study*. Langmuir, 2007. **23**(17): p. 8899-908.

100. Nachtigallova, D., et al., *The vibrational dynamics of carbon monoxide in a confined space - CO in zeolites*. Physical Chemistry Chemical Physics, 2006. **8**(42): p. 4849-4852.
101. Zukal, A., et al., *Experimental and theoretical determination of adsorption heats of CO₂ over alkali metal exchanged ferrierites with different Si/Al ratio*. Physical Chemistry Chemical Physics, 2010. **12**(24): p. 6413-6422.
102. Wu, H., et al., *Adsorption Sites and Binding Nature of CO₂ in Prototypical Metal-Organic Frameworks: A Combined Neutron Diffraction and First-Principles Study*. Journal of Physical Chemistry Letters, 2010. **1**(13): p. 1946-1951.
103. Nachtigall, P., et al., *The nature of cationic adsorption sites in alkaline zeolites-single, dual and multiple cation sites*. Physical Chemistry Chemical Physics, 2012. **14**(5): p. 1552-1569.
104. Areal, C.O., et al., *Variable-Temperature IR Spectroscopic and Theoretical Studies on CO₂ Adsorbed in Zeolite K-FER*. Chemphyschem, 2011. **12**(8): p. 1435-1443.
105. Lozinska, M.M., et al., *Understanding Carbon Dioxide Adsorption on Univalent Cation Forms of the Flexible Zeolite Rho at Conditions Relevant to Carbon Capture from Flue Gases*. Journal of the American Chemical Society, 2012. **134**(42): p. 17628-17642.

Chapter 6

EXPERIMENTAL AND COMPUTATIONAL STUDIES ON THE ADSORPTION OF CO₂ AND N₂ ON PURE SILICA ZEOLITES

6.1 Introduction

The atmospheric emission of anthropogenic carbon dioxide due to the burning of fossil fuels is one of the main causes of climate change [1]. In response to this problem there have been many studies of materials capable of selectively adsorbing CO₂ over other gas molecules [2-4]. Zeolites are used extensively as catalysts and adsorbents in many petroleum and chemical processes, and are effective materials for the selective adsorption and separation of carbon dioxide [5, 6]. Unfortunately the presence of polar molecules in flue gas streams, such as water, inhibits the CO₂ adsorption on diverse cationic forms of hydrophilic zeolites such as Li, Na-LSX, 13X, Na-Y, 4A [7]. This is because the energy of interaction of water with extra-framework cations is high and water then competes successfully for the strong adsorption sites of CO₂. Consequently, for these polar zeolitic materials a gas-drying step would be required before adsorptive CO₂ flue gas separation processes, increasing costs and reducing the commercial feasibility of this technology. Also, zeolites with high affinity for CO₂ hinder its desorption even at low pressure, requiring high temperatures for desorption and increasing energy consumption [7, 8].

Pure silica zeolites (PSZ) are hydrophobic and could be used to overcome the limits imposed by the competitive adsorption of water on hydrophilic zeolites containing high concentrations of cations. Purely siliceous zeolites, all polymorphs of

SiO₂, do not occur naturally and can be difficult to prepare in the laboratory. Cambor et al.[9-11] and Patarin[12] have demonstrated that preparing all-silica zeolite phases in fluoride media produces materials with fewer internal silanol/siloxy defects than those prepared in a hydroxide solution. The resulting materials are highly hydrophobic and could potentially be used for the selective adsorption of carbon dioxide from nitrogen in a water-containing stream.

Here a series of all-silica zeolites of framework types CHA, FER, MFI, STT, and BEA* have been prepared in fluoride media to obtain materials with a low defect density and high hydrophobic/organophilic character. Zeolite beta (BEA*), a disordered zeolite (an intergrowth of two pure polytypes A and B), has a three-dimensional structure composed of pores of 6.6 nm x 6.7 nm and 5.6 nm x 5.6 nm [13, 14]. Chabazite (CHA) contains large ellipsoidal cavities with internal dimensions of about 0.67 nm x 1.00 nm interconnected through six 8-membered ring windows [15, 16]. Ferrierite (FER) is traversed by two types of intersecting channels, one along the [001] direction with 10-membered ring straight channel (0.54 x 0.42 nm) and the other parallel to the [010] direction with pockets connected by 8-membered rings (0.35 x 0.48 nm) [17, 18]. Silicalite-1 (MFI) zeolite has a pore structure composed of 10-membered ring straight channels (0.56 nm x 0.53 nm) and 10-membered ring zigzag channels with windows of dimensions 0.51 x 0.55 nm [19, 20]. All PSZ zeolites have three dimensional networks, except SSZ-23 (STT), a peculiar zeolite containing two-dimensional arrays of cages with molecular access between the cages in the planes being restricted by seven (0.25 x 0.35 nm) and nine (0.38 x 0.54 nm) member-ring windows [21, 22].

Molecular simulation methods, such as Grand Canonical Monte Carlo (GCMC) and molecular dynamics (MD), are playing an important role in developing our understanding of the relation between microscopic and macroscopic properties of molecular fluids confined in zeolites, and are being used to generate adsorption isotherms for gases on microporous solid adsorbents [23-26]. Researchers have studied extensively CO₂ adsorption in various zeolites using molecular simulations. For example, Makrodimitris *et al.*[27] investigated the adsorption and diffusion of CO₂ and N₂ in silicalite and the Sholl group [28, 29] studied the adsorption and diffusion of CO₂ and N₂ in three all-silica zeolites (silicalite, ITQ-3, and ITQ-7). Liu and Smit [30] evaluated the separation performance of ZIF-68 and ZIF-69 for CO₂/N₂ mixtures. Computational investigations of CO₂ adsorption have also been performed [1, 5, 26, 31-35]. In this work, grand canonical Monte Carlo (GCMC) simulations have been used for predicting single adsorption isotherms and heats of adsorption of CO₂ and N₂ on these siliceous zeolites. The results are compared with the measurements we have made.

6.2 Methods

6.2.1 Experimental Section

Materials Synthesis

Reagents: Tetraethylammonium hydroxide (TEAOH, Alfa Aesar, 35% wt aqueous solution), tetraethylorthosilicate (TEOS, Sigma, 98% wt), HF (Sigma, 48% wt), *N,N,N*-trimethyladamantammonium hydroxide (TMAdaOH, 25% wt aqueous solution, Sachem), HF/Pyr (70% wt HF, Sigma), tetrapropylammonium hydroxide

(TPAOH; 40% wt, Sachem), *n*-propylamine (PrNH₂, 98% wt, Sigma), pyridine (Pyr, 99.8% wt, Sigma), ethanol (Fisher, >99% wt).

Pure silica zeolite beta [36]: 10.27 g of TEOAH, 0.32 g of deionized water and 9.41 g TEOS, were mixed overnight in a plastic vessel at room temperature to allow hydrolysis of TEOS. Then the mixture was heated to evaporate the ethanol (8.4 g), followed by the addition of 1.02 g of HF to form a white solid paste. The final mixture with the composition SiO₂ : 7.25 H₂O : 0.54 TEOAH : 0.54 HF was kept at 423 K for 14 days under rotation.

Pure silica chabazite [37]: 11.8 g of TEOS was hydrolyzed in 23.9 g of TMAdaOH and heated to remove the ethanol and water (23.8 g in total). Then 1.2 g of HF was added to the mixture to produce the final composition of 3 H₂O : 1 SiO₂ : 0.5 TMAdaOH : 0.5 HF. This thick paste was homogenized by hand in a Teflon container, and transferred to a 23 mL Teflon-lined stainless steel autoclave (Parr). The autoclave was kept at 423 K with rotation (~ 40 rpm) for 48 hours in a convection oven.

Siliceous ferrierite [38]: Appropriate amounts of pyridine (23.3 g), HF/Pyr (1.05 g), PrNH₂ (8.7 g), and distilled water (1.32 g) were mixed in the order into a plastic vessel and stirred until a clear solution was formed. Then Cabosil M-5 silica (1.66 g) was added to the solution under vigorous stirring to form a uniform mixture. The molar ratios in the synthesis mixture were 1.5 SiO₂ : 2HF/Pyr : 4 H₂O : 8 PrNH₂ : 16 Pyr. After mixing for 30 min, the mixture was transferred to a Teflon-lined stainless steel autoclave (Paar) and heat treated in an oven at 453 K for 7 days.

Silicalite-1 [14]:

Hydroxide medium (MFI-OH): The PSZ silicalite-1 (MFI) nanoparticles were prepared by adding 7.5 g of TPAOH to a mixture of 9.2 g of TEOS, 8.9 g of ethanol

and 9.4 g of water at room temperature with vigorous stirring. After hydrolysis of the TEOS, a clear homogeneous solution was formed with the following molar composition: 1 TPAOH : 3 SiO₂ : 52.4 H₂O : 13.1 EtOH. The solution was aged at room temperature for 1 day with stirring and then kept in a Teflon-lined autoclave at 393 K for 5 days. Note that this is the only sample prepared in the absence of HF.

Fluoride medium (MFI): Silicalite-1 in HF media was prepared by mixing 1.85 g Cabosil M-5 with 6.89 g TPAOH and 23.6 g H₂O under stirring for 1 hour, and then HF (0.65 g) was added to the mixture. The final gel composition of 50 H₂O: 0.44 TPAOH: 1 SiO₂: 0.5 HF was placed in Teflon-lined autoclave at 448 K in 5 days.

SSZ-23 [21]: The synthesis of siliceous SSZ-23 followed the preparation method of siliceous chabazite with a gel composition of 1 SiO₂:0.50 TMAOH : 0.50 HF : 15 H₂O. The mixture was heated at 423 K under rotation for 30 days in a Teflon-lined stainless steel reactor. By using the same SDA, but increasing the water content, a higher framework density (FD) material (FD_{STT}=17T/nm³, FD_{CHA}=15.1T/nm³) is formed.

To obtain the powder product, the autoclaves were cooled to room temperature in air and the crystalline product was recovered by filtration, washed several times with deionized water and dried at 353 K overnight in a drying oven. In the last step, the as-made samples were calcined at 823 K for 8 hours in an air furnace after heating at a ramping rate of 3 K/minute. The only exception is FER that was calcined at 1123 K in air for 16 hours.

Analytical Section

The Scanning Electron Microscopy (SEM) images of the pure silica zeolites were obtained using a JEOL JSM7400F microscope, operating at an acceleration

voltage of 3 keV, and a current of 10 μ A. The X-Ray Powder Diffraction (XRD) patterns were collected at room temperature on a Philips X'Pert Panalytical powder diffractometer using Cu K α radiation ($\lambda=1.5418$ Å). The data were collected in a stepwise fashion with 2θ ranging from 5.0° to 50.0° with a step size of 0.02° and 2 s per step. The micropore volume and surface area of the PSZ were measured using N₂ at 77 K with a Micromeritics ASAP 2020 device. The CO₂ and N₂ adsorption isotherms on the PSZ samples at different temperatures (273 K, 303 K and 343 K) up to the ambient pressure were also measured on this instrument. Before the adsorption measurements each sample was degased at a temperature of 623 K for 6 h.

²⁹Si MAS NMR: ²⁹Si magic angle spinning nuclear magnetic resonance (MAS NMR) spectra were recorded on a Bruker AVIII-500 solid-state NMR spectrometer, operating at a Larmor frequency of 500.138 MHz for ¹H and 99.362 MHz for ²⁹Si. A 4 mm HX MAS probe was used for all measurements. All spectra were recorded at a MAS frequency of 10 kHz, controlled to with +/- 2Hz using a Bruker MAS controller. ²⁹Si single pulse and cross polarization (CP) measurements have been performed on each sample. For ²⁹Si single pulse MAS experiments, a 90° pulse with a width of 4.3 μ s was used and the recycle delay was 30 s. For {¹H}-²⁹Si CP MAS experiments, ¹H 90° pulse duration was 2.5 μ s, a linear amplitude ramp (80-100%) on ¹H was used with a contact time of 4.5 ms, and the recycle delay was 5 s. SPINAL64 1H decoupling with rf field strength of 100 kHz was applied during the acquisition period for both SP and CP MAS measurements.

6.2.2 Simulations

The zeolites were treated as having a rigid framework with atomic positions fixed by using the X-ray diffraction data from the existing literature as described

below. The diffraction patterns were similar to those determined for our samples with the exception of zeolite beta.

The crystallographic atomic positions of pure silica chabazite were taken from the report of Diaz-Cabanas *et al.* [37]. The chabazite framework is constructed of eight double 6-member rings (D6R units) joined together by 4-member rings enclosing ellipsoidal cavities. Each cavity is linked, in the three orthogonal directions, to neighboring cavities by six 8-member ring windows. The unit cell has 36 Si atoms and 72 O atoms, and the lattice constants are $a = 13.5292 \text{ \AA}$, and $c = 14.7483 \text{ \AA}$ with space group $R3m$. The crystallographic atomic positions of siliceous ferrierite were taken from Morris *et al.* [38]. The framework has an orthorhombic unit cell of composition $\text{Si}_{36}\text{O}_{72}$. The lattice constants are $a = 18.7202 \text{ \AA}$, $b = 14.0703 \text{ \AA}$, and $c = 7.4197 \text{ \AA}$.

The crystallographic atomic positions of silicalite-1 were taken from Olson *et al.* [20]. Silicalite-1 has three distinct crystal forms: the monoclinic, Pnma and $\text{P}2_12_12_1$ orthorhombic structures. The diffraction pattern of our samples was indexed in the Pnma orthorhombic space group, which is what was used in our simulations. The unit cell has a composition of $\text{Si}_{96}\text{O}_{192}$, and the lattice constants are $a = 20.07 \text{ \AA}$, $b = 19.92 \text{ \AA}$, and $c = 13.42 \text{ \AA}$.

The structure of SSZ-23, taken from Cambor *et al.* [21], is a STT-type zeolite that contains channels bounded by seven and nine tetrahedral atom windows. The unit cell consists of 64 Si atoms and 128 O atoms, and the unit cell lattice constants used are $a = 13.0899 \text{ \AA}$, $b = 21.6701 \text{ \AA}$, $c = 13.7347 \text{ \AA}$, and $\beta = 102.578^\circ$ with space group $\text{P}2_1/\text{N}$.

Zeolite beta is an intergrowth of two polymorphs. Polymorph A has space group $\text{P}4_122$ or $\text{P}4_322$, while the space group of polymorph B is $\text{C}2/\text{c}$. In both

polymorphs, the 12-membered rings pore structure is three-dimensional, with two straight channels, each with a cross-section of approximately 6.7 Å, parallel to the [1 0 0] and the [0 1 0] directions and a tortuous channel of 5.6 Å along the [0 0 1] direction. The latter is formed by the intersections of the two linear channel systems. The x-ray diffraction patterns of our samples are typical of the disordered forms of zeolite beta, that is, an intergrowth of polymorphs A and B, so in our simulations we used both polymorphs A and B. The crystallographic atomic positions of these polymorphs were taken from Newsam *et al.*[39] and Corma *et al.*[40], respectively.

Carbon dioxide (CO₂) was modeled as a rigid linear triatomic molecule. The force field was taken from Harris and Yung [41], which is an elementary physical model (EPM) fitted to the experimental vapor-liquid equilibrium data of bulk CO₂. The partial charge on the C atom is 0.6512 e, and the partial charge on O atom is -0.3256 e. The CO bond length is 1.149 Å, and the O-C-O bond angle is 180°. Nitrogen (N₂) was modeled as a rigid diatomic molecule. The Lennard-Jones (LJ) potential parameters used are those fitted by Murthy *et al.*[42] The N₂ molecule is assigned a negative charge q_N on each N atom, and a positive charge $-2q_N$ at its center-of-mass to maintain electroneutrality. The partial charge of $q_N = -0.482e$ is used to reproduce the measured N₂ gas-phase quadrupole moment [43]. The zeolite and the adsorbates are assumed to interact through a pairwise-additive potential between atoms of the adsorbed molecules and atoms of the zeolite lattice. The site-site interactions were modeled with a 12-6 LJ plus Columbic point-charge potential. We have used the parameters of model LJCB.JBTLC reported by Makrodimitris *et al.*[27] as it was successful in reproducing experimental isotherms for CO₂ and N₂ on silicalite-1 at room temperature. For screening purposes, we assumed the potential parameters can

be transferred directly to model the same molecules adsorbed in other zeolites. All the site-site interaction potential parameters are listed in Table 6.1.

Table 6.1. LJ and Coulombic Potential Parameters. LJ parameters for the unlike-pair interactions are calculated with Lorentz-Berthelot combining rules.

Adsorbate/adsorbent	Site	σ (Å)	ϵ/k_B (K)	q (e)
CO ₂	C	2.757	28.129	0.6512
	O	3.033	80.507	-0.3256
N ₂	N	3.32	36.4	-0.482
	CofM*	0.0	0.0	0.964
Zeolites	Si	0.0	0.0	2.0
	O	2.806	89.6	-1.0

*CofM site is the charge placed on the center of mass position of N₂ molecule to neutralize the total charge of the molecule

The adsorption isotherms of CO₂ and N₂ in the above five all-silica zeolites were determined using the Grand Canonical Monte Carlo (GCMC) simulation method [44]. The imposed chemical potential is related to the fugacity and in general can be computed from an equation of state. However, the gas phase was treated as an ideal gas here, as the pressures considered were relatively low. We varied the number of unit cells of the zeolite frameworks in each simulation to ensure that the average loading was at least or greater than 50 molecules so that we could obtain statistically reliable results.

We performed GCMC simulations with four types of moves: (1) molecular translation based on center of mass (COM) positions, (2) molecular rotation around the on COM, (3) molecular insertion with random position and random orientation, and (4) deletion of a molecule. Each GCMC move was attempted with a probability ratio for displacement, rotation, insertion and deletion of 4:2:3:3, respectively. A

spherical cutoff length of 19.0 Å was used in all simulations so as to evaluate the intermolecular LJ interactions without long-range corrections. For orthorhombic zeolite frameworks, the Coulombic interaction was computed using Ewald sum technique [44]. For non-orthorhombic zeolite frameworks, the Coulombic interaction was calculated directly using a force-shifted Coulombic sum method [45, 46] and the cutoff radius was also set to 19.0 Å, which has proved to be sufficiently large for convergence.

To accelerate the simulation, the LJ and Coulombic interactions between adsorbate and adsorbent were calculated using a pre-tabulated energy map constructed throughout the unit cell of the adsorbent. The grid size used is 0.1 or 0.2 Å in each dimension depending on the unit cell length. The energy-bias scheme [47] was used to increase the insertion efficiency. The simulations were allowed to equilibrate for at least 2×10^7 Monte Carlo (MC) steps before data production, with another 5×10^7 MC steps to sample the thermodynamic properties of interest. The periodic boundary conditions and the minimum image convention were employed in all three dimensions. Unless otherwise noted, the uncertainties in the simulation results are smaller than the symbol sizes in the figures presented in the next section. Throughout the remainder of this paper, all adsorption data from the simulations are reported in terms of absolute adsorption since the correction to the excess adsorption that can be directly compared to experiments has proved to be negligible for pressures up to 10 bar [28].

In addition to calculating the equilibrium pore loading at each set of bulk phase conditions we considered, we also computed isosteric heats of adsorption, Q_{st} at zero occupancy and Henry's constants for adsorption. Assuming ideal behavior in the bulk

phase, the isosteric heat of adsorption at zero occupancy from simulations was calculated using [48]

$$Q_{st} = RT - \langle U \rangle - \langle N \rangle \left(\frac{\partial \langle U \rangle}{\partial \langle N \rangle} \right)_{T,V} \quad (6.1)$$

where $\langle U \rangle$ is mean potential energy per molecule in the adsorbed phase, R is the ideal gas constant, T is the temperature, V is unit cell volume and $\langle N \rangle$ is average loading per unit cell. We have fitted $\langle U \rangle$ with a polynomial in loading to calculate the partial derivatives in eq. (6.1).

The Henry's constants were calculated as

$$H \frac{\text{mol}}{\text{kg} \cdot \text{kPa}} = \lim_{P \rightarrow 0} \frac{\text{loading} (\text{mol} / \text{kg})}{P(\text{kPa})} \quad (6.2)$$

where P is the gas-phase pressure.

6.3 Results and Discussion

6.3.1 Materials characterization

The XRD patterns showed that all the samples are highly crystalline and of very good quality, with very small numbers of defects and with undetectable amounts of impurities or secondary crystal phases. All the samples, except for zeolite beta, display sharp peaks and are in good agreement with the published XRD patterns (BEA*[39], CHA [37], FER [38], MFI [20], and STT [21]). The shoulder at low angle of BEA* indicated more than 50 percent of stacking sequence of polymorph A in the material [39]: pure polymorph A is used in this work to simulate the adsorption isotherms of adsorbates CO₂ and N₂ on BEA* zeolite. The refinement of the unit cell

dimensions (by least-squares method using celref [49]) of our samples based on the in-house measured XRD patterns are shown in Table 6.2.

Table 6.2. Optimized unit cell dimensions and space group assigned to each of the pure silica zeolites

Materials	a (Å)	b (Å)	c (Å)	α (°)	β (°)	γ (°)	$V_{u.c}$ (Å³)	Space group
BEA	12.517	12.517	26.243	90	90	90	4111.5	P4 ₁ 22
CHA	13.544	13.544	14.735	90	90	120	2340.9	R3m
FER	18.678	14.092	7.411	90	90	90	1950.6	Immm
MFI	20.088	19.859	13.372	90	90	90	5334.5	Pnma
STT	13.108	21.652	13.704	90	102.2	90	3802.2	P12 ₁ /n1

Zeolite beta (Figure 6.2a) exhibits truncated tetragonal-bipyramid crystal morphology with particle sizes in the range of 1 to 3 μm . Chabazite (Figure 6.2b) consists of rhombohedral (pseudo-cubic) crystals with a uniform particle size of 10 μm . Figure 6.2c shows that the as-synthesized ferrierite crystals are composed of very large rhombohedral particles with a size of 100 μm . Silicalite-1 (MFI-OH) (Figure 6.2d) morphology is characterized by a very well-defined nearly hexagonal prism shape with no defects and a highly uniform particle size of 200 nm (Figure 6.2d). Silicalite-1 synthesized in HF media (MFI-figure 6.2e) is composed of twinned crystals with much larger particle size ($\sim 10\mu\text{m}$) compared to MFI-OH. STT (Figure 6.2f) exhibits aggregates of plate-like crystals, and each rectangular plate particle has the dimensions of about 2 x 5 μm . The surface areas and micropore volumes for all samples are reported in Table 6.3.

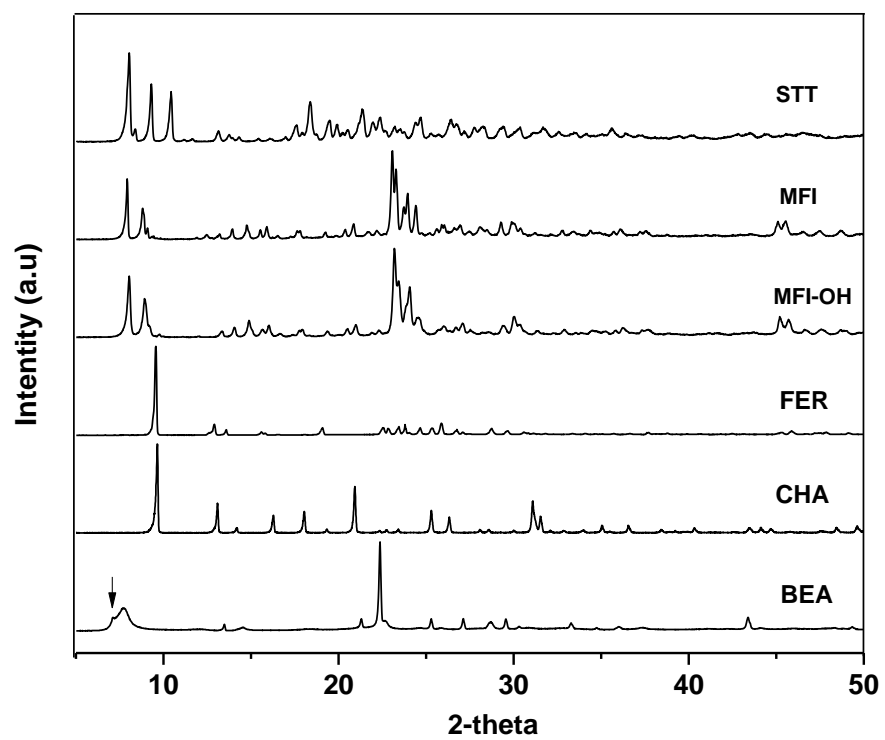


Figure 6.1. X-Ray diffraction patterns of calcined pure silica zeolites

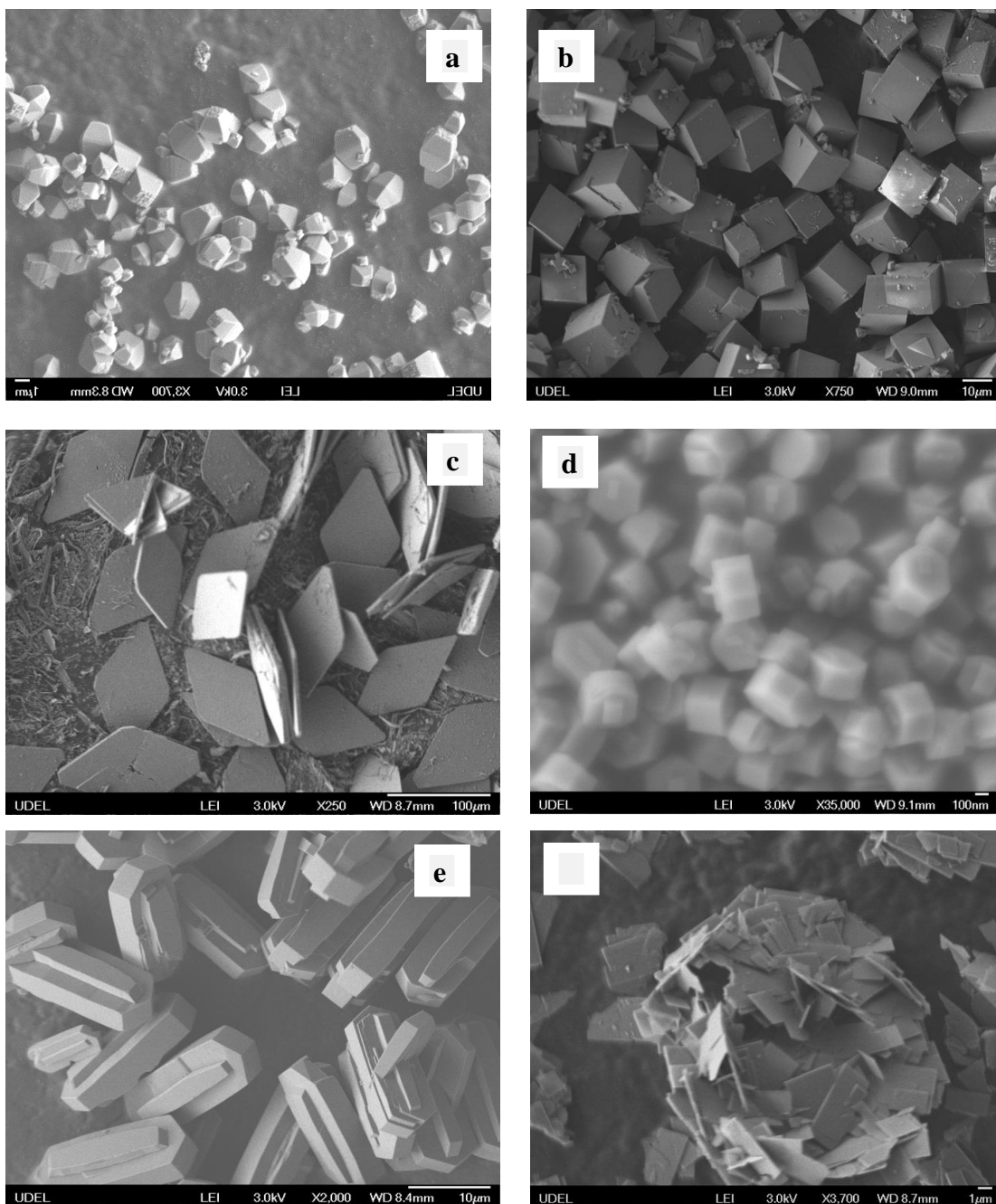


Figure 6.2. SEM images of calcined pure silica zeolites BEA (a), CHA (b), FER (c), MFI-OH (d), MFI (e), STT (f)

Table 6.3. Surface area and micropore volume of pure silica zeolites

Samples	Micropore Area, m ² /g	External Area m ² /g	Micropore Volume cm ³ /g
BEA	395	64	0.21
CHA	572	32	0.27
FER	282	51	0.13
MFI	312	78	0.14
MFI-OH	302	99	0.14
STT	411	51	0.19

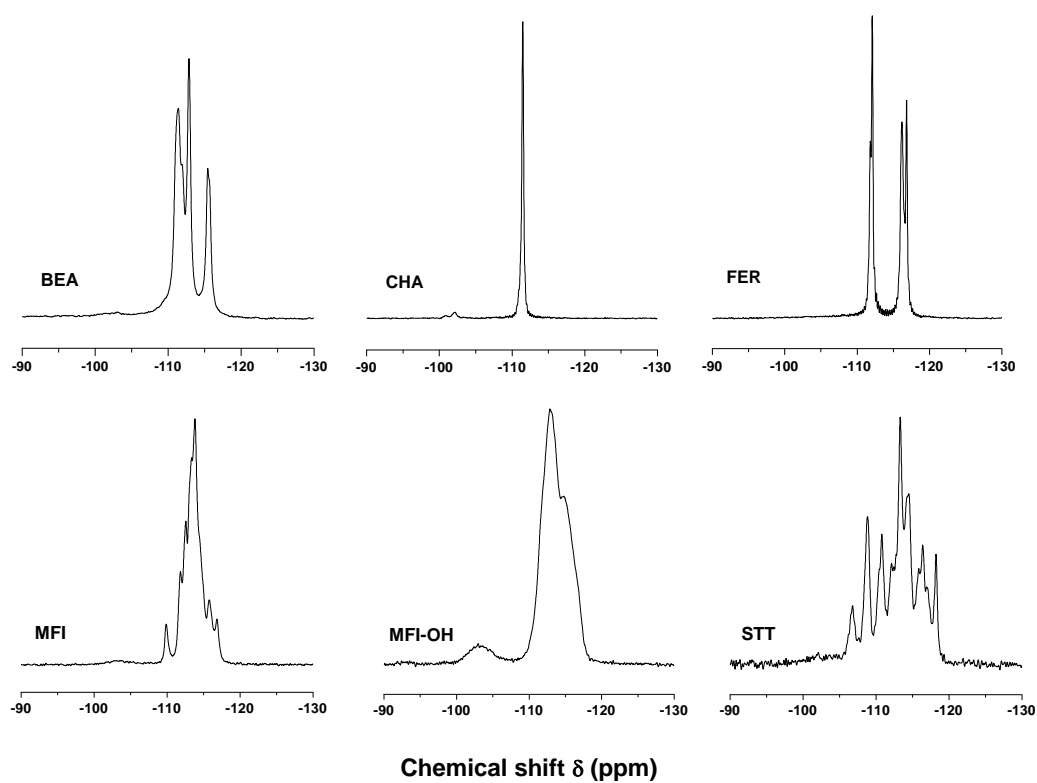


Figure 6.3. ²⁹Si MAS NMR spectra of BEA*, CHA, FER, MFI, MFI-OH, and STT samples

The single-pulse ^{29}Si MAS NMR spectrum of calcined pure-silica chabazite (Figure 6.3) showed only three peaks: two small peaks at chemical shift δ of -100.9 ppm and -102.1 ppm (assigned to $\text{Si}(\text{OSi})_3\text{OH}$, Q^3 , defect sites) and a much larger peak at \sim -111.5 ppm assigned to Q^4 ($\text{Si}(\text{OSi})_4$) species. The observation of just one Q^4 peak is consistent with the presence of only one T-atom in the asymmetric unit of the chabazite framework. The two Q^3 peaks are assigned to internal and external silanol groups. The $\{^1\text{H}\}$ - ^{29}Si CP MAS NMR spectrum (not shown) of this sample shows two peaks in the Q^3 region at the same positions that the MAS spectrum. Only a very small signal at \sim 112 ppm (Q^4) is detected for this zeolite. The ^{29}Si MAS NMR spectrum of zeolite beta (Figure 6.3) is also highly resolved and shows 4 peaks (110-116 ppm) belonging to Q^4 species, and a very weak Q^3 signal (100-104 ppm). A weak Q^3 signal is the only spectral feature detected in the ^1H - ^{29}Si CP MAS NMR spectrum: these results agree well the spectra of siliceous zeolite beta reported by Cambor *et al.*[36] and confirm the lack of silanol defects in this sample. The single pulse ^{29}Si MAS and the $\{^1\text{H}\}$ - ^{29}Si CP MAS NMR spectra of siliceous ferrierite (FER), silicalite-1 and SSZ-23 (STT) are all similar to the above spectra showing very low concentration of defects sites in the samples synthesized in HF medium, as expected. The only exception is the sample of silicalite-1 prepared in hydroxide medium that clearly showed the presence of a clear silanol peak in the single-pulse ^{29}Si MAS NMR spectrum. The fraction of Q_3 species is 9.5% in MFI-OH, which is higher than that in MFI (4.1%).

6.3.2 Adsorption of CO_2 and N_2 on siliceous zeolites

Figure 6.4 compares the simulated and measured isotherms of CO_2 at various temperatures and N_2 at 303 K on each siliceous zeolite. The results from the GCMC

simulations are in very good agreement with the measured isotherms over the range of pressures (0-1 atm) investigated, and especially so at the higher temperatures. The only exception is CO₂ in zeolite beta at low temperatures where the calculated adsorption isotherms are substantially lower than the observed adsorption isotherms. The origin of this anomalous result is unclear. Since the crystal structure of pure polymorph A was used in the simulation (while experiment showed only about 60% of polymorph A in the zeolite), simulations were also conducted using polymorphs B and C of zeolite beta (Figure 6.5) revealing similar adsorption isotherms for these polymorphs at the pressure ranges studied in this work. This is as expected because the local structure of the polymorphs is nearly the same [50]. It is possible that the models of polymorphs A and B are not good representations of the actual structure of the sample, but the X-ray diffraction patterns and ²⁹Si NMR spectra are fully consistent with a material that is an intergrowth of both polymorphs. Also note that calculated heats of adsorption of CO₂ and N₂ are comparable to the experimental values (Table 6.4).

Without cations in the framework, PSZ adsorb CO₂ and N₂ only by physical interactions. Since N₂ and CO₂ are both nonpolar molecules, the field-dipole (electrostatic) energy interaction between the adsorbate and the adsorbent is small compared to other polar molecules such as H₂O and NH₃. Besides, in agreement with the hydrophobic surface properties, the electric field in zeolites is small and consequently the energy of interaction of the linear quadrupole Q of the two adsorbates with an inhomogeneous electric field is only a minor contribution to the total enthalpy of adsorption. At the conditions investigated here, adsorbate-adsorbent

interactions dominate the total heat of adsorption and this can be divided into van der Waals and electrostatic contributions.

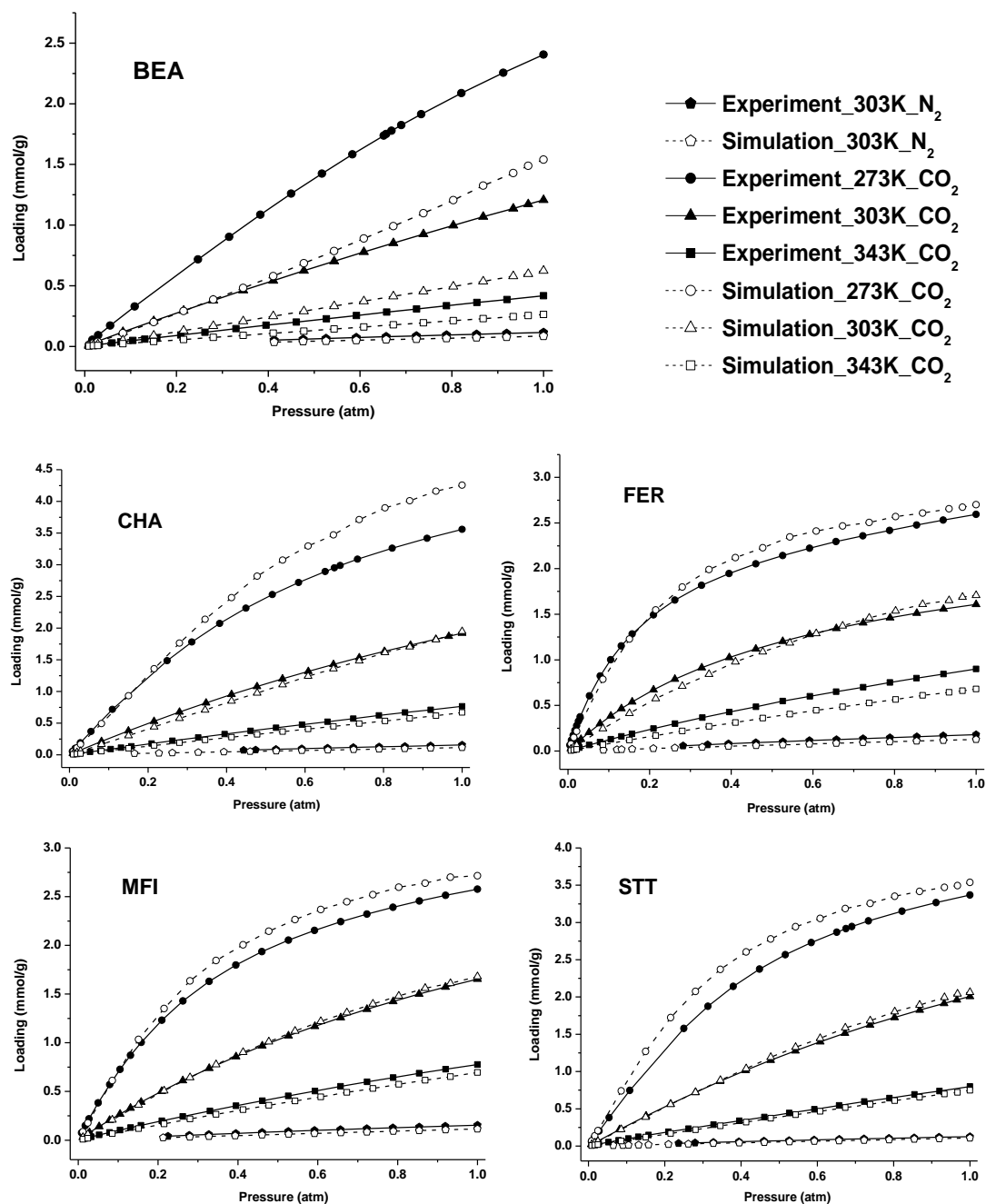


Figure 6.4. Computed and measured adsorption isotherms of CO₂ (273, 303, and 343 K) and N₂ (303 K) on BEA, CHA, FER, MFI, and STT-type zeolites

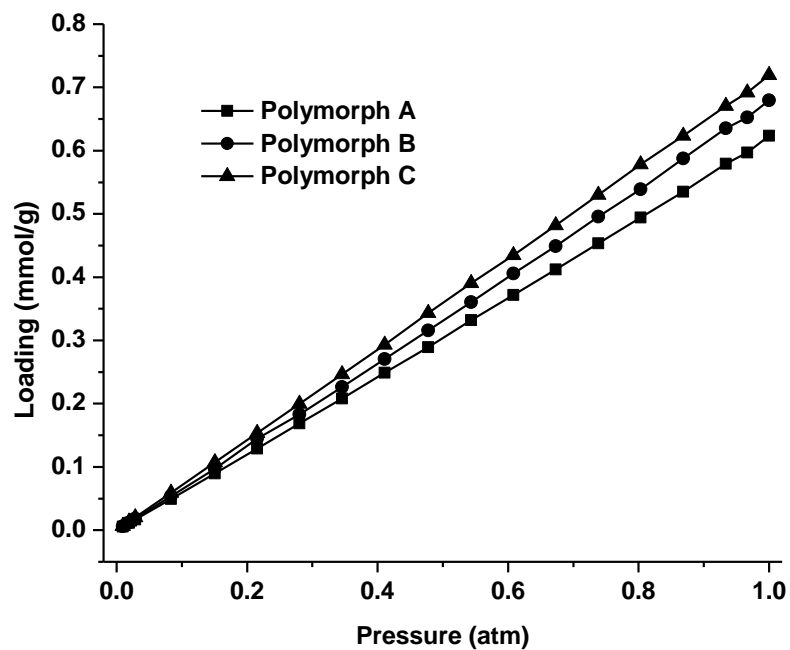


Figure 6.5. Computed adsorption isotherms of CO₂ (303 K) on BEA*, polymorphs A, B and C.

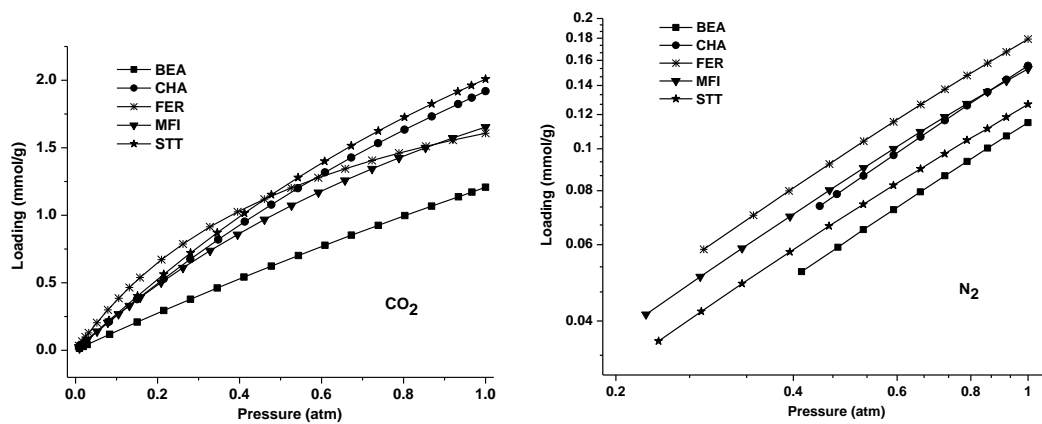


Figure 6.6. CO₂ and N₂ adsorbed on pure silica zeolites at 303K. Note the difference in the scale of the ordinate axis

Our simulations show that at low loading the adsorbate-adsorbate interaction is much weaker than the adsorbate-zeolite interaction (Figure 6.7), therefore adsorbate molecules tend to occupy the most energetically favorable positions, and the number of these attractive sites is higher in small pores. This explains the order of CO₂, N₂ adsorption capacity in the low-pressure region of PSZ adsorbents: FER > MFI ~ STT ~ CHA > BEA* (Figure 6.6). At high loadings, the adsorbed CO₂ molecules can occupy both the central and wall regions of the wider pores, leading to a higher packing density, hence the uptake of CO₂ in PSZ is in the order of STT ~ CHA > MFI > FER > BEA* (Figure 6.6). With even higher loading of CO₂, the wider pores and greater microporosity play a more important role, and at 273 K (Figure 6.8) the CHA adsorption capacity of CO₂ is higher than STT, and much higher than other zeolites that have smaller pores and micropore volumes. Rigas *et al.* [51] also showed that at low pressures, the adsorbate density is highest in materials with smaller pores, while larger pores exhibit higher adsorption capacity at high pressure.

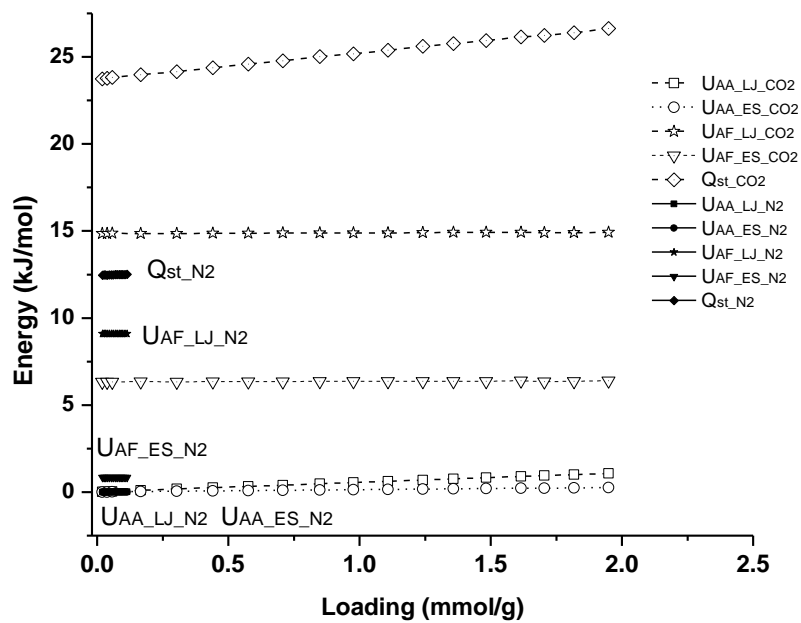


Figure 6.7. Interaction energies of CO₂ and N₂ adsorbed on siliceous chabazite CHA zeolite, U_{AA_LJ}: Lennard-Jones adsorbate-adsorbate interaction, U_{AA_ES}: electrostatic adsorbate-adsorbate interaction, U_{AF_LJ}: Lennard-Jones adsorbate-zeolite interaction, U_{AF_ES}: electrostatic adsorbate-zeolite interaction, Q_{st}: adsorption heat.

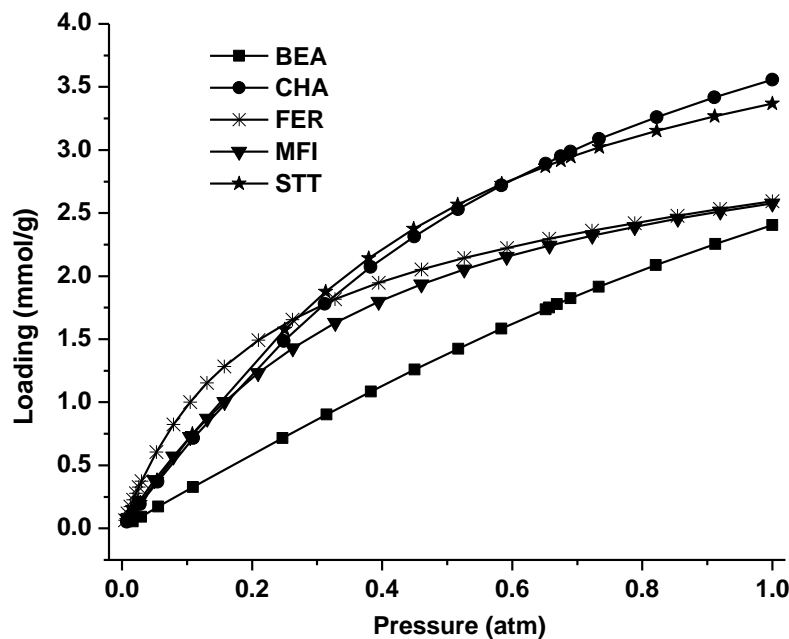


Figure 6.8. Adsorption isotherms of CO₂ on pure silica zeolites at 273 K

The Henry's constant (K_H) values for CO₂ and N₂ adsorption were determined by fitting $\ln(P/n)$ as a function of n (P : pressure in atm, n : adsorbed amount in mmol/g) in the low pressure-region of the measured isotherms and the straight line extrapolation of the results to the limit of $n \rightarrow 0$ [52]. Henry's constants reflect directly the affinity of CO₂ for each adsorbent, and the results on Table 6.4 clearly show that the affinity order of these materials in the Henry's law (low adsorption) region is FER > MFI > STT > CHA > BEA. The ratio of the Henry's constants of CO₂ to those of N₂ was used to calculate the intrinsic selectivity: $\alpha_{CO_2/N_2} = K_{H_CO_2}/K_{H_N_2}$. The heats of adsorption at zero coverage were estimated using *Clausius-Clapeyron* equation:

$$Q_{st}^o = -R \left[\frac{\partial \ln K_H}{\partial \left(\frac{1}{T} \right)} \right] \quad (6.3)$$

The heats of adsorption determined from the measured isotherms are in a very good agreement with the GCMC simulation results (Table 6.4) and are in accordance with the results obtained by Sircar [53] on MFI (24.1 and 15.1 kJ/mol for CO₂ and N₂, respectively, by the conventional volumetric method), by Fang *et al.* [54] on CHA (22.5 kJ/mol for CO₂) by the microcalorimetric method, and by Bourrelly *et al.* [55] on BEA (< 21 kJ/mol for CO₂) by the conventional volumetric method. FER has the highest heat of adsorption and BEA* has the lowest, which is expected since FER has 2 small straight channels with 8- and 10-membered ring windows and BEA* contains a 3D 12-member ring pore system. Although STT and CHA have 9- and 8-member ring windows, respectively, the bigger cages in these materials result in lower heats of adsorption compared to MFI and FER. As also shown in Table 6.4, the energy interaction between the non-polar adsorbates and silicalite zeolites prepared in hydroxide and hydrofluoride medium are similar. The difference might only appear if the adsorbates are polar molecules such as H₂O and NH₃.

The heats of adsorption versus the loadings of CO₂ are shown in Figure 6.9. As the loadings of the adsorbates increase, the isosteric heats of adsorption slightly increased indicating the presence of attractive adsorbate-adsorbate interactions. The small variation in Q_{st} over the range of loadings investigated could be considered as within the experimental error of the adsorption isotherm data. Thus, the results indicate a homogeneous adsorption system of CO₂ adsorbed on PSZ adsorbents.

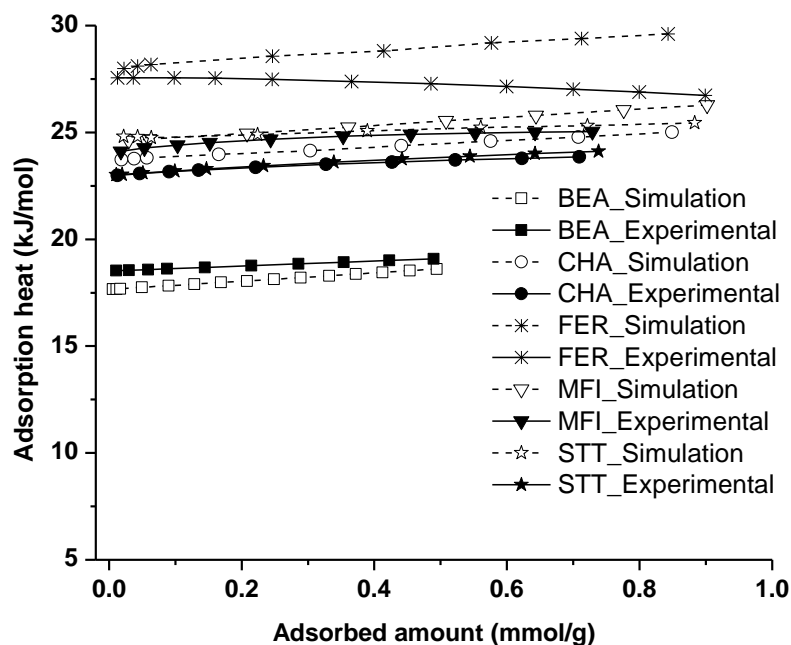


Figure 6.9. Heats of adsorption of CO₂ on PSZ at a function of amount adsorbed

Table 6.4. Heats of adsorption at zero coverage and Henry's constants (303K) of CO₂ and N₂ adsorbed on PSZ

Adsorbents	Q_{st}^o - CO ₂		Q_{st}^o - N ₂		K_H^{exp}		Selectivity CO ₂ /N ₂
	Sim	Exp	Sim	Exp	CO ₂	N ₂	
BEA	17.9	18.6	10.5	11.2	1.38	0.14	10
CHA	23.7	23.0	12.5	13.6	2.72	0.18	15
FER	28.0	27.2	15.4	17.6	4.35	0.22	20
MFI	24.6	24.2	13.9	16.2	2.83	0.17	17
MFI-OH	24.6	24.5	13.9	15.0	3.10	0.19	16
STT	26.0	23.6	13.1	14.1	2.87	0.16	17

Q_{st}^o : Heat of adsorption at zero coverage (kJ/mol), Sim: Simulation, Exp: Experiment,
 K_H^{exp} : Henry's constants at 303 K (mol.kg⁻¹.atm⁻¹)

Because of the very high adsorption affinity of CO₂ at low pressure, low silica zeolites such as 13X, Y, 4A have some advantages in terms of working capacity and

selectivity of CO₂ over N₂ in the low-pressure regime. For a Pressure Swing Adsorption (PSA) processes however, the adsorption step generally takes place at moderate or high pressures (>5 atm), and the desorption step is performed preferentially at atmospheric pressure. The pure silica zeolites have moderate adsorption capacity at 1 atm and only are saturated at high pressures, while low silica zeolites 13X, Y and 4A are almost saturated by CO₂ at ambient pressure. Therefore, the working capacity (that is, the difference of the uptake at adsorption and desorption pressures), and the regenerability (defined as the ratio between the working capacity and the uptake at adsorption pressure) of CO₂ adsorbed on siliceous zeolites are higher than for low silica zeolites, as was also pointed out by Miyamoto *et al.*[56] and Palomini *et al.*[57]. At high pressure, the CO₂ adsorption capacity is proportional to the pore volume of the adsorbents. On the basis of this information, the effectiveness of the adsorbents can be ranked as: CHA > STT ~ BEA > MFI~FER.

Commercial activated carbons have some advantages over siliceous zeolites in terms of the lower cost of the raw materials and higher CO₂ uptake at high pressure [58]. At ambient pressure and temperature, activated carbons and siliceous zeolites have similar adsorption capacity (~2 mmol/g), and because of their large microporous volume, activated carbons show lower CO₂ adsorption capacity when measured in units of mmol CO₂/microporous volume. Although similar in their hydrophobic character, the gradual oxidation of the carbon surface leads to the decrease in the carbon adsorption capacities in the presence of moisture [59]. For this reason, siliceous zeolites are, in fact, better candidates in the presence of moisture. Compared to aluminophosphates adsorbents [60], siliceous zeolites show similar adsorption capacities at room temperature and 1 atm (~ 2 mmol/g) even though the

aluminophosphate (ALPOs) adsorbents are more hydrophilic than PSZs (e.g., water isotherm capacity at ambient condition is ~ 10 mmol/g [60] on ALPOs compared to less than 3 mmol/g on silicalite-1 [61]): water vapor is more detrimental to ALPOs than PSZs.

In Figure 6.10, we show from simulations the center-of-mass (COM) density distribution of CO₂ adsorption in five zeolites to identify where the preferred adsorption sites are located at room temperature. These were generated at low pressure conditions under which the CO₂-zeolite interaction dominates adsorption and adsorbate-adsorbate interaction is negligible. The white- clouds represent the lowest-energy, preferred adsorption sites for CO₂ molecules. We observed that CO₂ molecules prefer the straight channels along the x or y directions in BEA* zeolite. For CHA zeolite, CO₂ molecules like to be in the straight channels along y direction connecting double 6-member rings (D6R units). For the FER zeolite, the preferred CO₂ adsorption sites are in the channels through the 8-member rings along y direction. For MFI zeolite, the preferred adsorption sites for CO₂ are in the zigzag channels along x direction, while for STT zeolite, the preferred adsorption sites for CO₂ are the channels through 7-rings along z direction.

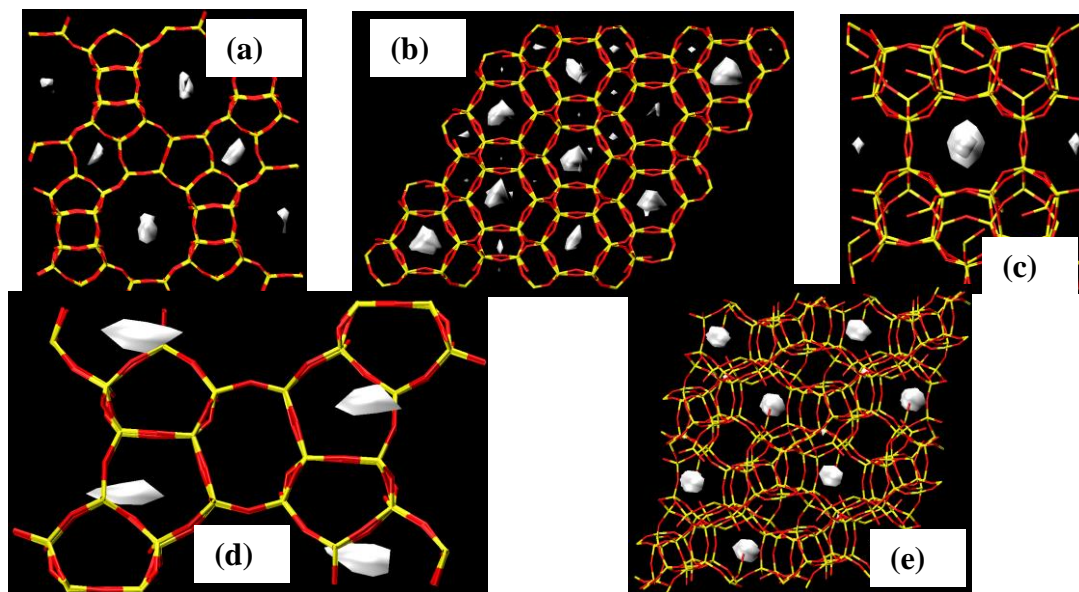


Figure 6.10. Density distribution shown for CO₂ adsorption in (a) BEA, (b) CHA, (c) FER, (d) MFI and (e) STT at low pressure. The white-color clouds show the lowest-energy adsorption sites. The number of unit cells in x, y, z dimensions used for visualization is (a) 2×2×1, (b) 2×2×2, (c) 2×1×1, (d) 1×1×1, and (e) 2×1×2. All zeolites are in show in [0,1,0] direction. Legend: orange color for silicon atoms and red color for oxygen atoms on zeolites.

6.4 Conclusions

Based on the analysis of the adsorption isotherms and the heats of adsorption, CO₂ and N₂ showed higher adsorption in the smaller pore/window size siliceous zeolites, and due to its larger polarizability, CO₂ interacts more strongly with the adsorbents than N₂. GCMC simulation predicts the sorption equilibria of CO₂ and N₂ successfully using the force fields available in the literature. In the case of BEA* zeolite, heats of adsorption of CO₂ and N₂ agree well with the experiment despite the fact that the calculations use only polymorph A. In agreement with the experiment, CO₂ was found to exhibit greater thermodynamic affinity (more steeply rising

isotherms, higher adsorption heats) for the zeolites than N₂. Consequently, GCMC simulation is a good method for testing the validity of the assumptions and calculating adsorption isotherms using gas-solid molecular interactions. Importantly, the method can identify the best candidates for CO₂ separation by PSA processes.

REFERENCES

1. Maurin, G., P.L. Llewellyn, and R.G. Bell, Adsorption mechanism of carbon dioxide in faujasites: Grand canonical Monte Carlo simulations and microcalorimetry measurements. *Journal of Physical Chemistry B*, 2005. **109**(33): p. 16084-16091.
2. Harlick, P.J.E. and F.H. Tezel, An experimental adsorbent screening study for CO₂ removal from N₂. *Microporous and Mesoporous Materials*, 2004. **76**(1-3): p. 71-79.
3. Li, J.-R., et al., Carbon dioxide capture-related gas adsorption and separation in metal-organic frameworks. *Coordination Chemistry Reviews*, 2011. **255**(15-16): p. 1791-1823.
4. Herm, Z.R., R. Krishna, and J.R. Long, CO₂/CH₄, CH₄/H₂ and CO₂/CH₄/H₂ separations at high pressures using Mg-2(dobdc). *Microporous and Mesoporous Materials*, 2012. **151**: p. 481-487.
5. Garcia-Perez, E., et al., A computational study of CO₂, N₂, and CH₄ adsorption in zeolites. *Adsorption-Journal of the International Adsorption Society*, 2007. **13**(5-6): p. 469-476.
6. Siriwardane, R.V., et al., Adsorption of CO₂ on molecular sieves and activated carbon. *Energy & Fuels*, 2001. **15**(2): p. 279-284.
7. Brandani, F. and D.M. Ruthven, The effect of water on the adsorption of CO₂ and C₃H₈ on type X zeolites. *Industrial & Engineering Chemistry Research*, 2004. **43**(26): p. 8339-8344.
8. Manabu Miyamoto, Y.F.a.K.Y., Pure silica CHA type zeolite for CO₂ separation using pressure swing adsorption at high pressure. *J. Mater. Chem.*, 2012(22): p. 20186-20189.
9. Burton, A.W., S.I. Zones, and S. Elomari, The chemistry of phase selectivity in the synthesis of high-silica zeolites. *Current Opinion in Colloid & Interface Science*, 2005. **10**(5-6): p. 211-219.
10. Cambor, M.A., L.A. Villaescusa, and M.J. Díaz-Cabañas, Synthesis of all-silica and high-silica molecular sieves in fluoride media. *Topics in Catalysis*, 1999. **9**(1-2): p. 59-76.
11. Villaescusa, L.A., P.A. Barrett, and M.A. Cambor, ITQ-7: A new pure silica polymorph with a three-dimensional system of large pore channels. *Angewandte Chemie-International Edition*, 1999. **38**(13-14): p. 1997-2000.
12. Trzpit, M., et al., The effect of local defects on water adsorption in silicalite-1 zeolite: A joint experimental and molecular simulation study. *Langmuir*, 2007. **23**(20): p. 10131-10139.

13. Higgins, J.B., et al., THE FRAMEWORK TOPOLOGY OF ZEOLITE-BETA. *Zeolites*, 1988. **8**(6): p. 446-452.
14. Piccione, P.M., et al., Thermochemistry of pure-silica zeolites. *Journal of Physical Chemistry B*, 2000. **104**(43): p. 10001-10011.
15. Smith, J.V., CRYSTAL STRUCTURES WITH A CHABAZITE FRAMEWORK .1. DEHYDRATED CA-CHABAZITE. *Acta Crystallographica*, 1962. **15**(SEP): p. 835-&.
16. Smith, J.V., L.S.D. Glasser, and F. Rinaldi, CRYSTAL STRUCTURES WITH A CHABAZITE FRAMEWORK .2. HYDRATED CA-CHABAZITE AT ROOM TEMPERATURE. *Acta Crystallographica*, 1963. **16**(1): p. 45-&.
17. VAUGHAN, P.A., The Crystal Structure of the Zeolite Ferrierite. *Acta Cryst.* , 1966. **21**: p. 983.
18. Kuperman, A., et al., NONAQUEOUS SYNTHESIS OF GIANT CRYSTALS OF ZEOLITES AND MOLECULAR-SIEVES. *Nature*, 1993. **365**(6443): p. 239-242.
19. Kokotailo, G.T., et al., STRUCTURE OF SYNTHETIC ZEOLITE ZSM-5. *Nature*, 1978. **272**(5652): p. 437-438.
20. Olson, D.H., et al., CRYSTAL-STRUCTURE AND STRUCTURE-RELATED PROPERTIES OF ZSM-5. *Journal of Physical Chemistry*, 1981. **85**(15): p. 2238-2243.
21. Cambor, M.A., et al., A synthesis, MAS NMR, synchrotron X-ray powder diffraction, and computational study of zeolite SSZ-23. *Chemistry of Materials*, 1999. **11**(10): p. 2878-2885.
22. Cambor, M.A., et al., SSZ-23: An odd zeolite with pore openings of seven and nine tetrahedral atoms. *Angewandte Chemie-International Edition*, 1998. **37**(15): p. 2122-2126.
23. Dubbeldam, D., et al., Incommensurate diffusion in confined systems. *Physical Review Letters*, 2003. **90**(24).
24. Maesen, T.L.M., et al., Understanding cage effects in the n-alkane conversion on zeolites. *Journal of Catalysis*, 2006. **237**(2): p. 278-290.
25. Krishna, R. and J.M. van Baten, Using molecular simulations for screening of zeolites for separation Of CO₂/CH₄ mixtures. *Chemical Engineering Journal*, 2007. **133**(1-3): p. 121-131.
26. Krishna, R. and J.M. van Baten, Segregation effects in adsorption of CO₂-containing mixtures and their consequences for separation selectivities in cage-type zeolites. *Separation and Purification Technology*, 2008. **61**(3): p. 414-423.
27. Makrodimitris, K., G.K. Papadopoulos, and D.N. Theodorou, Prediction of permeation properties of CO₂ and N₂ through silicalite via molecular simulations. *Journal of Physical Chemistry B*, 2001. **105**(4): p. 777-788.
28. Goj, A., et al., Atomistic simulations of CO₂ and N₂ adsorption in silica zeolites: The impact of pore size and shape. *Journal of Physical Chemistry B*, 2002. **106**(33): p. 8367-8375.

29. Selassie, D., et al., Atomistic Simulations of CO₂ and N₂ Diffusion in Silica Zeolites: The Impact of Pore Size and Shape. *Journal of Physical Chemistry C*, 2008. **112**(42): p. 16521-16531.
30. Liu, B. and B. Smit, Molecular Simulation Studies of Separation of CO₂/N₂, CO₂/CH₄, and CH₄/N₂ by ZIFs. *Journal of Physical Chemistry C*, 2010. **114**(18): p. 8515-8522.
31. Leyssale, J.-M., G.K. Papadopoulos, and D.N. Theodorou, Sorption thermodynamics of CO₂, CH₄, and their mixtures in the ITQ-1 zeolite as revealed by molecular Simulations. *Journal of Physical Chemistry B*, 2006. **110**(45): p. 22742-22753.
32. Himeno, S., M. Takenaka, and S. Shimura, Light gas adsorption of all-silica DDR- and MFI-type zeolite: computational and experimental investigation. *Molecular Simulation*, 2008. **34**(10-15): p. 1329-1336.
33. Babarao, R., et al., Storage and separation of CO₂ and CH₄ in silicalite, C-168 schwarzite, and IRMOF-1: A comparative study from monte carlo simulation. *Langmuir*, 2007. **23**(2): p. 659-666.
34. Plant, D.F., et al., Molecular dynamics simulation of the cation motion upon adsorption of CO₂ in faujasite zeolite systems. *Journal of Physical Chemistry B*, 2006. **110**(29): p. 14372-14378.
35. Papadopoulos, G.K. and D.N. Theodorou, Simulation studies of methane, carbon dioxide, hydrogen and deuterium in ITQ-1 and NaX zeolites. *Molecular Simulation*, 2009. **35**(1-2): p. 79-89.
36. Cambor, M.A., A. Corma, and S. Valencia, Spontaneous nucleation and growth of pure silica zeolite-beta free of connectivity defects. *Chemical Communications*, 1996(20): p. 2365-2366.
37. Diaz-Cabanas, M.J., P.A. Barrett, and M.A. Cambor, Synthesis and structure of pure SiO₂ chabazite: the SiO₂ polymorph with the lowest framework density. *Chemical Communications*, 1998(17): p. 1881-1882.
38. Morris, R.E., et al., A SYNCHROTRON X-RAY-DIFFRACTION, NEUTRON-DIFFRACTION, SI-29 MAS-NMR, AND COMPUTATIONAL STUDY OF THE SILICEOUS FORM OF ZEOLITE FERRIERITE. *Journal of the American Chemical Society*, 1994. **116**(26): p. 11849-11855.
39. Newsam, J.M., et al., STRUCTURAL CHARACTERIZATION OF ZEOLITE-BETA. *Proceedings of the Royal Society of London Series a- Mathematical Physical and Engineering Sciences*, 1988. **420**(1859): p. 375-&.
40. Corma, A., et al., Synthesis and structure of polymorph B of zeolite beta. *Chemistry of Materials*, 2008. **20**(9): p. 3218-3223.
41. Harris, J.G. and K.H. Yung, CARBON DIOXIDES LIQUID-VAPOR COEXISTENCE CURVE AND CRITICAL PROPERTIES AS PREDICTED BY A SIMPLE MOLECULAR-MODEL. *Journal of Physical Chemistry*, 1995. **99**(31): p. 12021-12024.
42. Murthy, C.S., et al., PAIRWISE ADDITIVE EFFECTIVE POTENTIALS FOR NITROGEN. *Molecular Physics*, 1980. **41**(6): p. 1387-1399.

43. Jiang, J. and S.I. Sandler, Separation of CO₂ and N₂ by Adsorption in C168 Schwarzite: A Combination of Quantum Mechanics and Molecular Simulation Study. *Journal of the American Chemical Society*, 2005. **127**(34): p. 11989-11997.
44. M.P. Allen, a.D.J.T., *Computer Simulation of Liquids*. Oxford Science Publications: Oxford, 1987.
45. Fennell, C.J. and J.D. Gezelter, Is the Ewald summation still necessary? Pairwise alternatives to the accepted standard for long-range electrostatics. *Journal of Chemical Physics*, 2006. **124**(23).
46. Wolf, D., et al., Exact method for the simulation of Coulombic systems by spherically truncated, pairwise r(-1) summation. *Journal of Chemical Physics*, 1999. **110**(17): p. 8254-8282.
47. Snurr, R.Q., A.T. Bell, and D.N. Theodorou, PREDICTION OF ADSORPTION OF AROMATIC-HYDROCARBONS IN SILICALITE FROM GRAND-CANONICAL MONTE-CARLO SIMULATIONS WITH BIASED INSERTIONS. *Journal of Physical Chemistry*, 1993. **97**(51): p. 13742-13752.
48. Heuchel, M., R.Q. Snurr, and E. Buss, Adsorption of CH₄-CF₄ Mixtures in Silicalite: Simulation, Experiment, and Theory. *Langmuir*, 1997. **13**(25): p. 6795-6804.
49. Bochu, J.L.a.B., CELREF.
50. Martinez-Inesta, M.M., et al., A pair distribution function analysis of zeolite beta. *Microporous and Mesoporous Materials*, 2005. **77**(1): p. 55-66.
51. Samios, S., et al., The structure of adsorbed CO₂ in slitlike micropores at low and high temperature and the resulting micropore size distribution based on GCMC simulations. *Journal of Colloid and Interface Science*, 2000. **224**(2): p. 272-290.
52. Pham, T.D., Q. Liu, and R.F. Lobo, Carbon Dioxide and Nitrogen Adsorption on Cation-Exchanged SSZ-13 Zeolites. *Langmuir : the ACS journal of surfaces and colloids*, 2013. **29**(2): p. 832-9.
53. Golden, T.C. and S. Sircar, GAS-ADSORPTION ON SILICALITE. *Journal of Colloid and Interface Science*, 1994. **162**(1): p. 182-188.
54. Fang, H., et al., Prediction of CO₂ Adsorption Properties in Zeolites Using Force Fields Derived from Periodic Dispersion-Corrected DFT Calculations. *Journal of Physical Chemistry C*, 2012. **116**(19): p. 10692-10701.
55. Bourrelly, S., G. Maurin, and P.L. Llewellyn, Adsorption microcalorimetry of methane and carbon dioxide on various zeolites, in *Molecular Sieves: From Basic Research to Industrial Applications*, Pts a and B, J. Cejka, N. Zilkova, and P. Nachtigall, Editors. 2005. p. 1121-1128.
56. Miyamoto, M., Y. Fujiokax, and K. Yogo, Pure silica CHA type zeolite for CO₂ separation using pressure swing adsorption at high pressure. *Journal of Materials Chemistry*, 2012. **22**(38): p. 20186-20189.

- 57. Palomino, M., et al., New Insights on CO₂-Methane Separation Using LTA Zeolites with Different Si/Al Ratios and a First Comparison with MOFs. *Langmuir*, 2010. **26**(3): p. 1910-1917.
- 58. Choi, S., J.H. Drese, and C.W. Jones, Adsorbent Materials for Carbon Dioxide Capture from Large Anthropogenic Point Sources. *Chemsuschem*, 2009. **2**(9): p. 796-854.
- 59. Verma, S.K. and P.L. Walker, Carbon Molecular-Sieves with Stable Hydrophobic Surfaces. *Carbon*, 1992. **30**(6): p. 837-844.
- 60. Liu, Q.L., et al., Aluminophosphates for CO₂ Separation. *Chemsuschem*, 2011. **4**(1): p. 91-97.
- 61. Zhang, K., et al., Adsorption of Water and Ethanol in MFI-Type Zeolites. *Langmuir*, 2012. **28**(23): p. 8664-8673.

Chapter 7

ADSORPTION EQUILIBRIA OF CO₂ AND SMALL HYDROCARBONS IN AEI-, CHA-, STT-, AND RRO-TYPE SILICEOUS ZEOLITES

7.1 Introduction

Zeolite adsorbents play an important role in molecular separation technology, industrial catalysis and pollution control [1-6]. Siliceous zeolites are hydrophobic and organophilic crystalline silica molecular sieves having preferential adsorption of organic molecules with a smaller kinetic diameter than the limiting pore size over water [7-9]. These materials can provide an energetically uniform and nonpolar environment for adsorption of relatively small gas molecules and hydrocarbons. These zeolites are also extremely stable to thermal and hydrothermal treatments [9, 10] for example, siliceous MFI is stable up to 1100°C. The siliceous zeolites also have very high silica to aluminum to minimize acid catalyzed reactions and minimize polymerization of any adsorbed olefins [11].

The separation of small olefins and paraffins, which currently relies on energy-intensive cryogenic distillation, is one of the most important separation processes in the petrochemical industry [11-13], and alternative technologies based on adsorption processes are being investigated [14]. Propane/propylene separation in 8-membered ring zeolites is based on the differences in diffusion rates [6, 13, 15], or kinetic effect, in which propylene enters the pores and becomes adsorbed faster than propane. Small pore zeolites have also been found to have high selectivity for CO₂/CH₄ separation [16, 17] in natural gas purification. The description of hydrocarbon adsorption is also

of importance in petroleum and petrochemical processes such as the catalytic isomerization of alkanes.

The adsorption of CO₂ and alkanes on silicalite (MFI) has been widely investigated [18-24]. In this report, we investigated the adsorption of CO₂ and small hydrocarbons in a series of siliceous zeolites of framework types AEI, CHA, RRO, and STT with low concentration of internal silanol groups and prepared in fluoride media. AEI (space group *Cmcm*) has a three-dimensional pore structure and is related to the CHA structure type: it consists of double-six rings and small 8-membered ring windows (Figure 7.1) [25]. CHA has large ellipsoidal cavities with internal dimensions of about 0.67 nm × 1.00 nm, which is different from AEI that has a pear-shaped cage [26, 27]. STT is peculiar in the sense that it contains two-dimensional arrays of cages with molecular access between the cages in the planes being restricted by seven (2.5 × 3.5 Å) and nine (3.8 × 5.4 Å) member-ring windows [28, 29]. RUB-41 (RRO) has a two-dimensional 8 × 10-membered ring pore system that belongs to the monoclinic *P2/c* space group (Figure 7.1). The pore aperture of RRO along the [100] direction is 6.5 × 4 Å and along the [001] direction is 5 × 2.7 Å. Since its aperture is too narrow to allow the passage of any hydrocarbons, the pore along [001] has no influence on the adsorption kinetics. This phenomena was also observed in 2 dimensional ITW zeolite which consists of one circular window (3.8 × 4.1 Å) and one restricted window (2.4 × 5.3 Å) [30]. Herein, we report a comparison of the adsorption capacities, enthalpies, and entropies of CO₂, methane, ethylene, ethane, propylene and propane on these four zeolites. The structure of studied zeolites, the polarizability and the geometry of hydrocarbons plays important roles in controlling the adsorption

behaviors of the adsorbates in the siliceous zeolites. AEI, CHA, and RRO are potential candidates for the kinetic separations of propylene and propane gas mixture.

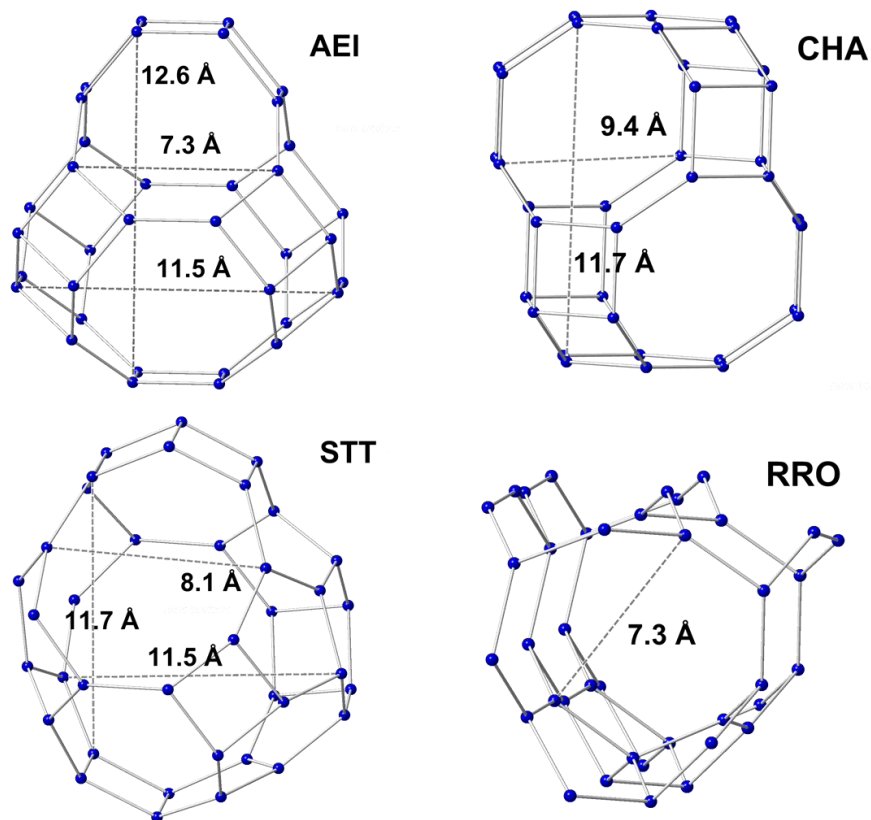


Figure 7.1. Structure of AEI, CHA, STT, and RRO framework-type zeolites. *Note:* Oxygen atoms were omitted for clarity. The distances reported in the pictures are Si-Si distances in each zeolite framework. The unrestrained distances for gas molecules to pass through are roughly obtained by subtracting O atoms diameters (~ 2.5 Å).

7.2 Experimental Section

7.2.1 Materials

Adsorbents: Pure silica chabazite (CHA) and SSZ-23 (STT) [31] were synthesized using the methodology described in Pham *et al* [31].

RUB-39 was prepared following the protocol reported by Gies *et al* [32] 2.87 g of Cabosil M-5 and 8.8 g of dimethyldipropylammonium hydroxide solution (DMDPA-OH 40 wt%, Sachem Inc.) was added to 3.33 g of deionized (DI) water to give the solution with the following molar composition: 3 SiO₂: 0.5 DMDP-OH: 10 H₂O. The mixture was stirred until a uniform gel was obtained, and then transferred into a 23 ml Teflon-lined stainless steel autoclave (Parr) and kept at 423 K with a 40 rpm rotating speed for 21 days. The solid product RUB-39 was separated by filtration, washed with DI water, and dried at 353 K overnight. The as-synthesized RUB-39 was calcined in air by heating at a rate of 3 K/min at 773 K for 6 hours, and then heating to 853 K for another 4 hours. The materials structure changes during calcination to become RUB-41 (RRO).

Synthesis of siliceous AEI (Si/Al=150): The first step consist in the synthesis of *N,N*-Diethyl-2,6-dimethylpiperidinium iodide (*DEDMP-I*) cation that was prepared following the procedure reported by Zones [33]. The iodide salt is converted to the hydroxide salt by exchanging overnight with Bio-Rad AG1-X8 anion exchange resin with the mass composition of 1 DEDMP-I: 2.5 resin: 5 H₂O. The resin suspension was filtered, washed with DI water, and then the filtrate was concentrated using a rotovapor at 313-323 K. The final OH-form concentration (12.9 %wt) was titrated by HCl using phenolphthalein as indicator.

AEI (Si/Al=12) was synthesized using a procedure similar to that reported in ref [33]. A solution of 5 g of sodium silicate (PQ corp., 28.5% SiO₂, 8.9% Na₂O), 0.4 g of NaOH 1M, and 6 g of DI water was added to 5.8 g DEDMP-OH 12.9% and stirred at room temperature for about 15 min. Then, 0.5 g of NH₄-Y (Zeolyst CBV712, Si/Al=6) was added to the solution and stirred for another 30 min. The resulting

solution was then transferred into 23 ml Teflon-lined autoclaves and heated at a temperature of 423 K under rotation for 7 days. The solid product was separated by vacuum filtration, washed with DI water, and dried at 353 K overnight. The as-made product was then calcined in air at 823 K for 8 h.

AEI ($Si/Al=150$) was prepared following a protocol similar to the one reported by Cao *et al* [34]. 0.298 g of $Al(NO_3)_3 \cdot 9H_2O$ predissolved in 3 g of DI water was added to 26.2 g of an aqueous solution of DEDMP-OH 12.9 %wt, followed by 7.5 g of tetraethylorthosilicate (TEOS). The resultant mixture was continuously stirred for about 2 hours at room temperature until all TEOS was completely hydrolyzed. 0.04 g seed of AEI ($Si/Al=12$) was added to the synthesis gel, and then the mixture was heated to remove EtOH and H_2O to have the final gel composition of 1 SiO_2 : 0.0028 Al_2O_3 : 0.5 DEDMP: 0.6F: 3 H_2O .

The resulting mixture of solids was transferred to 23 ml Teflon-lined autoclaves and heated at a temperature of 423 K under rotation for 5 days. After cooling, the resultant solid was recovered by centrifuging, washed with distilled water, and dried at 353 K overnight.

Adsorbates

Carbon dioxide, methane, ethane, ethylene, propylene and propane with purities of higher than 99% were purchased from Matheson and used without further purification.

7.2.2 Analytical Methods

Scanning Electron Microscopy (SEM) images of the calcined zeolites were obtained using a JEOL JSM7400F microscope, operating at an acceleration voltage of 3 keV, and a current of 10 μA . The X-Ray Powder Diffraction (XRD) patterns were

collected at room temperature on a Philips X'Pert Panalytical diffractometer using Cu K α radiation ($\lambda=1.5418$ Å). The data were collected in a stepwise fashion with 2θ ranging from 5.0° to 50.0° with a step size of 0.02° and 2 s per step.

The liquid N₂ isotherms were measured using N₂ at 77 K with a Micromeritics 3Flex apparatus. Prior to the adsorption measurements, the calcined samples were outgassed at 623 K overnight under vacuum. The specific surface area (S_{BET}) and microporous volume (V_{micro}) were calculated using the BET and t-plot methods, respectively. ^{29}Si magic angle spinning nuclear magnetic resonance (MAS NMR) spectra were recorded on a Bruker AVIII-500 solid-state NMR spectrometer, operating at a Larmor frequency of 500.138 MHz for ^1H and 99.362 MHz for ^{29}Si . A 4 mm HX MAS probe was used for all measurements. All spectra were recorded at a MAS frequency of 10 kHz, controlled to with ± 2 Hz using a Bruker MAS controller. ^{29}Si single pulse and cross polarization (CP) measurements have been performed on each sample. For ^{29}Si single pulse MAS experiments, a 90° pulse with a width of 4.3 μs was used and the recycle delay was 30 s. For ^1H - ^{29}Si CP MAS experiments, ^1H 90° pulse duration was 2.5 μs , a linear amplitude ramp (80-100%) on ^1H was used with a contact time of 4.5 ms, and the recycle delay was 5 s. SPINAL64 ^1H decoupling with rf field strength of 100 kHz was applied during the acquisition period for both single pulse and CP MAS measurements.

7.2.3 Adsorption Isotherm Measurements

The gas adsorption isotherms on these samples at different temperatures (273 K, 303 K and 343 K) up to the ambient pressure were measured on Micromeritics ASAP 2020 or on a 3Flex Micromeritics instruments. Before the adsorption measurements each sample was degassed at a temperature of 623 K for 6 h.

Langmuir (Eq. 7.1) and Toth (Eq. 7.2) models were used to fit the adsorption equilibrium isotherms:

$$q = q_m \frac{bP}{1+bP} \quad (7.1)$$

$$q = q_m \frac{bP}{(1+(bP)^t)^{1/t}} \quad (7.2)$$

where q is the amount adsorbed, q_m is the maximum adsorption capacity, P is the adsorption pressure, b and t are coefficients for Langmuir and Toth models.

The heats of adsorption (enthalpy of adsorption) at zero coverage were estimated using the *Clausius-Clapeyron* equation:

$$Q_{st}^o = -R \left[\frac{\partial \ln K_H}{\partial \left(\frac{1}{T} \right)} \right] \quad (7.3)$$

where K_H is Henry's law constant, which is the intercept of the function $\ln(P/q)$ vs q from the virial equation

$$\ln \frac{P}{q} = -\ln K_H + A_1 q + A_2 q^2 + \dots \quad (7.4)$$

The adsorption entropies were calculated as following[35]

$$\Delta S_{ads}^o = \frac{Q_{st}^o}{T} + R \ln K_{ads} \quad (7.5)$$

where $K_{ads} = bP^o$, and $P^o=10^5$ Pa

7.3 Results and Discussion

7.3.1 Materials characterization

The crystallinity and particle morphology of the prepared AEI, CHA, RRO, and STT zeolites were characterized by X-ray powder diffraction and SEM. The XRD patterns reported in Figure 7.2a and 7.2b clearly indicated single crystalline phases of the synthesized zeolites without any detectable impurities [32, 34, 36, 37]. For framework type RRO, the diffraction peaks of a layered silicate RUB-39 intercalated with an organic dimethyldipropylammonium cation shift to higher 2 theta degrees in

the diffraction pattern of *calcined* RUB-41 due to a topotactic condensation of the RUB-39 silicate layers during the calcination process. SEM images (Figure 7.3a) show that morphology of the AEI zeolite is characterized by a well-defined rectangular shape and a highly uniform particle size of 200 nm. RRO has a characteristic and uniform prismatic plate morphology of about 2 μm in length. CHA and STT exhibiting pseudo-cubic and aggregates of plate-like crystals, respectively are shown in Figure 7.3b.

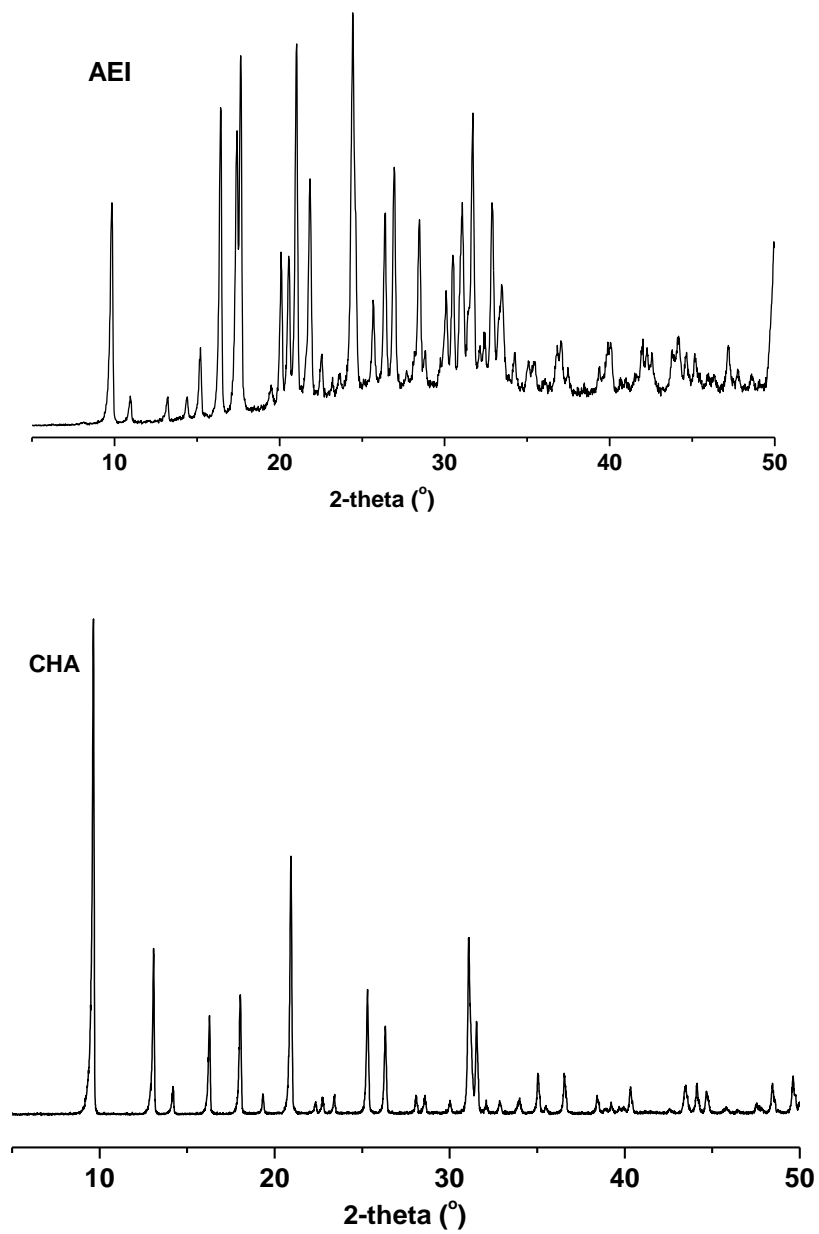


Figure 7.2a. X-ray diffraction patterns of CHA and STT zeolites

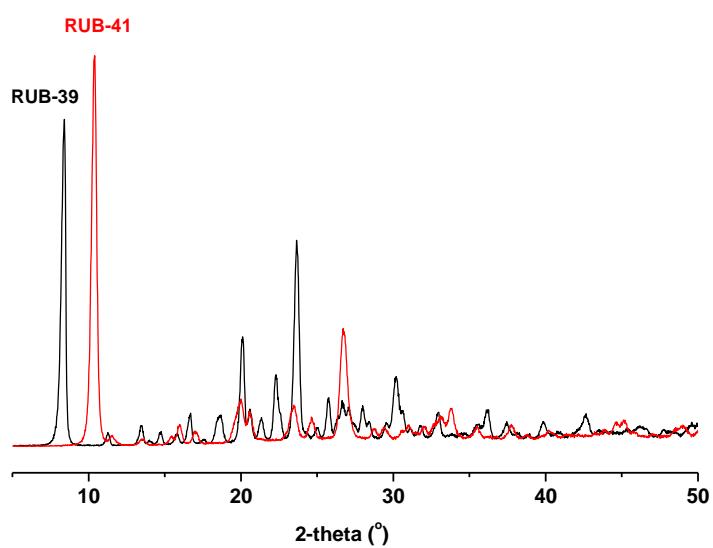
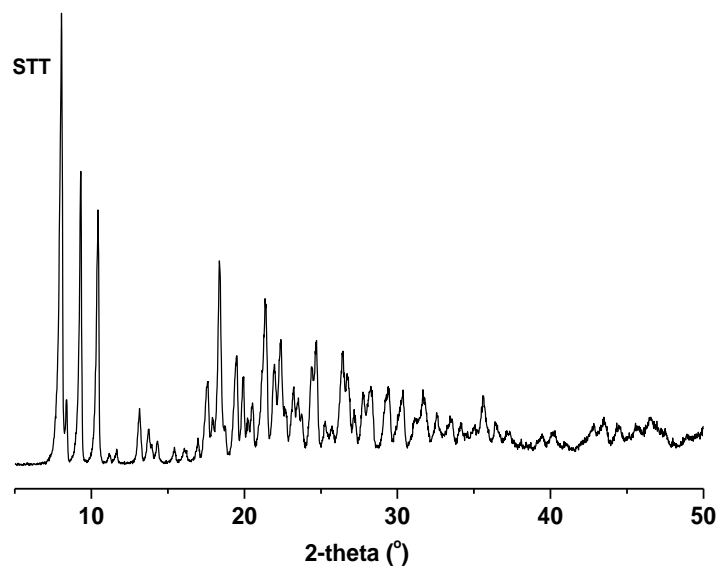


Figure 7.2b. X-ray diffraction patterns of AEI- and RRO-type materials. The second set of patterns displays the superposition of the as-made RUB-39 and the calcined RUB-41 zeolites.

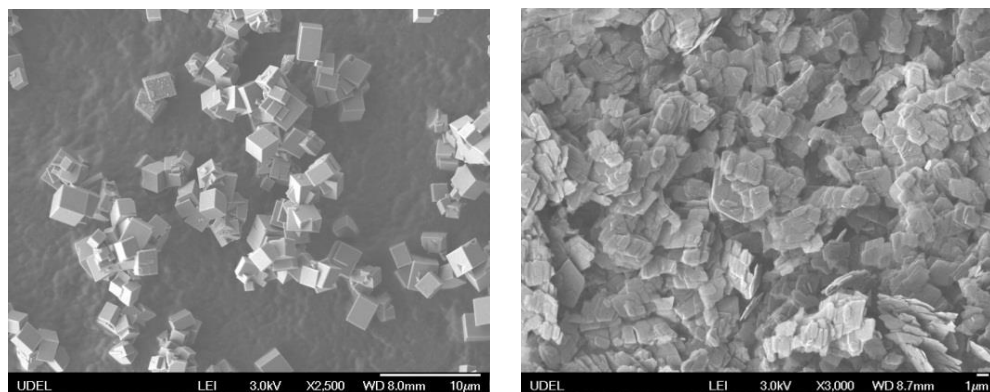


Figure 7.3a. SEM images and XRD patterns of AEI (left) and RRO (right) siliceous zeolites

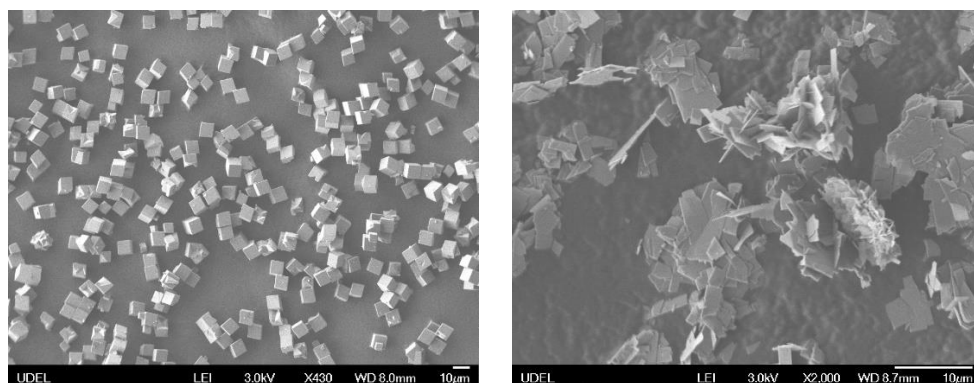


Figure 7.3b. SEM images of CHA (left) and STT (right) zeolites

Table 7.1. Pore shape, dimension, and surface area (m^2/g), micropore volume (cm^3/g) of pure silica zeolites

Adsorbents	Pore dimension (window size)	Pore Shape	Surface area m^2/g	Micropore volume cm^3/g
AEI	8x8x8	pear-shape		0.27
CHA	8x8x8	ellipsoidal	604	0.27
RRO	8x10	channels	452	0.19
STT	9x9	ellipsoidal	462	0.19

The associated Brunauer-Emmett-Teller (BET) surface area, microporous volume extracted by t-plots method, as well as the pore opening of the four synthesized zeolites are reported in Table 7.1. 3D zeolites AEI, CHA have narrower pore openings, but higher surface area and higher micropore volume compared to 2D zeolites RRO and STT.

The single-pulse ^{29}Si MAS NMR spectra of calcined high-silica AEI and RRO are showed in Figure 7.4a. Only two peaks are observed for AEI, one very small peak at chemical shift δ of about -101 ppm is assigned to $\text{Si}(\text{OSi})_3\text{OH}$, a surface Q^3 -silicate group carrying one hydroxyl functionality, and the other much larger peak at ~ -111.5 ppm is assigned to Q^4 ($\text{Si}(\text{OSi})_4$) species. The observation of just one Q^4 peak could be the result a very similar geometric environment of three T-atoms within the asymmetric unit of the AEI framework. The cross-polarization ^1H - ^{29}Si CP MAS NMR spectrum (not shown) of this sample shows one peak in the Q^3 region at the same positions that the MAS spectrum. The absence of connectivity defects in RRO zeolite is supported by the results of the ^{29}Si MAS NMR spectra, which showed no resonance at about 100 ppm indicative of Si-OH connectivity defects after calcination. We observed 4 peaks (110-116 ppm) belonging to Q^4 species by the ^{29}Si MAS NMR spectrum of this zeolite (Figure 7.4a), that is, one additional signal compared to a report by Gies et al [32]. There are 5 T-atoms in the RRO asymmetric unit and the observation of four peaks further confirms the high quality of the RRO sample synthesized here. The single pulse ^{29}Si MAS (Figure 7.4b) and the ^1H - ^{29}Si CP MAS NMR spectra of siliceous CHA and SSZ-23 (STT) are all similar to the above spectra showing very low concentration of defects sites in the samples synthesized in HF medium, as expected.

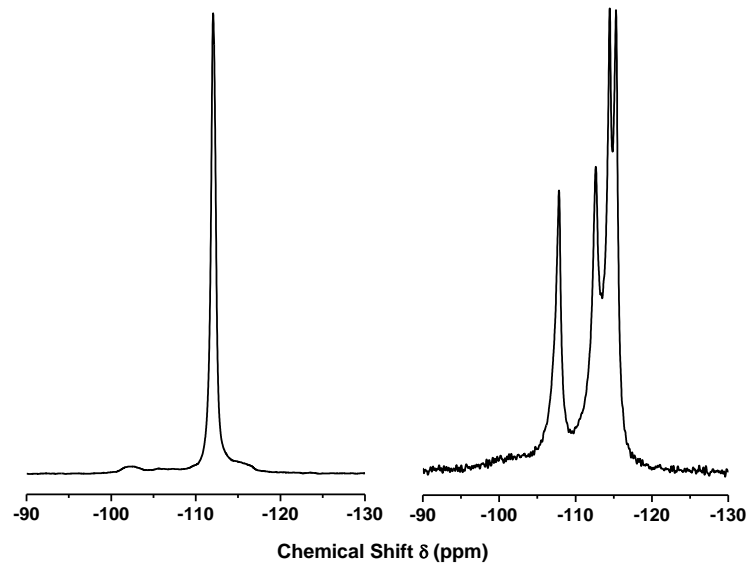


Figure 7.4a. ^{29}Si MAS NMR spectra of AEI (left) and RRO (right) siliceous zeolites

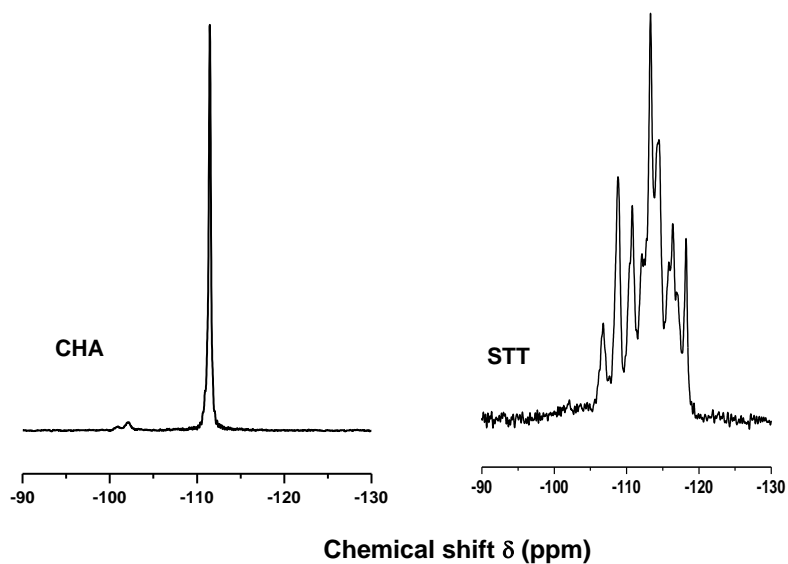


Figure 7.4b. ^{29}Si MAS NMR spectra of CHA (left) and STT (right) siliceous zeolites

7.3.2 Adsorption isotherms

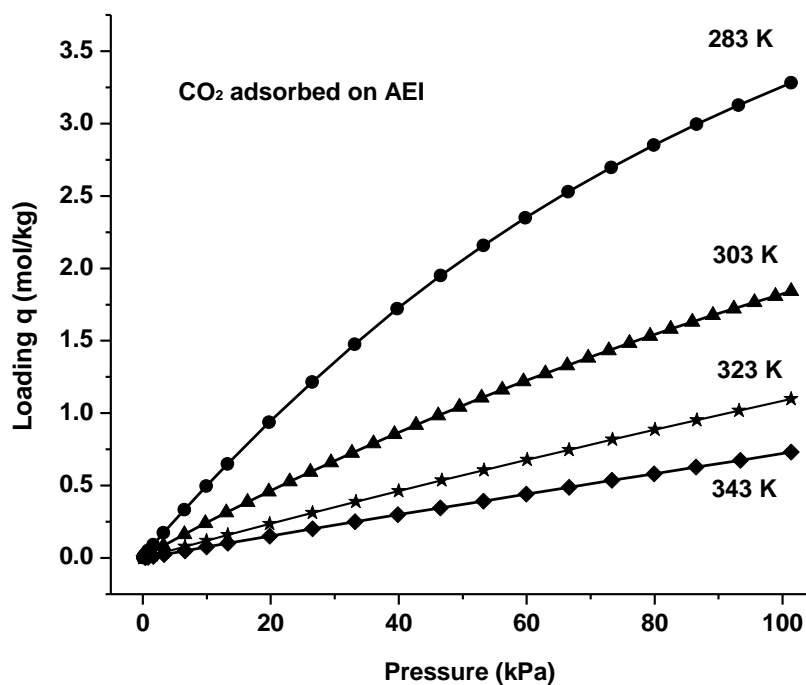
The physical properties of adsorbates are presented in Table 7.2.

Table 7.2. Properties of adsorbate gases: Kinetic diameters (K.D, Å), liquid volume (L.V, cm³/mol), Polarizability (P, x10²⁵ cm³), Dipole moment (D, x10¹⁸ esu.cm), Quadrupole (Q, x10²⁶ esu.cm²) [38]

Gas	K.D	L.V	P	D	Q
CH₄	3.8	37.8	26	0	0
C₂H₄	4.16	49.4	42.5	0	1.5
C₂H₆	4.44	55	44.5	0	0.65
C₃H₆	4.68	69.1	62.6	0.37	-
C₃H₈	4.75	75.7	63.8	0.08	-
CO₂	3.3	37.4	29.1	0	4.3
N₂	3.64	34.7	17.4	0	1.52

Adsorption isotherms of all adsorbates up to a total pressure of 101.3 kPa (Figure 7.5) reveal important differences between the properties of the adsorbates investigated (Table 7.2). The adsorption isotherms for each adsorbate (Figure 7.5) show a gradual decrease in the adsorbed amount with increasing temperature as typical behaviors of physical adsorption. The larger polarizability of CH₄ compared to N₂ leads to a stronger adsorption enthalpy despite the quadrupole moment of N₂, even in the presence of strong electric fields [39, 40]. In siliceous zeolites, materials with low gradient electric field, our results indicated that CH₄ is preferentially adsorbed compared to N₂ (Figure 7.6). The adsorption isotherms at low adsorbate loading indicate that adsorption capacity correlates mostly with polarizability. Siliceous zeolites adsorbed longer chain hydrocarbons preferably until the maximum adsorption capacity is reached. For the materials investigated, the slope of the isotherm for C₂ hydrocarbons is higher than C₃ hydrocarbons at a pressure near 101 kPa (Figures 7.5

and 7.6) because zeolites were saturated by C_3 hydrocarbons but by not C_2 hydrocarbons at this point. The electrostatic component of the heat of adsorption between CO_2 and the hydrophobic zeolites contributes 20-30% of the total adsorption heats due to the high quadrupole moment of CO_2 . This leads to higher adsorption heats and adsorption capacities of CO_2 compared to CH_4 (Figure 7.5). C_2 hydrocarbons are more polarizable than CO_2 , thus they adsorbed on STT zeolite preferentially over CO_2 in the low-pressure regions. However, more CO_2 molecules can be packed efficiently at high pressure due to lower liquid volume of CO_2 .



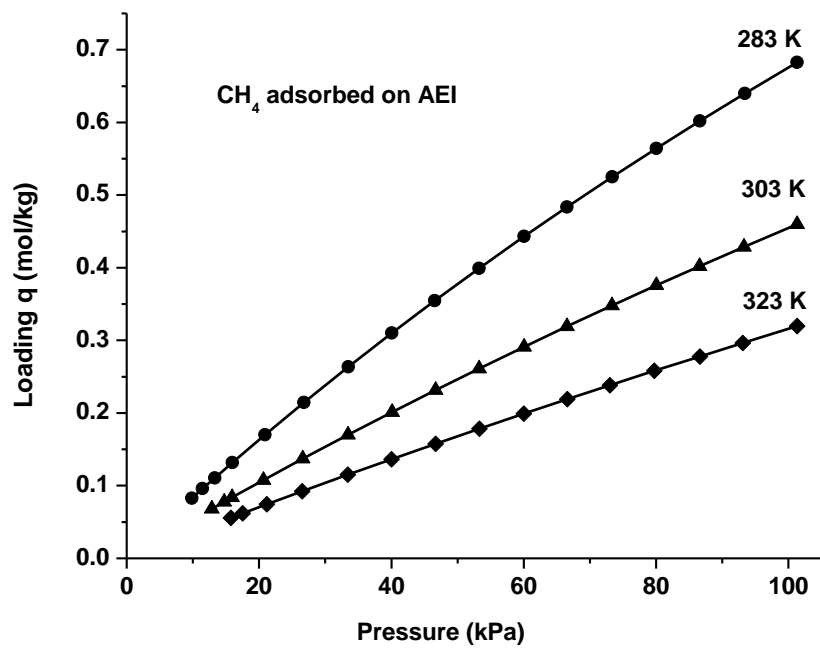


Figure 7.5a. Adsorption isotherms of CO₂ and CH₄ on AEI zeolite at various temperatures up to pressure 101.325 kPa

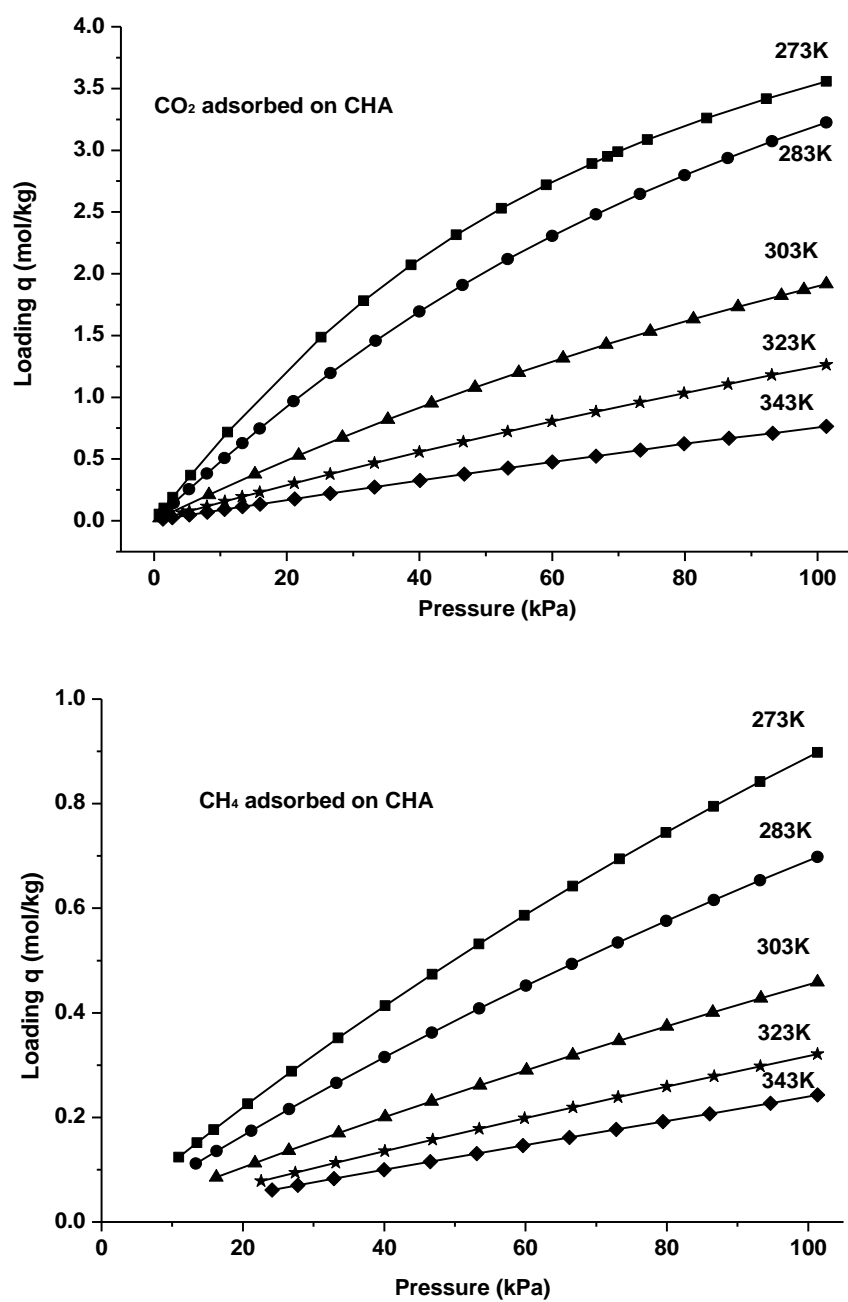


Figure 7.5b. Adsorption isotherms of CO₂ and CH₄ on CHA zeolite at various temperatures up to pressure 101.325 kPa

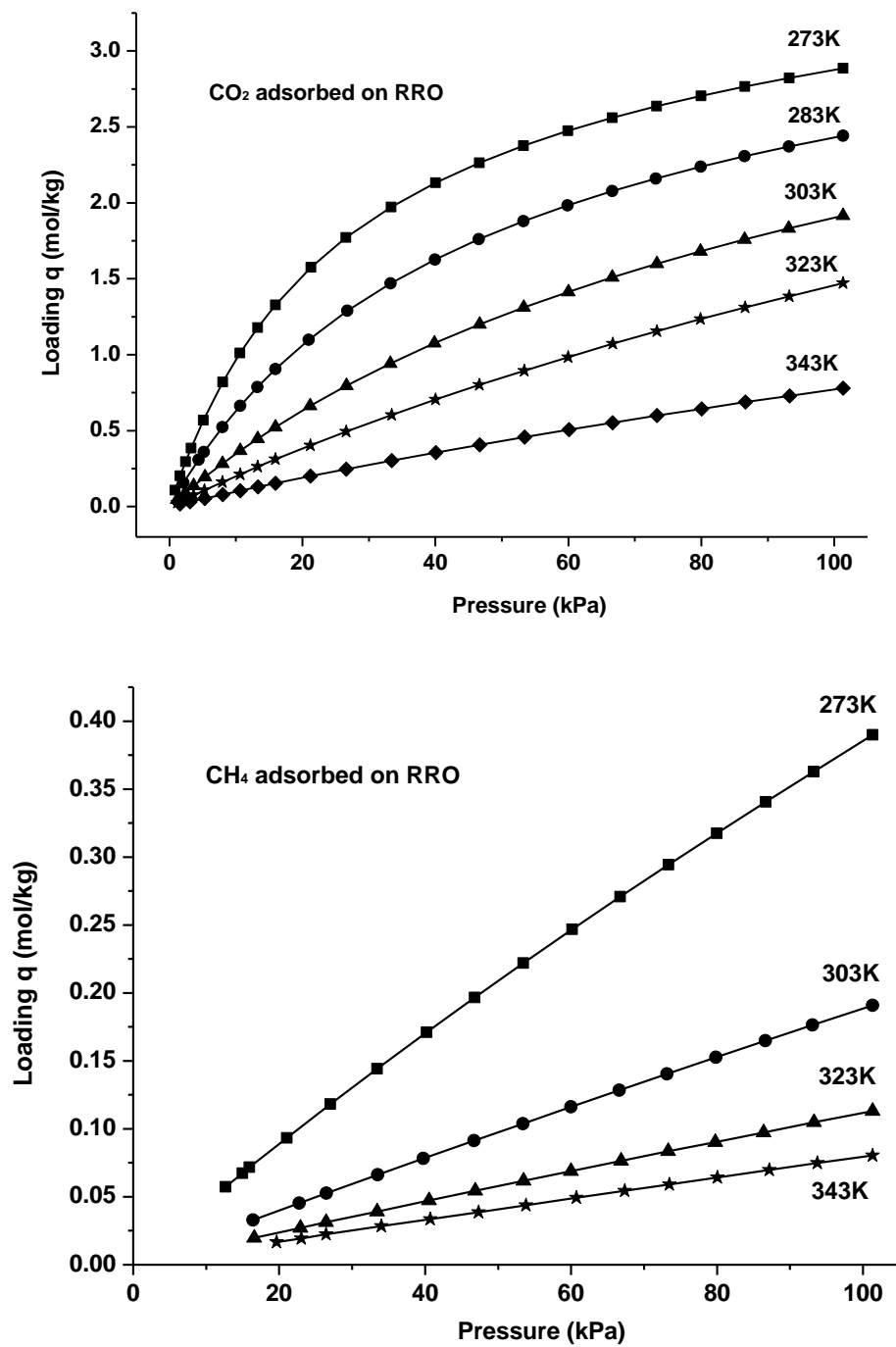


Figure 7.5c. Adsorption isotherms of CO₂ and CH₄ on RRO zeolite at various temperatures up to pressure 101.325 kPa

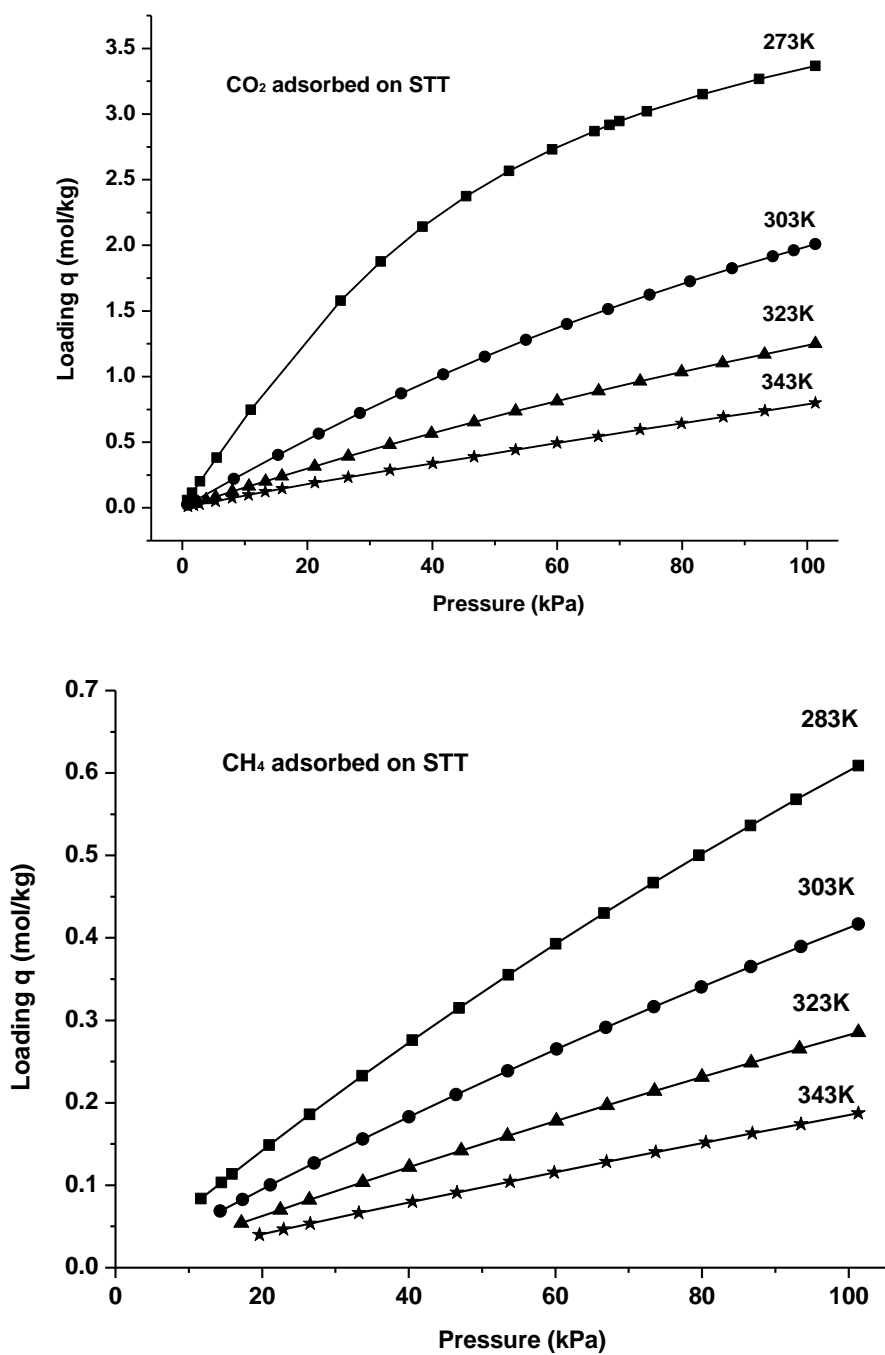


Figure 7.5d. Adsorption isotherms of CO₂ and CH₄ on STT zeolite at various temperatures up to pressure 101.325 kPa

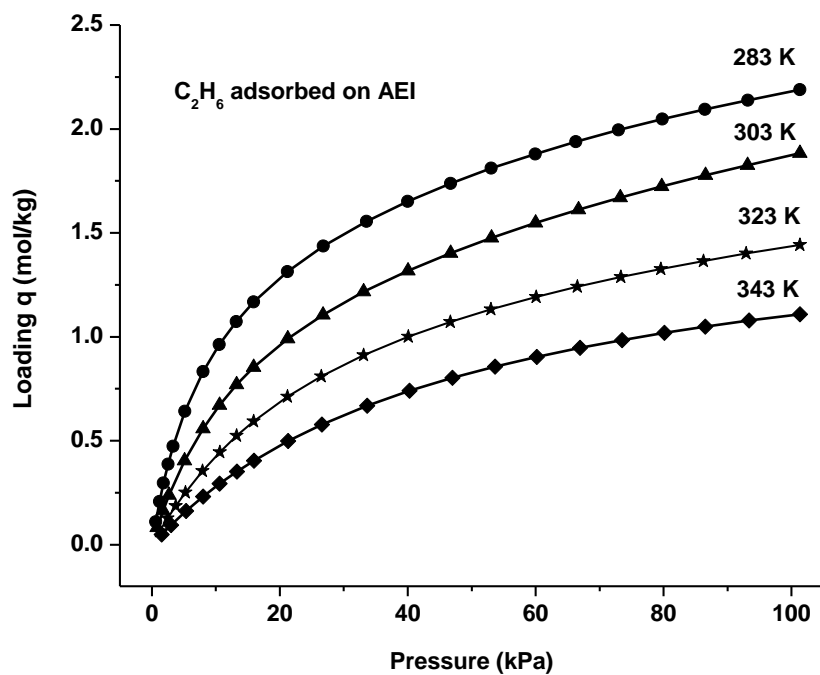
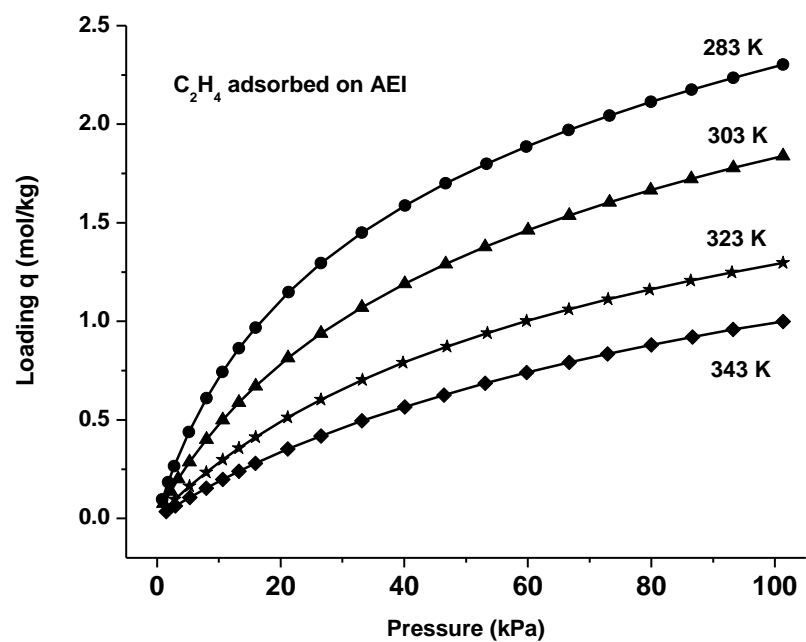


Figure 7.5e. Adsorption isotherms of C_2H_4 and C_2H_6 on AEI zeolite at various temperatures up to pressure 101.325 kPa

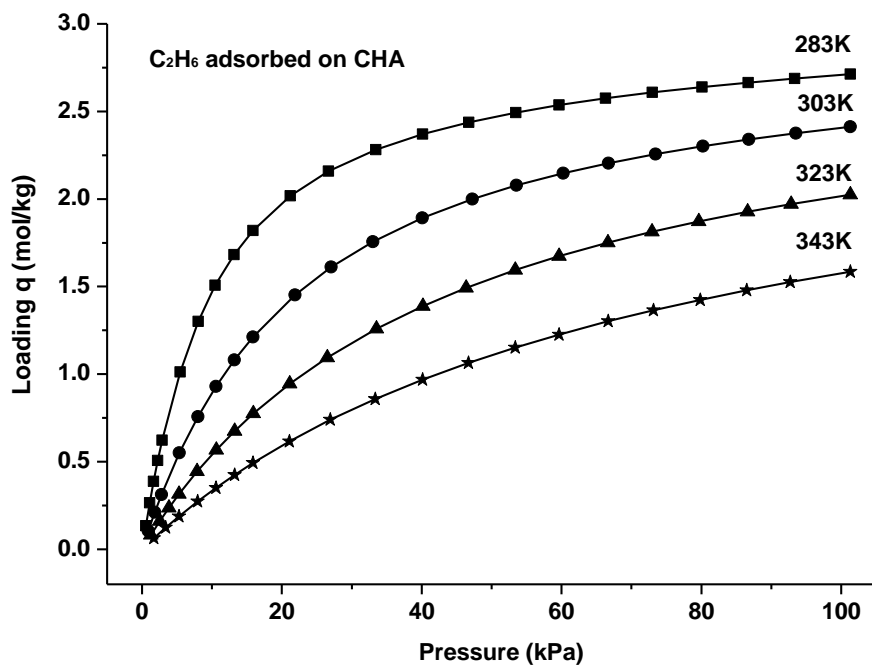
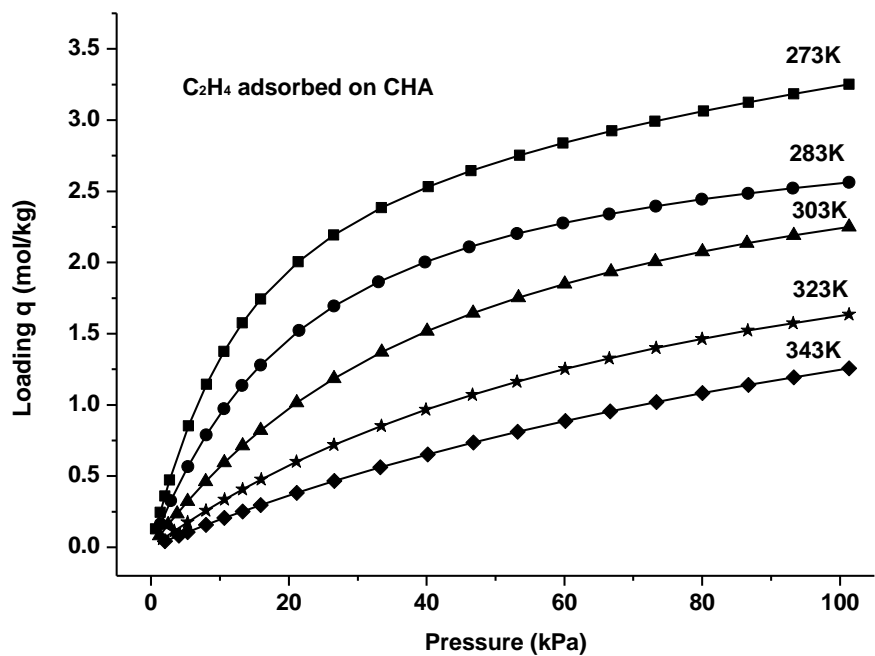


Figure 7.5f. Adsorption isotherms of C₂H₄ and C₂H₆ on CHA zeolite at various temperatures up to pressure 101.325 kPa

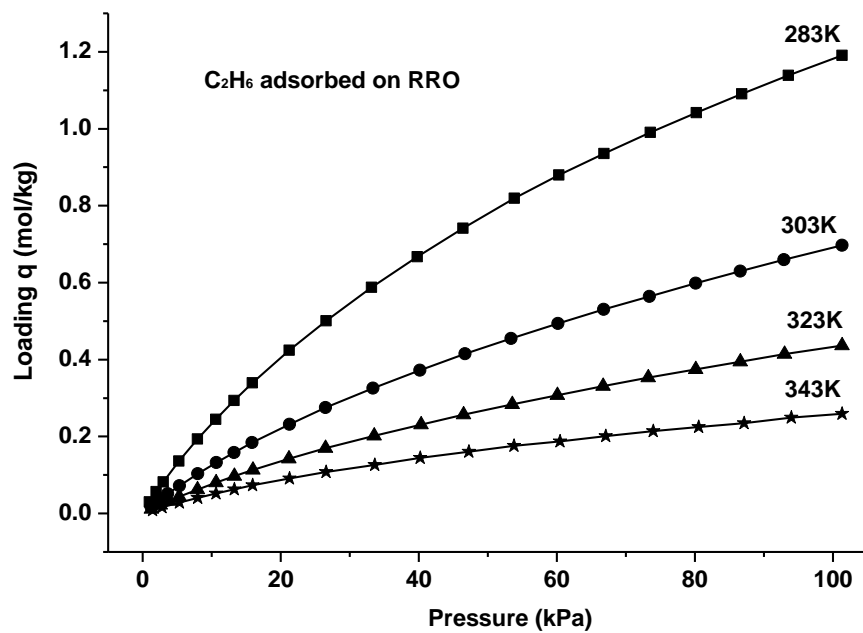
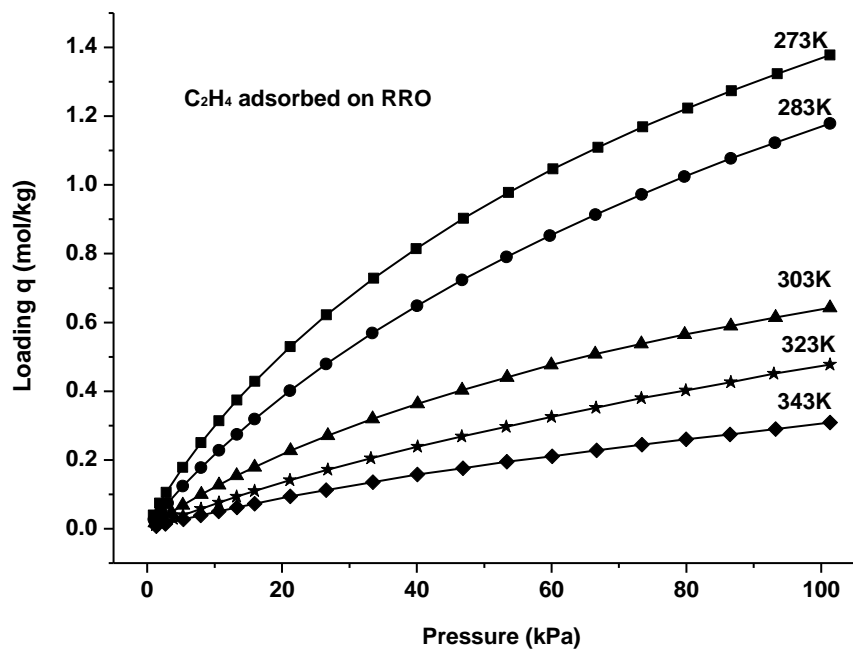


Figure 7.5g. Adsorption isotherms of C₂H₄ and C₂H₆ on RRO zeolite at various temperatures up to pressure 101.325 kPa

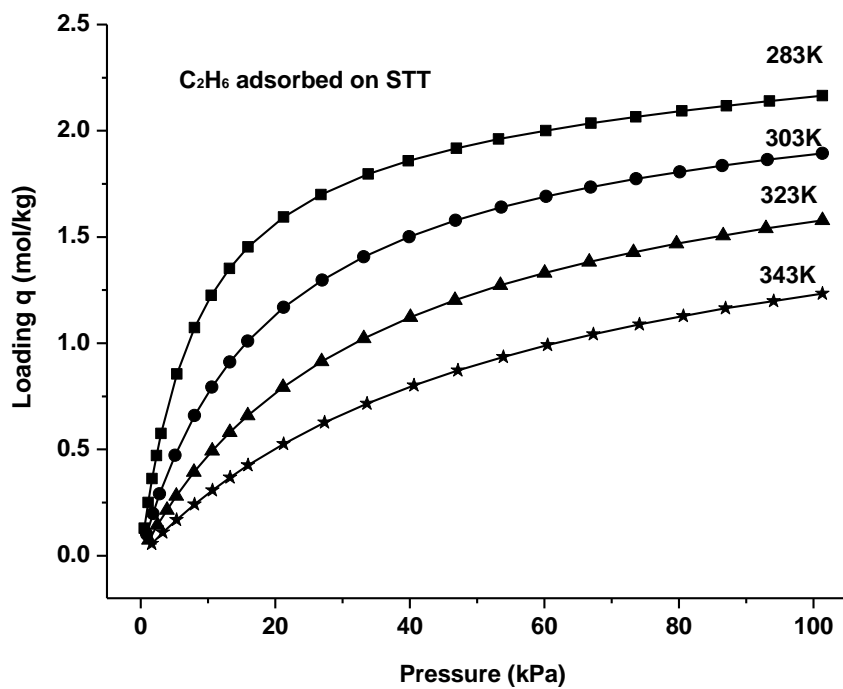
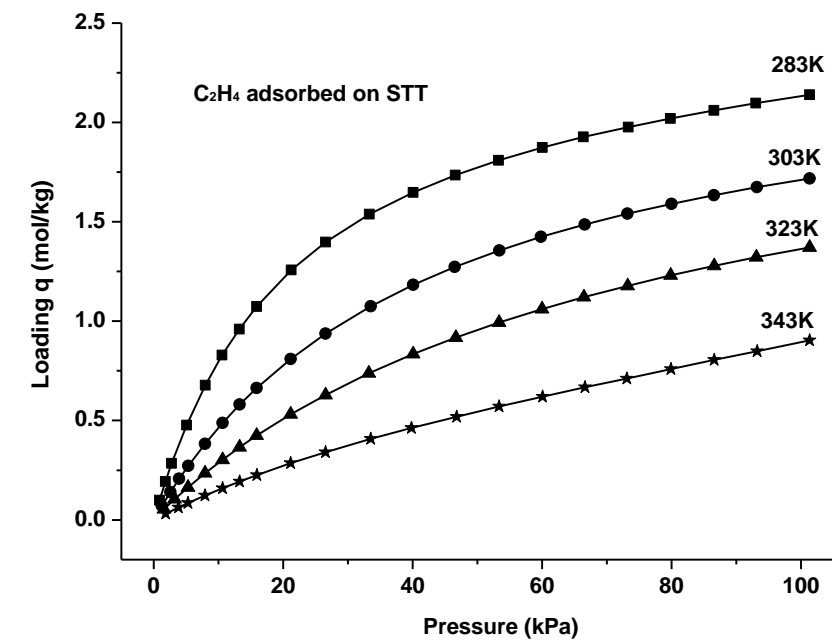


Figure 7.5h. Adsorption isotherms of C₂H₄ and C₂H₆ on STT zeolite at various temperatures up to pressure 101.325 kPa

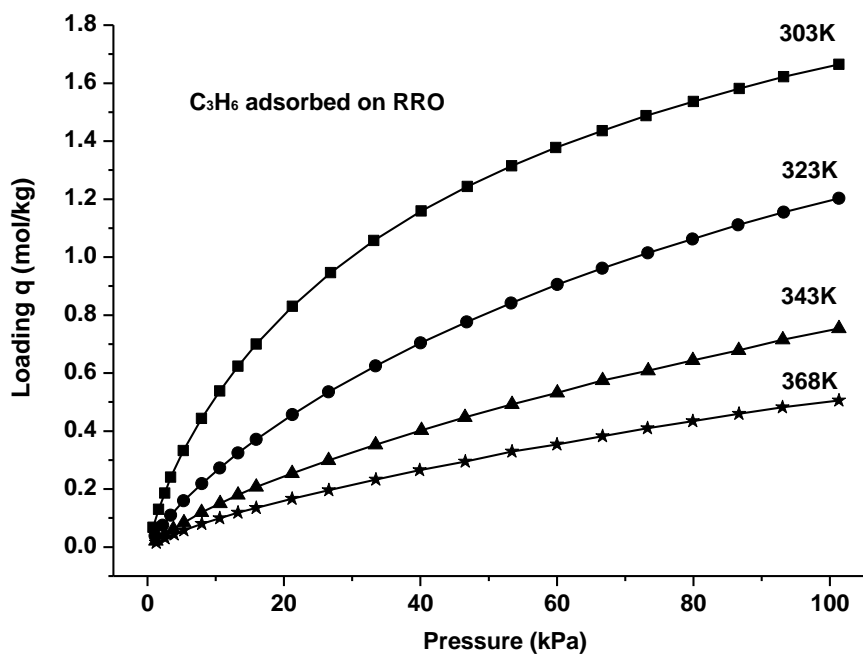
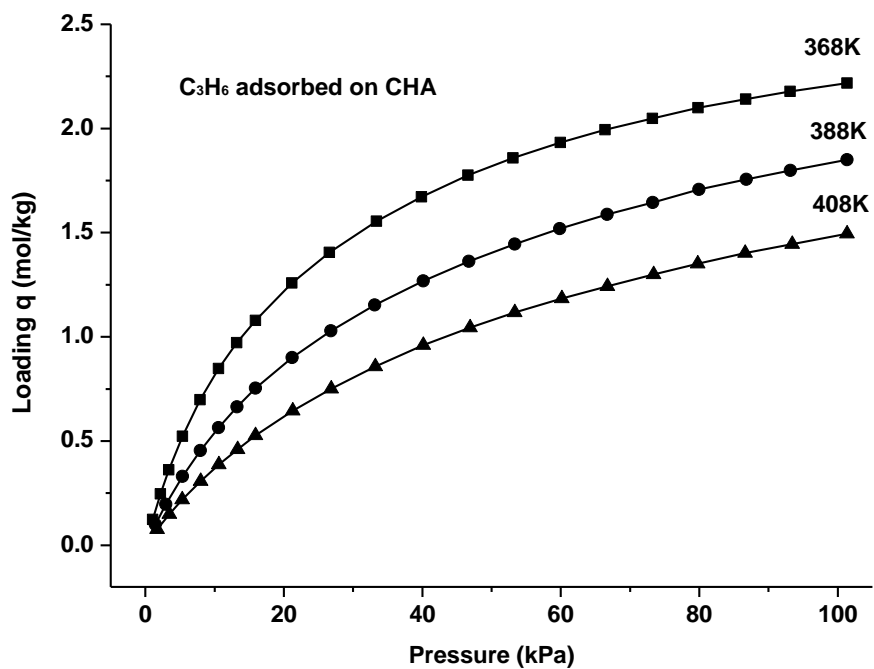


Figure 7.5i. Adsorption isotherms of C₃H₆ on CHA and RRO zeolites at various temperatures up to pressure 101.325 kPa

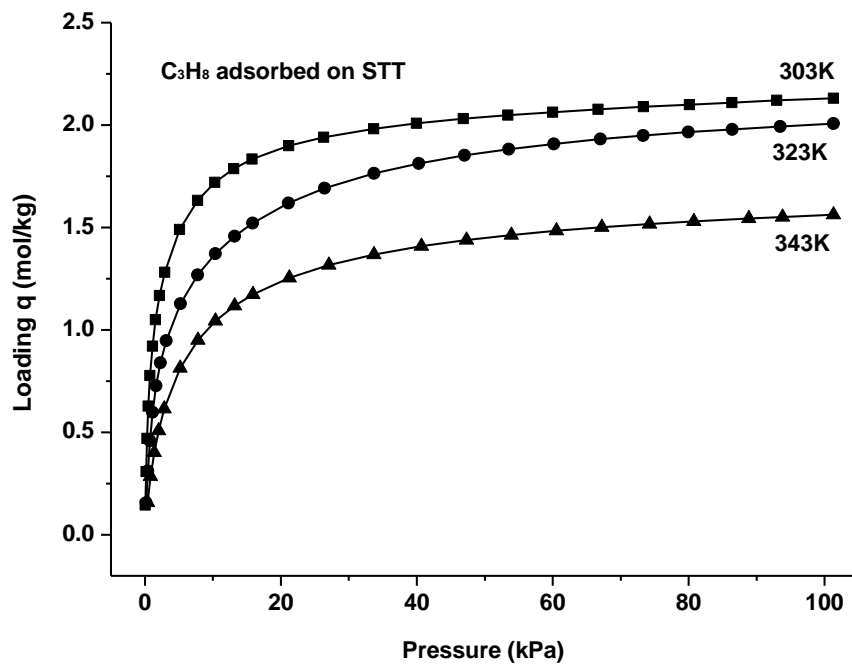
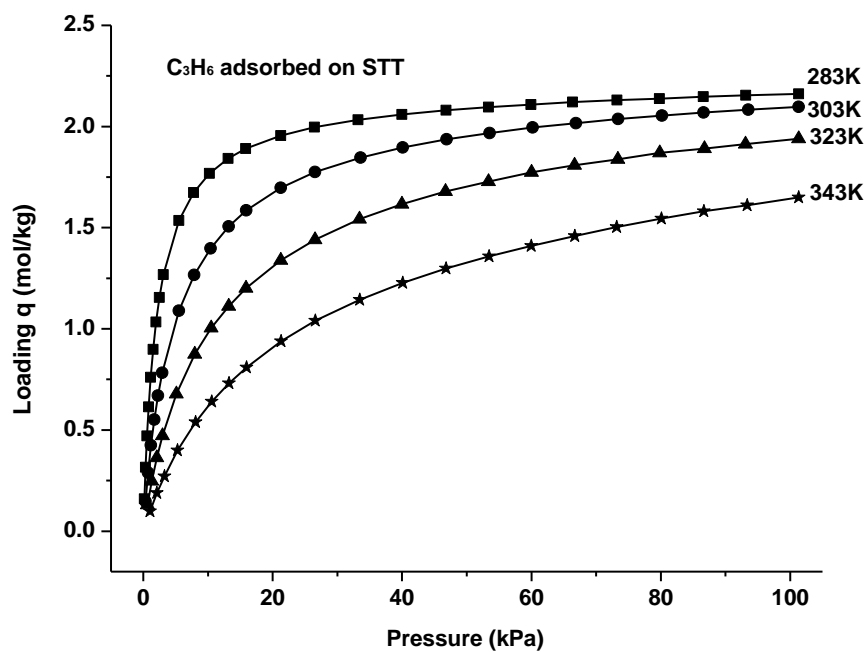


Figure 7.5j. Adsorption isotherms of C₃H₆ and C₃H₈ on STT zeolite at various temperatures up to pressure 101.325 kPa

Smit *et al* [41] used Grand Canonical Monte Carlo (GCMC) simulations to screen thousands of pure silica zeolites to identify optimum structures for the separation of ethane/ethylene mixtures. Most of the zeolite structures are not suitable for thermodynamic or kinetic separations of ethane/ethylene due to the geometric and physical similarities between the two gas molecules. However, the separation of C₂ from C₃ hydrocarbons are feasible based on the diffusion parameters of these compounds in 8-ring zeolites estimating by molecular dynamics simulations [42, 43]. We also observed from our experiments that the adsorption isotherms of C₃ in AEI, CHA, and RRO zeolites need to be collected at higher temperatures than the adsorption isotherms of C₂, indicating that C₂ has fast diffusion compared to C₃. In addition, the 8MR window have good match with the molecular geometry of propene allowing it to diffuse and be adsorbed much more rapidly than propane [6, 13, 30, 44]. The narrow 10MR material RRO has aperture dimensions compared to the 8MR of siliceous chabazite (Figure 7.1) and could present potential for the kinetic separation of C₂/C₃ and propylene/propane mixtures. We were unable to collect propane adsorption isotherms on siliceous AEI, CHA, and RRO at temperatures below 423 K due to the slow diffusion of propane into these zeolite structures. The pore openings of these three zeolites can discriminate between molecules with similar sizes, revealing potential for propane/propane separations. Due to the small pore apertures of RRO zeolites, the material shows low adsorption capacity for CH₄, C₂H₄, and C₂H₆ (Figure 7.7) compared to other zeolites even though the adsorption heats calculated for hydrocarbons on RRO zeolite are quite similar to adsorption heats of other zeolites (Table 7.3).

Snurr *et al.* [45] have indicated that the important features of nanoporous materials controlling methane adsorption are primarily surface area, followed by free volume, framework density, and heats of adsorption. In agreement with their predictions, the materials with the highest surface area, AEI- and CHA- zeolites, showed the highest methane adsorption capacity. Pore size and shape also affect how adsorbate molecules bind in porous solids. Since AEI, CHA, and STT contain similar pore cavities (Figure 7.1), the interactions of the zeolite walls with adsorbate molecules are similar among these zeolites at low pressure of adsorbates. This leads to similar adsorption capacity at low adsorbate loading (Figure 7.7). Since the free volumes of three-dimensional zeolites AEI and CHA are higher than that of the two-dimensional RRO and STT, they have more efficient molecular packing hydrocarbons in the larger cavities of AEI, CHA compared with two dimensional of RRO/STT. The adsorption capacity of AEI at high pressure is lower than that of CHA zeolite, especially in the case of the larger hydrocarbons. This likely due to the pear-shaped cavity of AEI that may not be efficient for hydrocarbon packing compared to the ellipsoidal cavity of CHA.

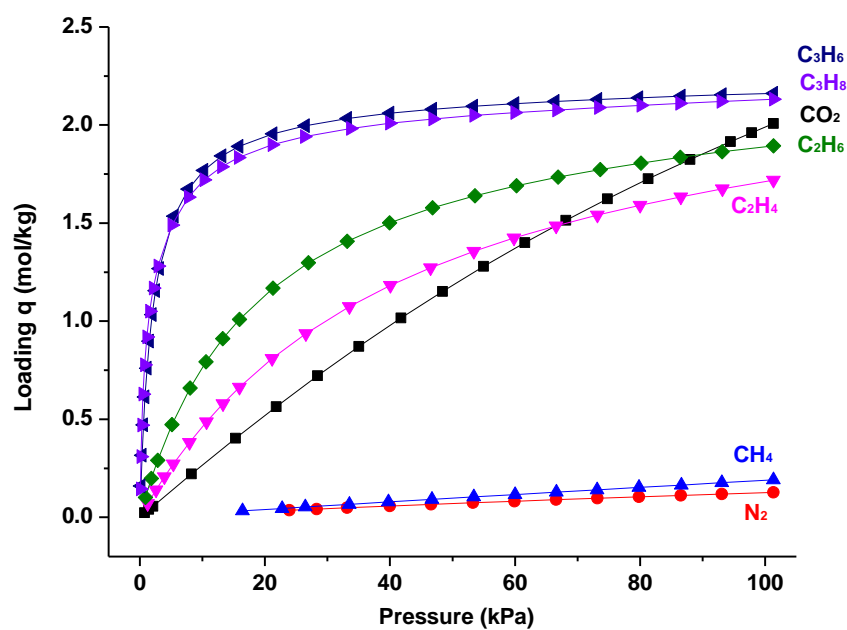


Figure 7.6. Adsorption isotherms of CO_2 , N_2 , CH_4 , C_2H_4 , C_2H_6 , C_3H_6 and C_3H_8 on STT siliceous zeolite at ambient temperature (303K) up to pressure 101.325 kPa

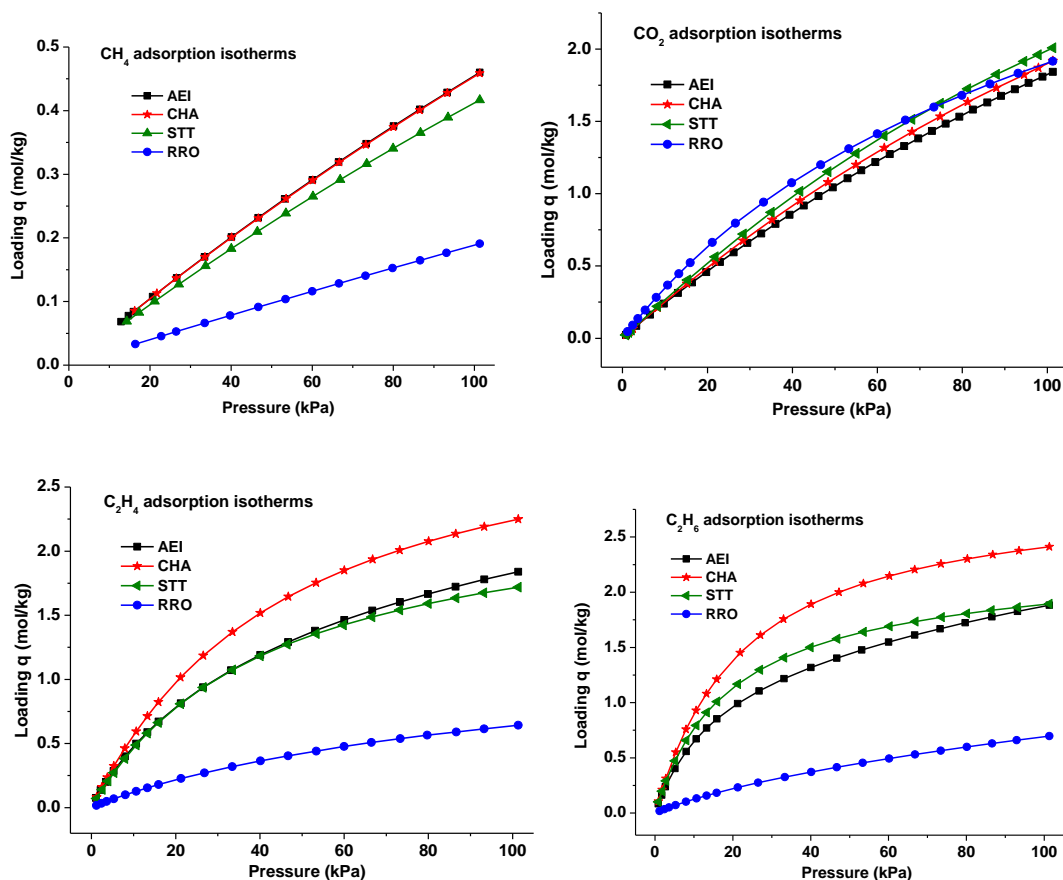


Figure 7.7. Adsorption isotherms of CO₂, CH₄, C₂H₄, and C₂H₆ on AEI, CHA, STT, and RRO siliceous zeolites at ambient temperature (303 K) up to pressure 101.325 kPa

7.3.3 Enthalpy and entropy of adsorption of CO₂ and hydrocarbons in siliceous zeolites

Adsorption enthalpies at the limit of zero coverage were calculated based on equation 7.3 and 7.4 (Table 7.3). The heats of adsorption of light alkanes in siliceous chabazite are similar to results reported by Olson *et al.* [13] (Q_o^{st} for propene, ethane, and ethene are 33.5, 28.9, and 27.2 kJ/mol, respectively). RRO has the most confined pore system among the studied zeolites and it showed the highest adsorption heats of

CO₂ and CH₄ (Table 7.3). This material also showed the highest pure-gas selectivity for CO₂/CH₄, indicating a potential for CO₂ separations from natural gas. Methane is a neutral probe due to the lack of any permanent electric moment. As such, similar methane enthalpy for adsorption has been observed in zeolites with similar pore structures (AEI, CHA and STT). The presence of small amount of Al in AEI framework may lead to slightly higher electric fields within the AEI cage, as compared to other zeolites. This leads to a higher quadrupole-electric field gradient interaction between CO₂ and this zeolite. This difference explains the larger zero coverage adsorption heat of CO₂ on AEI.

Table 7.3. Adsorption heats at zero coverage limit (Q_o^{st}) of gases and selectivity (Sel) of CO₂/CH₄ over studied zeolites

Ads	Q_o^{st} (kJ/mol)						Sel CO ₂ /C ₁₄
	CO ₂	C ₁₄	C ₂₄	C ₂₆	C ₃₆	C ₃₈	
AEI	26.2	16.6	23.4	26.7	-	-	4.7
CHA	23.1	16.8	25.5	26.4	33.8	-	5
STT	23.5	15.9	25.8	27.0	34.8	35.9	5.4
RRO	28.6	18.5	22.4	23.0	33.2	-	20

The isosteric heats of adsorption of small hydrocarbons at the limit of zero coverage increased as the polarizability of the adsorbates increases (Table 7.3), as was observed by Talu *et al.* [46]. Previous experimental [47-49] and simulation investigations [50-53] have shown that heats of adsorption in siliceous MFI increase approximately 10 kJ/mol with each carbon atom in the alkane chain. The data in Table 7.3 indicate that the incremental heat of adsorption per carbon atom is also about 10 kJ/mol for AEI, CHA, and STT adsorbents, but not in the case of RRO zeolite. This in

probably related to the pore size and tortuosity on the adsorption of hydrocarbons which has been studied by Lercher *et al* [54] in a number of zeolites frameworks.

Polarizability and permanent polar/quadrupole moments (Table 7.1) contribute important to the energy of interaction between gases and zeolite adsorbents.

Hydrophobic zeolites adsorb polar molecules to a lesser extent and preference for saturated hydrocarbons over unsaturated hydrocarbons is observed in Table 7.3 and Figure 7.6. On the other hand, hydrophilic zeolites have higher values of heats of adsorption at zero coverage of unsaturated hydrocarbon (ethylene) compared to saturated hydrocarbon (ethane). The large adsorption heats of unsaturated hydrocarbons arise from the electrostatic interaction of the π electrons of the double bond with the large electric field gradients, as has been observed in NaY [55] (23.6 and 36.5 kJ/mol, respectively) and in a recent study in Na-chabazite (Si/Al=6 with 31.6 and 40.8 kJ/mol, respectively). This phenomenon could be practically importance for the removal of small amounts of olefin impurities from hydrocarbon streams in refineries.

Adsorption entropies were obtained using equation 7.5 (Table 7.4). As observed, a general trend was observed for higher adsorption enthalpy correlated with an entropic cost as it leads to a loss in degrees of freedom. The limiting heat of adsorption of alkanes on STT zeolite is plotted against the polarizability of the adsorbates and the adsorption entropies (Figure 7.8). The results indicated that the limiting heat of adsorption increases linearly with polarizability, the adsorption entropies, and carbon number in *n*-alkanes (compensation effect) [35, 46].

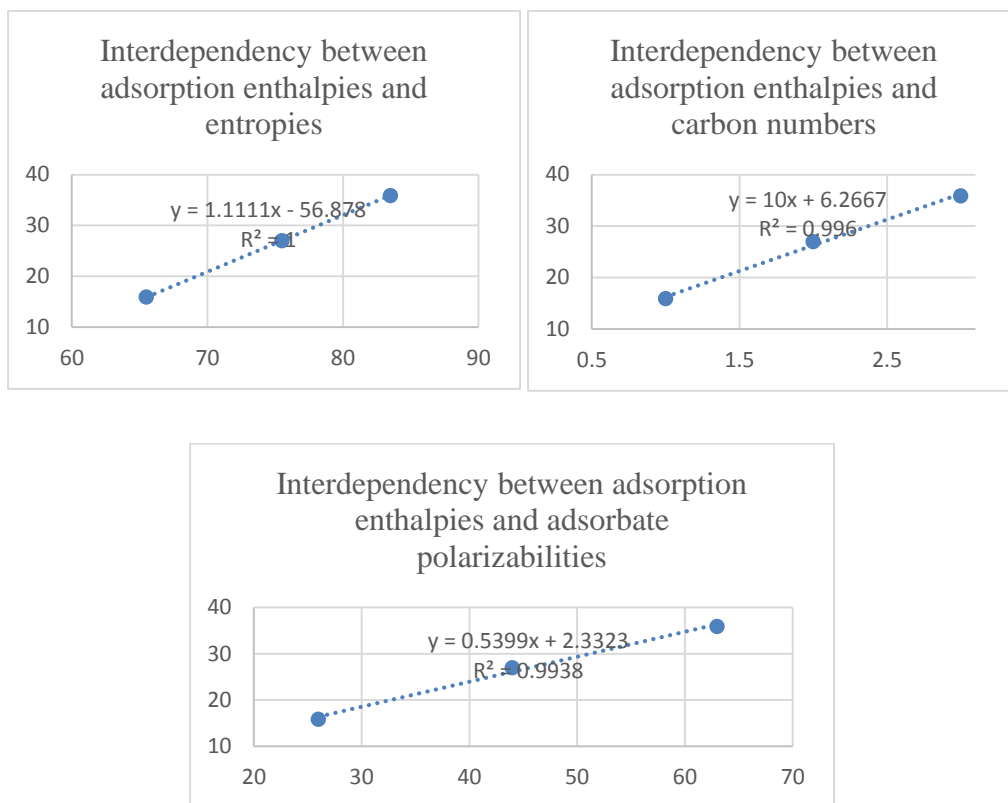


Figure 7.8. Interdependency between adsorption enthalpies and adsorbate polarizabilities, adsorption entropies, and the number of C atoms of alkanes in STT zeolite

Table 7.4. Experimental adsorption entropies of adsorbates in siliceous zeolites. The standard state for the gas phase hydrocarbons is taken as $P_o = 10^5$ Pa

Adsorbent	ΔS (J K ⁻¹ mol ⁻¹)					
	CO ₂	C ₁₄	C ₂₄	C ₂₆	C ₃₆	C ₃₈
AEI	91.5	68.5	72.3	74.2	-	-
CHA	83.5	70	77.8	74.4	81.4	-
STT	84.2	65.5	77	75.5	83	83.5
RRO	88.5	75.5	78.6	80.9	92.5	-

Isosteric heats of adsorption, Q_{st} , as a function of loading (Figure 7.9) were obtained from the isotherm data using the *Clausius–Clapeyron* equation. Materials

such as low silica zeolites have a heterogeneous adsorption landscape in which adsorbates will occupy the lower energy positions at low loading and higher energy positions at higher loading. This results in a decrease in the heat of adsorption with gas loading. Siliceous zeolites, in contrast, may be regarded as energetically homogeneous adsorbents because the absence of ions and OH- groups representing energetically preferred adsorption sites. Electrostatic energies are small in comparison to van der Waals energy, therefore the major adsorption energy contribution is related to the dispersion and repulsion terms. An increase in the heat of adsorption with gas loading (Figure 7.9) is characteristic of homogeneous adsorbents with constant gas-solid and increased adsorbate-adsorbate energies of interactions. The heat of adsorption of small gases such as CO₂, CH₄ increases only slightly over the whole range of coverage. However, as the size of the hydrocarbons increases, adsorbate-adsorbate interactions become more significant and the increase in the adsorption heat is more obvious. In the case of AEI zeolite, we observed a small decrease in adsorption heat of ethylene and ethane up to a coverage of 0.5-0.6 mmol/kg. The decrease in heat of adsorption with gas loading is characteristic of heterogeneous adsorbent with a wide distribution of gas-solid interaction energies caused either by the shape of AEI cavity or the presence of Al in this adsorbent.

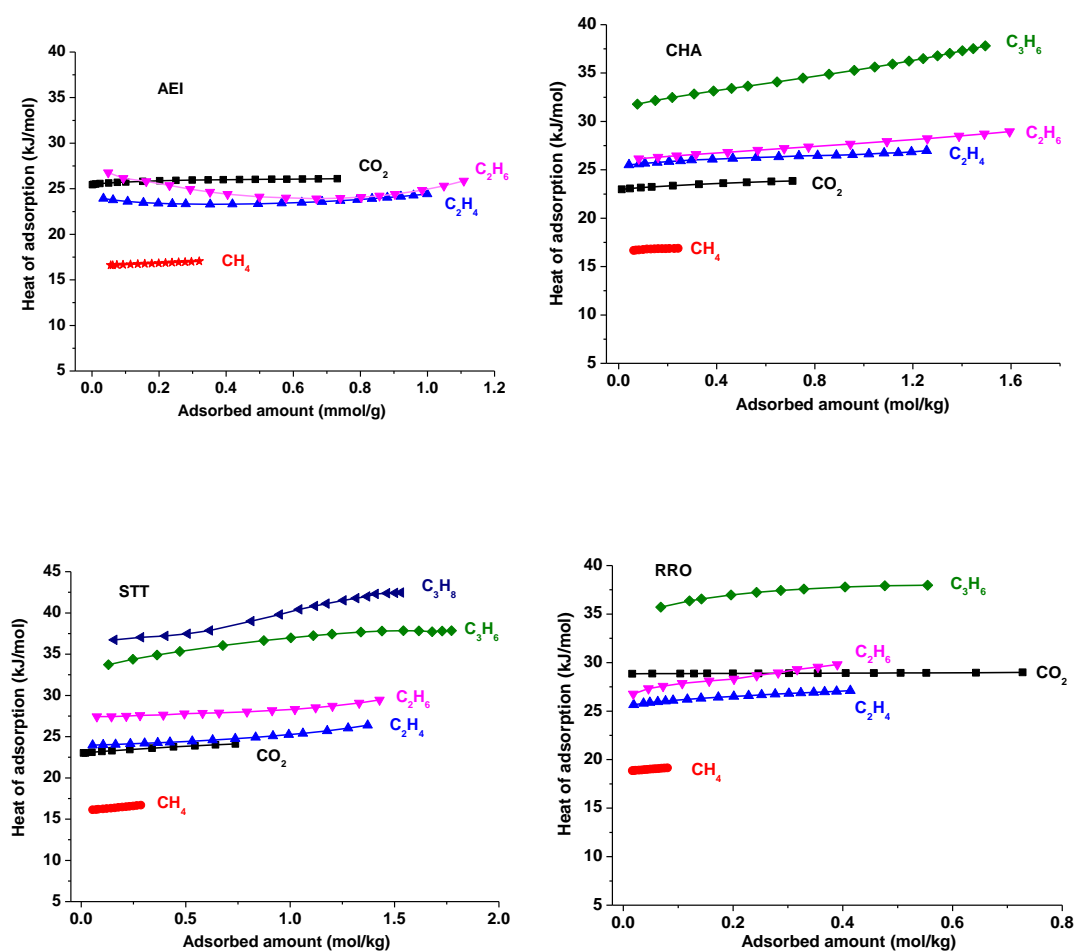


Figure 7.9. Adsorption heats of CO₂ and small hydrocarbons adsorbed on AEI, CHA, STT, and RRO siliceous zeolites

7.4 Conclusions

Hydrophobic siliceous zeolites of framework types AEI, CHA, RRO, and STT were prepared with low silanol group concentration, and fully characterized by analytical methods. The adsorption of CO₂ and light hydrocarbons has been investigated using volumetric adsorption isotherms. The polarizability affects significantly the adsorption properties such as adsorption capacities, enthalpies and

entropies of the hydrocarbons in the siliceous zeolites. For all the siliceous zeolites we have studied, the calculated heat of adsorption was found to increase linearly with alkane chain length, and alkanes adsorbed stronger than alkenes. Although the contribution of quadrupole- electric field gradient between CO₂ and siliceous zeolites to the total adsorption energy is low in comparison with low silica zeolites, we still observed a significant difference in the adsorption heats and adsorption capacity of CO₂ over CH₄ in these siliceous zeolites. With narrow pore openings, RRO seems to be a potential candidate for the separation of CO₂ from methane in natural gas mixture. At high adsorption pressure, lower liquid volume adsorbates pack more efficiently, thus occupied in the zeolite pores with higher concentration. The steric hindrance in AEI, CHA, and RRO zeolites allow only propylene to diffuse into the materials pores, but exclude larger molecules. The feasibility of AEI, CHA, and RRO zeolites for propane-propylene separations based on both kinetic and adsorption equilibria needed to be further studied, particularly measuring the diffusion coefficients. Our experimental data is also useful for testing the validity of the assumptions and calculated adsorption isotherms using gas-solid molecular simulations.

REFERENCES

1. Kh. M, M. and I. Ya. I, *Catalytic Properties of Zeolites?A General Review*, in *Molecular Sieves*. 1973, AMERICAN CHEMICAL SOCIETY. p. 451-460.
2. Primo, A. and H. Garcia, *Zeolites as catalysts in oil refining*. Chemical Society Reviews, 2014. **43**(22): p. 7548-7561.
3. Cheung, O. and N. Hedin, *Zeolites and related sorbents with narrow pores for CO₂ separation from flue gas*. RSC Advances, 2014. **4**(28): p. 14480-14494.
4. Li, J., et al., *Low-temperature selective catalytic reduction of NO_x with NH₃ over metal oxide and zeolite catalysts—A review*. Catalysis Today, 2011. **175**(1): p. 147-156.
5. Kesraoui-Ouki, S., C.R. Cheeseman, and R. Perry, *Natural zeolite utilisation in pollution control: A review of applications to metals' effluents*. Journal of Chemical Technology & Biotechnology, 1994. **59**(2): p. 121-126.
6. Reyes, S.C., et al., *Light hydrocarbon separation using 8-member ring zeolites*. 2008, Google Patents.
7. Saada, M.A., et al., *High-Pressure Water Intrusion Investigation of Pure Silica RUB-41 and S-SOD Zeolite Materials*sleng. Journal of Physical Chemistry C, 2011. **115**(2): p. 425-430.
8. Trzpit, M., et al., *Pure silica chabazite molecular spring: A structural study on water intrusion-extrusion processes*. Journal of Physical Chemistry B, 2008. **112**(24): p. 7257-7266.
9. Flanigen, E.M., et al., *Silicalite, a New Hydrophobic Crystalline Silica Molecular-Sieve*. Nature, 1978. **271**(5645): p. 512-516.
10. Niu, G.X., et al., *Thermal and hydrothermal stability of siliceous Y zeolite and its application to high-temperature catalytic combustion*. Applied Catalysis B-Environmental, 1999. **21**(1): p. 63-70.
11. Olson, D.H., *Light hydrocarbon separation using 8-member ring zeolites*. 2002, The Trustees of the University of Pennsylvania, USA . p. 23 pp., Cont.-in-part of U.S. Ser. No. 768,943, abandoned.
12. Eldridge, R.B., *Olefin Paraffin Separation Technology - a Review*. Industrial & Engineering Chemistry Research, 1993. **32**(10): p. 2208-2212.
13. Olson, D.H., et al., *Light hydrocarbon sorption properties of pure silica Si-CHA and ITQ-3 and high silica ZSM-58*. Microporous and Mesoporous Materials, 2004. **67**(1): p. 27-33.
14. Eldridge, R.B., *Olefin/paraffin separation technology: a review*. Industrial & Engineering Chemistry Research, 1993. **32**(10): p. 2208-2212.

15. Zhu, W., F. Kapteijn, and J. A. Moulijn, *Shape selectivity in the adsorption of propane/propene on the all-silica DD3R*. Chemical Communications, 1999(24): p. 2453-2454.
16. Palomino, M., et al., *Zeolite Rho: a highly selective adsorbent for CO₂/CH₄ separation induced by a structural phase modification*. Chemical Communications, 2012. **48**(2): p. 215-217.
17. Palomino, M., et al., *New Insights on CO₂-Methane Separation Using LTA Zeolites with Different Si/Al Ratios and a First Comparison with MOFs*. Langmuir, 2009. **26**(3): p. 1910-1917.
18. Himeno, S., M. Takenaka, and S. Shimura, *Light gas adsorption of all-silica DDR- and MFI-type zeolite: computational and experimental investigation*. Molecular Simulation, 2008. **34**(10-15): p. 1329-1336.
19. Zhu, W., F. Kapteijn, and J.A. Moulijn, *Equilibrium adsorption of light alkanes in silicalite-1 by the inertial microbalance technique*. Adsorption-Journal of the International Adsorption Society, 2000. **6**(2): p. 159-167.
20. Zhu, W., F. Kapteijn, and J.A. Moulijn, *Adsorption of light alkanes on silicalite-1: Reconciliation of experimental data and molecular simulations*. Physical Chemistry Chemical Physics, 2000. **2**(9): p. 1989-1995.
21. Schenk, M., et al., *Separation of alkane isomers by exploiting entropy effects during adsorption on silicalite-1: A configurational-bias Monte Carlo simulation study*. Langmuir, 2001. **17**(5): p. 1558-1570.
22. Krishna, R. and D. Paschek, *Molecular simulations of adsorption and siting of light alkanes in silicalite-1*. Physical Chemistry Chemical Physics, 2001. **3**(3): p. 453-462.
23. O'Malley, A.J. and C.R.A. Catlow, *Molecular dynamics simulations of longer n-alkanes in silicalite: a comparison of framework and hydrocarbon models*. Physical Chemistry Chemical Physics, 2013. **15**(43): p. 19024-19030.
24. Hussain, I. and J.O. Titiloye, *Molecular dynamics simulations of the adsorption and diffusion behavior of pure and mixed alkanes in silicalite*. Microporous and Mesoporous Materials, 2005. **85**(1-2): p. 143-156.
25. Simmen, A., et al., *The structure determination and rietveld refinement of the aluminophosphate AIPO₄-18*. Zeolites, 1991. **11**(7): p. 654-661.
26. Smith, J.V., *CRYSTAL STRUCTURES WITH A CHABAZITE FRAMEWORK .1. DEHYDRATED CA-CHABAZITE*. Acta Crystallographica, 1962. **15**(SEP): p. 835-&.
27. Smith, J.V., L.S.D. Glasser, and F. Rinaldi, *CRYSTAL STRUCTURES WITH A CHABAZITE FRAMEWORK .2. HYDRATED CA-CHABAZITE AT ROOM TEMPERATURE*. Acta Crystallographica, 1963. **16**(1): p. 45-&.
28. Cambor, M.A., et al., *A synthesis, MAS NMR, synchrotron X-ray powder diffraction, and computational study of zeolite SSZ-23*. Chemistry of Materials, 1999. **11**(10): p. 2878-2885.

29. Cambor, M.A., et al., *SSZ-23: An odd zeolite with pore openings of seven and nine tetrahedral atoms*. Angewandte Chemie-International Edition, 1998. **37**(15): p. 2122-2126.
30. Gutiérrez-Sevillano, J.J., et al., *Analysis of the ITQ-12 Zeolite Performance in Propane–Propylene Separations Using a Combination of Experiments and Molecular Simulations*. The Journal of Physical Chemistry C, 2010. **114**(35): p. 14907-14914.
31. Pham, T.D., et al., *Experimental and computational studies on the adsorption of CO₂ and N₂ on pure silica zeolites*. Microporous and Mesoporous Materials, 2014. **185**: p. 157-166.
32. Wang, Y.X., et al., *Synthesis and crystal structure of zeolite RUB-41 obtained as calcination product of a layered precursor: a systematic approach to a new synthesis route*. Chemistry of Materials, 2005. **17**(1): p. 43-49.
33. Zones, S.I., et al., *Synthesis, properties, and applications of small-pore zeolite SSZ-39 for use as petroleum refining catalysts*. 1999, Chevron U.S.A. Inc., USA . p. 13 pp.
34. Cao, G., et al., *Synthesis of AEI-type zeolites and their use in the conversion of oxygenates to olefins*. 2005, Exxonmobil Chemical Patents Inc., USA . p. 33 pp.
35. De Moor, B.A., et al., *Adsorption of C₂–C₈ n-Alkanes in Zeolites†*. The Journal of Physical Chemistry C, 2010. **115**(4): p. 1204-1219.
36. Cambor, M.A., et al., *SSZ-23: An Odd Zeolite with Pore Openings of Seven and Nine Tetrahedral Atoms*. Angewandte Chemie International Edition, 1998. **37**(15): p. 2122-2126.
37. Diaz-Cabanas, M.-J. and P. A. Barrett, *Synthesis and structure of pure SiO₂ chabazite: the SiO₂ polymorph with the lowest framework density*. Chemical Communications, 1998(17): p. 1881-1882.
38. Li, J.R., R.J. Kuppler, and H.C. Zhou, *Selective gas adsorption and separation in metal-organic frameworks*. Chemical Society Reviews, 2009. **38**(5): p. 1477-1504.
39. Dunne, J.A., et al., *Calorimetric heats of adsorption and adsorption isotherms .2. O₂, N₂, Ar, CO₂, CH₄, C₂H₆, and SF₆ on NaX, H-ZSM-5, and Na-ZSM-5 zeolites*. Langmuir, 1996. **12**(24): p. 5896-5904.
40. Liu, B. and B. Smit, *Molecular Simulation Studies of Separation of CO₂/N₂, CO₂/CH₄, and CH₄/N₂ by ZIFs*. Journal of Physical Chemistry C, 2010. **114**(18): p. 8515-8522.
41. Kim, J., et al., *Large-Scale Computational Screening of Zeolites for Ethane/Ethene Separation*. Langmuir, 2012. **28**(32): p. 11914-11919.
42. Combariza, A.F., D.A. Gomez, and G. Sastre, *Simulating the properties of small pore silica zeolites using interatomic potentials*. Chemical Society Reviews, 2013. **42**(1): p. 114-127.

43. Combariza, A.F., G. Sastre, and A. Corma, *Molecular Dynamics Simulations of the Diffusion of Small Chain Hydrocarbons in 8-Ring Zeolites*. The Journal of Physical Chemistry C, 2011. **115**(4): p. 875-884.
44. Zhu, W., F. Kapteijn, and J.A. Moulijn, *Shape selectivity in the adsorption of propane/propene on the all-silica DD3R*. Chemical Communications, 1999(24): p. 2453-2454.
45. Dueren, T., et al., *Design of New Materials for Methane Storage*. Langmuir, 2004. **20**(7): p. 2683-2689.
46. Sun, M.S., et al., *Adsorption Equilibria of C1 to C4 Alkanes, CO2, and SF6 on Silicalite*. The Journal of Physical Chemistry B, 1998. **102**(8): p. 1466-1473.
47. Sun, M.S., et al., *Adsorption Equilibria of C1 to C4 Alkanes, CO2, and SF6 on Silicalite*. J. Phys. Chem. B, 1998. **102**(8): p. 1466-1473.
48. Stach, H., K. Fiedler, and J. Janchen, *CORRELATION BETWEEN INITIAL HEATS OF ADSORPTION AND STRUCTURAL PARAMETERS OF MOLECULAR-SIEVES WITH DIFFERENT CHEMICAL-COMPOSITION - A CALORIMETRIC STUDY*. Pure and Applied Chemistry, 1993. **65**(10): p. 2193-2200.
49. Ryazantsev, Y.P., *EQUILIBRIUM ADSORPTION OF C5-C8 ALKANES ON MGNA ZEOLITE AT CRITICAL-TEMPERATURES*. Zhurnal Fizicheskoi Khimii, 1979. **53**(2): p. 504-506.
50. Smit, B. and J.I. Siepmann, *COMPUTER-SIMULATIONS OF THE ENERGETICS AND SITING OF N-ALKANES IN ZEOLITES*. Journal of Physical Chemistry, 1994. **98**(34): p. 8442-8452.
51. Bates, S.P., et al., *Energetics of n-Alkanes in Zeolites: A Configurational-Bias Monte Carlo Investigation into Pore Size Dependence*. J. Am. Chem. Soc., 1996. **118**(28): p. 6753-6759.
52. Bates, S.P., et al., *Location and conformation of N-alkanes in zeolites: An analysis of configurational-bias Monte Carlo calculations*. Journal of Physical Chemistry, 1996. **100**(44): p. 17573-17581.
53. Smit, B., *SIMULATING THE ADSORPTION-ISOTHERMS OF METHANE, ETHANE, AND PROPANE IN THE ZEOLITE SILICALITE*. Journal of Physical Chemistry, 1995. **99**(15): p. 5597-5603.
54. Eder, F. and J.A. Lercher, *On the Role of the Pore Size and Tortuosity for Sorption of Alkanes in Molecular Sieves*. The Journal of Physical Chemistry B, 1997. **101**(8): p. 1273-1278.
55. Rees, L. and D. Shen, *Chapter 13 Adsorption of gases in zeolite molecular sieves*, in *Introduction to Zeolite Science and Practice*. 2001, Elsevier. p. 579-631.

Chapter 8

CONCLUSIONS AND RECOMMENDATIONS

This thesis reports the synthesis and characterization of a variety of aluminosilicate zeolite materials including low, high and pure silica zeolites. The chabazite (CHA) and ZK-5 (KFI) samples have comparable adsorption capacity, similar to the adsorption capacity of low silica commercial zeolites such as faujasites (zeolites X and Y) and Linde type A (LTA). The adsorption capacities and the heats of adsorption depend closely on the electronic and acid-base properties of cations and zeolite frameworks. Separation parameters have been estimated for the PSA and VSA processes on both of these materials. 8-membered ring (8MR) zeolites with high adsorption heats showed better performance in VSA processes and hydrophobic siliceous zeolites are candidates for PSA processes with flue gas and in the presence of water. The adsorbed CO₂ chemical and physical properties were analyzed by FTIR spectroscopy. Dispersion and quadrupole-electric field gradient interactions of CO₂ with 8MR zeolites, in particular on CHA-type and KFI-type materials play an important role on the adsorption of CO₂. We identified CO₂ binding sites to elucidate the materials structure-property relationship for adsorption. We discovered that the preferred binding sites for CO₂ are within the 8MRs or along a crankshaft-like structure of the zeolites. Three dimensional, cage-like frameworks are necessary for the fast diffusion and accommodation of adsorbate species. Adsorbents containing small cages such as sodalite (SOD) cages could be detrimental to the CO₂ adsorption due to the impenetrability of CO₂ molecules into such systems, but not water. Li-, Na-

zeolites have high CO₂ adsorption capacities and Na-zeolites usually display higher adsorption selectivity of CO₂ over N₂. Large cations such as K, Cs locate at 8MR and show high selectivity of CO₂/N₂, especially in the low silica zeolites when large cations are located in the middle of the 8MR and block the entrance of low adsorption affinity molecules such as N₂ or CH₄. 8MR zeolites are potential for propane/propylene separation, and RRO would be a good candidate for CO₂/CH₄ separation.

8.1 Thesis Summary

In chapter 3 and the related manuscript published on *Chemsuschem* [1], we have shown that 8-membered rings zeolites chabazite (Si/Al = 6, 12) and ZK-5 (Si/Al = 3.75) ion-exchanged with different cations exhibited exceptional CO₂ adsorption working capacity and CO₂/N₂ selectivity. The adsorption isotherms show that all zeolite adsorbents have much higher affinity with CO₂ than with N₂, and Li cation exchanged zeolites give the highest total capacity and selectivity in the Henry's law region. The materials have been estimated for the CO₂ separation using PSA and VSA processes using the criteria suggested by Snurr *et al.* [2]. In general, the adsorbents with intermediate CO₂ adsorption heats (30-40 kJ/mol) give better performance for CO₂ separation in the PSA pressure region, and the adsorbents with high CO₂ heats of adsorption (40-50 kJ/mol) have better CO₂ separation performance in the VSA region. Therefore, our materials such as Li-, Na-, and K-ZK-5 display better CO₂ working capacity and CO₂/N₂ selectivity than samples of NaY and 13X in the VSA pressure region. The promising adsorbents for CO₂ separation are also dependent on the chosen PSA, VSA pressure regions. As mentioned in chapter 1, pressurizing a huge amount of

flue gas could be more challenging than evacuating the mixture. In addition, the selectivity of CO₂/N₂ in the low pressure regions are always higher than in the high pressure regions because the adsorbates and adsorbents interaction are more distinguishable at the low concentration of adsorbate investigated. As compared to low silica commercial zeolites such as LTA, NaY, Na13X, the studied materials CHA and ZK-5 have a high hydrothermal stability as well as a high potential for CO₂ capture especially using the adsorption-driven vacuum swing (VSA) technique. In industrial applications, Li-, Na- zeolites with high adsorption capacity and heats of adsorption would be potential in TSA processes.

In chapter 4, we performed a structural analysis of cation-exchanged chabazites with Si/Al = 6 and 12, and the siliceous form of zeolite chabazites with in situ CO₂ gas loading by X-ray and neutron diffraction. Li⁺ and Na⁺ cations were observed at site SII of the D6R, where the larger K⁺ cation were found at D6R and 8MR. These exchanged cations in chabazites are all open metal sites providing strong binding interactions with CO₂ through induced polarizability of the adsorbate. CHA-type zeolites have shown to have excellent properties of the adsorption of CO₂, with unexpectedly high adsorption capacity at relatively high Si/Al ratios (SAR~6). These zeolites show high dispersion energy and high charge-quadrupole interactions between CO₂ and 8-membered rings (8MR). In addition, these materials have accessible cation sites for adsorbates, and high pore volume (Li- and Na-CHA-6) leading to adsorption capacity comparable to low silica commercial faujasite and Linde type A zeolites. Measured experimental isosteric heats of adsorption of CO₂ depend significantly on the cation type, cation concentration, and on the amount of adsorbed CO₂ and were interpreted at the molecular level based on adsorption sites determined using the

Rietveld technique of synchrotron and neutron diffraction data. Two adsorption sites of CO₂ were found in all chabazite samples, in which CO₂ site in the 8MR is dominant. The decrease in the hardness of metal cations $\text{Li}^+ > \text{Na}^+ > \text{K}^+ > \text{Cu}^{2+}$ resulted in a decrease in the direct interaction of these cations with adsorbate CO₂. The formation of CO₂ adsorption complexes on dual cation sites was observed on K-CHA-6. The relationship of zeolite structures to their adsorption energy interactions and the adsorption properties were identified and discussed in detail.

Similar investigations were performed on ZK-5 materials with exchanged cations Li^+ , Na^+ , K^+ , and Mg^{2+} . Compared to CHA zeolites (contains one ellipsoidal cage type), KFI zeolite contains two different types of cages (*lta* and *pau* type cages) and a less uniform adsorption space. The adsorption behaviors of CO₂ in cation-exchanged ZK-5 zeolites were much more complicated than is the case for chabazite zeolites. As was found with chabazite, Li-forms of ZK-5 displayed the highest adsorption capacity at 1 bar pressure, and showed lower selectivity of CO₂/N₂ its higher electrostatic interaction with N₂ molecules. Mg-ZK-5 showed the lowest heats of adsorption among other studied cations because Mg^{2+} cations were located in the inaccessible positions and the electric fields could be more localized in the hidden location where CO₂ cannot interact with it. There was an indication of a slight migration of the extra-framework Li^+ and Mg^{2+} cations away from the D6R upon the adsorption with CO₂ molecules. The dual-cation sites between two Li^+ , Na^+ , and K^+ cations and CO₂ were found in these cation-exchanged ZK-5 materials. These dual-cation adsorption sites are the key factor that explains the observed high heats of adsorption of CO₂ on these adsorbents. The CO₂ site in the *pau*-cages of Na-ZK-5 could be in a bent mode due to a high energy interaction of CO₂ with two Na^+ cations.

Our findings of adsorption sites of CO₂ in the 8-membered ring zeolites and the correlation between structure properties and the adsorption behaviors have provided a molecule understanding of interactions between CO₂ and cations, CHA and ZK-5 zeolite frameworks.

In chapter 6, we have investigated in the effect of various hydrophobic zeolite framework structures on the adsorption properties of CO₂ and N₂. Both CO₂ and N₂ showed higher adsorption heats and adsorption capacities in the smaller pore/window size siliceous zeolites. In agreement with the experiment, GCMC simulation also showed that CO₂ exhibit higher affinity for the zeolites than N₂ and FER zeolite has the highest selectivity of CO₂ over N₂ among the samples investigated. The hydrophobic properties of the siliceous zeolites make them potential candidates for CO₂ separation by PSA processes, especially in the presence of water.

The last chapter focused on the characterization of hydrophobic siliceous zeolites of framework types AEI, CHA, RRO, and STT, their adsorption properties with respect to light hydrocarbons, and their separation properties of CO₂/CH₄ and propylene/propane. The adsorption capacities, enthalpies, and entropies of the hydrocarbons in the siliceous zeolites were mainly controlled by their polarizability. A significant difference in the adsorption heats and adsorption capacity of CO₂ over CH₄ in these siliceous zeolites is due to a higher quadrupole moment of CO₂ molecule. AEI, CHA, and RRO zeolites are feasible for propane-propylene separations based on the gases kinetic diffusion properties. RRO is a potential candidate for the separation of CO₂ from methane in natural gas mixtures. Our investigations also provide experimental data for testing the validity of molecular simulation such as Grand Canonical Monte Carlo or Molecular Dynamics.

8.2 Recommendations for Future Studies

8.2.1 The adsorption of CO₂ on various zeolite frameworks

Even though nanoporous materials have emerged as candidate for CO₂ capture, there are still limitations that make the adsorption process less effective: low selectivity and capacity of available adsorbent for CO₂, lower removal efficiency as compared to other technologies such as absorption and cryogenic, high cost, low performance under humid condition. Therefore, we need to develop new adsorbents or modify the surface and structure of existing adsorbents so that they can operate at higher temperatures in the presence of steam and to improved selectivity.

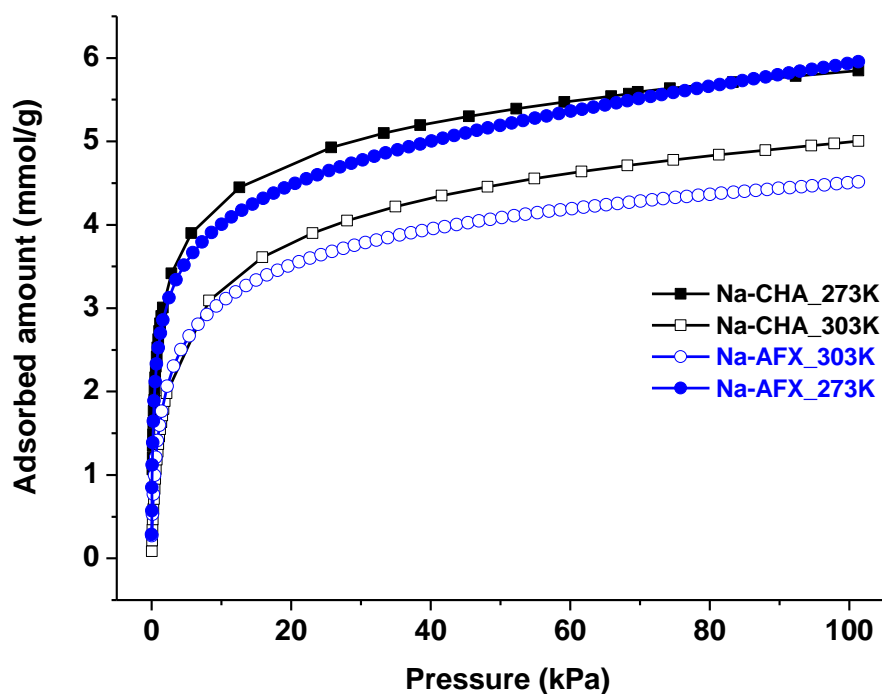


Figure 8.1. Adsorption isotherms of CO₂ on Na-CHA and Na-AFX at 273 K and 303 K

AFX, containing *gme*- and *aft*-cages (Figure 8.2), showed high adsorption capacities and different properties than CHA at 273 K and 303 K (Figure 8.1). AEI is also another model to study the adsorption sites of CO₂ on these zeolites to get more overall structure-properties relationships between 8MR zeolites for CO₂ adsorption and then help us to develop new adsorbents with higher CO₂ separation performance.

LTA and FAU zeolites with sodalite cages can be modified by occluding alkali halides [3] to improve the electric field inside the pores of these materials and thus the adsorption capacity and selectivity of CO₂. Large cages or large channels of faujasite, zeolite beta or similar frameworks could be grafted with amine functional groups to improve the basicity of the surface and selectivity of CO₂ over N₂ (Figure 8.3)[4].



Figure 8.2. The composite building units (*gme*-left, *aft*-right) of AFX zeolite

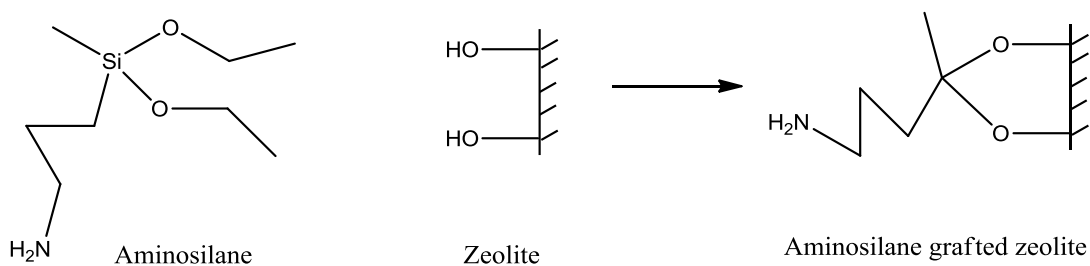


Figure 8.3. A schematic of the chemical modification of the zeolite surface

The substitution of framework Si^{4+} ions by Li^+ ([Li-Si-O]-MFI), an Li-substituted zincosilicate with ANA topology ($\text{Cs}_{12}\text{Li}_{13}[\text{Li}_3\text{Zn}_8\text{Si}_{37}\text{O}_{96}]\cdot 4\text{H}_2\text{O}$), and Li, Ni-exchanged zincosilicate materials (Li, Ni-CIT-6) have been reported recently [5-7]. Monovalent and divalent ions requires three/two times more charge-balancing M^+ extraframework cations, in comparison to Al^{3+} substitution. This might lead to new ion-exchange, and acid-base, and CO_2 gas adsorption properties of the new zeolite materials.

Metal-organic frameworks (MOFs), zeolitic imidazolate frameworks (ZIFs) [8, 9] have recently attracted intense research interest because of their high porous structures, tunable frameworks, and many of them possess superior surface areas relative to those of traditional adsorbents such as activated carbon and zeolites. The study of structure-property relationships of these materials for CO_2 adsorption by Rietveld refinements could be compensative to the understanding of CO_2 adsorption into nanoporous frameworks, and thus contribute to the development of new materials for CO_2 separation.

8.2.2 Effect of water on the adsorption of CO_2 in zeolites

The flue gas is saturated with 5–7% by volume of water [10], it is essential to consider the humidity effects on the CO_2 adsorption capacity and CO_2/N_2 selectivity of zeolite materials. Water has large dipole moment and has been found to have detrimental effects on CO_2 adsorption of zeolite adsorbents due to the high affinity of water molecule with extra-framework cations. Smit performed molecular simulations to model the adsorption of $\text{H}_2\text{O}/\text{CO}_2$ mixture in 13X and showed that H_2O reduces the CO_2 adsorption capacity of these materials by an order of magnitude; 13X will be

essentially saturated with H₂O at the partial pressures of H₂O relevant for post-combustion capture [11]. Since 13X is more hydrophilic than NaY, and much more hydrophilic than cation-exchanged CHA, Si-CHA zeolites (Figure 8.4), the adsorbents investigated in this thesis are more tolerant to water vapor than the commercial zeolites. Structural refinements of X-ray powder diffraction of co-adsorption of CO₂ and H₂O on Cu-CHA-6 (Cu (1.21 molecules/u.c), CO₂ (1.04 molecules/u.c), and H₂O (1.19 molecules/u.c)) showed that at low concentration of water (~0.55 mmol H₂O/g Cu-CHA-6), water prefers to adsorb on Cu²⁺ site by electrostatic interaction with a distance of O-Cu is 2.97(1) Å. CO₂ molecules are still predominantly located in the middle of 8MRs (Figure 8.5). The distance between O of water and O of CO₂ is 3.04(6) Å (close to Van der Waals sum of radii) indicate that small amount of water might promote the adsorption of CO₂ in Cu-CHA-6. At higher water pressures, we found that Cu²⁺ cations were pulled up into the ellipsoidal cages of chabazites zeolite. The quality of the data is not sufficient (peak broaden, peak shape, asymmetric peaks) to conclusively establish the effect of high H₂O content on CO₂ adsorption. To be able to understand better the effect of H₂O on CO₂ adsorption, the dual adsorption isotherms of the mixtures of CO₂ and water needed to be collected and adsorption sites of these adsorbates need to further studied by X-ray and neutron diffraction. FTIR spectroscopy may be helpful to characterize the species of water and carbon dioxide in the zeolites. Such an experimental investigation should be run as along with high-quality molecule simulations. For example, Siepmann et al [12] in a recent publication in *J. Phys. Chem. C* showed that the H-bond network properties of water change dramatically upon adsorption into (Si-MFI) due to the hydrophobicity of the interior

and structural confinement, and at high loading water has a high probability of forming long, contiguous H-bonded chains in Si-MFI.

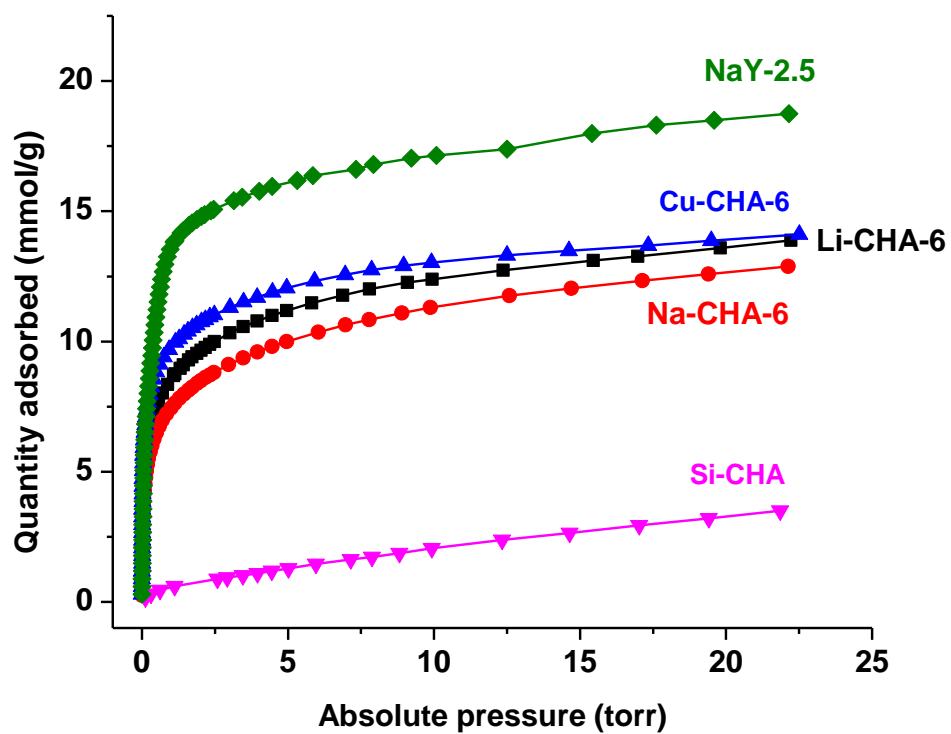


Figure 8.4. Adsorption isotherms of H₂O on NaY, Si-CHA and cation-exchanged CHA at 303 K

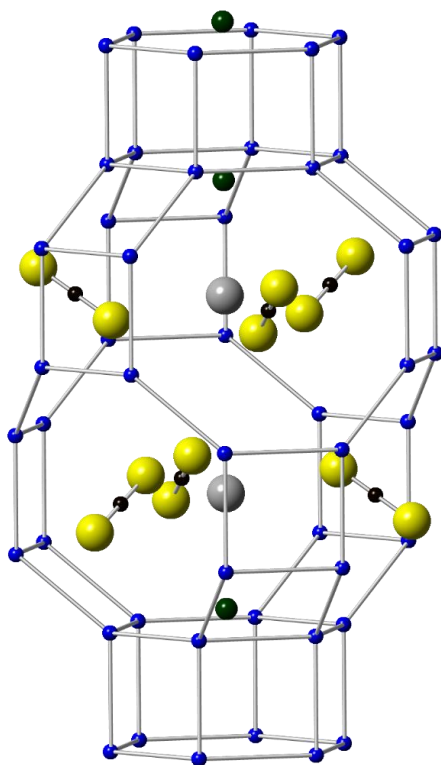


Figure 8.5. Adsorption sites of CO₂ and H₂O co-adsorbed on Cu-CHA-6

8.2.3 Other factors on the adsorption of CO₂

Other compounds such as O₂, NO_x, and SO_x are also present in the flue gas mixture (their properties are shown in table 8.1). NO and O₂ might have similar adsorption properties as N₂. However, NO₂, SO₂ and SO₃ are quite strong acids and would affect more severely the adsorption of CO₂. In addition, NO₂ and SO₂ have higher polarizability and dipole moment compared to CO₂. This could lead to strong effect of these two gases on CO₂ adsorption properties even the amount of these two gases in the flue gas mixture is not significant. The methods to study the effect of these gases on CO₂ adsorption are similar to what we use to study for H₂O. SO₃ with

large kinetic diameter would be excluded from 8MR windows, and would not affect severely on the adsorption of CO₂.

Table 8.1. Properties of several adsorbates in flue gas mixture [13]

Gas	Kinetics diameters (Å)	Polarizability (x10 ⁻²⁵ cm ³)	Dipole (x10 ⁻¹⁸ esu.cm)	Quadrupole (x10 ⁻²⁶ esu.cm ²)
CO ₂	3.3	29.1	0	4.3
NO	3.492	17	0.15872	-
NO ₂	-	30.2	0.316	-
SO ₂	4.112	37.2–42.8	1.63305	-
O ₂	3.467	15.812	-	0.39
N ₂	3.64	17.4	0	1.52

8.2.4 Other methods to study CO₂ adsorption

Dynamic adsorption of CO₂ should be measured through breakthrough experiments instead of equilibrium adsorption isotherms of CO₂ on zeolite materials because dynamic uptake is more representative of the materials properties needed for industrial applications. The set-up for break through experiments for single and dual adsorption isotherms is quite simple as described by Xiong Su *et al* [14].

Ideal adsorbed solution theory (IAST) [15] and RAST (Real Adsorption Solution Theory) [16, 17] are very helpful to predict multicomponent competitive interactions of the mixture CO₂, N₂ and other gas components in the flue gas mixtures. A combination of experimental methods with theoretical methods such as DFT, GCMC would be more helpful to understand the adsorption species of CO₂ in the zeolites and help us to screen the best adsorbents for CO₂ capture.

FTIR of CO₂ and N₂ at liquid nitrogen temperature would be very helpful to see the interaction of these gases in the zeolites. For example, the evidence for the direct interaction of N₂ with Li cations in Li-ZK-5 is more supportive if we see a shift in the vibration of N₂ in the adsorbed phase compared to the gas phase. The movement of CO₂ in Mg-ZK-5 can be seen by a shift to higher frequency of the asymmetric stretching vibration of CO₂ in the adsorbed phase compared to the CO₂ gas phase.

8.3 Thesis Accomplishments

We have investigated the effects of temperature, pressure, cation-type, zeolite frameworks, hydrophobicity of the adsorbents, and CO₂ adsorbed amount on the adsorption properties of CO₂. We identified potential zeolite materials for various separation processes of CO₂ from flue gas mixtures such as pressure/vacuum swing adsorption and temperature swing adsorption techniques. We combined experimental methods with GCMC simulations to compare and identify the structure-related performance for CO₂ separation. We correlated the structure-property relations of cation-exchanged zeolites for CO₂ adsorption using mainly X-ray and neutron powder diffraction techniques. We showed the ability to design and tune the properties of zeolite materials to make these adsorbents better for CO₂ separation based on our structural refinements of CO₂ adsorbed on zeolites and the measurements of adsorption isotherms. We also provided extensive experimental data to validate the host-guest energy interaction assumptions in molecular simulations. Important challenges will still need to be solved, but we are optimistic that new zeolites or nanoporous materials in general with overall better performance than the currently used amine scrubbing solutions will be discovered based on our studies and similar

reports from literature on the structure-properties relationships of adsorbents for CO₂ adsorption.

REFERENCES

1. Liu, Q., et al., *ZK-5: A CO₂-Selective Zeolite with High Working Capacity at Ambient Temperature and Pressure*. ChemSusChem, 2012. **5**(11): p. 2237-2242.
2. Bae, Y.-S. and R.Q. Snurr, *Development and Evaluation of Porous Materials for Carbon Dioxide Separation and Capture*. Angewandte Chemie International Edition, 2011. **50**(49): p. 11586-11596.
3. Seidel, A., et al., *²³Na solid state MAS NMR of sodium halides occluded in zeolites*. Solid State Nuclear Magnetic Resonance, 1997. **9**(2-4): p. 129-141.
4. Sanaeepur, H., A. Kargari, and B. Nasernejad, *Aminosilane-functionalization of a nanoporous Y-type zeolite for application in a cellulose acetate based mixed matrix membrane for CO₂ separation*. RSC Advances, 2014. **4**(109): p. 63966-63976.
5. Park, S.-H., et al., *[Li-Si-O]-MFI: A New Microporous Lithosilicate with the MFI Topology*. Chemistry of Materials, 2004. **16**(13): p. 2605-2614.
6. Park, S.-H., et al., *Characterization of a New Microporous Lithozincosilicate with ANA Topology*. Chemistry of Materials, 2002. **14**(7): p. 3187-3196.
7. Deimund, M.A., J. Labinger, and M.E. Davis, *Nickel-Exchanged Zincosilicate Catalysts for the Oligomerization of Propylene*. ACS Catalysis, 2014. **4**(11): p. 4189-4195.
8. Phan, A., et al., *Synthesis, Structure, and Carbon Dioxide Capture Properties of Zeolitic Imidazolate Frameworks*. Accounts of Chemical Research, 2010. **43**(1): p. 58-67.
9. Liu, J., et al., *Progress in adsorption-based CO₂ capture by metal-organic frameworks*. Chemical Society Reviews, 2012. **41**(6): p. 2308-2322.
10. Liu, Y., Z.U. Wang, and H.-C. Zhou, *Recent advances in carbon dioxide capture with metal-organic frameworks*. Greenhouse Gases: Science and Technology, 2012. **2**(4): p. 239-259.
11. Joos, L., J.A. Swisher, and B. Smit, *Molecular Simulation Study of the Competitive Adsorption of H₂O and CO₂ in Zeolite 13X*. Langmuir, 2013. **29**(51): p. 15936-15942.
12. Wang, C.-H., et al., *Deconstructing Hydrogen-Bond Networks in Confined Nanoporous Materials: Implications for Alcohol-Water Separation*. The Journal of Physical Chemistry C, 2014. **118**(34): p. 19723-19732.
13. Li, J.-R., R.J. Kuppler, and H.-C. Zhou, *Selective gas adsorption and separation in metal-organic frameworks*. Chemical Society Reviews, 2009. **38**(5): p. 1477-1504.

14. Su, X., et al., *Synthesis of DNL-6 with a High Concentration of Si (4 Al) Environments and its Application in CO₂ Separation*. ChemSusChem, 2013. **6**(5): p. 911-918.
15. Dickey, A.N., et al., *Screening CO₂/N₂ selectivity in metal-organic frameworks using Monte Carlo simulations and ideal adsorbed solution theory*. The Canadian Journal of Chemical Engineering, 2012. **90**(4): p. 825-832.
16. Sochard, S., N. Fernandes, and J.-M. Reneaume, *Modeling of adsorption isotherm of a binary mixture with real adsorbed solution theory and nonrandom two-liquid model*. AIChE Journal, 2010. **56**(12): p. 3109-3119.
17. Yun, J., H. Park, and H. Moon, *Multicomponent adsorption calculations based on adsorbed solution theory*. Korean Journal of Chemical Engineering, 1996. **13**(3): p. 246-254.

Appendix
PERMISSION LETTERS

**ELSEVIER LICENSE
TERMS AND CONDITIONS**

May 04, 2015

This is a License Agreement between Trong D Pham ("You") and Elsevier ("Elsevier") provided by Copyright Clearance Center ("CCC"). The license consists of your order details, the terms and conditions provided by Elsevier, and the payment terms and conditions.

All payments must be made in full to CCC. For payment instructions, please see information listed at the bottom of this form.

Supplier	Elsevier Limited The Boulevard, Langford Lane Kidlington, Oxford, OX5 1GB, UK
Registered Company Number	1982084
Customer name	Trong D Pham
Customer address	150 Academy St NEWARK, DE 19716
License number	3622101367432
License date	May 04, 2015
Licensed content publisher	Elsevier
Licensed content publication	Microporous and Mesoporous Materials
Licensed content title	Experimental and computational studies on the adsorption of CO ₂ and N ₂ on pure silica zeolites
Licensed content author	Trong D. Pham, Ruichang Xiong, Stanley I. Sandler, Raul F. Lobo
Licensed content date	1 February 2014
Licensed content volume number	185
Licensed content issue number	n/a
Number of pages	10
Start Page	157
End Page	166
Type of Use	reuse in a thesis/dissertation
Intended publisher of new work	other
Portion	full article
Format	both print and electronic
Are you the author of this Elsevier article?	Yes
Will you be translating?	No

Title of your thesis/dissertation	Experimental Investigations of the Structure-Property Relations of CO ₂ -Selective Zeolite Adsorbents
Expected completion date	May 2015
Estimated size (number of pages)	275
Elsevier VAT number	GB 494 6272 12
Permissions price	0.00 USD
VAT/Local Sales Tax	0.00 USD / 0.00 GBP
Total	0.00 USD
Terms and Conditions	

INTRODUCTION

1. The publisher for this copyrighted material is Elsevier. By clicking "accept" in connection with completing this licensing transaction, you agree that the following terms and conditions apply to this transaction (along with the Billing and Payment terms and conditions established by Copyright Clearance Center, Inc. ("CCC"), at the time that you opened your Rightslink account and that are available at any time at <http://myaccount.copyright.com>).

GENERAL TERMS

2. Elsevier hereby grants you permission to reproduce the aforementioned material subject to the terms and conditions indicated.

3. Acknowledgement: If any part of the material to be used (for example, figures) has appeared in our publication with credit or acknowledgement to another source, permission must also be sought from that source. If such permission is not obtained then that material may not be included in your publication/copies. Suitable acknowledgement to the source must be made, either as a footnote or in a reference list at the end of your publication, as follows:

"Reprinted from Publication title, Vol /edition number, Author(s), Title of article / title of chapter, Pages No., Copyright (Year), with permission from Elsevier [OR APPLICABLE SOCIETY COPYRIGHT OWNER]." Also Lancet special credit - "Reprinted from The Lancet, Vol. number, Author(s), Title of article, Pages No., Copyright (Year), with permission from Elsevier."

4. Reproduction of this material is confined to the purpose and/or media for which permission is hereby given.

5. Altering/Modifying Material: Not Permitted. However figures and illustrations may be altered/adapted minimally to serve your work. Any other abbreviations, additions, deletions and/or any other alterations shall be made only with prior written authorization of Elsevier Ltd. (Please contact Elsevier at permissions@elsevier.com)

6. If the permission fee for the requested use of our material is waived in this instance, please be advised that your future requests for Elsevier materials may attract a fee.

7. Reservation of Rights: Publisher reserves all rights not specifically granted in the

combination of (i) the license details provided by you and accepted in the course of this licensing transaction, (ii) these terms and conditions and (iii) CCC's Billing and Payment terms and conditions.

8. License Contingent Upon Payment: While you may exercise the rights licensed immediately upon issuance of the license at the end of the licensing process for the transaction, provided that you have disclosed complete and accurate details of your proposed use, no license is finally effective unless and until full payment is received from you (either by publisher or by CCC) as provided in CCC's Billing and Payment terms and conditions. If full payment is not received on a timely basis, then any license preliminarily granted shall be deemed automatically revoked and shall be void as if never granted. Further, in the event that you breach any of these terms and conditions or any of CCC's Billing and Payment terms and conditions, the license is automatically revoked and shall be void as if never granted. Use of materials as described in a revoked license, as well as any use of the materials beyond the scope of an unrevoked license, may constitute copyright infringement and publisher reserves the right to take any and all action to protect its copyright in the materials.

9. Warranties: Publisher makes no representations or warranties with respect to the licensed material.

10. Indemnity: You hereby indemnify and agree to hold harmless publisher and CCC, and their respective officers, directors, employees and agents, from and against any and all claims arising out of your use of the licensed material other than as specifically authorized pursuant to this license.

11. No Transfer of License: This license is personal to you and may not be sublicensed, assigned, or transferred by you to any other person without publisher's written permission.

12. No Amendment Except in Writing: This license may not be amended except in a writing signed by both parties (or, in the case of publisher, by CCC on publisher's behalf).

13. Objection to Contrary Terms: Publisher hereby objects to any terms contained in any purchase order, acknowledgment, check endorsement or other writing prepared by you, which terms are inconsistent with these terms and conditions or CCC's Billing and Payment terms and conditions. These terms and conditions, together with CCC's Billing and Payment terms and conditions (which are incorporated herein), comprise the entire agreement between you and publisher (and CCC) concerning this licensing transaction. In the event of any conflict between your obligations established by these terms and conditions and those established by CCC's Billing and Payment terms and conditions, these terms and conditions shall control.

14. Revocation: Elsevier or Copyright Clearance Center may deny the permissions described in this License at their sole discretion, for any reason or no reason, with a full refund payable to you. Notice of such denial will be made using the contact information provided by you. Failure to receive such notice will not alter or invalidate the denial. In no event will Elsevier or Copyright Clearance Center be responsible or liable for any costs, expenses or damage incurred by you as a result of a denial of your permission request, other than a refund of the amount(s) paid by you to Elsevier and/or Copyright Clearance Center for denied permissions.

LIMITED LICENSE

The following terms and conditions apply only to specific license types:

15. Translation: This permission is granted for non-exclusive world **English** rights only unless your license was granted for translation rights. If you licensed translation rights you may only translate this content into the languages you requested. A professional translator must perform all translations and reproduce the content word for word preserving the integrity of the article. If this license is to re-use 1 or 2 figures then permission is granted for non-exclusive world rights in all languages.

16. Posting licensed content on any Website: The following terms and conditions apply as follows: Licensing material from an Elsevier journal: All content posted to the web site must maintain the copyright information line on the bottom of each image; A hyper-text must be included to the Homepage of the journal from which you are licensing at <http://www.sciencedirect.com/science/journal/xxxxx> or the Elsevier homepage for books at <http://www.elsevier.com>; Central Storage: This license does not include permission for a scanned version of the material to be stored in a central repository such as that provided by Heron/XanEdu.

Licensing material from an Elsevier book: A hyper-text link must be included to the Elsevier homepage at <http://www.elsevier.com>. All content posted to the web site must maintain the copyright information line on the bottom of each image.

Posting licensed content on Electronic reserve: In addition to the above the following clauses are applicable: The web site must be password-protected and made available only to bona fide students registered on a relevant course. This permission is granted for 1 year only. You may obtain a new license for future website posting.

17. For journal authors: the following clauses are applicable in addition to the above:

Preprints:

A preprint is an author's own write-up of research results and analysis, it has not been peer-reviewed, nor has it had any other value added to it by a publisher (such as formatting, copyright, technical enhancement etc.).

Authors can share their preprints anywhere at any time. Preprints should not be added to or enhanced in any way in order to appear more like, or to substitute for, the final versions of articles however authors can update their preprints on arXiv or RePEc with their Accepted Author Manuscript (see below).

If accepted for publication, we encourage authors to link from the preprint to their formal publication via its DOI. Millions of researchers have access to the formal publications on ScienceDirect, and so links will help users to find, access, cite and use the best available version. Please note that Cell Press, The Lancet and some society-owned have different preprint policies. Information on these policies is available on the journal homepage.

Accepted Author Manuscripts: An accepted author manuscript is the manuscript of an article that has been accepted for publication and which typically includes author-incorporated changes suggested during submission, peer review and editor-author

communications.

Authors can share their accepted author manuscript:

- immediately
 - via their non-commercial person homepage or blog
 - by updating a preprint in arXiv or RePEc with the accepted manuscript
 - via their research institute or institutional repository for internal institutional uses or as part of an invitation-only research collaboration work-group
 - directly by providing copies to their students or to research collaborators for their personal use
 - for private scholarly sharing as part of an invitation-only work group on commercial sites with which Elsevier has an agreement
- after the embargo period
 - via non-commercial hosting platforms such as their institutional repository
 - via commercial sites with which Elsevier has an agreement

In all cases accepted manuscripts should:

- link to the formal publication via its DOI
- bear a CC-BY-NC-ND license - this is easy to do
- if aggregated with other manuscripts, for example in a repository or other site, be shared in alignment with our hosting policy not be added to or enhanced in any way to appear more like, or to substitute for, the published journal article.

Published journal article (JPA): A published journal article (PJA) is the definitive final record of published research that appears or will appear in the journal and embodies all value-adding publishing activities including peer review co-ordination, copy-editing, formatting, (if relevant) pagination and online enrichment.

Policies for sharing publishing journal articles differ for subscription and gold open access articles:

Subscription Articles: If you are an author, please share a link to your article rather than the full-text. Millions of researchers have access to the formal publications on ScienceDirect, and so links will help your users to find, access, cite, and use the best available version.

Theses and dissertations which contain embedded PJAs as part of the formal submission can be posted publicly by the awarding institution with DOI links back to the formal publications on ScienceDirect.

If you are affiliated with a library that subscribes to ScienceDirect you have additional

private sharing rights for others' research accessed under that agreement. This includes use for classroom teaching and internal training at the institution (including use in course packs and courseware programs), and inclusion of the article for grant funding purposes.

Gold Open Access Articles: May be shared according to the author-selected end-user license and should contain a [CrossMark logo](#), the end user license, and a DOI link to the formal publication on ScienceDirect.

Please refer to Elsevier's [posting policy](#) for further information.

18. For book authors the following clauses are applicable in addition to the above: Authors are permitted to place a brief summary of their work online only. You are not allowed to download and post the published electronic version of your chapter, nor may you scan the printed edition to create an electronic version. **Posting to a repository:** Authors are permitted to post a summary of their chapter only in their institution's repository.

19. Thesis/Dissertation: If your license is for use in a thesis/dissertation your thesis may be submitted to your institution in either print or electronic form. Should your thesis be published commercially, please reapply for permission. These requirements include permission for the Library and Archives of Canada to supply single copies, on demand, of the complete thesis and include permission for Proquest/UMI to supply single copies, on demand, of the complete thesis. Should your thesis be published commercially, please reapply for permission. Theses and dissertations which contain embedded PJAs as part of the formal submission can be posted publicly by the awarding institution with DOI links back to the formal publications on ScienceDirect.

Elsevier Open Access Terms and Conditions

You can publish open access with Elsevier in hundreds of open access journals or in nearly 2000 established subscription journals that support open access publishing. Permitted third party re-use of these open access articles is defined by the author's choice of Creative Commons user license. See our [open access license policy](#) for more information.

Terms & Conditions applicable to all Open Access articles published with Elsevier:

Any reuse of the article must not represent the author as endorsing the adaptation of the article nor should the article be modified in such a way as to damage the author's honour or reputation. If any changes have been made, such changes must be clearly indicated.

The author(s) must be appropriately credited and we ask that you include the end user license and a DOI link to the formal publication on ScienceDirect.

If any part of the material to be used (for example, figures) has appeared in our publication with credit or acknowledgement to another source it is the responsibility of the user to ensure their reuse complies with the terms and conditions determined by the rights holder.

Additional Terms & Conditions applicable to each Creative Commons user license:

CC BY: The CC-BY license allows users to copy, to create extracts, abstracts and new works from the Article, to alter and revise the Article and to make commercial use of the

Article (including reuse and/or resale of the Article by commercial entities), provided the user gives appropriate credit (with a link to the formal publication through the relevant DOI), provides a link to the license, indicates if changes were made and the licensor is not represented as endorsing the use made of the work. The full details of the license are available at <http://creativecommons.org/licenses/by/4.0>.

CC BY NC SA: The CC BY-NC-SA license allows users to copy, to create extracts, abstracts and new works from the Article, to alter and revise the Article, provided this is not done for commercial purposes, and that the user gives appropriate credit (with a link to the formal publication through the relevant DOI), provides a link to the license, indicates if changes were made and the licensor is not represented as endorsing the use made of the work. Further, any new works must be made available on the same conditions. The full details of the license are available at <http://creativecommons.org/licenses/by-nc-sa/4.0>.

CC BY NC ND: The CC BY-NC-ND license allows users to copy and distribute the Article, provided this is not done for commercial purposes and further does not permit distribution of the Article if it is changed or edited in any way, and provided the user gives appropriate credit (with a link to the formal publication through the relevant DOI), provides a link to the license, and that the licensor is not represented as endorsing the use made of the work. The full details of the license are available at <http://creativecommons.org/licenses/by-nc-nd/4.0>. Any commercial reuse of Open Access articles published with a CC BY NC SA or CC BY NC ND license requires permission from Elsevier and will be subject to a fee.

Commercial reuse includes:

- Associating advertising with the full text of the Article
- Charging fees for document delivery or access
- Article aggregation
- Systematic distribution via e-mail lists or share buttons

Posting or linking by commercial companies for use by customers of those companies.

20. Other Conditions:

v1.7

Questions? customercare@copyright.com or +1-855-239-3415 (toll free in the US) or +1-978-646-2777.

Gratis licenses (referencing \$0 in the Total field) are free. Please retain this printable license for your reference. No payment is required.



**JOHN WILEY AND SONS LICENSE
TERMS AND CONDITIONS**

May 04, 2015

This Agreement between Trong D Pham ("You") and John Wiley and Sons ("John Wiley and Sons") consists of your license details and the terms and conditions provided by John Wiley and Sons and Copyright Clearance Center.

License Number	3622100059217
License date	May 04, 2015
Licensed Content Publisher	John Wiley and Sons
Licensed Content Publication	ChemSusChem
Licensed Content Title	Molecular Basis for the High CO ₂ Adsorption Capacity of Chabazite Zeolites
Licensed Content Author	Trong D. Pham,Matthew R. Hudson,Craig M. Brown,Raul F. Lobo
Licensed Content Date	Oct 1, 2014
Pages	8
Type of use	Dissertation/Thesis
Requestor type	Author of this Wiley article
Format	Print and electronic
Portion	Full article
Will you be translating?	No
Title of your thesis / dissertation	Experimental Investigations of the Structure-Property Relations of CO ₂ -Selective Zeolite Adsorbents
Expected completion date	May 2015
Expected size (number of pages)	275
Requestor Location	Trong D Pham 150 Academy St Colburn Lab NEWARK, DE 19716 United States Attn: Trong D Pham
Billing Type	Invoice
Billing Address	Trong D Pham 150 Academy St Colburn Lab NEWARK, DE 19716 United States Attn: Trong D Pham
Total	0.00 USD

TERMS AND CONDITIONS

This copyrighted material is owned by or exclusively licensed to John Wiley & Sons, Inc. or one of its group companies (each a "Wiley Company") or handled on behalf of a society with which a Wiley Company has exclusive publishing rights in relation to a particular work (collectively "WILEY"). By clicking  accept  in connection with completing this licensing transaction, you agree that the following terms and conditions apply to this transaction (along with the billing and payment terms and conditions established by the Copyright Clearance Center Inc., ("CCC's Billing and Payment terms and conditions"), at the time that you opened your Rightslink account (these are available at any time at <http://myaccount.copyright.com>).

Terms and Conditions

- The materials you have requested permission to reproduce or reuse (the "Wiley Materials") are protected by copyright.
- You are hereby granted a personal, non-exclusive, non-sub licensable (on a stand-alone basis), non-transferable, worldwide, limited license to reproduce the Wiley Materials for the purpose specified in the licensing process. This license is for a one-time use only and limited to any maximum distribution number specified in the license. The first instance of republication or reuse granted by this licence must be completed within two years of the date of the grant of this licence (although copies prepared before the end date may be distributed thereafter). The Wiley Materials shall not be used in any other manner or for any other purpose, beyond what is granted in the license. Permission is granted subject to an appropriate acknowledgement given to the author, title of the material/book/journal and the publisher. You shall also duplicate the copyright notice that appears in the Wiley publication in your use of the Wiley Material. Permission is also granted on the understanding that nowhere in the text is a previously published source acknowledged for all or part of this Wiley Material. Any third party content is expressly excluded from this permission.
- With respect to the Wiley Materials, all rights are reserved. Except as expressly granted by the terms of the license, no part of the Wiley Materials may be copied, modified, adapted (except for minor reformatting required by the new Publication), translated, reproduced, transferred or distributed, in any form or by any means, and no derivative works may be made based on the Wiley Materials without the prior permission of the respective copyright owner. You may not alter, remove or suppress in any manner any copyright, trademark or other notices displayed by the Wiley Materials. You may not license, rent, sell, loan, lease, pledge, offer as security, transfer or assign the Wiley Materials on a stand-alone basis, or any of the rights granted to you hereunder to any other person.
- The Wiley Materials and all of the intellectual property rights therein shall at all times remain the exclusive property of John Wiley & Sons Inc, the Wiley Companies, or their respective licensors, and your interest therein is only that of having possession of and the right to reproduce the Wiley Materials pursuant to Section 2 herein during the continuance of this Agreement. You agree that you own no right, title or interest in or

to the Wiley Materials or any of the intellectual property rights therein. You shall have no rights hereunder other than the license as provided for above in Section 2. No right, license or interest to any trademark, trade name, service mark or other branding ("Marks") of WILEY or its licensors is granted hereunder, and you agree that you shall not assert any such right, license or interest with respect thereto.

- NEITHER WILEY NOR ITS LICENSORS MAKES ANY WARRANTY OR REPRESENTATION OF ANY KIND TO YOU OR ANY THIRD PARTY, EXPRESS, IMPLIED OR STATUTORY, WITH RESPECT TO THE MATERIALS OR THE ACCURACY OF ANY INFORMATION CONTAINED IN THE MATERIALS, INCLUDING, WITHOUT LIMITATION, ANY IMPLIED WARRANTY OF MERCHANTABILITY, ACCURACY, SATISFACTORY QUALITY, FITNESS FOR A PARTICULAR PURPOSE, USABILITY, INTEGRATION OR NON-INFRINGEMENT AND ALL SUCH WARRANTIES ARE HEREBY EXCLUDED BY WILEY AND ITS LICENSORS AND WAIVED BY YOU
- WILEY shall have the right to terminate this Agreement immediately upon breach of this Agreement by you.
- You shall indemnify, defend and hold harmless WILEY, its Licensors and their respective directors, officers, agents and employees, from and against any actual or threatened claims, demands, causes of action or proceedings arising from any breach of this Agreement by you.
- IN NO EVENT SHALL WILEY OR ITS LICENSORS BE LIABLE TO YOU OR ANY OTHER PARTY OR ANY OTHER PERSON OR ENTITY FOR ANY SPECIAL, CONSEQUENTIAL, INCIDENTAL, INDIRECT, EXEMPLARY OR PUNITIVE DAMAGES, HOWEVER CAUSED, ARISING OUT OF OR IN CONNECTION WITH THE DOWNLOADING, PROVISIONING, VIEWING OR USE OF THE MATERIALS REGARDLESS OF THE FORM OF ACTION, WHETHER FOR BREACH OF CONTRACT, BREACH OF WARRANTY, TORT, NEGLIGENCE, INFRINGEMENT OR OTHERWISE (INCLUDING, WITHOUT LIMITATION, DAMAGES BASED ON LOSS OF PROFITS, DATA, FILES, USE, BUSINESS OPPORTUNITY OR CLAIMS OF THIRD PARTIES), AND WHETHER OR NOT THE PARTY HAS BEEN ADVISED OF THE POSSIBILITY OF SUCH DAMAGES. THIS LIMITATION SHALL APPLY NOTWITHSTANDING ANY FAILURE OF ESSENTIAL PURPOSE OF ANY LIMITED REMEDY PROVIDED HEREIN.
- Should any provision of this Agreement be held by a court of competent jurisdiction to be illegal, invalid, or unenforceable, that provision shall be deemed amended to achieve as nearly as possible the same economic effect as the original provision, and the legality, validity and enforceability of the remaining provisions of this Agreement shall not be affected or impaired thereby.
- The failure of either party to enforce any term or condition of this Agreement shall not constitute a waiver of either party's right to enforce each and every term and condition of this Agreement. No breach under this agreement shall be deemed waived or excused by either party unless such waiver or consent is in writing signed by the party granting such waiver or consent. The waiver by or consent of a party to a breach of

any provision of this Agreement shall not operate or be construed as a waiver of or consent to any other or subsequent breach by such other party.

- This Agreement may not be assigned (including by operation of law or otherwise) by you without WILEY's prior written consent.
- Any fee required for this permission shall be non-refundable after thirty (30) days from receipt by the CCC.
- These terms and conditions together with CCC's Billing and Payment terms and conditions (which are incorporated herein) form the entire agreement between you and WILEY concerning this licensing transaction and (in the absence of fraud) supersedes all prior agreements and representations of the parties, oral or written. This Agreement may not be amended except in writing signed by both parties. This Agreement shall be binding upon and inure to the benefit of the parties' successors, legal representatives, and authorized assigns.
- In the event of any conflict between your obligations established by these terms and conditions and those established by CCC's Billing and Payment terms and conditions, these terms and conditions shall prevail.
- WILEY expressly reserves all rights not specifically granted in the combination of (i) the license details provided by you and accepted in the course of this licensing transaction, (ii) these terms and conditions and (iii) CCC's Billing and Payment terms and conditions.
- This Agreement will be void if the Type of Use, Format, Circulation, or Requestor Type was misrepresented during the licensing process.
- This Agreement shall be governed by and construed in accordance with the laws of the State of New York, USA, without regards to such state's conflict of law rules. Any legal action, suit or proceeding arising out of or relating to these Terms and Conditions or the breach thereof shall be instituted in a court of competent jurisdiction in New York County in the State of New York in the United States of America and each party hereby consents and submits to the personal jurisdiction of such court, waives any objection to venue in such court and consents to service of process by registered or certified mail, return receipt requested, at the last known address of such party.

WILEY OPEN ACCESS TERMS AND CONDITIONS

Wiley Publishes Open Access Articles in fully Open Access Journals and in Subscription journals offering Online Open. Although most of the fully Open Access journals publish open access articles under the terms of the Creative Commons Attribution (CC BY) License only, the subscription journals and a few of the Open Access Journals offer a choice of Creative Commons Licenses:: Creative Commons Attribution (CC-BY) license [Creative Commons Attribution Non-Commercial \(CC-BY-NC\) license](#) and [Creative Commons Attribution Non-Commercial-NoDerivs \(CC-BY-NC-ND\) License](#). The license type is clearly identified on the article.

Copyright in any research article in a journal published as Open Access under a Creative Commons License is retained by the author(s). Authors grant Wiley a license to publish the article and identify itself as the original publisher. Authors also grant any third party the right to use the article freely as long as its integrity is maintained and its original authors, citation details and publisher are identified as follows: [Title of Article/Author/Journal Title and Volume/Issue. Copyright (c) [year] [copyright owner as specified in the Journal]. Links to the final article on Wiley's website are encouraged where applicable.

The Creative Commons Attribution License

The [Creative Commons Attribution License \(CC-BY\)](#) allows users to copy, distribute and transmit an article, adapt the article and make commercial use of the article. The CC-BY license permits commercial and non-commercial re-use of an open access article, as long as the author is properly attributed.

The Creative Commons Attribution License does not affect the moral rights of authors, including without limitation the right not to have their work subjected to derogatory treatment. It also does not affect any other rights held by authors or third parties in the article, including without limitation the rights of privacy and publicity. Use of the article must not assert or imply, whether implicitly or explicitly, any connection with, endorsement or sponsorship of such use by the author, publisher or any other party associated with the article.

For any reuse or distribution, users must include the copyright notice and make clear to others that the article is made available under a Creative Commons Attribution license, linking to the relevant Creative Commons web page.

To the fullest extent permitted by applicable law, the article is made available as is and without representation or warranties of any kind whether express, implied, statutory or otherwise and including, without limitation, warranties of title, merchantability, fitness for a particular purpose, non-infringement, absence of defects, accuracy, or the presence or absence of errors.

Creative Commons Attribution Non-Commercial License

The [Creative Commons Attribution Non-Commercial \(CC-BY-NC\) License](#) permits use, distribution and reproduction in any medium, provided the original work is properly cited and is not used for commercial purposes.(see below)

Creative Commons Attribution-Non-Commercial-NoDerivs License

The [Creative Commons Attribution Non-Commercial-NoDerivs License](#) (CC-BY-NC-ND) permits use, distribution and reproduction in any medium, provided the original work is properly cited, is not used for commercial purposes and no modifications or adaptations are made. (see below)

Use by non-commercial users

For non-commercial and non-promotional purposes, individual users may access, download, copy, display and redistribute to colleagues Wiley Open Access articles, as well as adapt, translate, text- and data-mine the content subject to the following conditions:

- The authors' moral rights are not compromised. These rights include the right of "paternity" (also known as "attribution" - the right for the author to be identified as such) and "integrity" (the right for the author not to have the work altered in such a way that the author's reputation or integrity may be impugned).
- Where content in the article is identified as belonging to a third party, it is the obligation of the user to ensure that any reuse complies with the copyright policies of the owner of that content.
- If article content is copied, downloaded or otherwise reused for non-commercial research and education purposes, a link to the appropriate bibliographic citation (authors, journal, article title, volume, issue, page numbers, DOI and the link to the definitive published version on **Wiley Online Library**) should be maintained. Copyright notices and disclaimers must not be deleted.
- Any translations, for which a prior translation agreement with Wiley has not been agreed, must prominently display the statement: "This is an unofficial translation of an article that appeared in a Wiley publication. The publisher has not endorsed this translation."

Use by commercial "for-profit" organisations

Use of Wiley Open Access articles for commercial, promotional, or marketing purposes requires further explicit permission from Wiley and will be subject to a fee. Commercial purposes include:

- Copying or downloading of articles, or linking to such articles for further redistribution, sale or licensing;
- Copying, downloading or posting by a site or service that incorporates advertising with such content;
- The inclusion or incorporation of article content in other works or services (other than normal quotations with an appropriate citation) that is then available for sale or licensing, for a fee (for example, a compilation produced for marketing purposes, inclusion in a sales pack)
- Use of article content (other than normal quotations with appropriate citation) by for-profit organisations for promotional purposes
- Linking to article content in e-mails redistributed for promotional, marketing or educational purposes;
- Use for the purposes of monetary reward by means of sale, resale, licence, loan, transfer or other form of commercial exploitation such as marketing products
- Print reprints of Wiley Open Access articles can be purchased from:
corporatesales@wiley.com

Further details can be found on Wiley Online Library

<http://olabout.wiley.com/WileyCDA/Section/id-410895.html>

Other Terms and Conditions:

v1.9

Questions? customercare@copyright.com or +1-855-239-3415 (toll free in the US) or +1-978-646-2777.

Gratis licenses (referencing \$0 in the Total field) are free. Please retain this printable license for your reference. No payment is required.



RightsLink®

[Home](#)[Account Info](#)[Help](#)**Title:**

Carbon Dioxide and Nitrogen
Adsorption on Cation-Exchanged
SSZ-13 Zeolites

Logged in as:

Trong Pham

[LOGOUT](#)**Author:**

Trong D. Pham, Qingling Liu,
Raul F. Lobo

Publication: Langmuir**Publisher:** American Chemical Society**Date:** Jan 1, 2013

Copyright © 2013, American Chemical Society

PERMISSION/LICENSE IS GRANTED FOR YOUR ORDER AT NO CHARGE

This type of permission/license, instead of the standard Terms & Conditions, is sent to you because no fee is being charged for your order. Please note the following:

- Permission is granted for your request in both print and electronic formats, and translations.
- If figures and/or tables were requested, they may be adapted or used in part.
- Please print this page for your records and send a copy of it to your publisher/graduate school.
- Appropriate credit for the requested material should be given as follows: "Reprinted (adapted) with permission from (COMPLETE REFERENCE CITATION). Copyright (YEAR) American Chemical Society." Insert appropriate information in place of the capitalized words.
- One-time permission is granted only for the use specified in your request. No additional uses are granted (such as derivative works or other editions). For any other uses, please submit a new request.

[BACK](#)[CLOSE WINDOW](#)

Copyright © 2015 [Copyright Clearance Center, Inc.](#) All Rights Reserved. [Privacy statement.](#) [Terms and Conditions.](#)
Comments? We would like to hear from you. E-mail us at customercare@copyright.com